

# **Guided Wave Propagation and Damage Interaction in Isotropic and Composite Structures**

by

Matthew Bridger Obenchain

A dissertation submitted in partial fulfillment  
of the requirements for the degree of  
Doctor of Philosophy  
(Aerospace Engineering)  
in the University of Michigan  
2014

Doctoral Committee:

Professor Carlos E. S. Cesnik, Chair  
Professor Daniel J. Inman  
Professor Jerome P. Lynch  
Professor Anthony M. Waas

©Matthew Bridger Obenchain

---

2014

To Amy, Caleb, and Colby

## ACKNOWLEDGMENTS

I am deeply thankful for the many people who have joined me in this journey over the past three years. I wouldn't have accomplished any of this without the support of so many friends and colleagues.

I would first like to thank the Department of Engineering Mechanics at the United States Air Force Academy for selecting me to pursue this program. I am grateful for the financial support of the United States Air Force, which allowed me to spend an entire assignment completing this degree. I would also like to acknowledge the funding support of the National Rotorcraft Technology Center (NRTC) Vertical Lift/Rotorcraft Center of Excellence (VLRCoE), with Mr. Mahendra J. Bhagwat as the technical monitor, which sponsored much of the work contained in this dissertation.

I am deeply indebted to my advisor, Prof. Carlos Cesnik, for his sound guidance and encouragement. I appreciate the countless hours he spent discussing my research, reviewing my work, and helping me to navigate the path towards completing this degree. His positive attitude always made the challenges seem a little bit smaller and the obstacles that much easier to overcome. I would also like to acknowledge the members of my dissertation committee, Prof. Dan Inman, Prof. Jerome Lynch, and Prof. Anthony Waas, for their advice and guidance during the completion of this dissertation. I am extremely grateful for the hours of fruitful discussions with Dr. Kalyan Nadella. I would not have made it through the early stages of my research without his willingness to answer all my questions about guided waves, lab equipment, and FORTRAN.

The technical staff members here were a huge help to me in the experimental stages of this project. Thanks to Terry Larrow, Tom Griffin, Chris Chartier, Dave McLean for great advice and help. I also appreciate the long-distance help from Dr. Andrew Makeev and Dr. Yuri Nikishkov at the University of Texas, Arlington while I worked on the impact damage study. Thanks to Denise Phelps for all her help navigating the requirements of this PhD program.

I have been surrounded by great friends during my time here at Michigan. I can't imagine completing this program without the camaraderie of Major Matt Dillsaver and Major Justin Rufa. I am grateful to Dr. Jared Hobeck and Alex Pankonien for the hours

spent studying for prelims and the good times at conferences. I was fortunate to have tremendous colleagues in the Active Aeroelasticity and Structures Research Lab: Dr. Nate Falkiewicz, Dr. Torstens Skujins, Dr. Devesh Kumar, Prof. Weihua Su, Jessica Jones, Ryan Klock, Ryan Kitson, Zi Yang Pang, Lucas Rocha, and Christopher Lupp. Thanks to Brian Justusson for great running advice and composites help. Thanks to Dr. Mike Sekerak for great discussions on college football, IPAs, and even research when absolutely necessary.

I am also thankful for a tremendous group of friends at Huron Hills Church. Their fellowship during this program helped me keep life in balance. Thanks to all the guys in my Friday morning mens' group for your support, challenge, encouragement, and prayers: Kevin, Dan, James, John, Josh, Skip, Dale, and Peter. Friday breakfast won't be the same without you guys.

The support of my family has been amazing during my time at Michigan. My parents have always encouraged me to challenge myself, and they have stood by me, Amy, and the boys through a tough three years. Thanks, Mom and Dad, for fervent prayers and for helping me persevere! Chuck and Judy, thanks for cheering me on, strong espresso when I needed it most, and being the best in-laws anyone could ever ask for. Jenny, Ryan, Dave, Jen, Brad, and Lauren, thanks for the great family times over the past three years. Caleb and Colby, your energy defies explanation, and your smiles have been a refreshing light for me. If you ever dust off a copy of this from our bookshelves, I hope it inspires you to never stop learning about the amazing creation God has given us to explore. Words cannot describe the support I've received from my wife, Amy. She has celebrated my successes, encouraged me during my struggles, and helped me keep things in perspective. She's been a rock keeping our family happy and healthy. She's sacrificed her own time and desires countless times to give me the space I needed to complete this program. Amy, I love you, and I've been blessed to share this journey with you!

Finally, I give all honor to my Lord and Savior Jesus Christ for giving me the abilities to complete this degree and for opening the doors needed for me to pursue my goals. May this work be for his glory.

The views expressed in this dissertation are those of the author and do not reflect the official policy or position of the United States Air Force, Department of Defense, or the U.S. Government.

# TABLE OF CONTENTS

<b>Dedication</b> . . . . .	<b>ii</b>
<b>Acknowledgments</b> . . . . .	<b>iii</b>
<b>List of Figures</b> . . . . .	<b>viii</b>
<b>List of Tables</b> . . . . .	<b>xv</b>
<b>List of Appendices</b> . . . . .	<b>xvii</b>
<b>Abstract</b> . . . . .	<b>xviii</b>
<b>Chapter</b>	
<b>1 Introduction and Literature Review</b> . . . . .	<b>1</b>
1.1 Introduction and Motivation . . . . .	1
1.2 Structural Health Monitoring . . . . .	4
1.3 Guided Wave Structural Health Monitoring . . . . .	5
1.4 Lamb Wave Fundamentals . . . . .	6
1.5 Literature Review . . . . .	10
1.5.1 Actuator and Sensor Design . . . . .	11
1.5.2 Analytical and Semi-analytical Approaches to Solve the Guided Wave Equations . . . . .	13
1.5.3 Numerical Approaches . . . . .	15
1.5.4 Guided Wave Interaction with Damage . . . . .	17
1.5.5 Time-Frequency Analysis of Guided Wave Signals . . . . .	23
1.5.6 Assessment of the State of the Art in Guided Wave SHM . . . . .	25
1.6 Dissertation Overview . . . . .	26
<b>2 Global Matrix Method</b> . . . . .	<b>28</b>
2.1 Global Matrix Formulation . . . . .	28
2.2 Axisymmetric Solution for Isotropic Lamina . . . . .	35
2.3 Anisotropic Plate Displacement Solution . . . . .	40
2.3.1 Previous Solution Method . . . . .	40
2.3.2 Updated Solution Method . . . . .	42
2.4 Square Actuator Solution . . . . .	45
2.5 Results for Cross-ply Laminate . . . . .	51
2.5.1 Experimental Setup . . . . .	51

2.5.2	Comparison of Results . . . . .	53
2.6	Summary . . . . .	58
<b>3</b>	<b>LISA Hybrid Model . . . . .</b>	<b>59</b>
3.1	LISA Hybrid Model . . . . .	59
3.2	LISA Theoretical Background . . . . .	61
3.3	Actuator Modeling . . . . .	68
3.4	Comparison of Results . . . . .	69
3.4.1	Circular Actuator Case . . . . .	70
3.4.2	CLOVER Actuator Case . . . . .	82
3.4.3	Square Actuator Case . . . . .	87
3.5	Summary . . . . .	93
<b>4</b>	<b>Guided Wave Interaction with Hole Damage . . . . .</b>	<b>95</b>
4.1	Theoretical Formulation . . . . .	95
4.1.1	Hole Modeling Strategy . . . . .	95
4.1.2	Simulated Sensor Model . . . . .	96
4.2	Holes in Isotropic Plates . . . . .	97
4.2.1	Simulation Studies . . . . .	97
4.2.2	Comparison with Experimental Results . . . . .	100
4.3	Holes in Composite Plates . . . . .	105
4.3.1	Simulation Studies . . . . .	105
4.3.2	Comparison with Experimental Data . . . . .	112
4.4	Summary . . . . .	117
<b>5</b>	<b>Guided Wave Interaction with Impact Damage . . . . .</b>	<b>118</b>
5.1	Low-velocity Impact Damage in Composite Plates . . . . .	118
5.2	Experimental Characterization of Guided Wave Interaction with Impact Damage . . . . .	124
5.2.1	Sensor Results for 0-degree Damage Site . . . . .	127
5.2.2	Sensor Results for 45-degree Damage Site . . . . .	132
5.2.3	Sensor Results for 90-degree Damage Site . . . . .	132
5.2.4	Laser Vibrometry Results . . . . .	137
5.3	Simulation of Impact Damage . . . . .	142
5.3.1	Reduction of Stiffness Properties . . . . .	145
5.3.2	Reduction of Stiffness and Density . . . . .	147
5.3.3	Simulated Delamination with Stiffness and Density Reductions . . . . .	156
5.3.4	Analysis of Simulation Results for Impact Damage Located at 0-degrees . . . . .	159
5.3.5	Comparison of Experimental and Simulation Results for Damage Located at 45 and 90 Degrees . . . . .	164
5.4	Summary . . . . .	165
<b>6</b>	<b>Damage Location and Characterization Using Matching Pursuit and a LISA Library . . . . .</b>	<b>167</b>
6.1	Theoretical Background . . . . .	167

6.1.1	Matching Pursuit Decomposition . . . . .	167
6.1.2	Choice of Waveform Dictionary . . . . .	168
6.2	Matching Pursuit Algorithm Development . . . . .	170
6.3	Matching Pursuit Algorithm: 1-D Scenario . . . . .	173
6.3.1	Identification of Hole Location . . . . .	174
6.3.2	Variation of Hole Size . . . . .	176
6.3.3	Variation of Hole Size and Location . . . . .	181
6.3.4	Robustness to Noise . . . . .	181
6.3.5	Experimental Validation . . . . .	183
6.4	Matching Pursuit Algorithm: 2-D Scenario . . . . .	187
6.4.1	2-D Analysis Using a Single Sensor . . . . .	187
6.4.2	Effect of Using Multiple Sensor and Actuator Locations . . . . .	190
6.4.3	Location of Holes Not Included in Damage Library . . . . .	191
6.5	Summary . . . . .	195
<b>7</b>	<b>Concluding Remarks . . . . .</b>	<b>196</b>
7.1	Summary . . . . .	196
7.2	Key Contributions . . . . .	198
7.3	Recommendations for Future Work . . . . .	199
	<b>Appendices . . . . .</b>	<b>203</b>
	<b>Bibliography . . . . .</b>	<b>249</b>



## LIST OF FIGURES

### Figure

1.1	Plate structure used in Lamb wave derivation. . . . .	7
1.2	Phase velocity dispersion curve for aluminum. . . . .	11
2.1	Schematic of laminated plate structure numbering scheme. . . . .	31
2.2	Actuation signal time history and frequency content for a Hann-modulated toneburst with 75 kHz center frequency. . . . .	35
2.3	Out-of-plane displacement time histories for total axisymmetric solution at 40, 60, and 80 mm locations. Results are for a circular actuator on an aluminum laminate. . . . .	37
2.4	Out-of-plane displacement time histories for outward axisymmetric solution at 40, 60, and 80 mm locations. Results are for a circular actuator on an aluminum laminate. . . . .	39
2.5	Out-of-plane displacement time histories for the total anisotropic solution for a circular actuator on an aluminum laminate at 40, 60, and 80 mm locations. . .	41
2.6	Out-of-plane displacement time histories using the previous inversion method for a circular actuator on an aluminum laminate at 40, 60, and 80 mm locations. . .	43
2.7	Out-of-plane displacement time histories using the previous inversion method for a circular actuator on an aluminum laminate at 200 mm location. . . . .	44
2.8	Correction procedure for displacement time history at 40 mm location. Results are for a circular actuator on an aluminum laminate. . . . .	46
2.9	Comparison of old and new inversion methods with exact solution at 40, 60, and 80 mm locations. Results are for a circular actuator on an aluminum laminate. . . . .	47
2.10	Original square actuator solution at 40, 60, and 80 mm locations for an aluminum laminate. . . . .	48
2.11	Corrected square actuator solution at 40, 60, and 80 mm locations for an aluminum laminate. . . . .	49
2.12	Corrected square actuator solution at 60 mm location at 15, 30, and 45 degrees for an aluminum laminate. . . . .	50
2.13	Azimuthal angles for square actuator displacement time history comparisons. . .	51
2.14	Experimental setup for cross-ply wave propagation experiment. . . . .	52
2.15	Comparison of Global Matrix and experimental results for 0-degree azimuth at 40, 60, and 80 mm locations. Results are for a circular actuator on a $[0/90]_{3S}$ laminate. . . . .	54

2.16	Comparison of Global Matrix and experimental results for 45-degree azimuth at 40, 60, and 80 mm locations. Results are for a circular actuator on a $[0/90]_{3S}$ laminate. . . . .	55
2.17	Comparison of Global Matrix and experimental results for 90-degree azimuth at 40, 60, and 80 mm locations. Results are for a circular actuator on a $[0/90]_{3S}$ laminate. . . . .	56
3.1	Schematic of displacement input field for LISA hybrid wave propagation model.	60
3.2	Overview of LISA theoretical derivation. . . . .	62
3.3	Representation of the 18 neighbors of a generic point in LISA and the Cartesian system used in the analysis [88]. . . . .	64
3.4	Additional points used for SIM continuity requirements [88]. . . . .	65
3.5	Original LISA actuation scheme for a circular actuator using specified in-plane surface displacements. . . . .	68
3.6	Original LISA actuation scheme for a CLoVER actuator sector using specified in-plane surface displacements. . . . .	69
3.7	Comparison of Global Matrix, LISA original, and LISA hybrid time histories for an aluminum plate with a circular actuator. Locations 20, 50, and 80 mm from the actuator center are shown. The Hilbert transform envelopes are included for reference. . . . .	71
3.8	Comparison of Global Matrix, LISA original, and LISA hybrid time histories for a cross-ply plate with a circular actuator, 40 mm from the actuator center. The 0, 45, and 90-degree directions are shown. The Hilbert transform envelopes are included for reference. . . . .	73
3.9	Comparison of Global Matrix, LISA original, and LISA hybrid time histories for a unidirectional plate with a circular actuator, 40 mm from the actuator center. The 0, 45, and 90-degree directions are shown. The Hilbert transform envelopes are included for reference. . . . .	74
3.10	Comparison of Global Matrix, LISA original, and LISA hybrid time histories for a quasi-isotropic plate with a circular actuator, 40 mm from the actuator center. The 0, 45, and 90-degree directions are shown. The Hilbert transform envelopes are included for reference. . . . .	75
3.11	Comparison of Global Matrix and LISA hybrid results for out-of-plane displacement of a cross-ply plate with a circular actuator at $80 \mu s$ . . . . .	76
3.12	Comparison of various LISA Hybrid in-plane discretizations for an aluminum plate with a circular actuator. Locations 20, 50, and 80 mm from the actuator center are shown. The Hilbert transform envelopes are included for reference. . . . .	78
3.13	Comparison of various LISA hybrid in-plane discretizations for the cross-ply laminate with a circular actuator at a point 70 mm away from the actuator center. The 0, 45, and 90-degree directions are shown. The Hilbert transform envelopes are included for reference. . . . .	79
3.14	Comparison of various LISA hybrid in-plane discretizations for the unidirectional laminate with a circular actuator at a point 70 mm away from the actuator center. The 0, 45, and 90-degree directions are shown. The Hilbert transform envelopes are included for reference. . . . .	80

3.15	Comparison of various LISA hybrid in-plane discretizations for the quasi-isotropic laminate with a circular actuator at a point 70 mm away from the actuator center. The 0, 45, and 90-degree directions are shown. The Hilbert transform envelopes are included for reference. . . . .	81
3.16	Comparison of Global Matrix, LISA original, and LISA hybrid time histories for an aluminum plate with a CLoVER actuator with the 0-degree sector active. The 0, 45, and 90-degree directions are shown for points 70 mm from the actuator center. The Hilbert transform envelopes are included for reference. . .	83
3.17	Comparison of Global Matrix, LISA original, and LISA hybrid time histories for a cross-ply plate with a CLoVER actuator with the 0-degree sector active. The 0, 45, and 90-degree directions are shown for points 70 mm from the actuator center. The Hilbert transform envelopes are included for reference. . .	84
3.18	Comparison of Global Matrix, LISA original, and LISA hybrid time histories for a cross-ply plate with a CLoVER actuator with the 45-degree sector active. The 0, 45, and 90-degree directions are shown for points 70 mm from the actuator center. The Hilbert transform envelopes are included for reference. . .	85
3.19	Comparison of Global Matrix, LISA original, and LISA hybrid time histories for a cross-ply plate with a CLoVER actuator with the 90-degree sector active. The 0, 45, and 90-degree directions are shown for points 70 mm from the actuator center. The Hilbert transform envelopes are included for reference. . .	86
3.20	Comparison of Global Matrix and LISA hybrid results for out-of-plane displacement of a cross-ply plate at $80 \mu s$ with various active CLoVER sectors. . .	88
3.21	Comparison of Global Matrix, LISA original, and LISA hybrid time histories for an aluminum plate with a square actuator. Locations 20, 50, and 80 mm from the actuator center are shown. The Hilbert transform envelopes are included for reference. . . . .	89
3.22	Comparison of Global Matrix, LISA original, and LISA hybrid time histories for a cross-ply plate 40mm from the square actuator center. The 0, 45, and 90-degree directions are shown. The Hilbert transform envelopes are included for reference. . . . .	90
3.23	Comparison of Global Matrix, LISA original, and LISA hybrid time histories for a unidirectional plate 40mm from the square actuator center. The 0, 45, and 90-degree directions are shown. The Hilbert transform envelopes are included for reference. . . . .	91
3.24	Comparison of Global Matrix, LISA original, and LISA hybrid time histories for a quasi-isotropic plate 40mm from the square actuator center. The 0, 45, and 90-degree directions are shown. The Hilbert transform envelopes are included for reference. . . . .	92
4.1	Damage models for a $r = 2t$ hole for in-plane dimensions $\Delta x, \Delta y = 2t/3$ (left), $t/3$ (center), and $t/6$ (right). . . . .	96
4.2	Schematic of setup for isotropic simulations. . . . .	98
4.3	Azimuthal variation of the out-of-plane difference signal's maximum amplitude for aluminum hole simulations. Results are for points 50 mm from the hole center. . . . .	99

4.4	Configuration of aluminum hole experiment. . . . .	100
4.5	Comparison of LISA and experimental results for through-thickness hole scenario in an aluminum plate. Sensor difference signals are normalized as a percentage of the maximum pristine signal amplitude at sensor 1, which corresponds to the 180-degree direction. . . . .	101
4.6	Comparison of experimental and LISA results for $r = 1t$ hole in an aluminum plate. . . . .	103
4.7	Comparison of experimental and LISA difference signals for $r = 1t$ hole in an aluminum plate. . . . .	104
4.8	Schematics of simulation setup for cross-ply damage simulations. . . . .	106
4.9	Azimuthal variation of the out-of-plane difference signal's maximum amplitude for cross-ply hole simulations. Results are for points 50 mm from the hole center for varying hole radius (a) and hole depth (b). . . . .	107
4.10	Out-of-plane displacement fields for through and half-depth holes. . . . .	109
4.11	Azimuthal variation of the out-of-plane difference signal's maximum amplitude for cross-ply hole simulations. Results are for points 50 mm from the hole center for (a) varying hole location normalized by maximum amplitude at 0-degree location, and (b) varying hole location normalized by max out-of-plane displacement at respective hole location. . . . .	111
4.12	Configuration of cross-ply hole experiment. . . . .	112
4.13	Comparison of LISA and experimental results for through-thickness hole scenario in a cross-ply laminate. Sensor difference signals are normalized as a percentage of the maximum pristine signal amplitude at sensor 1, which corresponds to the 180-degree direction. . . . .	113
4.14	Comparison of experimental and LISA sensor results for $r = 1t$ hole in a cross-ply laminate. . . . .	115
4.15	Comparison of experimental and LISA sensor difference signals for $r = 1t$ hole in a cross-ply laminate. . . . .	116
5.1	Impact specimen. . . . .	119
5.2	Drop-weight impactor. . . . .	120
5.3	Surface features from 5-J impact. . . . .	120
5.4	Impact damage specimen in CT system at the University of Texas, Arlington. . . . .	121
5.5	In-plane views of impact damage at various depths through specimen. . . . .	122
5.6	Section views in X-Z plane. . . . .	123
5.7	Section views in Y-Z plane. . . . .	125
5.8	Impact dent on surface of composite plate. . . . .	126
5.9	5-J impact damage in cross-ply laminate: sensor signals at 0-degree damage location. . . . .	128
5.10	5-J impact damage in cross-ply laminate: sensor signals at 0-degree damage location. . . . .	129
5.11	5-J impact damage in cross-ply laminate: sensor difference signals at 0-degree damage location. . . . .	130
5.12	5-J impact damage in cross-ply laminate: sensor difference signals at 0-degree damage location. . . . .	131

5.13	5-J impact damage in cross-ply laminate: sensor signals at 45-degree damage location on plate 2. . . . .	133
5.14	5-J impact damage in cross-ply laminate: sensor difference signals at 45-degree damage location on plate 2. . . . .	134
5.15	5-J impact damage in cross-ply laminate: sensor signals at 90-degree damage location on plate 2. . . . .	135
5.16	5-J impact damage in cross-ply laminate: sensor difference signals at 90-degree damage location on plate 2. . . . .	136
5.17	Hanging-plate setup used for laser vibrometer experiments during impact damage study. . . . .	138
5.18	Azimuthal variation of out-of-plane difference signals from laser vibrometry experiments for the three impact damage sites. Results are normalized as a percentage of the pristine amplitude in the 180-degree direction with respect to each damage site. . . . .	139
5.19	Azimuthal variation of the standard deviation of the out-of-plane difference signals from laser vibrometry experiments for the three impact damage sites. Results are normalized as a percentage of the pristine amplitude in the 180-degree direction with respect to each damage site. . . . .	141
5.20	Side view of impact damage model for a cross-ply graphite-epoxy laminate subjected to 5-J impact. . . . .	143
5.21	Comparison of top and side views of impact damage model for a cross-ply graphite-epoxy laminate subjected to 5-J impact. . . . .	144
5.22	Effect of reducing inner region stiffness properties to given percentage of original values. . . . .	146
5.23	Effect of reducing inner and middle region stiffness properties to given percentage of original values. . . . .	147
5.24	Effect of reducing inner region density to given percentage of original value. Inner region stiffness values are set to 10% of original values. . . . .	149
5.25	Effect of reducing middle region stiffness to given percentage of original value. Inner region stiffness and density values are set to 10% of original values. . . . .	150
5.26	Effect of reducing outer region stiffness to given percentage of original value. Inner region stiffness and density values are set to 10% of original values. Middle region stiffness values are set to 50% of original values. . . . .	152
5.27	Effect of reducing middle region density to given percentage of original value. Inner region stiffness and density values are set to 10% of original values. Middle region stiffness values are set to 50% of original values. Outer region stiffness values are set to 80% of original values. . . . .	153
5.28	Results of impact damage model sensitivity study. Each block represents a parameter change of 10% on either side of the baseline value. Blocks with a negative slope show an increase in the difference signal when the given property is reduced in value. . . . .	154
5.29	Best matching impact damage models using stiffness and density reductions. . . . .	156

5.30	Side view of impact damage model with simulated delamination. The large delamination between the bottom two layers is circled in the top image. The location of the void region in the model is indicated by the black rectangle. . . . .	157
5.31	Best matching impact damage models using simulated delamination along with stiffness and density reductions. . . . .	158
5.32	Comparison of selected LISA simulation with results from 5-J impact experiments for sensor 1. . . . .	160
5.33	Comparison of selected LISA simulation with results from 5-J impact experiments for sensor 2. . . . .	162
5.34	Comparison of selected LISA simulation with results from 5-J impact experiments for sensor 5. . . . .	163
5.35	Impact damage models for damage at 45 and 90 degrees. . . . .	165
6.1	Stationary Gaussian-modulated atom. . . . .	169
6.2	Gaussian chirplet atom. . . . .	170
6.3	Matching pursuit algorithm flow chart. . . . .	171
6.4	First matched atom for an example damage difference signal. . . . .	172
6.5	Possible damage locations in matching pursuit damage library (1-D analysis). . . . .	174
6.6	Matching pursuit algorithm location results for hole damage in an isotropic plate at various damage sites (1-D analysis). . . . .	175
6.7	Matching pursuit algorithm location results for hole damage in a cross-ply laminate at various damage sites (1-D analysis). . . . .	177
6.8	Matching pursuit algorithm size identification results for hole damage in an isotropic plate with varying radius (1-D analysis). . . . .	179
6.9	Matching pursuit algorithm size identification results for hole damage in a cross-ply laminate with varying radius (1-D analysis). . . . .	180
6.10	Matching pursuit algorithm damage identification results for hole damage in an aluminum plate (1-D analysis, sensor 1 only). . . . .	182
6.11	Matching pursuit algorithm performance with a noisy sensor signal (isotropic plate with $r = 1t$ hole at 125 mm from the actuator center). . . . .	184
6.12	Matching pursuit algorithm characterization of experimental hole damage in an aluminum plate. Actual damage size of $r = 1t$ located at $x = 125$ mm (1-D analysis, sensor 1 only). . . . .	185
6.13	Matching pursuit algorithm experimental damage characterization for a cross-ply laminate (1-D analysis, sensor 1 only). . . . .	186
6.14	Schematic for 2-D matching pursuit analysis showing actuator positions (A1, A2), sensor configuration (S1, S2, ..., S10), and possible locations included in damage library. . . . .	188
6.15	Matching pursuit algorithm damage location results for a cross-ply laminate using only sensor S1 (2-D scenario). . . . .	189
6.16	Improvement in matching pursuit algorithm location results for a cross-ply laminate when data from multiple sensors are used (2-D scenario with hole at (50, 90) mm). . . . .	190
6.17	Matching pursuit algorithm location results for a cross-ply laminate at various damage sites when all 10 sensors are used (2-D scenario). . . . .	192

6.18	Location of non-located simulated test points (TP1-TP5) for 2-D analysis. . . . .	193
6.19	Matching pursuit algorithm location results for a cross-ply laminate with damage at non-simulated locations (2-D scenario). . . . .	194
B.1	CLOVER actuator. . . . .	207
C.1	Global Matrix process for a circular actuator. . . . .	210
C.2	Block diagram of coarse phase velocity program (PhaseVel_Coarse.f90). . . . .	213
C.3	Block diagram of refined phase velocity program (PhaseVel_Refined.f90). . . . .	216
C.4	Block diagram of displacement kernel program (DisplacementKernelGeneralized.f90). . . . .	218
C.5	Global Matrix process for a CLOVER actuator. . . . .	220
C.6	Block diagram for Fourier inversion program. . . . .	222
D.1	Block diagram of LISA hybrid program. . . . .	224
D.2	Block diagram of LISA hybrid initialization steps. . . . .	226
D.3	Block diagram of LISA grid definition steps. . . . .	227
D.4	Block diagram of LISA actuation definition steps. . . . .	229
D.5	Block diagram of LISA damage definition, output definition, and material assignment sections. . . . .	232
D.6	Block diagram of LISA iterative equation section. . . . .	234
E.1	Correction procedure for displacement time history at 60 mm location. Results are for a circular actuator on an aluminum laminate. . . . .	237
E.2	Displacement time histories for an aluminum laminate at 60 and 80 mm, showing the artifact present in the previous solution. . . . .	238
E.3	Inward propagating wave solution for an aluminum laminate at 40, 50, and 60 mm, showing the artifact present in the previous solution. . . . .	239
E.4	Displacement time histories for an aluminum laminate at 60 mm, showing the effect of further reducing the region of integration. . . . .	240
E.5	Outward propagating wave solution for an aluminum laminate at 40, 60, and 80 mm, showing the effect of reducing the region of integration to $\theta \pm 45^\circ$ . . . . .	241
E.6	Outward propagating wave solution for an aluminum laminate at 40, 60, and 80 mm, showing the the effect of adding the cosine term to the inversion equation. . . . .	242
E.7	Inward propagating wave solution for an aluminum laminate at 40, 50, and 60 mm, showing the the effect of adding the cosine term to the inversion equation. . . . .	243
E.8	Displacement time histories for an aluminum laminate at 60 mm, showing the effect of only switching the sign of the inward wave solution. . . . .	244
E.9	Filter profiles for various filter exponent values, $b$ . The profile of the cosine function is shown for comparison purposes in each figure. . . . .	246
E.10	Outward propagating wave solution for an aluminum laminate at 60 mm, showing the the effect of various filter exponent values, $b$ , less than 2. . . . .	247
E.11	Outward propagating wave solution for an aluminum laminate at 60 mm, showing the the effect of various filter exponent values, $b$ , greater than or equal to 2. . . . .	248

## LIST OF TABLES

### Table

2.1	Aluminum material properties . . . . .	38
2.2	CYCOM IM7 977-3 Material Properties . . . . .	52
2.3	Amplitude results for cross-ply wave propagation in 0-degree direction. . . . .	57
2.4	Amplitude results for cross-ply wave propagation in 45-degree direction. . . . .	57
2.5	Amplitude results for cross-ply wave propagation in 90-degree direction. . . . .	57
2.6	Amplitude attenuation power law constants for cross-ply wave propagation comparisons. . . . .	58
4.1	Comparison of LISA and experimental results for through-thickness hole scenario in an aluminum plate. The maximum difference signal amplitude is shown as a percentage of the pristine signal at sensor 1. . . . .	102
4.2	Comparison of LISA and experimental results for through-thickness hole scenario in a cross-ply laminate. The maximum difference signal amplitude is shown as a percentage of the pristine signal at sensor 1. . . . .	114
5.1	HEXCEL IM7 8552 Material Properties . . . . .	119
5.2	Comparison of standard deviation values for 5-J impact damage laser vibrometry experiments at 0, 45, and 90 degrees. SD values are reported as a percentage of the pristine signal amplitude in the respective cases' 0-degree azimuth. . . . .	142
5.3	Selected impact damage simulation models in LISA (stiffness and density reductions). Error is measured as the average value of the difference between the simulated and experimental difference signal amplitude for the five sensors, measured as a percentage of the pristine signal at sensor 1. Baseline dimensions were used in all models. . . . .	155
5.4	Selected impact damage simulation models in LISA (stiffness and density reductions with simulated delamination). Error is measured as the average value of the difference between the simulated and experimental difference signal amplitude for the five sensors, measured as a percentage of the pristine signal at sensor 1. Baseline dimensions were used in all models. . . . .	157
5.5	Comparison of selected LISA impact model with average experimental results for damage at 0-degree location. The maximum difference signal amplitude is shown as a percentage of the pristine signal at sensor 1. . . . .	159
6.1	Damage characterization results for 1-D matching pursuit algorithm with variable hole size and hole location. All values are measured in mm. . . . .	183



6.2	Matching pursuit algorithm damage location results for a cross-ply laminate using only sensor S1 (2-D scenario). . . . .	189
6.3	Improvement in matching pursuit algorithm location results for a cross-ply laminate when data from multiple sensors are used (2-D scenario with hole at (50, 90) mm). . . . .	191
6.4	Matching pursuit algorithm location results for a cross-ply laminate at various damage sites when all 10 sensors are used (2-D scenario). . . . .	192
6.5	Matching pursuit algorithm location results for a cross-ply laminate with damage at non-simulated locations (2-D scenario). . . . .	195

## LIST OF APPENDICES

### Appendix

<b>A Eigenvectors for Global Matrix Method . . . . .</b>	<b>203</b>
<b>B Global Matrix Forcing Terms for CLoVER . . . . .</b>	<b>207</b>
<b>C Implementation of Global Matrix Method . . . . .</b>	<b>209</b>
<b>D Implementation of LISA Hybrid Program . . . . .</b>	<b>223</b>
<b>E Comments on 2-D Fourier Inversion . . . . .</b>	<b>236</b>

# **ABSTRACT**

## **Guided Wave Propagation and Damage Interaction in Isotropic and Composite Structures**

by

**Matthew Bridger Obenchain**

**Chair: Professor Carlos E. S. Cesnik**

Guided wave structural health monitoring methods offer many of the capabilities needed to move from a schedule-based maintenance paradigm to a more cost-effective condition-based system. This dissertation explores several key aspects of guided wave propagation and damage interaction in both isotropic and composite structures. First, a reliable method of computing displacement time histories from guided wave excitation is presented. This formulation, based on the Global Matrix Method, is directly applicable to composite laminates. It improves upon previous methods that were unable to properly separate inbound and outbound wave solutions. Second, a comprehensive wave propagation simulation tool is presented that combines the best features of the Global Matrix Method and the recently developed local interaction simulation approach (LISA). This LISA hybrid model accurately captures guided wave generation from both piezoceramic and piezocomposite actuators. Wave propagation results from the new model compare favorably with semi-analytical models for both isotropic plates and composite laminates. Following that, the dissertation describes the application of the LISA hybrid model to examine guided

wave interaction with holes in plate structures. Simulations are used to analyze the influence of various damage parameters, such as hole radius and depth, and the results are compared with experimental measurements. The effect of hole orientation relative to fiber direction in composite laminates is also explored. Subsequently, the dissertation examines guided wave interaction with low-velocity impact damage in composite laminates. Diagnostic imagery of laboratory-produced impact damage is presented to help characterize the size, shape, and composition of the damage. Experimental results from guided wave interrogation of the damage region are also presented. Together, these are used to evaluate various methods to model the impact damage in LISA. Finally, this dissertation introduces a damage characterization tool based on the matching pursuit method. The new algorithm uses a library of LISA simulations that capture the effects of various damage sizes and locations. The ability of the algorithm to locate damage is demonstrated in both 1-D and 2-D scenarios.

# CHAPTER 1

## Introduction and Literature Review

This chapter introduces the field of guided wave structural health monitoring (SHM). It begins with a brief overview of the different philosophies that have guided the design and sustainment of aerospace structures. The field of SHM is introduced in this context and its potential benefits are considered. The fundamentals of guided waves for isotropic structures are briefly reviewed to provide background. A literature review is included to present the state of the art in guided wave SHM for isotropic and composite structures. Finally, an outline of this dissertation is presented.

### 1.1 Introduction and Motivation

From the days of the Wright brothers, ensuring the structural integrity of aerospace structures has been a top priority. From that time until the WWII years, this was primarily achieved in the design process. Stress analysis and preservation of sufficient factors of safety were the primary methods by which aircraft were deemed safe to operate. Structural inadequacies found during operation and testing were corrected as needed. As years passed, factor of safety margins dropped as higher performance aircraft were constructed with less well-defined materials, but this paradigm proved successful for decades [1].

In the 1950s, civil and military attention to the dangers of fatigue damage skyrocketed. High-profile fatigue failures of the de Havilland Comet and the USAF B-47 as well as

numerous other incidents helped to advance new design practices based on safe-life or fail-safe philosophies. In safe-life designs, component fatigue lives were calculated/estimated and components were replaced before the safe life was reached. In fail-safe designs, eventual component failure was assumed, and designs included redundancies and mitigation factors to reduce the effect of these failures. During the next few years, advancements in the field of fracture mechanics allowed engineers to better understand the behavior of fatigue cracks. Testing methodologies also improved, which provided better awareness about potential locations for fatigue problems. Full-scale fatigue testing of aircraft became more common as designers tried to more accurately make safe-life predictions at the component and system levels. The practice of inspecting in-service airframes for fatigue damage also increased as fatigue problems were detected in various aircraft.

The next major evolution in design and maintenance philosophies was accelerated in 1969 with the crash of a USAF F-111 after only 107 flight hours [2]. Investigation of the incident revealed that a flaw in the swing-wing pivot assembly had not been detected during post-manufacturing inspections, and a crack originating from this flaw resulted in catastrophic failure of the airframe [3]. This incident reinforced growing knowledge that safe-life predictions could not be trusted if components had pre-existing damage. This ushered in a new philosophy known as damage-tolerant design. The underlying assumption in damage-tolerant design is that flaws and damage will always be present in an aircraft structure, and the aircraft should be treated as if it was initially flawed. The linchpin to damage tolerance is the ability to detect damage before it reaches a critical size so the affected component or system can be replaced before catastrophic failure. The need for reliable inspections has driven the advancement of numerous non-destructive inspection (NDI) and non-destructive testing (NDT) techniques such as ultrasonic inspection, eddy current testing, dye penetrant application, and others.

Several factors have complicated the task of detecting damage in aircraft using schedule-based inspection routines. First, modern inventories have a large number of aging

aircraft which must be kept in an acceptable state of readiness [4]. Analysis of predicted load spectra and better fracture mechanics capabilities have allowed for the design of appropriate inspection strategies that identify fatigue-critical locations and target inspections to specific times in the aircraft flight history, but these decisions often have occurred in the design phase or early in the life cycle of an aircraft type. More recent incidents have increased public awareness of the advanced age of many in-service airplanes [5]. The Dan Air 707 crash in 1977 highlighted the need to augment original inspections with supplementary inspections [2]. The 1988 Aloha Airlines 737 accident brought renewed focus on the interplay between environmental effects, changes from predicted usage history, and maintenance shortfalls in aging aircraft. The 1989 United Airlines DC-10 crash in Sioux City resulted from a metallurgical defect in a fan disc that was not detected [5]. Events like these have demanded that inspections be conducted more often and more thoroughly.

A second and related challenge is the significant cost involved with conducting inspections. As much as 60 percent of the total life-cycle cost of a system is used for sustainment [6], and a large portion of that cost can be attributed to inspection requirements. The current practice of time-based NDI inspections leaves much to be desired in this regard. Some large aircraft can have as many as 22,000 critical fastener holes in the lower wing alone [4], and each of these must be inspected. Aside from direct monetary costs, the opportunity cost incurred when taking an aircraft out of service can bear huge burdens in terms of lost revenue for airlines and lower mission capability rates for military units.

Finally, the increased use of advanced materials is changing the playing field for those working to preserve the integrity of aircraft over their entire life cycle. While fatigue crack behavior is relatively well understood for metals, knowledge of composite damage is much less mature. Composite damage can take multiple forms, and the damage is often distributed in nature. New aircraft are using ever-increasing amounts of fiber-reinforced composites to reduce weight and gain improved structural properties, and one of the most difficult problems to overcome during the certification process is to guarantee the structural

integrity of the large composite structures over the 30 years lifespan of the airframe. Detection of damage and prediction of its propagation behavior continue to be major research challenges.

The above factors are leading many in the aerospace industry to push for a move towards condition-based maintenance. While most of the current inspection regimes used to detect damage in modern aerospace structures are time-based, the DoD intends to migrate to a process that initiates maintenance based on the current condition of the system instead of a schedule [6]. To support this goal, the Air Force Office of Scientific Research has noted that advances in science and technology are needed to reduce the burden of detecting and identifying structural damage, reduce downtime, and increase availability of the aircraft fleet [4]. At the forefront of this technology push is the growing field of structural health monitoring.

## **1.2 Structural Health Monitoring**

The role of an SHM system is to provide a real-time assessment of the condition of the vehicle, building, or system [6]. While many of the tools of SHM are derivatives of the techniques of NDI/NDT [5], SHM can be differentiated from traditional NDI/NDT in that it involves the integration of sensors into structural components, which allows for continuous monitoring of the structure [7]. A suitable SHM system for aerospace structures would ideally answer four questions:

- Does damage exist?
- Where is the damage?
- What type of damage is present?
- How severe is the damage?

Adoption of SHM technologies has the potential to provide numerous benefits. SHM can allow for current time-based maintenance practices to evolve into more cost effective



condition-based practices [8]. Because the sensors used for SHM are permanently attached to the structure, interrogation can be performed in an on-demand basis without moving the structure to a different location where lengthy manual inspections are conducted. This will likely result in increased aircraft availability, and it also has the potential to greatly reduce total life-cycle ownership costs. Additionally, SHM has the potential to allow companies in the airframe, jet engines, and large equipment businesses to move to a leasing model by extending the maintenance cycles, keeping equipment in the field longer, and determining the amount of life used up during lease time [8]. It is also likely that confidence levels in operating structures will increase because of new safeguards against unpredictable system failure, particularly for aging structures [9].

### **1.3 Guided Wave Structural Health Monitoring**

SHM schemes can be classified as active or passive. Passive schemes continuously observe the structure and include methods such as acoustic emission and strain/load monitoring. While passive SHM schemes have definite advantages in certain applications, significant drawbacks include the high sensor density required and the need to continuously operate. On the other hand, active SHM schemes excite the structure in a prescribed manner when required. Active SHM methods are of greater interest due to their ability to perform on-demand interrogation of a structure while the structure is still in service [10].

Among active schemes, guided wave SHM has emerged as one of the most promising techniques. Guided waves are elastic waves that are guided by the finite dimensions of the structure in which they exist. For most aerospace SHM applications, the most relevant guided waves are ultrasonic Lamb waves, which are guided by the two parallel surfaces of a plate-like structure. The use of ultrasonic waves for inspections is well-established in the NDI/NDT community where they are usually generated using hand-held transducers during scheduled maintenance/inspections [9]. In these applications, the waves are nor-

mally generated in the thickness dimension of the structure in order to examine a particular location. For guided wave SHM, on the other hand, the Lamb waves are generated using actuators that are permanently attached to the structure. The waves propagate along the lateral dimensions of the structure, which allows for simultaneous inspection of a large region rather than one specific site.

## **1.4 Lamb Wave Fundamentals**

For isotropic materials, pure analytical solutions exist for various types of guided wave propagation. Numerous textbooks such as those by Achenbach [11], Graff [12], Auld [13], and Rose [14] contain detailed descriptions of these formulations. As shown in these references, several types of guided waves have been characterized. Rayleigh waves [15] propagate along free surfaces in elastic media. Other guided waves, such as Stoneley [16] and Love [17] waves, exist at material interfaces. The guided waves most relevant to aerospace applications are those that propagate between the free surfaces of a plate-like structure, which were proposed by Horace Lamb [18] in 1917 and bear his name, even though he never experimentally produced them. Most recent sources have credited Worlton [19] as the first person to definitively state the potential of using guided waves for non-destructive inspection purposes.

This section presents the general principles governing free Lamb wave propagation. The results of this derivation illustrate important principles that explain wave propagation in isotropic structures and can be expanded to also describe wave behavior in more complicated laminated plates. A schematic of the plate structure used in the derivation is shown in Fig. 1.1.

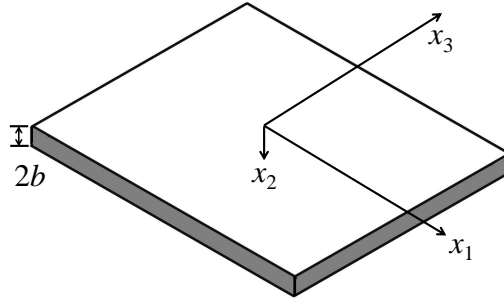


Figure 1.1: Plate structure used in Lamb wave derivation.

The starting point for the derivation is Navier's equation, which is the equilibrium equation for isotropic materials cast in terms of displacements:

$$(\lambda + \mu)\nabla\nabla\mathbf{u} + \mu\nabla^2\mathbf{u} = \rho\ddot{\mathbf{u}} \quad (1.1)$$

In Eq. 1.1,  $\lambda$  and  $\mu$  are the Lamé constants for the material,  $\rho$  is the density, and  $\mathbf{u}$  is the displacement vector. At this point, it is advantageous to use the Helmholtz decomposition to break the displacement field into the sum of the gradient of a scalar,  $\phi$ , and the curl of a zero-divergence vector,  $\mathbf{H}$ :

$$\mathbf{u} = \nabla\phi + \nabla \times \mathbf{H} \quad \text{and} \quad \nabla \cdot \mathbf{H} = 0 \quad (1.2)$$

Substitution of the new displacement field expression into Navier's equation results in the formation of two separate differential equations which must be satisfied to produce equilibrium:

$$\nabla^2\phi = \frac{\ddot{\phi}}{c_P^2} \quad (1.3)$$

$$\nabla^2\mathbf{H} = \frac{\ddot{\mathbf{H}}}{c_S^2} \quad (1.4)$$

The first of these equations represents the propagation of longitudinal waves in the medium. The second equation represents the three equations governing shear waves in the three vector directions. The  $c_P$  and  $c_S$  terms are the bulk velocities of the longitudinal and shear wave components, which can be defined as:

$$c_P = \sqrt{(\lambda + 2\mu)/\rho} \quad (1.5)$$

$$c_S = \sqrt{\mu/\rho} \quad (1.6)$$

It is common to consider only the plane strain case, which describes the behavior of the longitudinal (P) and shear-vertical (SV) components of the Lamb waves. For this case, only the scalar and  $H_3$  component of the vector are non-zero, and time-harmonic plane wave solutions with frequency  $\omega$  are assumed for these two quantities:

$$\begin{aligned} \phi &= f(x_2)e^{i(\xi x_1 - \omega t)} \\ H_3 &= h_3(x_2)e^{i(\xi x_1 - \omega t)} \end{aligned} \quad (1.7)$$

The  $\xi$  term in Eq. 1.7 is known as the wavenumber, which is a function of the frequency  $\omega$  and the phase velocity of the wave,  $c_{PH}$ :

$$\xi = \frac{\omega}{c_{PH}} \quad (1.8)$$

Consideration of solutions of these forms results in the following equations,

$$\frac{d^2 f}{dx_2^2} + \alpha^2 f = 0 \quad (1.9)$$

$$\frac{d^2 h_3}{dx_2^2} + \beta^2 h_3 = 0 \quad (1.10)$$

where the coefficients  $\alpha$  and  $\beta$  depend on the frequency, applicable wave velocity, and wavenumber:

$$\alpha^2 = \frac{\omega^2}{c_p^2} - \xi^2 \quad (1.11)$$

$$\beta^2 = \frac{\omega^2}{c_s^2} - \xi^2 \quad (1.12)$$

The solutions of Eqs. 1.9 and 1.10 are of the form,

$$f(x_2) = A \sin \alpha x_2 + B \cos \alpha x_2 \quad (1.13)$$

$$h_3(x_2) = C \sin \beta x_2 + D \cos \beta x_2 \quad (1.14)$$

where  $A$ ,  $B$ ,  $C$ , and  $D$  are displacement amplitude constants. In order to determine the values for these constants, the appropriate boundary conditions must be applied. For Lamb waves, traction-free conditions are assumed for the two parallel surfaces of the plate, which has a thickness of  $2b$ :

$$\sigma_{21} = \sigma_{22} = 0 \quad \text{at } x_2 = \pm b \quad (1.15)$$

The applicable stresses can be represented in terms of displacements as:

$$\sigma_{22} = (\lambda + 2\mu)\nabla^2\phi - 2\mu\left(\frac{\partial^2\phi}{\partial x_1^2} + \frac{\partial^2 H_3}{\partial x_1\partial x_2}\right) \quad (1.16)$$

$$\sigma_{21} = \mu\left(2\frac{\partial^2\phi}{\partial x_1\partial x_2} + \frac{\partial^2 H_3}{\partial x_2^2} - \frac{\partial^2 H_3}{\partial x_1^2}\right) \quad (1.17)$$

Substitution of the solutions in Eqs. 1.13 and 1.14 into the boundary conditions in Eq. 1.15 yields two matrix equations that describe the wave propagation of the anti-symmetric and symmetric portions of the Lamb wave, respectively. From these two equations, it is clear that admissible wave solutions are only produced when the wavenumber  $\xi$  forces the deter-

minant of the coefficient matrix to have a zero value.

$$\begin{bmatrix} -(\xi^2 - \beta^2) \sin \alpha b & -2i\xi\beta \sin \beta b \\ 2i\xi\alpha \cos \alpha b & (\xi^2 - \beta^2) \cos \beta b \\ -(\xi^2 - \beta^2) \cos \alpha b & 2i\xi\beta \cos \beta b \\ -2i\xi\alpha \sin \alpha b & (\xi^2 - \beta^2) \sin \beta b \end{bmatrix} \begin{bmatrix} A \\ D \\ B \\ C \end{bmatrix} = \begin{bmatrix} 0 \\ 0 \\ 0 \\ 0 \end{bmatrix} \quad (1.18)$$

With this fact in mind, it is possible to rewrite Eq. 1.18 in the following form, which is commonly known as the Rayleigh-Lamb frequency equation for the plate:

$$\frac{\tan \beta b}{\tan \alpha b} = \left( \frac{-4\alpha\beta\xi^2}{(\xi^2 - \beta^2)^2} \right)^{\pm 1} \quad (1.19)$$

The exponent in Eq. 1.19 takes a positive value when considering symmetric waves and a negative value when considering anti-symmetric waves.

Examination of this equation helps to illustrate two important properties of Lamb waves: they are multimodal and dispersive. It is immediately seen that for each value of the exponent, multiple solutions exist. These solutions are often represented in graphical form using a phase velocity dispersion curve, illustrated in Fig. 1.2 for aluminum. For any frequency, one or more values of the phase velocity result in wavenumbers that satisfy the Rayleigh-Lamb frequency equation. At low frequencies, only the fundamental modes,  $A_0$  and  $S_0$ , exist. At higher frequencies, an increasing number of modes are possible, such as the  $A_1$  and  $S_1$  modes shown in the upper right corner of Fig. 1.2. The slope of the curve describes how dispersive a particular mode is in a given frequency range, and extremely dispersive modes can prove to be troublesome for practical applications.

## 1.5 Literature Review

This section provides an overview of previous work relevant to the scope of this dissertation. While guided wave SHM is a relatively recent area of interest, it has its roots in

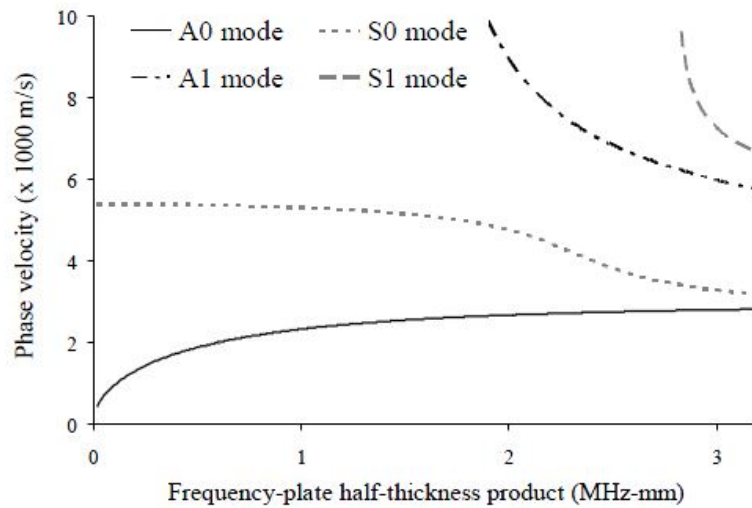


Figure 1.2: Phase velocity dispersion curve for aluminum.

a considerable amount of research from the NDI/NDT community. A thorough review of guided wave SHM was presented by Raghavan and Cesnik [9], and that work can be referenced for numerous resources beyond those contained in this chapter.

### 1.5.1 Actuator and Sensor Design

In traditional NDI/NDT applications using guided waves, the waves have been generated and sensed using a wide variety of external transducers such as wedge transducers [20], comb transducers [21], and electromagnetic acoustic transducers (EMAT) [22–24]. However, many of these are quite large, and the need to integrate SHM actuators and sensors with the existing structure of the system makes these devices impractical. Some researchers have used fiber optic sensors such as fiber Bragg gratings (FBG) [25, 26], which have the potential to act as both load monitors and guided wave sensors. Others have considered magnetostrictive transducers [27, 28].

Piezoelectric materials have been the most popular and most widely researched alternatives. They offer the ability to generate guided waves with small, lightweight, and unobtrusive actuators that can be permanently attached to a structure. Piezoelectric wafer

actuators have been widely used due to their simplicity and relatively low cost. One candidate material for these wafers is polyvinylidene fluoride (PVDF), which is a polymer film. Researchers such as Monkhouse et al. [29] have applied backing layers with electrode patterns to the film to produce flexible transducers. Piezoceramic wafers constructed with lead zirconium titanate (PZT) have been more attractive. Crawley and De Luis [30] noted the potential to use piezoceramic wafers as part of an intelligent structure, and Keilers and Chang [31] were early proponents of using piezoceramic wafers to detect damage in composite structures. Giurgiutiu and Zagari [32], Kessler et al. [33], and Diaz-Valdés and Soutis [34] made notable early contributions to the use of these materials in SHM applications.

Efforts to improve the performance and utility of piezoelectric actuators in general have resulted in a number of more advanced actuator designs broadly categorized as anisotropic piezocomposite transducers. Unlike PZT wafers which are very brittle, these transducers are very flexible and conformable to the curved surfaces often found in aerospace structures. Bent and Hagood [35] developed the active fiber composite (AFC), which uses extruded piezoceramic fibers that are embedded in an epoxy resin. Interdigitated electrode patterns provide the necessary electric field for the piezoelectric effect to be present. Wilkie and High [36] developed the macro-fiber composite (MFC) actuator, which is very similar to the AFC except the piezoelectric material is now cut from a wafer using a dicing saw. Based on these fundamentals, Salas and Cesnik [37, 38] have developed the Composite Long-range Variable-direction Emitting Radar (CLOVER) specifically for SHM applications. The CLOVER is composed of a series of wedge-shaped sectors that can be individually excited to provide directional interrogation and/or sensing of a structure while also providing 360-degree coverage. Senesi and Ruzzene [39,40] have developed the Frequency Selective Acoustic Transducer (FSAT), which arranges the piezoelectric material in a spiral pattern. When used as a sensor, this device produces a signal with the dominant frequency



component dependent on the direction of the incoming waves. It can also be used as a directional guided wave generator.

## **1.5.2 Analytical and Semi-analytical Approaches to Solve the Guided Wave Equations**

Early work considering actuator design was accompanied by numerous studies on how to describe the propagating waves. Because SHM applications use structurally-integrated actuators to generate guided waves in the structure of interest, there is a need to not only describe free propagation, but also to represent wave generation. Analytical solutions for guided wave generation are possible for isotropic media. Viktorov [41] developed 2-D models for Lamb wave propagation in isotropic plates. Santosa and Pao [42] solved for the transient response of a thick, infinite plate to a point force using a normal mode expansion method. Several studies used reduced-order plate theories to develop simplified wave propagation solutions. Lin and Yuan [43] modeled waves originating from surface-mounted piezoceramic discs on an infinite plate. They used Mindlin plate theory and considered both transverse shear and rotary inertia effects. Rose and Wang [44] also used Mindlin plate theory to develop solutions for point forces and moments, which were then combined to form solutions for circular and rectangular piezo actuators.

More recently, Giurgiutiu [45] presented 2-D analytical solutions for the displacement response of an isotropic plate to excitation from semi-infinite piezoceramic wafers. He extended his analysis to consider how best to tune the excitation for maximum amplitude response. Raghavan and Cesnik [46] subsequently developed analytical solutions based on 3-D elasticity theory for arbitrarily-shaped, finite-dimension actuators. They also provided solutions for the particular cases of rectangular, ring, and circular piezoceramic wafer actuators. They used contour integration and the residue theorem to handle the complex integrals contained in the formulations.

As composite materials gained popularity, more attention was focused on how to describe guided wave generation and propagation in laminated structures. As was the case for isotropic materials, most of the theoretical approaches for guided wave propagation in composites were initially limited to 2-D representations or reduced plate theories. Ditri and Rose [47] used a normal mode expansion technique to model excitation of anisotropic layers based on a 2-D elasticity model. Datta et al. [48] used approximate plate theories to avoid the complexity of equations resulting from the full 3-D theory of elasticity. Moulin et al. [49] used a coupled model based on finite element analysis and normal mode expansion to simulate piezo-actuated guided wave propagation in composites. Velichko and Wilcox [50] developed another method that uses dispersion relationships and mode shapes obtained from 2-D analysis to model displacements from finite-sized transducers.

Matrix approaches have been the most successful in moving towards complete 3-D theoretical modeling of guided waves in composite laminates. Lowe [51] provided a thorough overview of both the Transfer Matrix and Global Matrix methods. The Transfer Matrix approach was developed by Thomson [52] and Haskell [53] as a method to characterize wave propagation in layered media. Nayfeh [54] later expanded the Transfer Matrix to composite laminates by allowing for anisotropic lamina in the formulation. Bottai et al. [55] have used Nayfeh's formulation of the Transfer Matrix methodology to obtain dispersion curves in support of analytical and experimental studies. Mienczakowski et al. [56] used the Transfer Matrix approach to model composite panels and showed favorable comparisons with experimental results for displacement time history.

The Global Matrix Method was introduced by Knopoff [57] to overcome instabilities in the Transfer Matrix approach for laminates with large frequency-thickness products. Mal [58] and Lih and Mal [59] used the Global Matrix Method as the basis for a formulation to consider forced guided wave excitation from finite-dimensional sources. They used a numerical scheme to handle the Fourier spatial inversions resulting from the formulation. Mal and Banerjee [60] and Banerjee et al. [61] proposed a semi-analytical solution for the

evaluation of the spatial inversion integrals using the residue theorem in one direction and numerical integration in the other. More recently, Raghavan and Cesnik [62] outlined a framework to determine the displacements resulting from finite-dimensional piezoelectric actuators attached to the surface of a composite laminate. They adapted the Global Matrix formulation of Lih and Mal [59] and introduced a distinct inversion method using the residue theorem.

### **1.5.3 Numerical Approaches**

Although theoretical models are capable of characterizing the guided wave propagation in an infinite medium, they often become intractable when modeling complex-geometry structures because of the interface conditions and the need to account for the shape and reflections in the formulation. Researchers have turned to numerical simulations to facilitate the modeling of waves, which can better deal with complex structural systems, interfaces, and damage [63]. Lee and Staszewski [64] provided a good review of the many different numerical techniques used to model guided waves. Among the more popular choices have been the finite difference method, the finite element method, the boundary element method, and the spectral element method.

The finite difference method [65] has been used for decades to model bulk wave propagation and more recently guided waves. Virieux [66] used the finite difference method to model wave propagation in heterogeneous media, specifically for seismology applications. Yamawaki and Saito [67] developed a finite difference-based scheme to model ultrasonic wave propagation that was applicable to both isotropic and anisotropic materials.

The finite element method [68] has been by far the most popular technique for numerical guided wave modeling. Talbot and Przemieniecki [69] presented an early study using finite elements where they introduced new elements to aid in analyzing the dispersion behavior of guided waves in wave guides of arbitrary cross section. Alleyne [70] presented guidelines on the number of elements required based on the minimum wavelength present.

Many other studies have employed the finite element method, and some will be covered later in this review.

The spectral element method [71, 72] is a more recent development where functions are approximated using sums of trigonometric or polynomial functions, which can be differentiated exactly. Ostachowicz and Krawczuk [73] used spectral elements to model crack detection in a cantilever rod. Zak et al. [74] demonstrated the spectral element method for use in modeling wave propagation in pristine composite plates using elements based on Legendre polynomials, and they later used the method to consider damaged aluminum components [75]. Kim et al. [76] developed a coupled model for piezoelectric generation and sensing of guided waves using the spectral element method.

The boundary element method [77] has been the subject of several recent studies due to its reduced computational requirements. In this method, only the boundaries of the structure are discretized. Surface integrals replace volume integrals, resulting in considerably smaller systems of equations. Cho and Rose [78] used the boundary element method to study mode conversion of Lamb waves from a free edge. Zou et al. [79] used a dual boundary element approach to model wave propagation and interaction with a surface crack in an aluminum specimen.

While these numerical techniques for modeling wave propagation have been successful, many have proved to be high in computational cost [9]. The local interaction simulation approach (LISA), originally developed by Delsanto et al. [80–82], has emerged as an efficient numerical option for modeling guided waves. This method is based on a set of iterative equations for unit cells that discretize the structure, and it uses a sharp interface model to handle material discontinuities and layer interfaces. Recent implementations of this method have shown good results. Lee and Staszewski [64, 83–85] used LISA to model guided wave propagation in pristine and damaged aluminum plates, focusing on 2-D models. Sinor [86] presented a thorough derivation of the LISA iterative equations for orthotropic lamina in principal directions which allowed for variable discretization in the

three dimensions. Sundararaman and Adams [63] used LISA to model damage in isotropic and orthotropic plates and later investigated the effects of grid size [87]. Nadella and Cesnik [88–90] extended LISA to laminates containing transversely isotropic lamina in non-principal directions and developed a fully-coupled LISA formulation that captures the electromechanical effects of piezoelectric actuators and sensors [91]. Their work has previously demonstrated LISA’s usefulness in modeling a variety of composite configurations including unidirectional, cross-ply, and quasi-isotropic laminates.

## **1.5.4 Guided Wave Interaction with Damage**

The previous work developing reliable analytical and numerical tools has allowed for numerous studies intended to characterize the interaction of guided waves with damage. This section of the literature review highlights a representative cross-section of those works. Damage studies considering both isotropic and composite structures are included.

### **1.5.4.1 Holes and Notches**

Many of the early efforts considering guided wave interaction with damage focused on simple forms of damage such as holes and notches. These features are straight-forward to model, and they can be incorporated into experimental studies with little complexity.

Research in this area began with isotropic materials. Alleyne and Cawley [92] investigated the use of Lamb waves to detect notches in metal plates. Finite element modeling was used to consider the  $S_0$ ,  $A_0$ , and  $A_1$  Lamb modes interacting with notches of various depths. Experiments were also conducted to validate the finite element models. Ghosh et al. [93] experimentally investigated hole damage in steel and aluminum plates. They considered holes oriented both transverse and parallel to the plates’ free surfaces, and they concluded Lamb waves were more sensitive to the holes drilled parallel to the plate surface.

A few notable studies focused on incorporating damage effects into various plate theories. McKeon and Hinders [94] used Mindlin plate theory while modeling the hole as

a point source to capture the scattering effects of the damage. Fromme and Sayir [95] compared classical plate theory, Mindlin plate theory, and experimental results for the scattering effects of a through hole. They also examined the scattering effects of a line of holes. Grahn [96] developed models based on 3-D elasticity and low-order plate theories to describe partial-thickness holes, but these models were only applicable to very low frequencies.

One of the major tasks for these early studies was to prove damage could be reliably detected. Several researches considered the use of sensor arrays to increase the capabilities of the guided wave methods. Among these were Giurgiutiu [97], who experimentally demonstrated detection of a crack originating from a rivet in an aluminum plate using a pulse-echo configuration and array approaches. Yu and Giurgiutiu [98] later presented results using a 2-D array of piezoelectric wafer active sensors to detect damage in an isotropic plate. They demonstrated the ability of 2-D arrays to offer improved results over 1-D arrays. They considered multiple array configurations and experimentally demonstrated the ability of a rectangular array to locate both a crack and a pin-hole in an aluminum plate.

Along with holes and notches, other authors began to examine how stiffness changes at various locations in their models affected guided wave propagation. Basri and Chiu [99] used the finite element method to explore the effect of stiffness changes and notches in isotropic and orthotropic structures. They used 2-D and 3-D analyses to examine wave propagation in both the wavenumber-frequency domain and the wavenumber-time domain. They determined that the  $S_0$  mode was more sensitive to small notch depths than the  $A_0$  mode for isotropic beams. Sundararaman and Adams [63] used LISA to model damage in isotropic plates. Damages such as holes and cracks were simulated as local changes in material density and/or stiffness. They investigated models with single and multiple damage and conducted several parametric studies involving various sizes of holes and notches and various magnitudes of material property changes.

More recently, studies have begun to consider the presence of holes in composite laminates. Giurgiutiu and Bottai [100] presented experimental results using piezoelectric wafer active sensors to detect hole damage in composite specimens. They were able to detect holes in both unidirectional composite strips and a quasi-isotropic plate using sensors in the pitch-catch configuration. Ng and Veidt [101] considered the use of a transducer network to sequentially scan a composite laminate. Hole damage was simulated in a finite element model, and a damage localization image was constructed using the information from the four transducer elements. An experimental study involving bonded masses was used to confirm the ability of the approach to reliably locate damage features. Veidt and Ng [102] studied guided wave scattering due to through-holes in unidirectional, cross-ply, and quasi-isotropic laminates. They used both finite element models and experimental measurements to characterize the azimuthal scattering from the holes, and they investigated the influence of stacking sequence on the guided wave response.

#### **1.5.4.2 Delamination in Composite Laminates**

The increasing focus on composite materials has inspired many researchers to shift their focus from holes and notches to damage types more typical of composite structures, such as delaminations. Some of these efforts have considered the effect of the through-thickness location of the delamination. One of the earliest examples came from Guo and Cawley [103], who examined the effect of delamination on the propagation of the  $S_0$  Lamb mode using the finite element method and experiments. A 2-D plane strain model was used for the numerical analysis. Experimental delaminations were produced by spraying release agent on the interface between appropriate layers during layup. Numerical and experimental results showed that at interface locations where the  $S_0$  mode shape produced zero shear stress, it was insensitive to the delamination defect. Li et al. [104] used the spectral element model to analyze the effect of a square delamination contained at various interface locations in composite laminates. Their simulations demonstrated that the  $A_0$  mode was more sensitive

to the delamination than the  $S_0$  mode. They also showed that mid-plane delaminations were not detectable with the  $S_0$  mode.

Several studies have considered the effect of the delamination size on the success of damage detection. Hu et al. [105] considered a laminated beam using the  $S_0$  Lamb mode. Experimental results allowed detection of delaminations with a length above a certain threshold. Results from an intact beam were compared with results from a delaminated beam. The authors noted that using a higher frequency would allow for smaller delaminations to be detected. Ip and Mai [106] considered detection of through-width delaminations in Kevlar-epoxy composite beams. Delaminations were introduced by including Teflon film between the 4th and 5th layers of the 6-ply laminate. Three damaged configurations were tested along with one pristine sample, and the authors quantified the effect of delamination length on location error. A 3-D case was considered by Ng and Veidt [107], who studied the directionality of the Lamb waves scattered from a circular delamination in a quasi-isotropic laminate. A laser vibrometer was used to record out-of-plane displacement along a circle surrounding the delamination. Experimental results were used to validate a 3-D finite element model, and the model was used to investigate the dependence of the scattering on delamination size and through-thickness location. The results indicated that as the delamination diameter increases relative to the wavelength of the  $A_0$  mode, the scattering of the Lamb wave favors forward scattering in the direction of wave propagation over back scattering towards the actuator.

Other related works have illustrated how delaminations affect the speed, frequency, and modal characteristics of the guided waves. Toyama et al. [108] examined the changes in Lamb wave velocity in the presence of both transverse cracking damage and delamination. Both glass-fiber and carbon-fiber reinforced cross-ply specimens were studied in their experiments. Delaminations were created by including Teflon sheets between the outer and inner layers of the specimen. Duflo et al. [109] considered the attenuation of the Lamb waves in the frequency spectrum due to mode conversion. They constructed a compos-



ite plate with simulated defects by including various materials to prevent complete curing. They used laser vibrometry to examine wave propagation generated with a wedge transducer, and they were able to evaluate the size of the delaminations. Ramadas et al. [110] described mode conversion found due to a delamination. The  $A_0$  mode partially converted into an  $S_0$  mode in sublayers above and below the delamination. Both finite element models and experiments were used to characterize the effect. Subsequently [111], they expanded on this work and demonstrated the presence of turning modes when a delamination was located asymmetrically in the thickness direction. These modes transfer from one sublayer to the other at the endpoint of the delamination.

#### **1.5.4.3 Impact Damage in Composite Laminates**

Along with delamination, the presence of impact damage has been of particular interest among SHM researchers. The majority of these studies have been experimental in nature. Kaczmarek [112] investigated impact damage in quasi-isotropic carbon-epoxy laminates using the  $A_0$  mode. Impact damage was produced using static indentation to create multiple delaminations. The authors demonstrated the attenuation effects of the delaminated region, and they showed a region of geometric shadow behind the damage region. Their results indicated the damage acted as a soft scattering center that resulted in an increase in received energy in directions away from the propagation direction of the actuation signal. Schubert et al. [113] used 3-D vibrometry to observe Lamb wave interaction with damage from a 7-J impact in a quasi-isotropic plate. They built a difference signal from the out-of-plane displacement data. From the difference data they were able to identify strong interaction between the  $A_0$  mode and the impact damaged area as well as mode conversion of the  $S_0$  mode to an  $A_0$  mode. Giurgiutiu and Bottai [100] experimentally detected impact damage in a quasi-isotropic plate using both the pulse-echo and pitch-catch configurations, and they found the  $A_0$  mode was superior to the  $S_0$  mode in detecting the damaged regions.

A few studies have used impact damage to demonstrate detection algorithms using various sensing techniques. Soma Sekhar et al. [114] used drop-weight impacts to create a damaged plate in order to demonstrate the concept of tomography, where the Lamb wave signals from a series of sensors placed around the perimeter of the plate are used to image the condition of the plate. Reynolds et al. [115] developed a procedure to utilize multiple sensor-actuator pairs to detect impact damage in a cross-ply laminate. Each pair was used to create an ellipse of possible damage locations based on the time of flight of a guided wave interacting with the damage site. Multiple ellipse maps were correlated to locate the damage site. Sohn et al. [116] conducted laser vibrometry experiments with an impact damaged composite plate and were able to demonstrate damage detection through a new image processing algorithm. Additionally, they showed the ability to locate disbond damage in an aircraft wing section.

In comparison to the number of experimental studies concerning impact damage, fewer researchers have attempted to create numerical models that represent the impact damage. Diamanti et al. [117] used a linear array of transmitters to generate guided waves in a damaged quasi-isotropic composite plate. Damage was initiated by including a Teflon disc in the mid-plane of the laminate. Subsequently, drop-weight impacts were conducted at the damage location at various energy levels. A finite element model was used to simulate the experiments, and damage was simulated by reducing the elastic properties in a region at the center of the plate by 50%. Rogge and Leckey [118] used finite elements to simulate guided wave interaction with disbond damage resulting from an impact. The damage was simulated as a cylindrical void with a finite thickness. Experimental results were obtained for comparison using a laser vibrometer. Pavelko et al. [119] used a 2-D finite element model to simulate Lamb wave interaction with low-velocity impact damage in a carbon fiber reinforced laminate. The impact damage was modeled as a single delamination, and the authors noted the reflections obtained from the delamination had a very small amplitude. Singh et al. [120] used the finite element method to study the effect of simulated

impact damage in a carbon fiber reinforced laminate. The impact damage was simulated as an inverted cone region of 80% reduced stiffness. The interaction of the  $A_0$  mode was studied, and the out-of-plane displacement behavior of points at a given radius from the defect area was observed. They showed the scattering behavior in directions toward the guided wave source did not change much relative to the damage region size, but it did change shape significantly in directions opposite the source.

#### **1.5.4.4 Damage in Built-up Composite Structures**

Recently, there has been increased attention to guided wave propagation and damage interaction in more complex composite structures, and several numerical and experimental studies have emerged. Among these, Balasubramaniam et al. [121] experimentally characterized the propagation of Lamb waves in T-joint structures composed of glass fiber reinforced sublayers. They considered the effect of interface delaminations at the joint. Lamboul et al. [122] conducted an experimental study of impacted sandwich plates. They produced energy maps from laser vibrometry data, and from these maps they were able to determine the location of the damaged area and its extents. Liu and Chattopadhyay [123] also studied impact damage of a sandwich composite UAV wing, and they used their results to validate a signal processing algorithm. They used two MFC sensors to record guided wave signals after each of 10 successive impact events, which were confined to a small region. They demonstrated how successive low-velocity impacts can lead to catastrophic structural failure. Finally, Ajith and Goopalakrishnan [124] used the spectral element method to simulate guided wave interaction with skin-stiffener debonding, and showed good agreement between their model and 2-D finite element results.

#### **1.5.5 Time-Frequency Analysis of Guided Wave Signals**

The methods used to analyze guided wave signals and derive useful information comprise a significant field of research. These procedures are first intended to identify signal features

due to damage present in the structure. Subsequently, the identified signal features are used to locate and characterize the damage. Staszewski and Worden [125] provided a comprehensive review of the numerous dimensions of signal processing used for damage detection. One of the most prominent categories of processing procedures for guided wave signals is time-frequency analysis. These methods are used to describe how the frequency content of signals change over the time history of the signals, and the information provided can offer insight needed to distinguish and characterize different damage signal features. In many cases, the product of these methods is a time-frequency representation, which is a 2-D plot showing the frequency content with respect to time. Several methods have been used in previous studies to produce these images.

Niethammer et al. [126] provided a good overview of many time-frequency methods. The short-time Fourier transform divides a time-history signal into small overlapping pieces, and then each of the pieces is windowed. The Fourier transform of each windowed piece is taken to produce an energy density with respect to frequency and time, which is called a spectrogram. A closely related method is the Wigner-Ville distribution, which provides a measure of the signal's local time-frequency energy. The major drawback of the Wigner-Ville distribution is the presence of interference terms which must be removed through a smoothing procedure. This smoothing procedure unfortunately results in a smearing effect that reduces the ability to exactly locate certain signal features.

Wavelet methods have seen increased use in the analysis of guided wave signals, and they involve the decomposition of a signal into packets based on some type of basis. Wavelet transforms can be categorized as either continuous wavelet transforms or discrete wavelet transforms. Several different bases of wavelets have been used in the literature, but the Morlet (Gabor) and Daubechies wavelets have been the most popular for guided wave decomposition [9]. Kim and Kim [127] used the continuous wavelet transform to analyze dispersive waves and demonstrated the superiority of the method over the short-time Fourier transform. More recently, Okabe et al. [128] used the continuous wavelet trans-

form to examine signals from a composite beam containing a delamination. The transform results were used to discern between delaminations of different lengths. Sohn et al. [129] used the Morlet wavelet to analyze guided wave signals from a damaged composite plate instrumented with an array of sensors.

Mallat and Zhang [130] introduced the matching pursuit approach, which decomposes a signal into a combination of waveforms from a pre-defined dictionary. This approach uses an iterative process to select the best matching waveforms. They proposed using a library of Gaussian-modulated time-frequency functions, called atoms, as candidate waveforms. The atoms in this library had a stationary time-frequency behavior, which means the frequency at which the maximum energy occurs does not change with time. Zhang et al. [131] used matching pursuit to de-noise signals. Hong et al. [132] used this type of dictionary in their studies, and they were able to successfully capture very small reflections from a crack in a rod. Das et al. [133] combined matching pursuits with a Monte Carlo method to reduce the size of the dictionary and rapidly decompose a signal. Vizzini and Chattopadhyay [134] used matching pursuit to characterize signals in a delaminated composite panel, and they were able to detect the damage features for a variety of temperatures ranging from 20 °C to 80 °C. The major drawback to the originally-proposed dictionary is that it does not capture dispersive signals well, which have non-stationary time-frequency behaviors. Gribonval [135] introduced an alternative dictionary based on Gaussian-modulated chirplet atoms, which have a linear time-frequency behavior. Raghavan and Cesnik [136] developed a chirplet matching pursuit approach, and they were able to successfully resolve overlapping, multimodal guided wave signals from damage in aluminum plates.

### **1.5.6 Assessment of the State of the Art in Guided Wave SHM**

Based on this literature review, four key areas have been identified where this dissertation can advance current capabilities:

- **Guided Wave Generation in LISA:** Currently, a need exists to improve the method by which guided waves are generated in the simulations to ensure they accurately model the effects of various actuators.
- **Damage Modeling in LISA:** While some preliminary studies exist, considerable work is still needed to fully validate LISA's ability to capture the effects of guided wave interaction with damage. Proper modeling strategies need to be identified for various types of damage expected in structures of interest.
- **Guided Wave Damage Characterization:** The SHM community is still at the beginning stages of understanding how various damage types effect guided wave propagation, especially in composite structures. More information is needed to help differentiate between damage of different types, shapes, and sizes.
- **Matching Pursuit:** The matching pursuit method has shown great promise as a way to identify important features of guided wave signals. Opportunity exists to combine the power of matching pursuit with LISA simulation capabilities to produce a model-based framework for locating and classifying damage.

## 1.6 Dissertation Overview

The remainder of this dissertation is organized as follows:

- **Chapter 2** focuses on the Global Matrix Method for modeling guided wave propagation in laminated plates. The theoretical development of this model is thoroughly explained, and shortcomings of previous employments of this method are noted. A new method is presented that produces accurate time histories of the displacements that result from excitation using finite dimension actuators. The method is demonstrated for both piezoceramic wafer actuators and CLoVER.
- **Chapter 3** introduces the LISA hybrid method, which utilizes the Global Matrix Method to model an actuator and uses LISA to describe the wave propagation in

a finite plate. Background on the development of LISA is provided, and the process for deriving the iterative equations is summarized. The advantages of the new method are explained in comparison with previous methods of representing guided wave actuation mechanisms. Results for circular, square, and CLoVER actuators are presented and compared with Global Matrix results to demonstrate the success of the new method.

- **Chapter 4** considers guided wave interaction with holes in isotropic and composite plates. A series of simulations using the LISA hybrid method are used to characterize the effect of this type of damage in plate structures. Both through-thickness and half-depth holes are considered. The effect of hole size and location on guided wave propagation are also explored. Experimental data are presented to validate the simulation results for both the isotropic and composite cases.
- **Chapter 5** presents another set of damage interaction studies for impact-damaged composite plates. Diagnostic results are presented to examine the damage features resulting from laboratory-produced low-velocity impact. Experimental results are then presented to characterize the effect of low-velocity impact on guided wave propagation. These results are used as the basis for evaluating impact damage modeling techniques in LISA.
- **Chapter 6** introduces a matching pursuit method which uses a library of LISA simulation results to locate and classify damage regions found using guided wave signals. Results for a 1-D scenario are presented for through-thickness hole damage in both isotropic and composite plates, and the new algorithm's ability to locate damage and identify its size is demonstrated. The algorithm is also demonstrated in a 2-D scenario for a composite laminate, successful hole damage location results are shown.
- **Chapter 7** concludes the dissertation with a summary of the key contributions of this dissertation. It also offers several recommendations for future study.

## CHAPTER 2

# Global Matrix Method

While no closed form solution exists for Lamb wave propagation in composite laminates, the matrix approaches have been very successful in moving towards complete 3-D theoretical modeling of guided waves. The objective of this chapter is to introduce an improved methodology to fully develop the displacement time histories resulting from the Global Matrix Method. First, the chapter reviews the fundamentals of the Global Matrix Method and the general process for obtaining the displacement time history. The axisymmetric case involving actuation from a piezoelectric disc bonded to a plate with isotropic layers is considered to illustrate the presence of inbound and outbound waves in the general solution, and previous solution techniques are reviewed. The general solution for transversely isotropic lamina is described next, and the new solution process is explained. Results from the improved solution are compared with those from a previous solution as well as an exact isotropic formulation for both circular and square actuators. Finally, results for a cross-ply laminate are verified using experimental results to reinforce the utility of the new approach.

### 2.1 Global Matrix Formulation

The Global Matrix Method used in this work is largely adapted from the work of Lih and Mal [59] and Raghavan and Cesnik [62]. The first step in this method is to describe the wave propagation in an individual lamina. The starting point for the analysis is the



displacement form of the equilibrium equation for a transversely isotropic bulk medium,

$$\nabla \mathbf{S} \nabla^T \mathbf{u} = \rho \ddot{\mathbf{u}} \quad (2.1)$$

where  $\mathbf{S}$  is the material stiffness matrix,  $\mathbf{u}$  is the displacement vector, and  $\rho$  is the material density. Harmonic excitation of the medium at frequency  $\omega$  is assumed, which produces a wave field of the form,

$$\mathbf{u} = \mathbf{C} e^{-i(\xi_1 x_1 + \xi_2 x_2 + \zeta x_3 - \omega t)} \quad (2.2)$$

where  $\mathbf{C}$  is a vector of displacement amplitude constants. In-plane wavenumbers are represented as  $\xi_1$  and  $\xi_2$ , while through-thickness wavenumbers are represented as  $\zeta$ . Based on this assumed solution, the equilibrium equation can be reformed into the Christoffel equation:

$$\begin{bmatrix} S_{11}\xi_1^2 + S_{55}(\xi_2^2 + \zeta^2) & (S_{12} + S_{55})\xi_1\xi_2 & (S_{12} + S_{55})\xi_1\zeta \\ (S_{12} + S_{55})\xi_1\xi_2 & S_{55}\xi_1^2 + S_{22}\xi_2^2 + S_{44}\zeta^2 & (S_{23} + S_{44})\xi_2\zeta \\ (S_{12} + S_{55})\xi_1\zeta & (S_{23} + S_{44})\xi_2\zeta & S_{55}\xi_1^2 + S_{44}\xi_2^2 + S_{22}\zeta^2 \end{bmatrix} \begin{bmatrix} u_1 \\ u_2 \\ u_3 \end{bmatrix} = \rho \omega^2 \begin{bmatrix} u_1 \\ u_2 \\ u_3 \end{bmatrix} \quad (2.3)$$

In the Christoffel equation, the  $S_{ij}$  terms are components of the material stiffness matrix for a transversely isotropic lamina. For a given frequency and fixed values of the in-plane wavenumbers, this equation admits six possible values for the through-thickness wavenumber,  $\pm\zeta_i$ , where  $i = 1$  to 3. The general solution for the displacement vector can then be expressed as,

$$\mathbf{u} = (C_1^u \mathbf{e}_1 e^{i\zeta_1 x_3} + C_2^u \mathbf{e}_2 e^{i\zeta_2 x_3} + C_3^u \mathbf{e}_3 e^{i\zeta_3 x_3} + C_1^d \mathbf{e}_4 e^{-i\zeta_1 x_3} + C_2^d \mathbf{e}_5 e^{-i\zeta_2 x_3} + C_3^d \mathbf{e}_6 e^{-i\zeta_3 x_3}) e^{-i(\xi_1 x_1 + \xi_2 x_2 - \omega t)} \quad (2.4)$$

where  $C_1^u$  and  $C_1^d$  are displacement amplitude constants associated with upward and downward traveling waves, respectively. The eigenvectors for the displacement field correspond to the  $\mathbf{e}_j$  variables.

Having determined a solution for the displacement in a single lamina, the next step is to account for the multilayer structure of the plate. A 2-D Fourier transform is used to move from the spatial domain to the wavenumber domain, and another Fourier transform is used to move from the time domain to the frequency domain. Coordinate transformations are used to convert local in-plane wavenumbers to global in-plane wavenumbers in polar coordinates. Subsequently, the Global Matrix is formed by enforcing displacement and stress continuity at the layer interfaces of the laminate. It is convenient to represent the stress and displacement quantities for a single lamina  $m$  in vector form as,

$$\begin{bmatrix} L^m & 0 \\ 0 & L^m \end{bmatrix} \begin{bmatrix} Q_{11}^m & Q_{12}^m \\ Q_{21}^m & Q_{22}^m \end{bmatrix} \begin{bmatrix} E_u^m & 0 \\ 0 & E_d^m \end{bmatrix} \begin{bmatrix} C_u^m \\ C_d^m \end{bmatrix} = Q^m C^m \quad (2.5)$$

where  $L^m$  is the transformation matrix corresponding to the orientation of the  $m$ th lamina. The  $Q_{ij}^m$  terms represent submatrices containing the stress and displacement eigenvectors in the local coordinate system. The contents of these submatrices can be found in detail in Appendix A. The  $E$  terms are the exponentials from Eq. 2.4. The displacements and the three stresses contained in this vector are assumed to be continuous at the lamina interface between the bottom of lamina  $m$  and the top of lamina  $m + 1$ ,

$$Q_{Bottom}^m C^m = Q_{Top}^{m+1} C^{m+1} \quad (2.6)$$

where Fig. 2.1 shows the layer numbering scheme used in this formulation. The interface between lamina  $m$  and lamina  $m + 1$  can be represented as:

$$\begin{bmatrix} Q_{Bottom}^m & -Q_{Top}^{m+1} \end{bmatrix} \begin{bmatrix} C^m \\ C^{m+1} \end{bmatrix} = \begin{bmatrix} 0 \\ 0 \end{bmatrix} \quad (2.7)$$

Applying this relationship to each interface results in the formation of the banded Global Matrix, which completely represents the laminated plate structure. The Global



phase velocities and to form dispersion curves for the plate. On the other hand, a complete solution of Eq. 2.8 is needed to determine the displacement solution for the plate. Determination of the  $C_1^u$  and  $C_1^d$  constants requires the forcing vector for the actuator to be represented in terms of a 2-D spatial Fourier transform. Any actuator can be modeled using this approach as long as the tractions it produces can be represented in the wavenumber domain. Previous works have demonstrated the use of rectangular, ring, and circular actuators [62, 137]. Cramer's rule provides a convenient way to determine the constant values once the forcing vector is in wavenumber space.

Once the constants for each lamina are determined, it is possible to determine the displacements at any point on the plate. Most implementations of this method have only allowed for determination of the out-of-plane displacement component at the top surface of the plate. This implementation extends the method to calculate all three displacement components at any through-thickness location on the plate. The displacement vector at a given point is represented in the wavenumber and frequency domain as,

$$\mathbf{U}(K_1, K_2, X_3, \omega) = \begin{bmatrix} Q_{11}^m & Q_{12}^m \end{bmatrix} \begin{bmatrix} E_u & 0 \\ 0 & E_d \end{bmatrix} \begin{bmatrix} C_u^m \\ C_d^m \end{bmatrix} \quad (2.9)$$

where  $K_1$  and  $K_2$  are the in-plane components of the global wavenumber,  $X_3$  is the through-thickness location of the point of interest in global coordinates,  $\omega$  is the frequency, and  $Q_{11}^m$  and  $Q_{12}^m$  are the displacement eigenvectors for the lamina containing the point of interest. The  $C$  constants used in the calculation also correspond to the lamina containing the point of interest.

The matrix of exponentials in Eq. 2.9 must be calculated based on the through-thickness location of the point of interest. This matrix is in terms of the applicable lamina's local coordinate system and is given by:

$$\begin{bmatrix} E_u & 0 \\ 0 & E_d \end{bmatrix} = \begin{bmatrix} e^{i\zeta_1 x_3} & 0 & 0 & 0 & 0 & 0 \\ 0 & e^{i\zeta_2 x_3} & 0 & 0 & 0 & 0 \\ 0 & 0 & e^{i\zeta_3 x_3} & 0 & 0 & 0 \\ 0 & 0 & 0 & e^{-i\zeta_1 x_3} & 0 & 0 \\ 0 & 0 & 0 & 0 & e^{-i\zeta_2 x_3} & 0 \\ 0 & 0 & 0 & 0 & 0 & e^{-i\zeta_3 x_3} \end{bmatrix} \quad (2.10)$$

Once the individual matrices in Eq. 2.9 are calculated, they can be multiplied to determine the value of the displacement vector at the given wavenumber, through-thickness location, and frequency. It can be shown that this results in an expression for displacement component  $i$  of the form,

$$U_i(K_1, K_2, X_3, \omega) = \frac{\Psi_i(K, \Gamma, X_3, \omega)}{\Delta(K, \Gamma, \omega)} \quad (2.11)$$

where the  $\Delta$  term represents the determinant of the Global Matrix. The  $\Psi_i$  term is a function of the global radial wavenumber  $K$ , the global azimuthal wavenumber  $\Gamma$ , and the constants associated with the layer of interest.

In order to determine the values of the displacement component in the spatial and time domains, a series of inverse transformations is necessary. First, a 2-D inverse Fourier transform is used to move from the wavenumber domain to the spatial domain. The inversion formula in polar coordinates is given by:

$$u_i(r, \theta, X_3, \omega) = \frac{1}{4\pi^2} \int_0^\infty \int_0^{2\pi} \frac{\Psi_i(K, \Gamma, X_3, \omega)}{\Delta(K, \Gamma, \omega)} e^{-iKr \cos(\theta - \Gamma)} K d\Gamma dK \quad (2.12)$$

In Eq. 2.12, the integrand is singular at wavenumber values that set the determinant of the Global Matrix to zero. These are exactly the values of the propagating wavenumbers for the plate. Previous works [61, 62, 137] have shown the employment of the residue formula to perform the complex integration needed to overcome this difficulty and complete the in-

version. Residue calculus is used in this work as well, and for the form of the displacement formula in Eq. 2.12, the applicable formula [138] is:

$$\int_0^{\infty} IdK = \pi i \sum_{\hat{K}} Res(I(\hat{K})) \quad (2.13)$$

Application of the residue formula in Eq. 2.13 produces an inversion formula containing only one integral, which is more easily handled via numerical integration:

$$u_i(r, \theta, X_3, \omega) = \sum_{\hat{K}} \frac{i}{4\pi} \int_0^{2\pi} \frac{\Psi_i(\hat{K}, \Gamma, X_3, \omega)}{\Delta'(\hat{K}, \Gamma, \omega)} \hat{K} e^{-i\hat{K}r\cos(\theta-\Gamma)} d\Gamma \quad (2.14)$$

In Eq. 2.13 and Eq. 2.14, the  $\hat{K}$  values correspond to those radial wavenumbers that produce a zero determinant. The  $\Delta'$  term is the derivative of the Global Matrix determinant with respect to the global radial wavenumber. The result of the 2-D inversion is the displacement harmonic for the given spatial location and frequency.

Finally, an inverse Fourier transform is used to move from the frequency domain to the time domain. The nature of the actuation must be considered during this step. In this work, a Hann-modulated toneburst signal with a given center frequency is used to excite the plate. An example with a 75 KHz center frequency is shown in Fig. 2.2. To determine the frequency spectrum of the displacement at a given point, the Fourier transform of the actuation signal is multiplied by the displacement harmonic at each frequency. The inverse transform then produces the displacement time history at the point of interest.

In practice, this formulation was implemented with a series of FORTRAN and MATLAB codes. A detailed description of the construction of each of those programs and an explanation of how they work together is included in Appendix C.

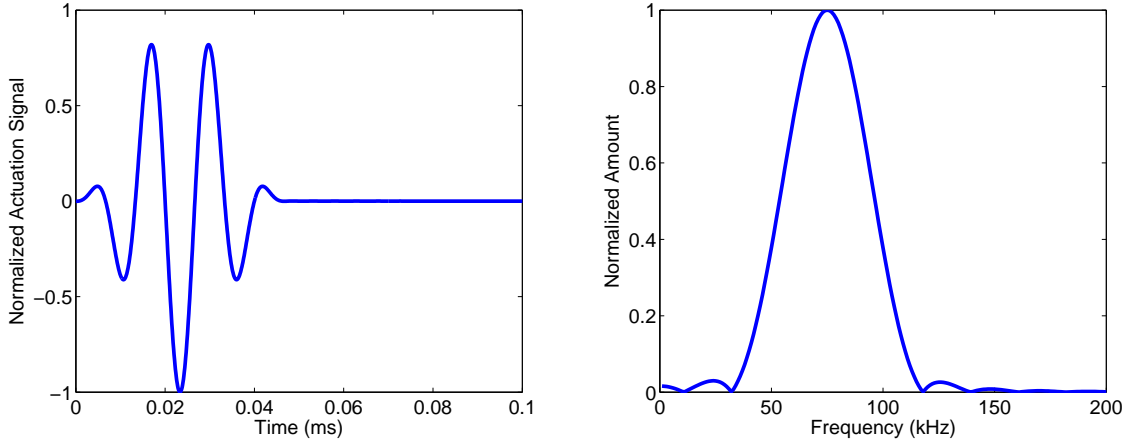


Figure 2.2: Actuation signal time history and frequency content for a Hann-modulated toneburst with 75 kHz center frequency.

## 2.2 Axisymmetric Solution for Isotropic Lamina

It is instructive to first consider the case of a circular actuator mounted on the surface of a plate consisting of isotropic layers, which allows for an axisymmetric solution. For a circular actuator, the transformed forcing vector has previously [137] been shown to be,

$$\begin{aligned} F_1 &= -i\tau_0 R J_1(KR) \cos \Gamma \\ F_2 &= -i\tau_0 R J_1(KR) \sin \Gamma \end{aligned} \quad (2.15)$$

where  $\tau_0$  is an amplitude constant for the stress transferred to the plate,  $R$  is the radius of the actuator, and  $J_1$  represents the first-order Bessel function of the first kind.

Using the process previously outlined, it can be shown that this forcing vector will produce an expression for the displacement in the plate of the form:

$$u_i(r, \theta, X_3, \omega) = \frac{\tau_0}{4\pi^2} \int_0^\infty \int_0^{2\pi} \frac{\Psi_i(K, \Gamma, X_3, \omega)}{\Delta(K, \Gamma, \omega)} e^{-iKr \cos(\theta - \Gamma)} K d\Gamma dK \quad (2.16)$$

Because the host plate is isotropic and the circular actuator provides axisymmetric actuation, many of the terms do not vary with respect to the azimuthal wavenumber. These can

be moved outside the inner integral:

$$u_i(r, \theta, X_3, \omega) = \frac{\tau_0}{4\pi^2} \int_0^\infty \frac{\Psi_i(K, X_3, \omega)}{\Delta(K, \omega)} K \int_0^{2\pi} e^{-iKr \cos(\theta - \Gamma)} d\Gamma dK \quad (2.17)$$

Conveniently, the inner integral is an integral representation of a zero-order Bessel function of the first kind, i.e.,

$$J_0(Kr) = \frac{1}{2\pi} \int_0^{2\pi} e^{-iKr \cos(\theta - \Gamma)} d\Gamma \quad (2.18)$$

and Eq. 2.17 can be rewritten with only one integral with respect to the global radial wavenumber:

$$u_i(r, \theta, X_3, \omega) = \frac{\tau_0}{2\pi} \int_0^\infty \frac{\Psi_i(K, X_3, \omega)}{\Delta(K, \omega)} K J_0(Kr) dK \quad (2.19)$$

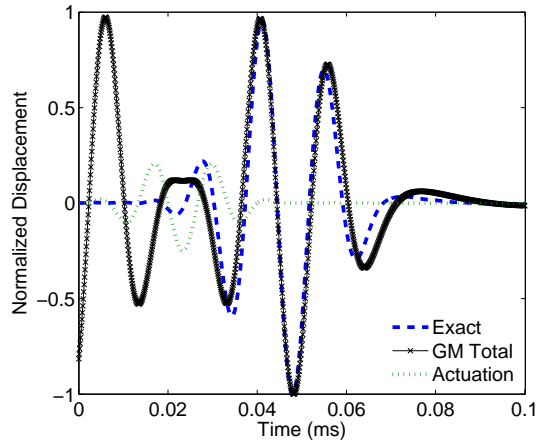
Application of the residue theorem produces the following formula for the displacement harmonic for a given frequency and position:

$$u_i(r, \theta, X_3, \omega) = \sum_{\hat{K}} \frac{i\tau_0}{2} \frac{\Psi_i(\hat{K}, X_3, \omega)}{\Delta'(\hat{K}, \omega)} \hat{K} J_0(\hat{K}r) \quad (2.20)$$

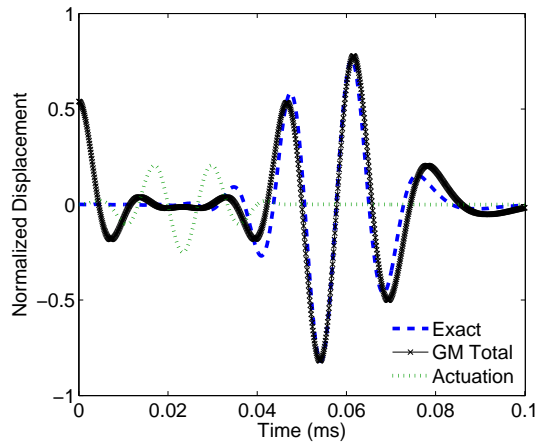
The final step needed to produce the time history for a given point on the plate is to transform the displacement from the frequency domain to the time domain.

The plots in Fig. 2.3 show the time histories for the out-of-plane displacements of three points on the surface of a 1.5 mm plate consisting of six 0.25 mm aluminum laminae with the properties given in Table 2.1. The points are located 40, 60, and 80 mm from the center of the circular actuator. The Global Matrix results are plotted with an exact solution for an isotropic plate developed by Raghavan and Cesnik [46]. These results should match for the case under consideration. Additionally, the actuation signal used to drive the circular actuator is shown. The results show the Global Matrix solution does not start at zero displacement as it should. A closer look at the Global Matrix results shows that at all spatial locations, the signal is actually mirrored about the time corresponding to half of the actu-

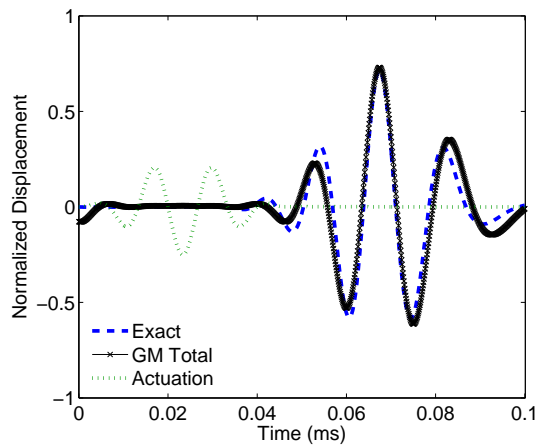




(a) 40 mm



(b) 60 mm



(c) 80 mm

Figure 2.3: Out-of-plane displacement time histories for total axisymmetric solution at 40, 60, and 80 mm locations. Results are for a circular actuator on an aluminum laminate.

Table 2.1: Aluminum material properties

Property	$E$	$\nu$	$\rho$
Value	70 GPa	0.3	2700 kg/m <sup>3</sup>

ation time span. The source of this mirroring effect can be understood by considering that Eq. 2.20 admits a solution to the wave equation composed of the superposition of an inward propagating wave and an outward propagating wave. The outward propagating wave is the desired solution. The inward wave, while an admissible mathematical solution to the equation, does not satisfy the physical nature of the scenario and should be disregarded.

For this axisymmetric case, correcting for the presence of the inward wave is relatively straight-forward, as shown previously [139]. The Bessel function can be rewritten as the sum of two Hankel functions:

$$u_i(r, \theta, X_3, \omega) = \sum_{\hat{K}} \frac{i\tau_0}{4} \frac{\Psi_i(\hat{K}, X_3, \omega)}{\Delta'(\hat{K}, \omega)} \hat{K} (H_0^{(1)}(\hat{K}r) + H_0^{(2)}(\hat{K}r)) \quad (2.21)$$

The following asymptotic expressions apply to the Hankel functions:

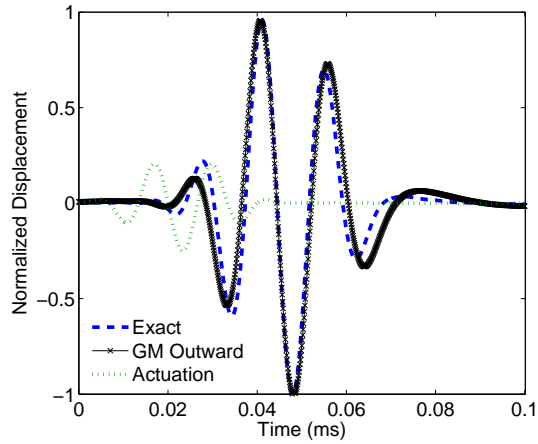
$$\lim_{Kr \rightarrow \infty} H_0^{(1)}(Kr) = \sqrt{\frac{2}{\pi Kr}} e^{i(Kr - \frac{\pi}{4})} \quad (2.22)$$

$$\lim_{Kr \rightarrow \infty} H_0^{(2)}(Kr) = \sqrt{\frac{2}{\pi Kr}} e^{-i(Kr - \frac{\pi}{4})} \quad (2.23)$$

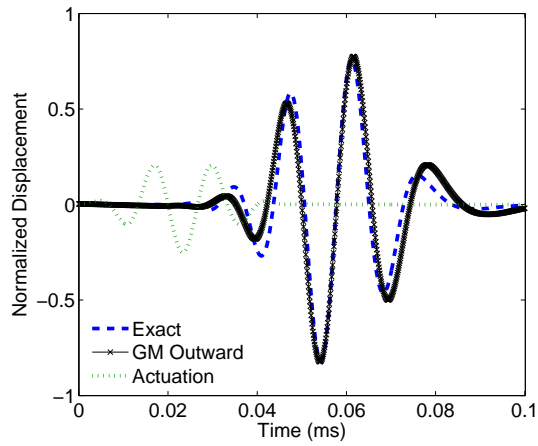
The Hankel function of the first type corresponds to an inward propagating wave, and can be excluded on physical grounds. This yields a displacement solution,

$$u_i(r, \theta, X_3, \omega) = \sum_{\hat{K}} \frac{i\tau_0}{4} \frac{\Psi_i(\hat{K}, X_3, \omega)}{\Delta'(\hat{K}, \omega)} \hat{K} H_0^{(2)}(\hat{K}r) \quad (2.24)$$

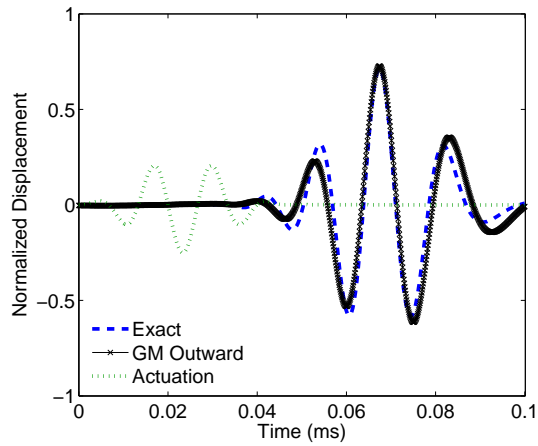
which closely matches the exact solution, as shown in Fig. 2.4.



(a) 40 mm



(b) 60 mm



(c) 80 mm

Figure 2.4: Out-of-plane displacement time histories for outward axisymmetric solution at 40, 60, and 80 mm locations. Results are for a circular actuator on an aluminum laminate.

## 2.3 Anisotropic Plate Displacement Solution

For the more general case where the individual layers may be transversely isotropic and oriented in various directions, axisymmetry no longer applies. Simplification of Eq. 2.16 is not possible. However, the residue formula can still be applied to the unsimplified equation to produce a displacement solution. This yields a displacement in the frequency domain:

$$u_i(r, \theta, X_3, \omega) = \sum_{\hat{K}} \frac{\tau_0}{4\pi} \int_0^{2\pi} \frac{\Psi_i(\hat{K}, \Gamma, X_3, \omega)}{\Delta'(\hat{K}, \Gamma, \omega)} \hat{K} e^{-i\hat{K}r \cos(\theta-\Gamma)} d\Gamma \quad (2.25)$$

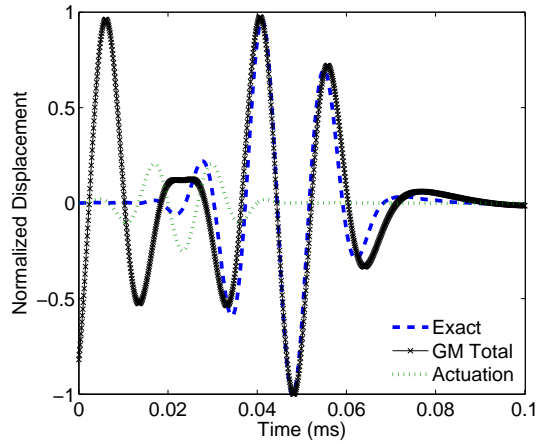
If numerical integration is applied to complete the 2-D inverse transform and the displacements are then transformed to the time domain, the time histories in Fig. 2.5 result for the aluminum laminate previously considered. These are identical to those found in Fig. 2.3, which is not surprising, since Eq. 2.25 inherently retains both the inward and outward wave solutions considered in the axisymmetric case. Another method is needed to separate the two parts of the solution and retain only the outward solution.

### 2.3.1 Previous Solution Method

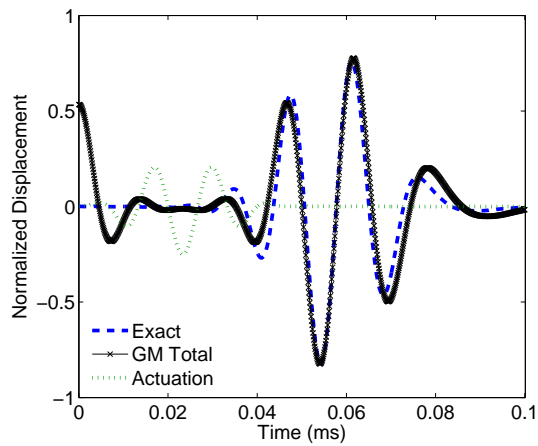
In order to avoid the presence of the inward wave, Raghavan and Cesnik [62] proposed a method that recasts the inversion formula by changing the limits of integration found in Eq. 2.16, resulting in:

$$u_i(r, \theta, X_3, \omega) = \frac{\tau_0}{4\pi^2} \int_{\theta-\frac{\pi}{2}}^{\theta+\frac{\pi}{2}} \int_{-\infty}^{\infty} \frac{\Psi_i(K, \Gamma, X_3, \omega)}{\Delta(K, \Gamma, \omega)} e^{-iKr \cos(\theta-\Gamma)} K d\Gamma dK \quad (2.26)$$

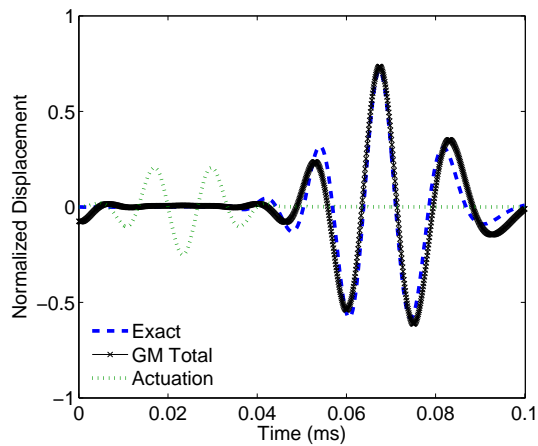
By changing the limits of integration, the coefficient of  $K$  in the complex exponential remains positive over the entire domain of integration. This step is intended to eliminate inward propagating waves from the subsequent wave solutions. As before, the residue for-



(a) 40 mm



(b) 60 mm



(c) 80 mm

Figure 2.5: Out-of-plane displacement time histories for the total anisotropic solution for a circular actuator on an aluminum laminate at 40, 60, and 80 mm locations.

mula is used to simplify the 2-D inversion process, yielding a summation equation with only one integral:

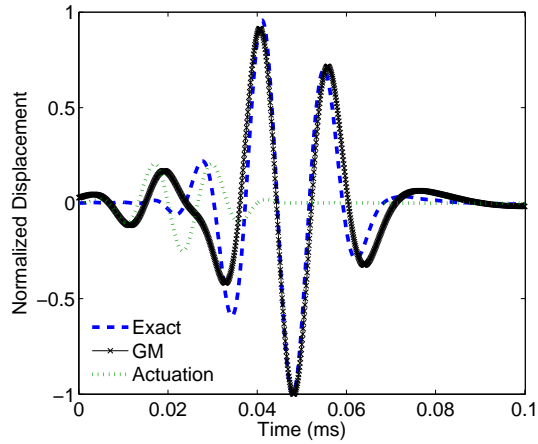
$$u_i(r, \theta, X_3, \omega) = \sum_{\hat{K}} \frac{\tau_0}{2\pi} \int_{\theta-\frac{\pi}{2}}^{\theta+\frac{\pi}{2}} \frac{\Psi_i(\hat{K}, \Gamma, X_3, \omega)}{\Delta'(\hat{K}, \Gamma, \omega)} e^{-i\hat{K}r \cos(\theta-\Gamma)} \hat{K} d\Gamma \quad (2.27)$$

In the original implementation of this method, the results were examined in both the frequency and time domains. The harmonic results were able to correctly predict energy steering phenomena in unidirectional composite plates. Time domain results in the form of field plots also showed good agreement with finite element results when examined at specific points in time.

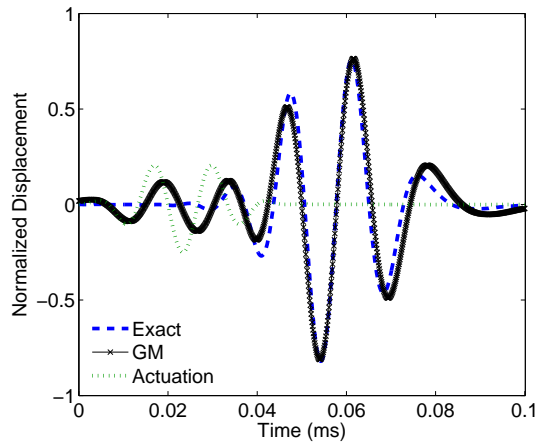
However, more detailed examination of this method reveals that while it removes the majority of the inward wave, it produces a non-physical artifact in the time history. Figure 2.6 shows the time histories for the 1.5 mm thick aluminum laminate. From these plots, a small wave is visible between 0 and 0.4 ms that is not present in the exact solution. Consideration of additional spatial points, such as the point 200 mm from the center of the actuator shown in Fig. 2.7, reveals that this disturbance is present during this time period at all points on the plate simultaneously, although it does decrease in amplitude as the distance from the actuator increases. In many cases, this small disturbance is of little consequence. In the far field, the artifact is well separated from the real outbound propagating wave and can be truncated on physical grounds. For points near the actuator, such as the 40 mm case shown here, the disturbance interferes with the real solution and this simple truncation is not feasible.

### 2.3.2 Updated Solution Method

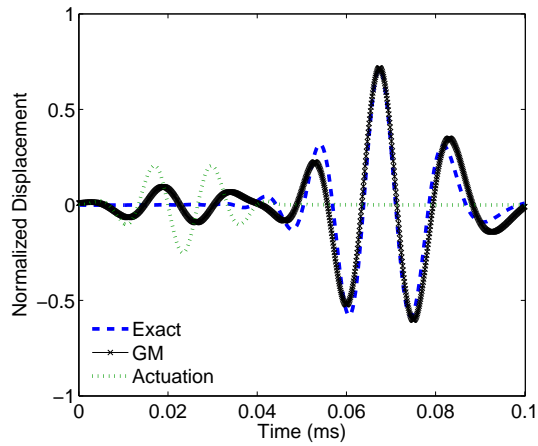
This section demonstrates a new process to complete the 2-D Fourier inversion, eliminate the presence of the inward wave, and prevent the non-physical artifacts seen previously. Returning to the displacement formula in Eq. 2.25 as a starting point, both the inward and



(a) 40 mm



(b) 60 mm



(c) 80 mm

Figure 2.6: Out-of-plane displacement time histories using the previous inversion method for a circular actuator on an aluminum laminate at 40, 60, and 80 mm locations.

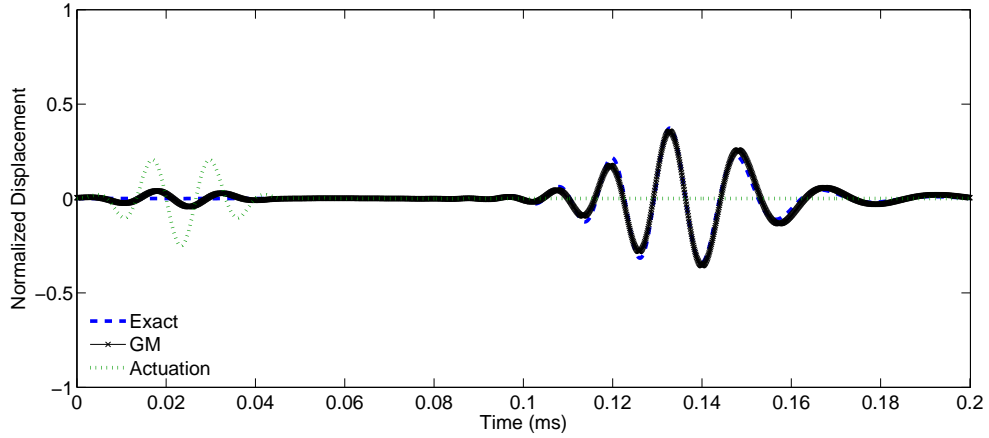


Figure 2.7: Out-of-plane displacement time histories using the previous inversion method for a circular actuator on an aluminum laminate at 200 mm location.

outward wave solutions are present. This solution will now be called the original signal:

$$u_i^O(r, \theta, X_3, \omega) = \sum_{\hat{K}} \frac{\tau_0}{4\pi} \int_0^{2\pi} \frac{\Psi_i(\hat{K}, \Gamma, X_3, \omega)}{\Delta'(\hat{K}, \Gamma, \omega)} \hat{K} e^{-i\hat{K}r \cos(\theta - \Gamma)} d\Gamma \quad (2.28)$$

A two-step process is used to extract the outbound wave from the total solution. First, a correction signal is produced using the following formula:

$$u_i^C(r, \theta, X_3, \omega) = \sum_{\hat{K}} \frac{\tau_0}{4\pi} \int_0^{2\pi} \frac{\Psi_i(\hat{K}, \Gamma, X_3, \omega)}{\Delta'(\hat{K}, \Gamma, \omega)} \hat{K} e^{-i\hat{K}r \cos(\theta - \Gamma)} \cos(\theta - \Gamma) d\Gamma \quad (2.29)$$

As seen in Fig. 2.8, this correction signal alters the original time history signal. The sign of the inbound portion of the wave is reversed, while the outbound wave is unchanged. Second, the desired outbound wave is obtained by adding the original signal and the correction signal, and then dividing the resulting signal in half:

$$u_i^{corrected} = \frac{u_i^O + u_i^C}{2} \quad (2.30)$$



Figure 2.9 compares the exact isotropic solution for the aluminum laminate with the Global Matrix results using the previous and updated methods. The time history signals produced using the updated method are a very good match to the exact solution.

## 2.4 Square Actuator Solution

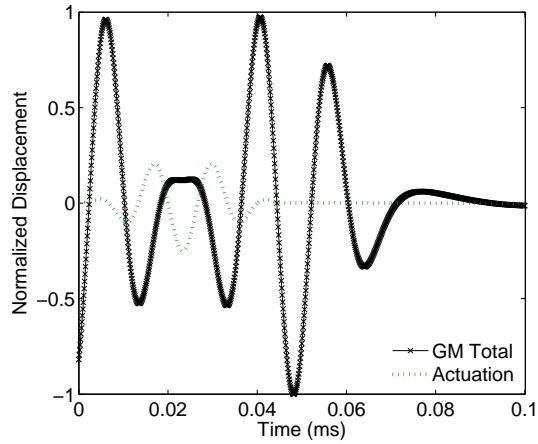
The improved method introduced here is not restricted to circular actuators. In this section, results are presented for a square piezo wafer actuator bonded to the surface of the aluminum laminate. The terms of the forcing vector needed for the Global Matrix equation have been previously presented [62] for rectangular actuators. When applied to a square actuator, the forcing terms can be represented in the wavenumber domain as,

$$\begin{aligned} F_1 &= -4\tau_0 \sin(K_1 A) \sin(K_2 A) / iK_2 \\ F_2 &= -4\tau_0 \sin(K_1 A) \sin(K_2 A) / iK_1 \end{aligned} \tag{2.31}$$

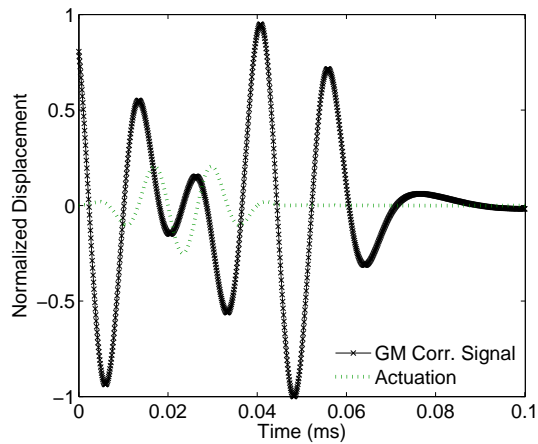
where  $A$  is the half length of the sides of the actuator. The different forcing vector due to the square actuator results in a different solution for the displacement constants when the Global Matrix equation in Eq. 2.8 is solved using Cramer's rule. Following through with the remainder of the process yields a displacement solution of the same form as that found in Eq. 2.28 through Eq. 2.30.

Figure 2.10 shows the original, uncorrected, displacement time histories for the square actuator case with an aluminum plate. The results are shown for points 40, 60, and 80 mm from the center of the actuator, measured along the 0-degree azimuth. The presence of the inbound portion of the solution is visible and shows the same symmetry as was seen in the circular actuator case. Figure 2.11 shows the corrected solution along with the exact solution from the formulation in [46], indicating a very close match.

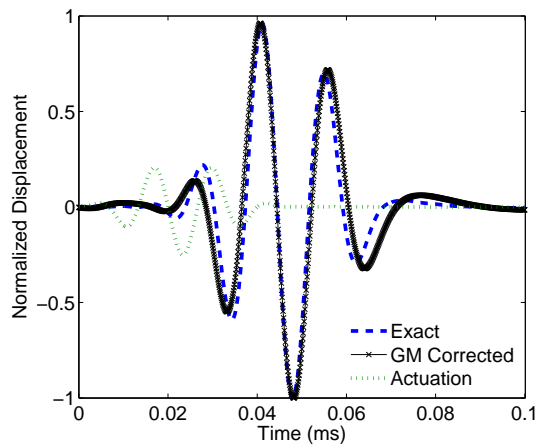
Since the solution for the square actuator case is not axisymmetric in the near field, results along the 15, 30, and 45-degree azimuths are also shown in Fig. 2.12 to demon-



(a) Original Signal

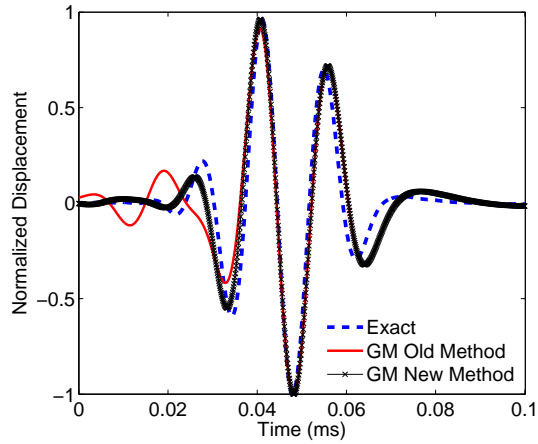


(b) Correction Signal

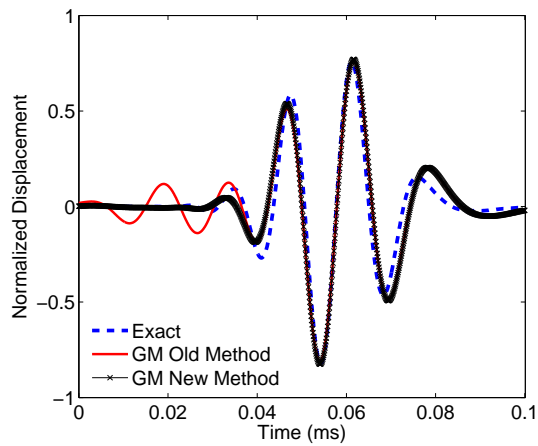


(c) Final Corrected Signal

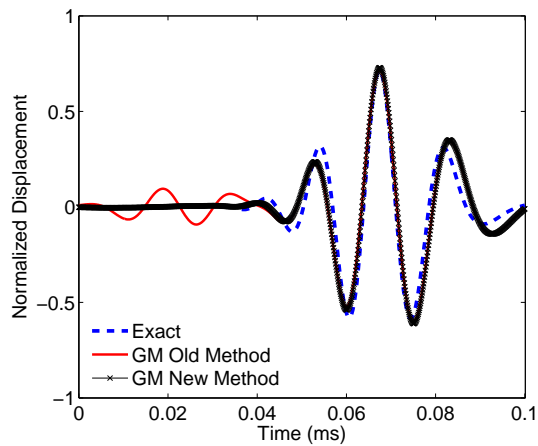
Figure 2.8: Correction procedure for displacement time history at 40 mm location. Results are for a circular actuator on an aluminum laminate.



(a) 40 mm

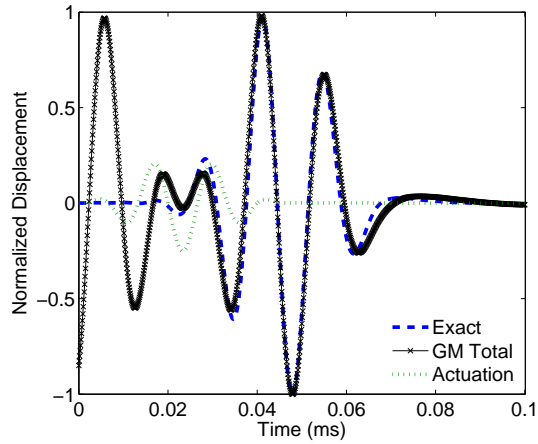


(b) 60 mm

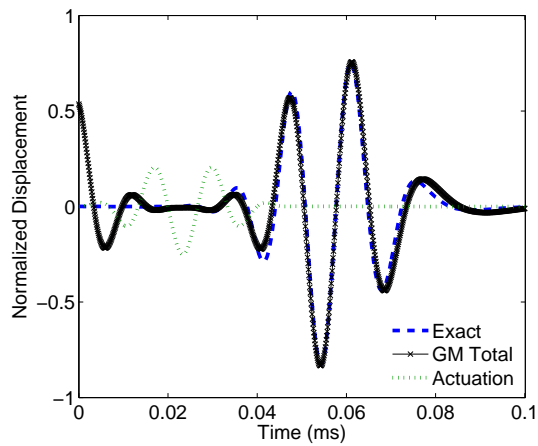


(c) 80 mm

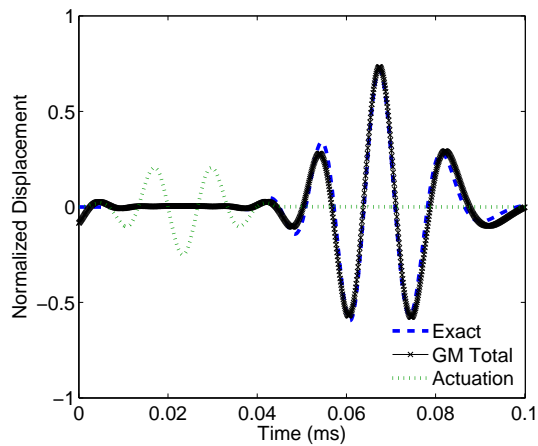
Figure 2.9: Comparison of old and new inversion methods with exact solution at 40, 60, and 80 mm locations. Results are for a circular actuator on an aluminum laminate.



(a) 40 mm

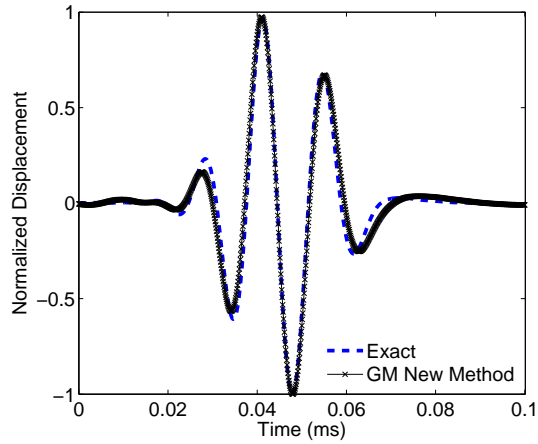


(b) 60 mm

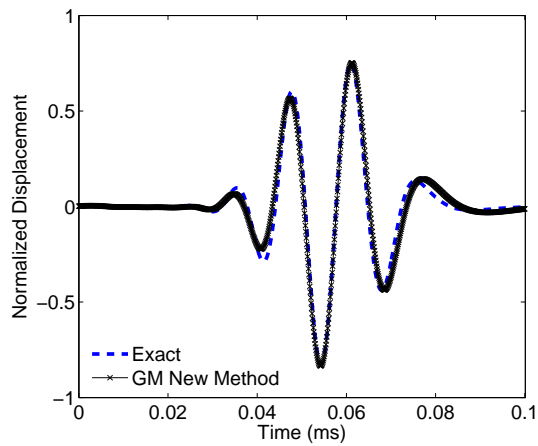


(c) 80 mm

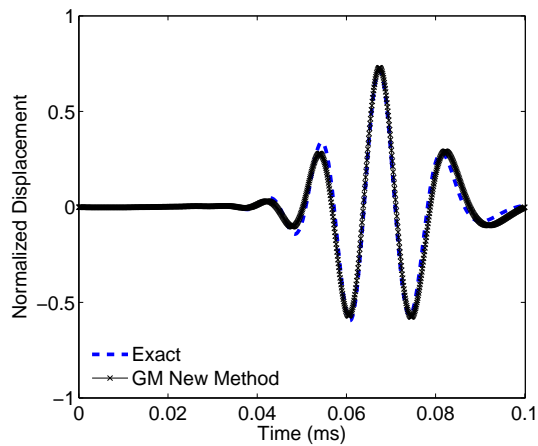
Figure 2.10: Original square actuator solution at 40, 60, and 80 mm locations for an aluminum laminate.



(a) 40 mm

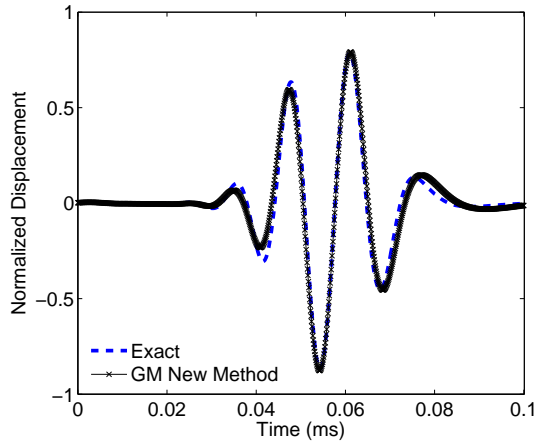


(b) 60 mm

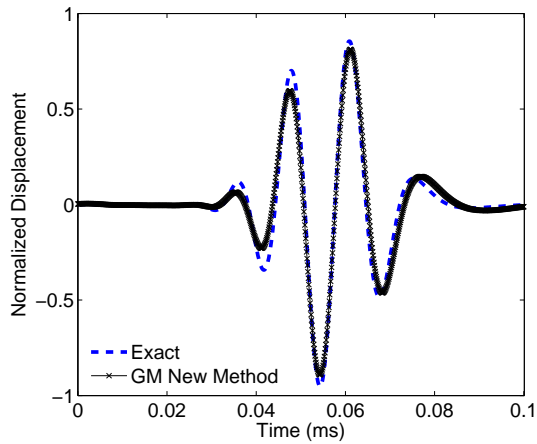


(c) 80 mm

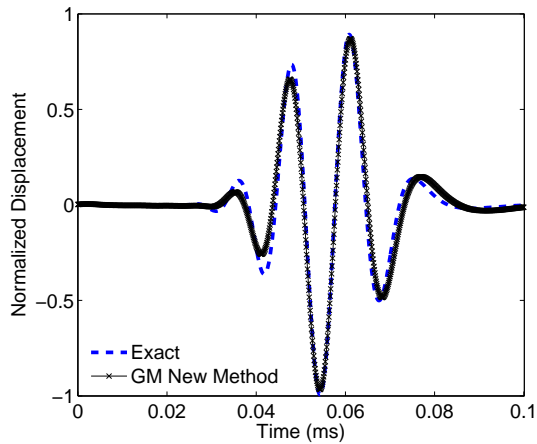
Figure 2.11: Corrected square actuator solution at 40, 60, and 80 mm locations for an aluminum laminate.



(a) 40 mm



(b) 60 mm



(c) 80 mm

Figure 2.12: Corrected square actuator solution at 60 mm location at 15, 30, and 45 degrees for an aluminum laminate.

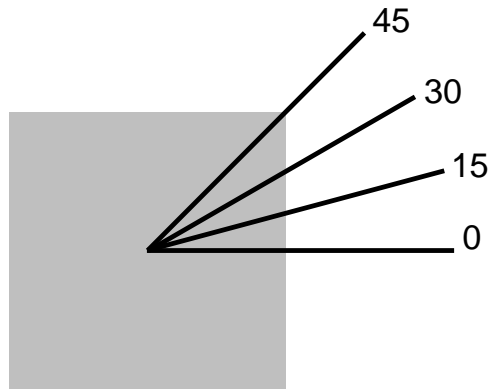


Figure 2.13: Azimuthal angles for square actuator displacement time history comparisons.

strate the agreement between the new solution results and the exact results. The azimuthal directions relative to the actuator shape are shown in Fig. 2.13

## 2.5 Results for Cross-ply Laminate

In this section, the updated solution method is used to create displacement time histories for a cross-ply laminate with graphite-epoxy lamina. No completely analytical solutions exist for this case, so the Global Matrix results are presented with experimental results for verification. First, the experimental setup and procedures are explained. The experimental and Global Matrix results are then compared to demonstrate the success of the new method.

### 2.5.1 Experimental Setup

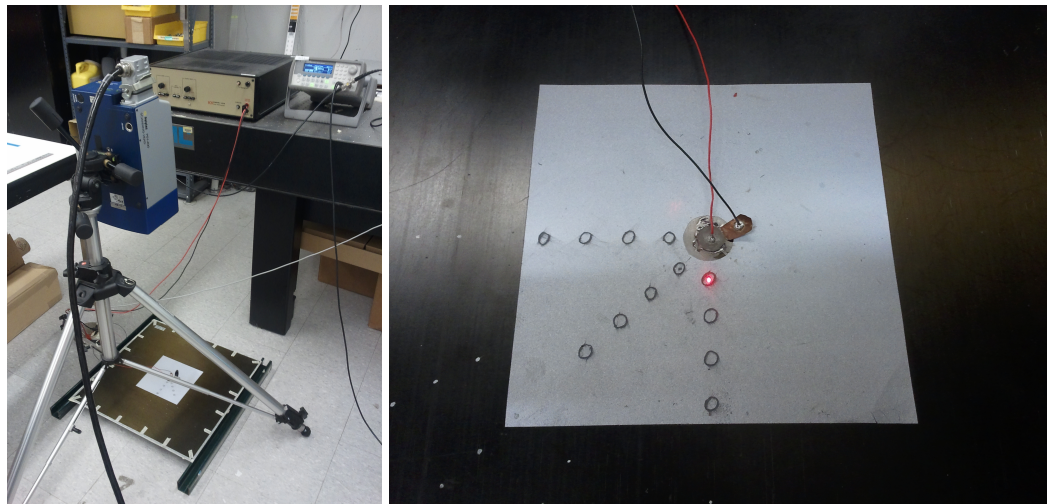
The composite plate used in the experiment had a cross-ply construction ( $[0/90]_{3S}$ ) and was fabricated in house using the CYCOM IM7 977-3 material system with the properties included in Table 2.2. Each lamina was 0.125 mm thick, resulting in a 1.5 mm thick plate. The side length of the plate was 0.5 m.

Table 2.2: CYCOM IM7 977-3 Material Properties

Property	$E_1$	$E_2$	$G_{12}$	$G_{23}$	$\nu_{12}$	$\rho$
Value	147 GPa	9.8 GPa	2.35 GPa	3.3 GPa	0.405	1558 kg/m <sup>3</sup>

The guided waves were generated with a circular actuator bonded to the geometric center of the plate. The actuator was a PZT-5A wafer with a diameter of 12.8 mm. The actuation pulse used for the experiment was a Hann-modulated toneburst with the parameters shown earlier in Fig. 2.2. To generate the toneburst signal, an Agilent 33220A function generator was programmed with the applicable parameters. This function generator was connected to a Krohn-Hite 7500 amplifier, which supplied a 100X amplification to the signal. A digital oscilloscope was used to monitor the signal before and after the amplifier to verify the quality of the toneburst provided to the actuator.

The resulting out-of-plane behavior of the plate was measured using a Polytec PSV-400 laser vibrometer, as shown in Fig. 2.14 (a). Reflective tape was applied to the surface of the plate in the area around the actuator to ensure an adequate laser return reached the



(a) Laser vibrometer setup.

(b) Actuator and reflective tape configuration.

Figure 2.14: Experimental setup for cross-ply wave propagation experiment.



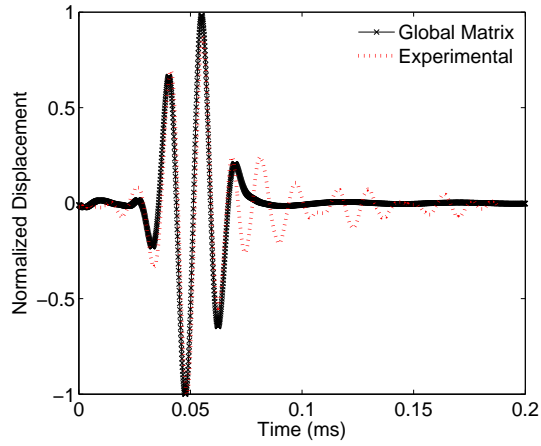
vibrometer for measurement. This is shown in Fig. 2.14 (b). Additionally, the locations of the desired scan points are visible. For each of the observed points on the plate, 100 measurements were taken and averaged to reduce the effects of noise in the vibrometer signal. The resulting time histories were recorded and saved using the Polytec software on a connected desktop computer.

## 2.5.2 Comparison of Results

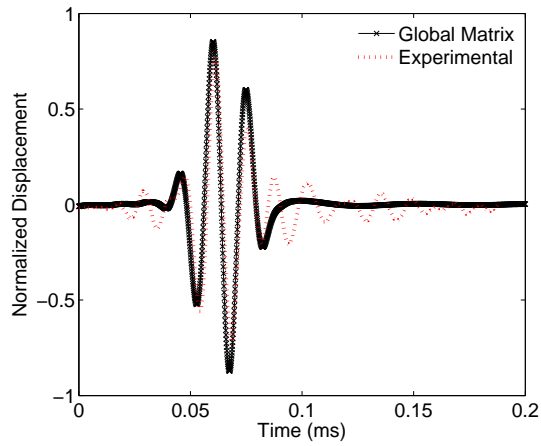
Due to the anisotropic nature of the cross-ply plate, it was valuable to compare results at various azimuth angles to verify the new method captured the directional nature of wave propagation in the plate. Figures 2.15 through 2.17 show the Global Matrix and experimental results at 0, 45, and 90-degree azimuth angles. The results were normalized so the maximum amplitude of each data set was 1 for the 0-degree, 40mm case. All other results were normalized with respect to this scale.

In each case, the results from the updated Global Matrix Method showed good general agreement with the experimental results. For each direction, the arrival time of the large  $A_0$  wave packet was consistent between the experiment and the Global Matrix results at each of the observed distances. Only a few small discrepancies were present. First, the amplitude of the  $S_0$  mode was higher in the experiment than in the Global Matrix results. This was most noticeable at the 80 mm location in the 0-degree direction between 0.02 and 0.05 ms. Some additional peaks were also present in the experimental results after the passage of the main wave packet. These were most likely a combination of noise in the experiment along with some boundary reflections from the fast-moving  $S_0$  mode.

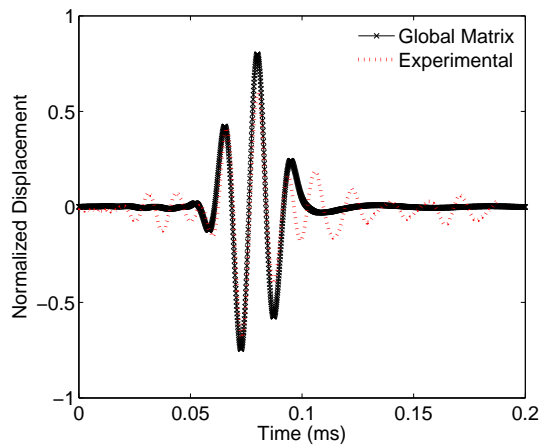
Numerical comparisons of the amplitude results for each direction are shown in Tables 2.3 to 2.5. The percent difference between the maximum amplitude of the Global Matrix and experimental results ranged from 2.5% to 41.7%, with 6 of the 8 cases having less than 16% difference.



(a) 40 mm

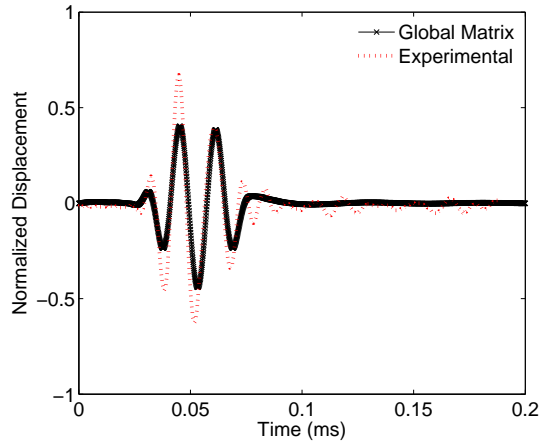


(b) 60 mm

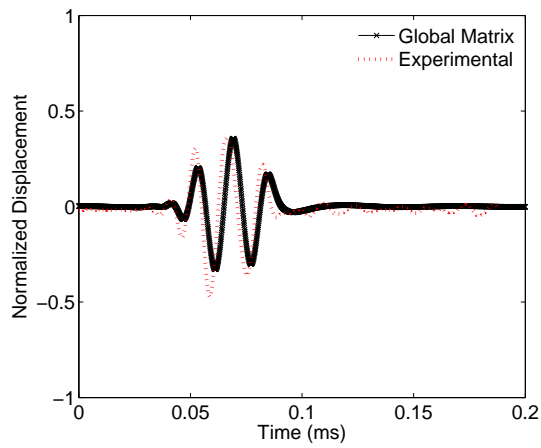


(c) 80 mm

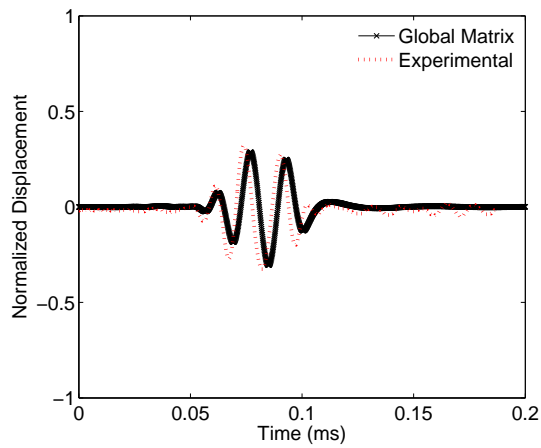
Figure 2.15: Comparison of Global Matrix and experimental results for 0-degree azimuth at 40, 60, and 80 mm locations. Results are for a circular actuator on a  $[0/90]_{3S}$  laminate.



(a) 40 mm

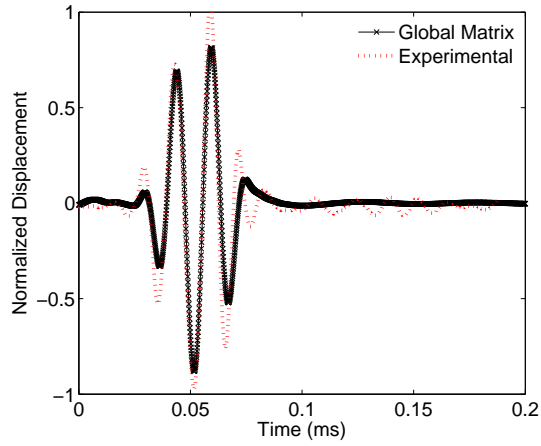


(b) 60 mm

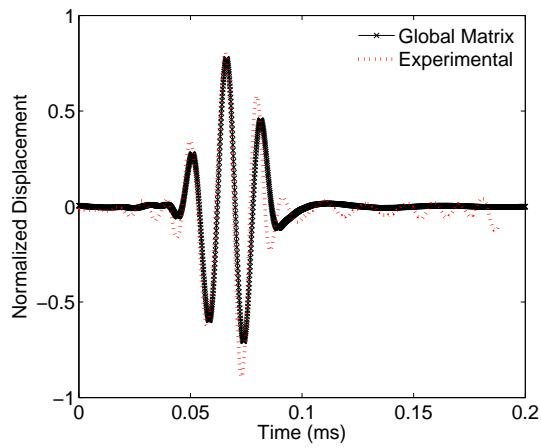


(c) 80 mm

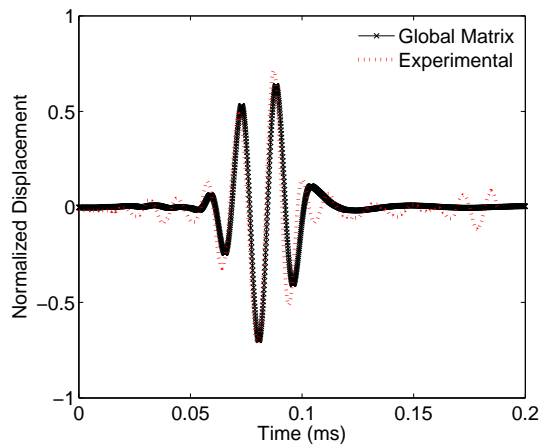
Figure 2.16: Comparison of Global Matrix and experimental results for 45-degree azimuth at 40, 60, and 80 mm locations. Results are for a circular actuator on a  $[0/90]_{3S}$  laminate.



(a) 40 mm



(b) 60 mm



(c) 80 mm

Figure 2.17: Comparison of Global Matrix and experimental results for 90-degree azimuth at 40, 60, and 80 mm locations. Results are for a circular actuator on a  $[0/90]_{3S}$  laminate.

Table 2.3: Amplitude results for cross-ply wave propagation in 0-degree direction.

Distance	GM	Experiment	Difference	% Difference
40 mm	1	1	0	0
60 mm	0.87	0.77	0.10	12.7
80 mm	0.80	0.69	0.11	15.4

Table 2.4: Amplitude results for cross-ply wave propagation in 45-degree direction.

Distance	GM	Experiment	Difference	% Difference
40 mm	0.44	0.67	0.23	41.7
60 mm	0.36	0.47	0.12	28.7
80 mm	0.31	0.33	0.02	6.7

Table 2.5: Amplitude results for cross-ply wave propagation in 90-degree direction.

Distance	GM	Experiment	Difference	% Difference
40 mm	0.88	1	0.12	12.8
60 mm	0.77	0.89	0.12	14.3
80 mm	0.70	0.72	0.02	2.5

The amplitude attenuation seen in the Global Matrix and experimental results showed agreement in terms of the general trend. The attenuation for each case can be modeled as a power law:

$$u = ax^b \quad (2.32)$$

where  $u$  is the amplitude,  $x$  is the distance from the actuator, and  $a$  and  $b$  are power law constants. The values for the  $a$  and  $b$  constants are shown in Table 2.6 for each direction. Overall, the experiment showed more attenuation as the distance from the actuator increased. This is to be expected, since the Global Matrix Method did not take into account material damping.

Table 2.6: Amplitude attenuation power law constants for cross-ply wave propagation comparisons.

		GM	Experiment
0 deg	a	3.31	7.56
	b	-0.33	-0.55
45 deg	a	3.09	30.82
	b	-0.53	-1.03
90 deg	a	3.01	7.43
	b	-0.33	-0.53

## 2.6 Summary

This chapter presented a new methodology to complete the 2-D Fourier inversion needed to produce displacement time histories using the Global Matrix method. The need to separate inward and outward propagating waves was demonstrated, and problems with previous solution attempts were highlighted. The updated method produced a correction signal for the displacement time history that was added to the original time history to eliminate the presence of the inward wave. The success of the new procedure was demonstrated for both circular and square actuators bonded to an aluminum laminate using comparisons with previously published exact solutions. The reliability of the method was further proven by comparing Global Matrix results for a cross-ply plate with those from laser vibrometry experiments. The new method was found to produce accurate time history results that also capture the directionality found in composite laminates.

## CHAPTER 3

# LISA Hybrid Model

This chapter introduces a hybrid Global Matrix/LISA model for wave propagation in composite laminates. First, a description of the architecture of the model is included, showing how the Global Matrix Method is used in conjunction with LISA to produce a full wave propagation model. Next, the procedure for deriving the LISA iterative equations is briefly explained, and the methods used to model actuators in previous LISA implementations are reviewed. Finally, results are presented to demonstrate the LISA hybrid model's ability to accurately represent wave propagation from circular, square, and CLoVER actuators.

### 3.1 LISA Hybrid Model

This section describes the overarching structure of the LISA hybrid model. While the Global Matrix Method is well suited to capture the effects of finite-dimensional actuators, it cannot capture damage or lateral plate boundaries. On the other hand, numerical formulations can successfully model finite-dimensional plates. One such formulation is LISA. As introduced in Chapter 1, LISA is a finite-difference-based numerical scheme which is gaining popularity for guided wave propagation analysis. It is based on the derivation of a set of iterative equations that can be used to calculate displacements at a series of nodes over the course of a time-based simulation. While LISA is quite powerful, representing the effects of surface-mounted actuators is challenging. As an alternative to using solely the Global Matrix Method or LISA, the LISA hybrid model is introduced that leverages the

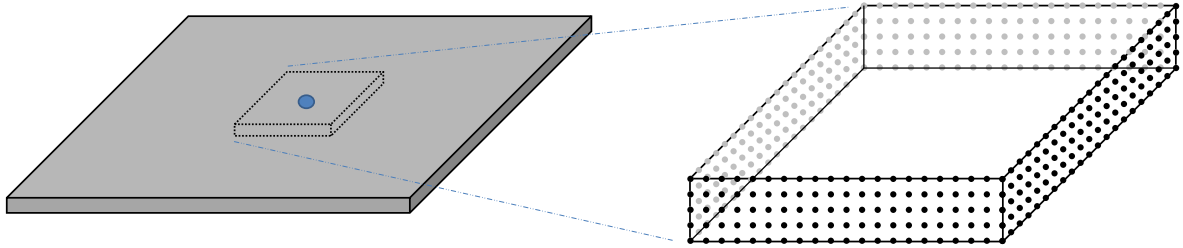


Figure 3.1: Schematic of displacement input field for LISA hybrid wave propagation model.

strengths of both methods. It uses the Global Matrix approach to represent the effects of the actuator while using LISA for the majority of the plate structure.

First, the overall LISA model is defined according to the structure of the plate, including any material differences between layers for a laminate. As in previous LISA models, air cells are included at the plate boundaries to allow for traction-free boundary conditions. Next, a cut-out region around the actuator is defined as in Fig. 3.1, and the nodes within the LISA model located on the boundary of this region are identified and tabulated. Third, the time histories of the three displacement components resulting from the piezoelectric actuation are calculated at each of the cut-out boundary points using the Global Matrix Method. Because the entire time history of the displacements is calculated and stored, this step only needs to be run once for the plate configuration used in the simulation. Finally, the square cut-out region surrounding the actuator is segregated from the remainder of the model, and the LISA simulation is started. At each time step in the LISA simulation, the displacement values for the boundary nodes of this region are specified according to the Global Matrix time history. The LISA model is run as usual to completely capture the wave propagation behavior for the remainder of the plate.

With this architecture comes a few important limitations. Because the Global Matrix displacements are specified at the cut-out boundary during the entire time actuation is occurring, reflecting waves cannot pass through to the cut-out region. This means no sensors can be modeled in the cut-out region. Additionally, the presence of any damage features



present in the cut-out region cannot be accurately depicted. One other limitation comes from the fact that the model does not directly account for the piezoelectric coupling effects in the actuator. Since the model specifies tractions and not the voltages that would be applied to the actuator, direct displacement amplitude comparisons cannot be made with experimental results. Only normalized comparisons are facilitated.

While the LISA hybrid model still specifies displacements, the actuation modeling method is distinct from previous LISA implementations. Because the LISA hybrid model uses the Global Matrix Method to capture the behavior of the actuator, it inherently assumes the actuator imposes tractions, not displacements, on the plate surface. These tractions are included in the solution process used to determine the displacement time histories at all points along cut-out boundaries.

## 3.2 LISA Theoretical Background

The LISA formulation used in this dissertation was developed by Nadella and Cesnik [90], and their work should be consulted for the details of the theoretical background. This section provides a brief introduction to the steps used to derive the iterative equations needed to implement the method. Figure 3.2 summarizes the typical process of deriving the equations for LISA.

The starting point for the derivation is the elastodynamic equilibrium equation, which was presented earlier in Eq. 2.1. For the purposes of the derivation, it is advantageous to recast the equilibrium equations using Voigt notation, which results in:

$$\sum_{m=1}^3 \sum_{\eta=1}^6 S_{\eta\lambda} u_{m,\lambda} = \rho \ddot{u}_k \quad (3.1)$$

where the  $k$  subscript takes values of 1, 2, or 3 depending on the applicable displacement component. The  $S_{\eta\lambda}$  term is a component of the stiffness matrix for the material in the Voigt system. The repeated  $\lambda$  indices imply summation over the range of values 1 to 6. It should

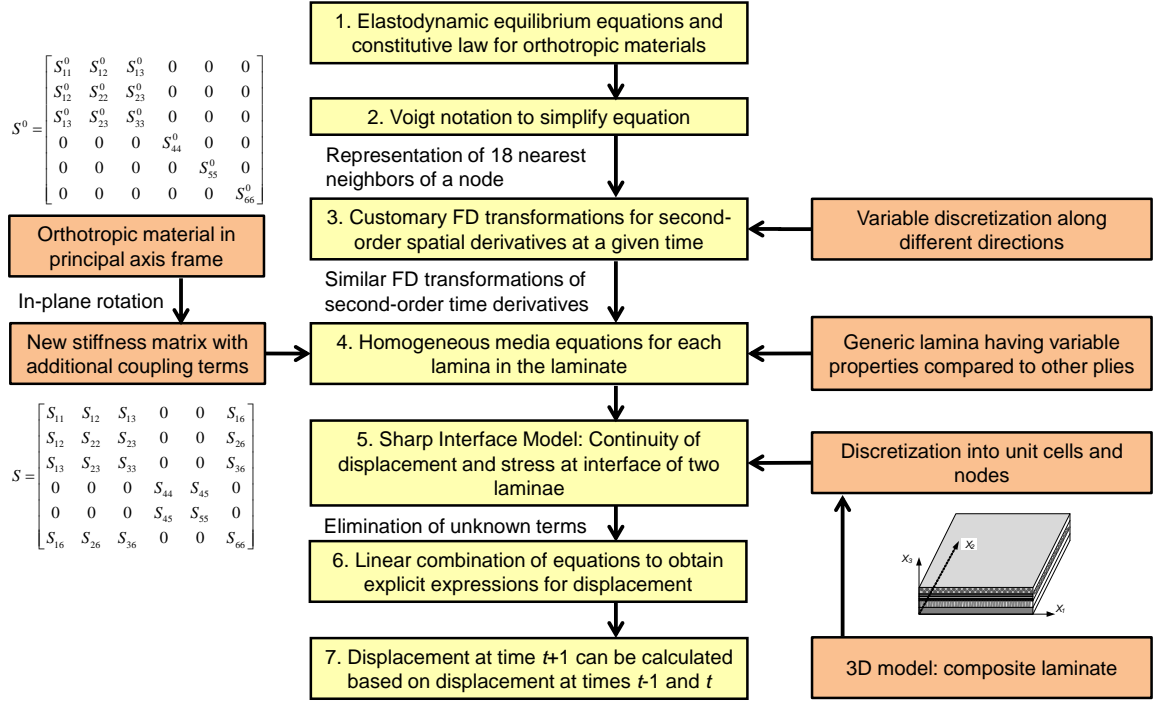


Figure 3.2: Overview of LISA theoretical derivation.

be noted, however, that  $u_{m,\lambda}$  is the second derivative of the  $u_m$  displacement component with respect to the parent indices of the Voigt index  $\lambda$ , not a first derivative. The transformations to Voigt indices are found using,

$$\begin{aligned} (k,l) &\rightarrow \lambda = k\delta_{kl} + (1 - \delta_{kl})(9 - k - l) & (\lambda = 1, \dots, 6) \\ (m,n) &\rightarrow \eta = m\delta_{mn} + (1 - \delta_{mn})(9 - m - n) & (\eta = 1, \dots, 6) \end{aligned} \quad (3.2)$$

where  $\delta_{ij}$  is the Kronecker delta.

Most previous implementations of LISA have assumed an orthotropic material oriented in the principal reference frame, which has a stiffness matrix of the form:

$$\mathbf{S}^0 = \begin{bmatrix} S_{11}^0 & S_{12}^0 & S_{13}^0 & 0 & 0 & 0 \\ S_{12}^0 & S_{22}^0 & S_{23}^0 & 0 & 0 & 0 \\ S_{13}^0 & S_{23}^0 & S_{33}^0 & 0 & 0 & 0 \\ 0 & 0 & 0 & S_{44}^0 & 0 & 0 \\ 0 & 0 & 0 & 0 & S_{55}^0 & 0 \\ 0 & 0 & 0 & 0 & 0 & S_{66}^0 \end{bmatrix} \quad (3.3)$$

Nadella and Cesnik [90] have extended the formulation to apply to orthotropic materials with arbitrary orientation angles, and the stiffness matrix is obtained using a standard coordinate transformation:

$$\mathbf{S} = \begin{bmatrix} S_{11} & S_{12} & S_{13} & 0 & 0 & S_{16} \\ S_{12} & S_{22} & S_{23} & 0 & 0 & S_{26} \\ S_{13} & S_{23} & S_{33} & 0 & 0 & S_{36} \\ 0 & 0 & 0 & S_{44} & S_{45} & 0 \\ 0 & 0 & 0 & S_{45} & S_{55} & 0 \\ S_{16} & S_{26} & S_{36} & 0 & 0 & S_{66} \end{bmatrix} \quad (3.4)$$

For homogeneous materials, Eq. 3.1 can be expanded using standard finite difference formulas for the spatial and time derivatives. For a given point  $C$ , as shown in Fig. 3.3, the equation can then be rearranged to calculate that point's displacement as a function of the displacements of its 18 neighbor points at the previous two time steps. Because the displacement for a given point depends only on information from previous time steps, the displacement at each point can be calculated completely independent of the other points. This is the source of the immense potential for parallelization identified by Delsanto et al. [80] in the original LISA formulation.

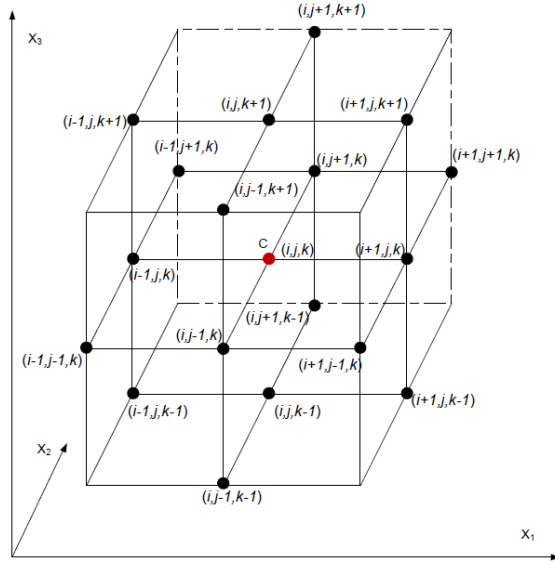


Figure 3.3: Representation of the 18 neighbors of a generic point in LISA and the Cartesian system used in the analysis [88].

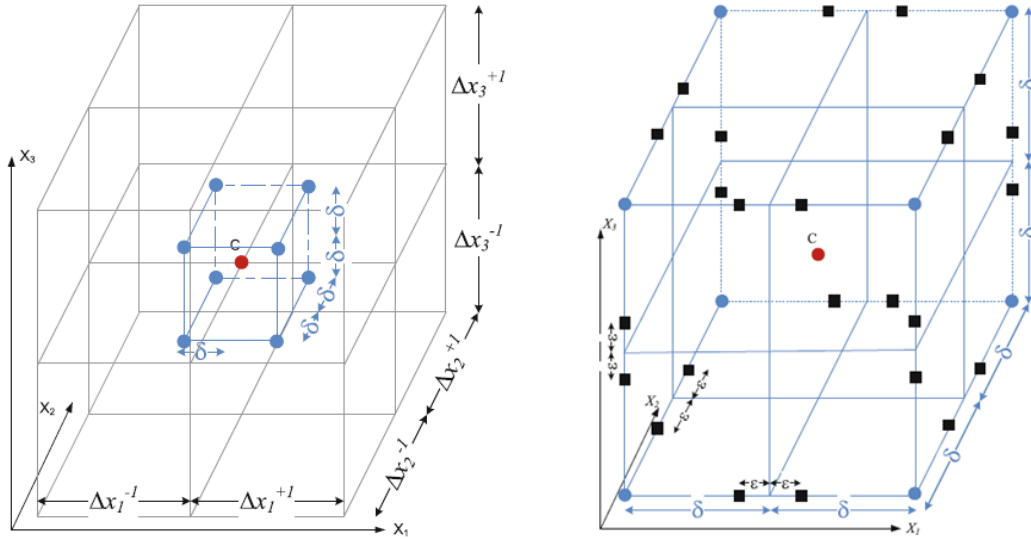
For non-homogeneous materials, it is necessary to account for differences in material properties in different cells. LISA accomplishes this using the sharp interface method (SIM), in which stress and displacement continuity relationships are enforced at the boundaries between cells. Material properties are assumed to be constant within a cell, but they are allowed to vary from one cell to the next. The continuity relationships required in SIM are enforced using a series of points in addition to the 18 nearest neighbors of the point of interest  $C$ .

Figure 3.4 (a) shows the 8 points used to enforce displacement continuity. The equilibrium equations for these 8 points are represented as,

$$\sum_{m=1}^3 \sum_{\eta=1}^6 S_{\eta\lambda}^{i+\alpha\delta, j+\beta\delta, k+\gamma\delta} u_{m,\lambda}^{i+\alpha\delta, j+\beta\delta, k+\gamma\delta} = \rho \ddot{u}_k^{i+\alpha\delta, j+\beta\delta, k+\gamma\delta} \quad (3.5)$$

$$\alpha, \beta, \gamma = \pm 1, \quad k = 1, 2, 3$$

where the applicable point is determined by the values of  $\alpha$ ,  $\beta$ , and  $\gamma$ . The parameter  $\delta$  is a small arbitrary distance much less than the dimensions of the cell. As in the case for the homogeneous material, Eq. 3.5 can be expanded further using standard finite difference



(a) Points used for displacement continuity, shown in blue. (b) Points used for stress continuity, shown in black.

Figure 3.4: Additional points used for SIM continuity requirements [88].

formulas for the spatial and time derivatives. These formulas can be found in Refs. [90] and [86]. This substitution results in 24 equations with 48 independent unknowns. The remaining equations needed to complete the full system are obtained by considering stress continuity. Figure 3.4 (b) shows the 12 pairs of points used to enforce stress continuity. For each of these pairs of points, three stress components can be enforced to be equal, as represented by:

$$\begin{aligned}
 \tau_{p1}^{i+\varepsilon, j+\beta\delta, k+\gamma\delta} &= \tau_{p1}^{1-\varepsilon, j+\beta\delta, k+\gamma\delta} \\
 \tau_{p2}^{i+\alpha\delta, j+\varepsilon, k+\gamma\delta} &= \tau_{p2}^{1+\alpha\delta, j-\varepsilon, k+\gamma\delta} \\
 \tau_{p3}^{i+\alpha\delta, j+\beta\delta, k+\varepsilon} &= \tau_{p3}^{1+\alpha\delta, j+\beta\delta, k-\varepsilon} \quad (p = 1, 2, 3)
 \end{aligned} \tag{3.6}$$

In Eq. 3.6,  $\varepsilon$  represents a small arbitrary distance much less than  $\delta$ . While 36 total stress continuity equations exist, only 24 are independent, and these complete the set needed to completely solve the system.

The process of solving for the three displacement components involves linearly combining the displacement continuity equations and then using the stress equations to eliminate

the unknown terms. Using that process, Nadella and Cesnik [90] produced the following iterative equations which include in-plane rotation of the orthotropic lamina:

$$\begin{aligned}
u^{i,j,k,t+1} = & -u^{i,j,k,t-1} + 2u^{i,j,k} - \frac{2\chi}{8} u^{i,j,k} \sum_{\alpha,\beta,\gamma=\pm 1} \left[ (\eta_x^2 \tilde{S}_{11} + \eta_y^2 \tilde{S}_{66} + \eta_z^2 \tilde{S}_{55}) \right] \\
& + \frac{\chi}{8} \sum_{\alpha,\beta,\gamma=\pm 1} \left[ 2\eta_x^2 \tilde{S}_{11} u^{i+\alpha,j,k} + 2\eta_y^2 \tilde{S}_{66} u^{i,j+\beta,k} + 2\eta_z^2 \tilde{S}_{55} u^{i,j,k+\gamma} \right] \\
& + \frac{\chi}{8} \sum_{\alpha,\beta,\gamma=\pm 1} \left[ \alpha\beta\eta_x\eta_y (\tilde{S}_{12} + \tilde{S}_{66}) (v^{i+\alpha,j+\beta,k} - v^{i,j,k}) \right] + \frac{\chi}{8} \sum_{\alpha,\beta,\gamma=\pm 1} \left[ \alpha\beta\eta_x\eta_y (\tilde{S}_{12} - \tilde{S}_{66}) (v^{i,j+\beta,k} - v^{i+\alpha,j,k}) \right] \\
& + \frac{\chi}{8} \sum_{\alpha,\beta,\gamma=\pm 1} \left[ \alpha\gamma\eta_x\eta_z (\tilde{S}_{13} + \tilde{S}_{55}) (w^{i+\alpha,j,k+\gamma} - w^{i,j,k}) \right] + \frac{\chi}{8} \sum_{\alpha,\beta,\gamma=\pm 1} \left[ \alpha\gamma\eta_x\eta_z (\tilde{S}_{13} - \tilde{S}_{55}) (w^{i,j,k+\gamma} - w^{i+\alpha,j,k}) \right] \\
& - \frac{2\chi}{8} \sum_{\alpha,\beta,\gamma=\pm 1} \left[ \alpha\beta\eta_x\eta_y \tilde{S}_{16} (u^{i,j,k} - u^{i+\alpha,j+\beta,k}) \right] - \frac{2\chi}{8} v^{i,j,k} \sum_{\alpha,\beta,\gamma=\pm 1} \left[ \eta_x^2 \tilde{S}_{16} + \eta_y^2 \tilde{S}_{26} \right] \\
& - \frac{\chi}{8} \sum_{\alpha,\beta,\gamma=\pm 1} \left[ \beta\gamma\eta_y\eta_z (\tilde{S}_{36} + \tilde{S}_{45}) w^{i,j,k} \right] + \frac{2\chi}{8} \sum_{\alpha,\beta,\gamma=\pm 1} \left[ \eta_x^2 \tilde{S}_{16} v^{i+\alpha,j,k} + \eta_y^2 \tilde{S}_{26} v^{i,j+\beta,k} \right] \\
& + \frac{\chi}{8} \sum_{\alpha,\beta,\gamma=\pm 1} \left[ \beta\gamma\eta_y\eta_z \tilde{S}_{36} (w^{i,j+\beta,k+\gamma} + w^{i,j,k+\gamma} - w^{i,j+\beta,k}) \right] \\
& + \frac{\chi}{8} \sum_{\alpha,\beta,\gamma=\pm 1} \left[ \beta\gamma\eta_y\eta_z \tilde{S}_{45} (w^{i,j+\beta,k+\gamma} - w^{i,j,k+\gamma} + w^{i,j+\beta,k}) \right] + \frac{2\chi}{8} \sum_{\alpha,\beta,\gamma=\pm 1} \eta_z^2 \tilde{S}_{45} (v^{i,j,k+\gamma} - v^{i,j,k})
\end{aligned} \tag{3.7}$$

$$\begin{aligned}
v^{i,j,k,t+1} = & -v^{i,j,k,t-1} + 2v^{i,j,k} \\
& - \frac{2\chi}{8} v^{i,j,k} \sum_{\alpha,\beta,\gamma=\pm 1} \left[ \eta_x^2 \tilde{S}_{66} + \eta_y^2 \tilde{S}_{22} + \eta_z^2 \tilde{S}_{44} \right] + \frac{\chi}{8} \sum_{\alpha,\beta,\gamma=\pm 1} \left[ 2\eta_x^2 \tilde{S}_{66} v^{i+\alpha,j,k} + 2\eta_y^2 \tilde{S}_{22} v^{i,j+\beta,k} + 2\eta_z^2 \tilde{S}_{44} v^{i,j,k+\gamma} \right] \\
& + \frac{\chi}{8} \sum_{\alpha,\beta,\gamma=\pm 1} \left[ \alpha\beta\eta_x\eta_y (\tilde{S}_{12} + \tilde{S}_{66}) (u^{i+\alpha,j+\beta,k} - u^{i,j,k}) \right] + \frac{\chi}{8} \sum_{\alpha,\beta,\gamma=\pm 1} \left[ \alpha\beta\eta_x\eta_y (\tilde{S}_{12} - \tilde{S}_{66}) (u^{i+\alpha,j,k} - u^{i,j+\beta,k}) \right] \\
& + \frac{\chi}{8} \sum_{\alpha,\beta,\gamma=\pm 1} \left[ \beta\gamma\eta_y\eta_z (\tilde{S}_{23} + \tilde{S}_{44}) (w^{i,j+\beta,k+\gamma} - w^{i,j,k}) \right] + \frac{\chi}{8} \sum_{\alpha,\beta,\gamma=\pm 1} \left[ \beta\gamma\eta_y\eta_z (\tilde{S}_{23} - \tilde{S}_{44}) (w^{i,j,k+\gamma} - w^{i,j+\beta,k}) \right] \\
& - \frac{2\chi}{8} \sum_{\alpha,\beta,\gamma=\pm 1} \left[ \alpha\beta\eta_x\eta_y \tilde{S}_{26} (v^{i,j,k} - v^{i+\alpha,j+\beta,k}) \right] - \frac{2\chi}{8} u^{i,j,k} \sum_{\alpha,\beta,\gamma=\pm 1} \left[ \eta_x^2 \tilde{S}_{16} + \eta_y^2 \tilde{S}_{26} \right] \\
& + \frac{2\chi}{8} \sum_{\alpha,\beta,\gamma=\pm 1} \left[ \eta_x^2 \tilde{S}_{16} u^{i+\alpha,j,k} + \eta_y^2 \tilde{S}_{26} u^{i,j+\beta,k} \right] - \frac{\chi}{8} \sum_{\alpha,\beta,\gamma=\pm 1} \left[ \alpha\gamma\eta_x\eta_z (\tilde{S}_{36} + \tilde{S}_{45}) w^{i,j,k} \right] \\
& + \frac{\chi}{8} \sum_{\alpha,\beta,\gamma=\pm 1} \left[ \alpha\gamma\eta_x\eta_z \tilde{S}_{36} (w^{i+\alpha,j,k+\gamma} + w^{i,j,k+\gamma} - w^{i+\alpha,j,k}) \right] \\
& + \frac{\chi}{8} \sum_{\alpha,\beta,\gamma=\pm 1} \left[ \alpha\gamma\eta_x\eta_z \tilde{S}_{45} (w^{i+\alpha,j,k+\gamma} - w^{i,j,k+\gamma} + w^{i+\alpha,j,k}) \right] + \frac{2\chi}{8} \sum_{\alpha,\beta,\gamma=\pm 1} \left[ \eta_z^2 \tilde{S}_{45} (u^{i,j,k+\gamma} - u^{i,j,k}) \right]
\end{aligned} \tag{3.8}$$

$$\begin{aligned}
w^{i,j,k,t+1} &= -w^{i,j,k,t-1} + 2w^{i,j,k} - \frac{2\chi}{8} w^{i,j,k} \sum_{\alpha,\beta,\gamma=\pm 1} \left[ \eta_x^2 \tilde{S}_{55} + \eta_y^2 \tilde{S}_{44} + \eta_z^2 \tilde{S}_{33} \right] \\
&+ \frac{\chi}{8} \sum_{\alpha,\beta,\gamma=\pm 1} \left[ 2\eta_x^2 \tilde{S}_{55} w^{i+\alpha,j,k} + 2\eta_y^2 \tilde{S}_{44} w^{i,j+\beta,k} + 2\eta_z^2 \tilde{S}_{33} w^{i,j,k+\gamma} \right] \\
&+ \frac{\chi}{8} \sum_{\alpha,\beta,\gamma=\pm 1} \left[ \beta\gamma\eta_y\eta_z (\tilde{S}_{23} + \tilde{S}_{44}) (v^{i,j+\beta,k+\gamma} - v^{i,j,k}) \right] + \frac{\chi}{8} \sum_{\alpha,\beta,\gamma=\pm 1} \left[ \beta\gamma\eta_y\eta_z (\tilde{S}_{23} - \tilde{S}_{44}) (v^{i,j+\beta,k} - v^{i,j,k+\gamma}) \right] \\
&+ \frac{\chi}{8} \sum_{\alpha,\beta,\gamma=\pm 1} \left[ \alpha\gamma\eta_x\eta_z (\tilde{S}_{13} + \tilde{S}_{55}) (u^{i+\alpha,j,k+\gamma} - u^{i,j,k}) \right] + \frac{\chi}{8} \sum_{\alpha,\beta,\gamma=\pm 1} \left[ \alpha\gamma\eta_x\eta_z (\tilde{S}_{13} - \tilde{S}_{55}) (u^{i+\alpha,j,k} - u^{i,j,k+\gamma}) \right] \\
&- \frac{\chi}{8} \sum_{\alpha,\beta,\gamma=\pm 1} \left[ \beta\gamma\eta_y\eta_z (\tilde{S}_{36} + \tilde{S}_{45}) (u^{i,j,k} - u^{i,j+\beta,k+\gamma}) \right] - \frac{\chi}{8} \sum_{\alpha,\beta,\gamma=\pm 1} \left[ \alpha\gamma\eta_x\eta_z (\tilde{S}_{36} + \tilde{S}_{45}) (v^{i,j,k} - v^{i+\alpha,j,k+\gamma}) \right] \\
&- \frac{\chi}{8} \sum_{\alpha,\beta,\gamma=\pm 1} \left[ \beta\gamma\eta_y\eta_z (\tilde{S}_{36} - \tilde{S}_{45}) (u^{i,j,k+\gamma} - u^{i,j+\beta,k}) \right] - \frac{\chi}{8} \sum_{\alpha,\beta,\gamma=\pm 1} \left[ \alpha\gamma\eta_x\eta_z (\tilde{S}_{36} - \tilde{S}_{45}) (v^{i,j,k+\gamma} - v^{i+\alpha,j,k}) \right] \\
&+ \frac{2\chi}{8} \sum_{\alpha,\beta,\gamma=\pm 1} \left[ \alpha\beta\eta_x\eta_y\tilde{S}_{45} (w^{i+\alpha,j+\beta,k} - w^{i,j,k}) \right]
\end{aligned} \tag{3.9}$$

In these equations, the current time step is assumed when it is not specifically mentioned. Stiffness terms with a tilde, such as  $\tilde{S}_{11}$ , indicate that the value of that term is defined by the value for one of the eight surrounding cells, depending on the current value of  $\alpha, \beta, \gamma$ . The  $\eta_x, \eta_y, \eta_z$ , and  $\chi$  terms characterize the spatial and time discretization used in the model and are defined according to:

$$\begin{aligned}
\eta_x &= 1/\Delta x_1 \\
\eta_y &= 1/\Delta x_2 \\
\eta_z &= 1/\Delta x_3 \\
\chi &= \Delta t^2/\rho
\end{aligned} \tag{3.10}$$

In each of the LISA models used in this dissertation, the spatial and time discretizations have been chosen to meet the Courant-Friedric-Lewy (CFL) criterion,

$$\text{CFL} = c_{max}\Delta t \sqrt{\frac{1}{\Delta x_1^2} + \frac{1}{\Delta x_2^2} + \frac{1}{\Delta x_3^2}} \leq 1 \tag{3.11}$$

which is a necessary condition for stability for FD-based numerical schemes [63]. As defined in Eq. 3.11, the CFL number must remain less than or equal to 1, and it is dependent on both the time step used in the model as well as the spatial discretization. The  $c_{max}$  term represents the maximum propagating wave velocity in the medium.

### 3.3 Actuator Modeling

In most previous LISA studies, actuation was modeled by prescribing in-plane displacements at surface nodes located within the profile of the actuator. Schematics of this actuation method for circular PZT and CLoVER actuators are shown in Figs. 3.5 and 3.6. Two major difficulties have emerged with actuator modeling of this type. First, as seen in the schematics, the Cartesian grid associated with current LISA implementations does not lend itself well to capturing the nonlinear boundaries of circular actuators or more sophisticated actuators such as CLoVER. In many circumstances, the boundaries of the actuator are located between nodes, and some judgment must be exercised to determine which nodes to include in the actuator profile. The second difficulty is the need to assume values for the displacements applied at the nodes contained in the actuator profile. For example, the scheme illustrated for the circular actuator shows a linear increase in the radial displacement based on the radial distance from the actuator center, but that assumption may not truly reflect

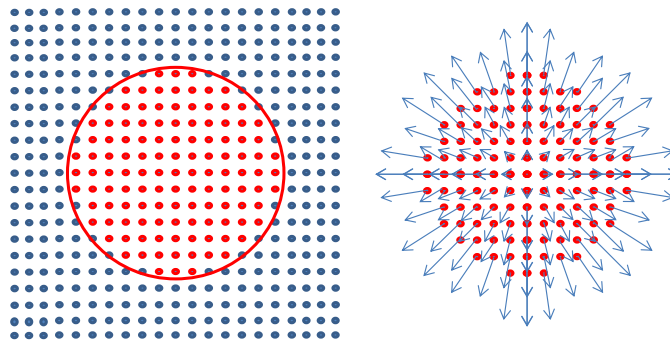


Figure 3.5: Original LISA actuation scheme for a circular actuator using specified in-plane surface displacements.



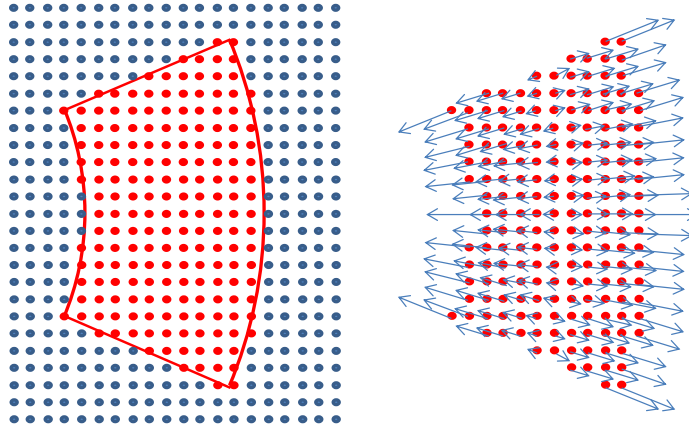


Figure 3.6: Original LISA actuation scheme for a CLoVER actuator sector using specified in-plane surface displacements.

the displacements created by the actuator – especially for anisotropic materials. The LISA hybrid model presented in this chapter avoids both of these difficulties. In the next section, the effectiveness of both the previous approach and the LISA hybrid model in generating waves from surface-mounted piezoelectric actuators is examined with respect to theoretical results.

### 3.4 Comparison of Results

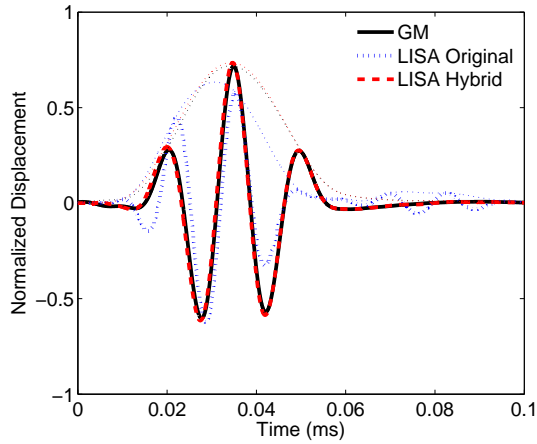
To evaluate the effectiveness of the LISA hybrid model in comparison with the previous LISA implementations, a series of models were evaluated for an aluminum plate, a cross-ply plate ( $[0/90]_{3S}$ ), a unidirectional plate ( $[0]_{12T}$ ), and a quasi-isotropic plate ( $[0/30/60/-60/-30/90]_S$ ). Each plate had a thickness of 1.5 mm, and the composite plates contained 12 layers of the graphite-epoxy lamina from Table 2.2. Material properties for the aluminum plate are shown in Table 2.1. In most of the LISA models, a cell size of 0.25 x 0.25 x 0.125 mm was used along with a time step of 10 ns. These parameters met

the CFL criterion explained in the previous section. A brief discretization study was also performed using coarser in-plane cell sizes, which also met the CFL criterion.

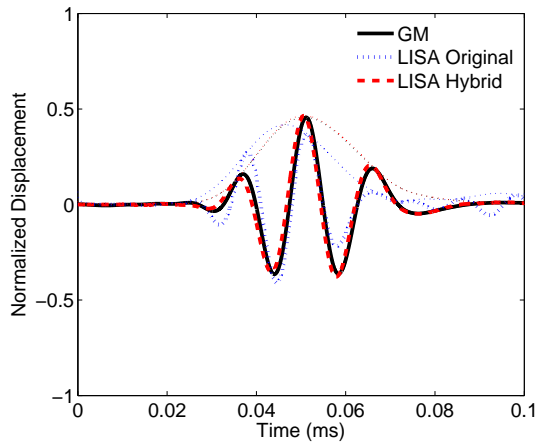
In this chapter, results for circular, CLoVER, and square actuators are presented. The actuation was specified as a Hann-modulated toneburst with a 75-kHz center frequency, as shown in Fig. 2.2. Traction-free boundary conditions were implemented using a layer of air cells surrounding the plate. The initial set of LISA models for each actuator type used the previous method of prescribed displacements to model the actuator, and these results are henceforth referred to as the LISA original model. Subsequently, each actuator was modeled using the LISA hybrid approach. The cut-out region was defined as a 20 by 20 mm region for the circular and square actuator models and as a 60 by 60 mm region for the CLoVER models. All models were compared against the results from the Global Matrix Method, since that approach was shown to produce results that agree well with experiments. Since the displacements on the boundary of the cut-out were specified as the Global Matrix displacements, the hybrid model exactly matched the Global Matrix results for all points located on this boundary and within the cut-out region. If the LISA hybrid model was successful in capturing the propagating wave, the model results also matched the Global Matrix results at locations farther away from the actuator.

### **3.4.1 Circular Actuator Case**

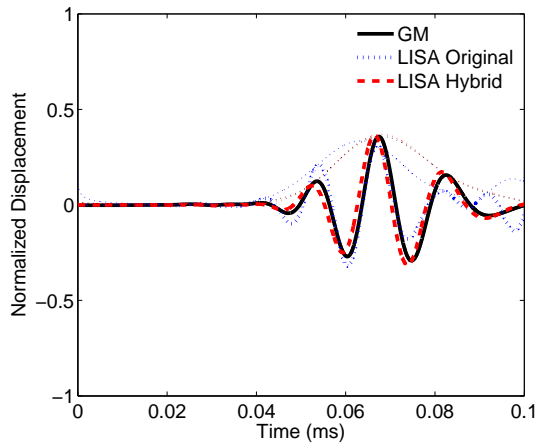
The first group of simulations considered a 6.4 mm radius circular actuator on the previously identified plates. For the aluminum plate, the time histories predicted at three different radial distances from the center of the actuator are shown for the two LISA models as well as the Global Matrix Method in Fig 3.7. At each of the three locations it can be seen that the LISA original results showed some discrepancies from the baseline Global Matrix results, but for the most part the results matched reasonably well – particularly at the 80 mm distance. The duration of the pulse in the LISA original model did seem to be shorter than that in the Global Matrix results, as indicated by the Hilbert transform envelope in-



(a) 20 mm



(b) 50 mm



(c) 80 mm

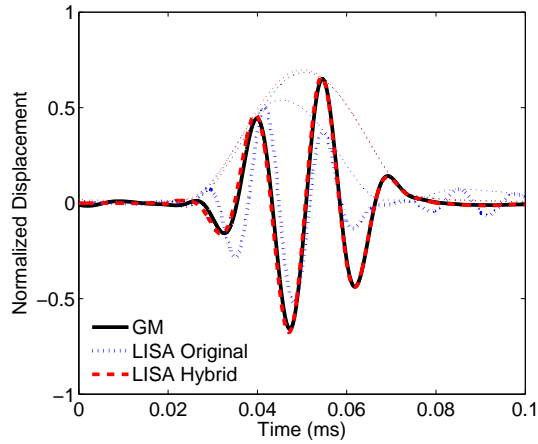
Figure 3.7: Comparison of Global Matrix, LISA original, and LISA hybrid time histories for an aluminum plate with a circular actuator. Locations 20, 50, and 80 mm from the actuator center are shown. The Hilbert transform envelopes are included for reference.

cluded in the figures. The LISA hybrid model, in contrast, appeared to match the Global Matrix results almost perfectly at each of the three distances shown.

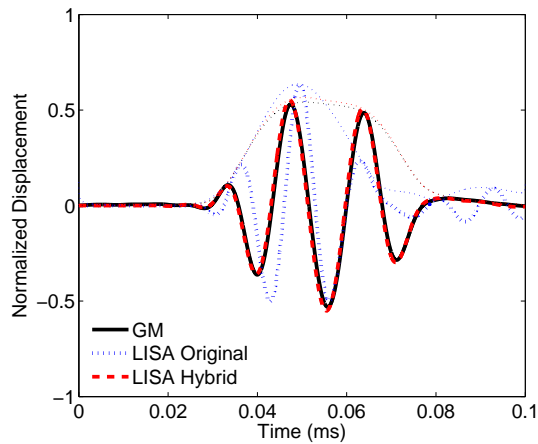
The results from the models considering the circular actuator on the three composite plates are shown in Figs. 3.8-3.10. Each of the time histories is for a point 40 mm from the actuator center. Results at 0, 45, and 90 degrees are presented for each plate since the results are not axisymmetric like in the aluminum case. The ability of the LISA original model to capture the wave propagation time histories was much worse for these models where the group velocities and attenuation varied with azimuthal direction. For each of the three plates, results at the three angles showed the LISA original model did not closely match the baseline Global Matrix time history. While the arrival times of the wave packets were roughly the same for all three models, the LISA original model showed discrepancies in the duration, amplitude, and shape of the wave packet in comparison to the baseline model. The LISA hybrid model again produced time histories matching closely with the Global Matrix results.

#### **3.4.1.1 LISA Hybrid Displacement Field**

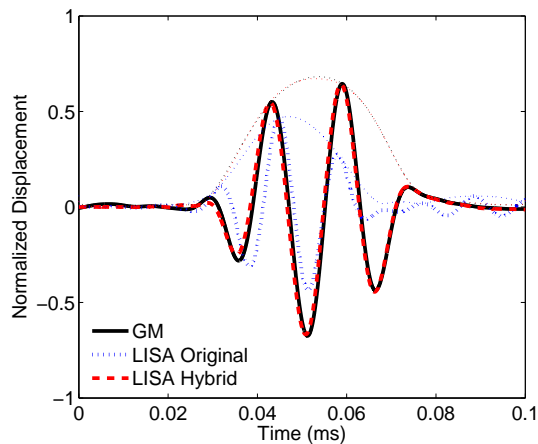
The ability of the LISA hybrid model to capture the wave propagation time histories for a circular actuator at various points has been demonstrated. To better see the effectiveness of the LISA hybrid model in representing the directional dependence of the wave propagation in a composite plate, Fig. 3.11 shows field plots of the out-of-plane displacement of the cross-ply plate. The Global Matrix and LISA hybrid results are compared at 80  $\mu$ s. The preponderance of energy propagating in the 0 and 90-degree directions was preserved well in the new modeling approach. Figure 3.11 (c) shows the amplitude error present at each point on the plate as a percentage of the maximum amplitude in the propagating wave. The error was consistently less than 10% of the maximum amplitude.



(a) 0 degrees

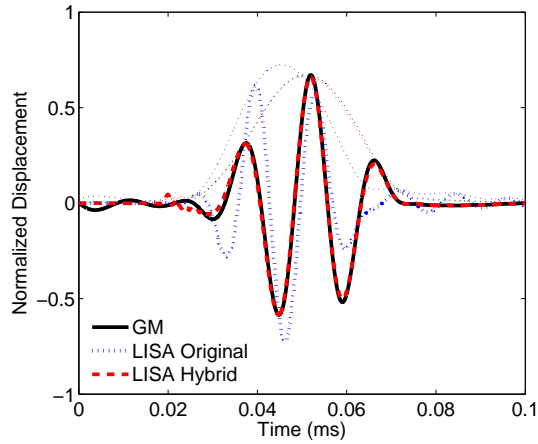


(b) 45 degrees

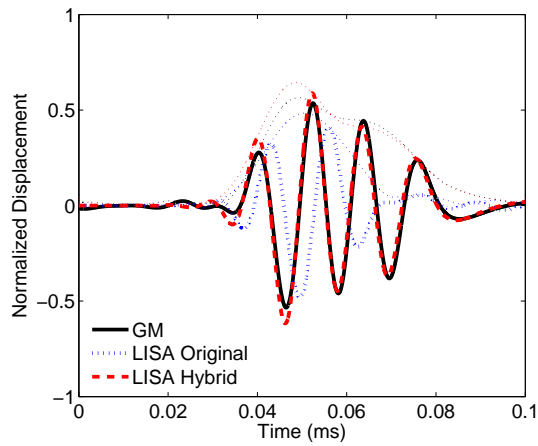


(c) 90 degrees

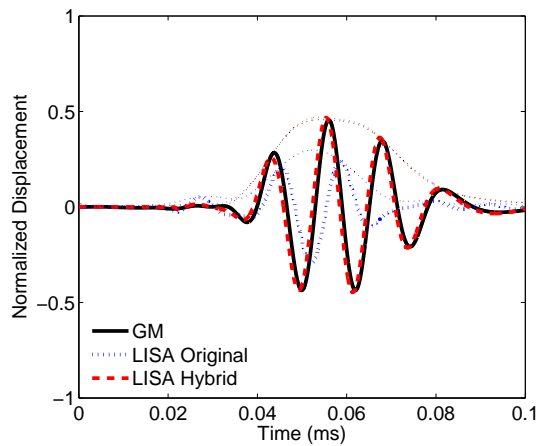
Figure 3.8: Comparison of Global Matrix, LISA original, and LISA hybrid time histories for a cross-ply plate with a circular actuator, 40 mm from the actuator center. The 0, 45, and 90-degree directions are shown. The Hilbert transform envelopes are included for reference.



(a) 0 degrees

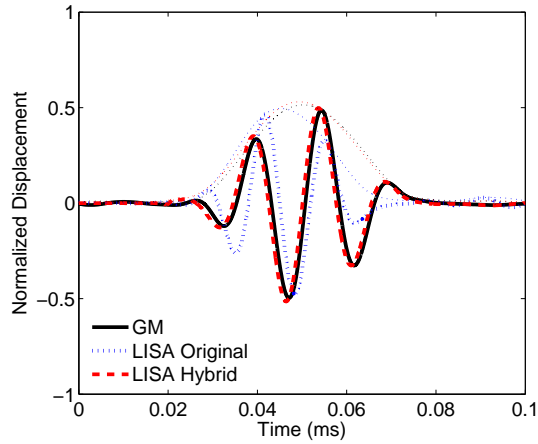


(b) 45 degrees

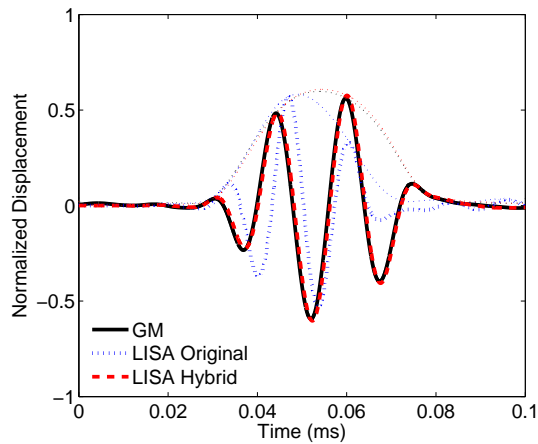


(c) 90 degrees

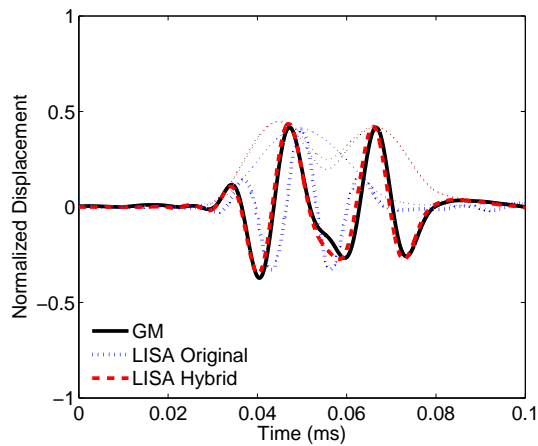
Figure 3.9: Comparison of Global Matrix, LISA original, and LISA hybrid time histories for a unidirectional plate with a circular actuator, 40 mm from the actuator center. The 0, 45, and 90-degree directions are shown. The Hilbert transform envelopes are included for reference.



(a) 0 degrees

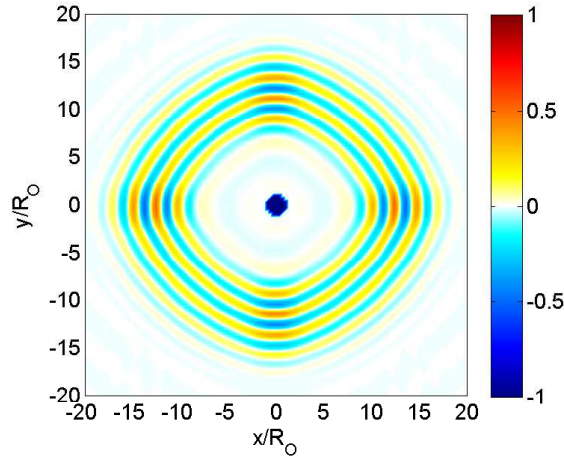


(b) 45 degrees

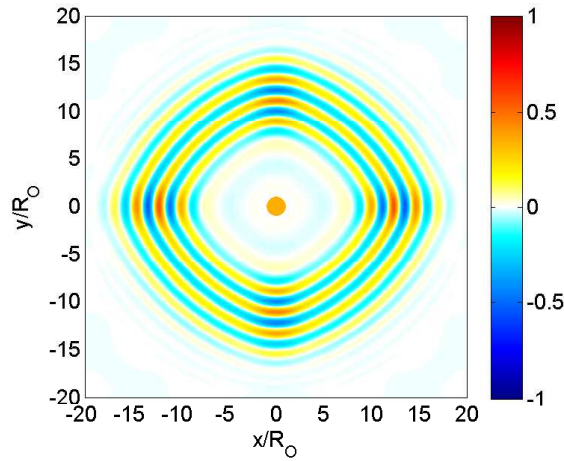


(c) 90 degrees

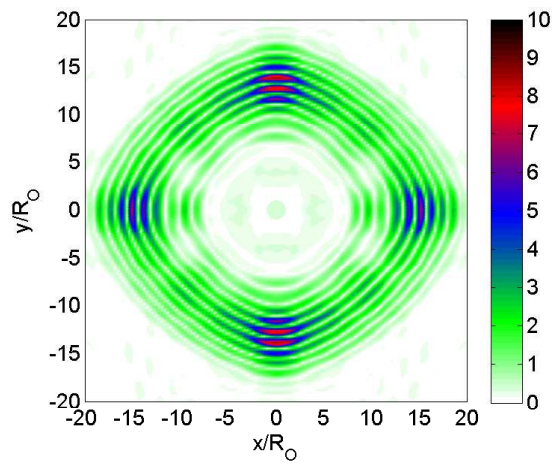
Figure 3.10: Comparison of Global Matrix, LISA original, and LISA hybrid time histories for a quasi-isotropic plate with a circular actuator, 40 mm from the actuator center. The 0, 45, and 90-degree directions are shown. The Hilbert transform envelopes are included for reference.



(a) GM  $80 \mu s$



(b) LISA hybrid  $80 \mu s$



(c) Error as % of max amplitude

Figure 3.11: Comparison of Global Matrix and LISA hybrid results for out-of-plane displacement of a cross-ply plate with a circular actuator at  $80 \mu s$ .

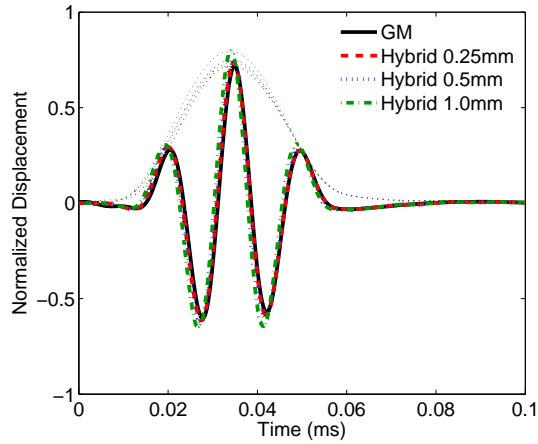


### 3.4.1.2 Effect of In-plane Discretization

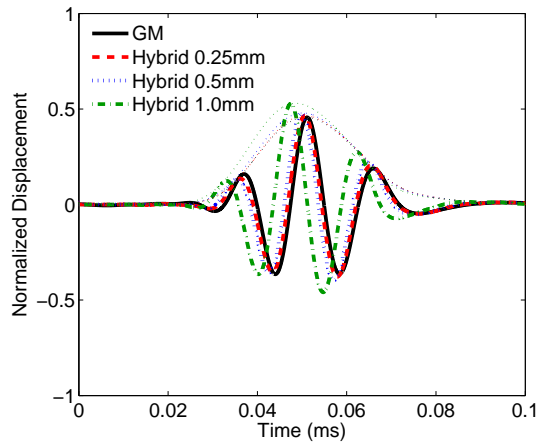
Previous researchers [87] have noted the dependence of LISA results on the in-plane discretization. This dependence was also seen in the present LISA hybrid results, particularly in the group velocity of the propagating wave. The four circular actuator models were run with in-plane cell sizes of 1.0, 0.5, and 0.25 mm ( $\frac{2}{3}t$ ,  $\frac{1}{3}t$ , and  $\frac{1}{6}t$ ). The through-thickness discretization was held constant at 0.125 mm ( $\frac{1}{12}t$ ). The results indicated the group velocity predicted by the LISA hybrid model increased as the in-plane cell size increased. This trend was very noticeable for the aluminum plate. As shown in Fig. 3.12, the results for each of the three discretization sizes agreed very well with the baseline model at 20 mm. However, at more distant points the effect of the group velocity differences was more apparent. The plot for the 80 mm location demonstrates the effect of overly coarse discretizations on the model results.

This effect was also seen in the composite models, and not surprisingly the effect was direction dependent. The three discretization sizes were compared for the 0, 45, and 90-degree directions at points 70 mm from the actuator center. At this distance the group velocity differences had time to manifest themselves. Compared to the aluminum model, the cross-ply model shown in Fig. 3.13 and the quasi-isotropic model shown in Fig. 3.15 were much less sensitive to the cell size, but the results were affected more for the 90-degree direction than the 0-degree direction. For the unidirectional model, the directional dependence was even more pronounced, as seen in Fig. 3.14. Here all three cell sizes produced good results at 0 degrees, but the results for coarse discretizations worsened as the azimuth increased from 0 to 90 degrees.

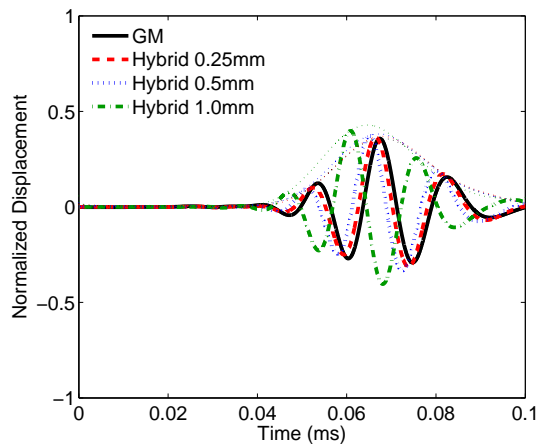
In the LISA hybrid model, as in previous LISA implementations, the group velocity was clearly a function of not only the material properties of the structure and the azimuthal direction, but also the discretization used in the model. Errors in the group velocity due to the chosen discretization resulted in errors in the arrival time of the propagating wave. For a given discretization and azimuthal direction, the group velocity error remained constant,



(a) 20 mm

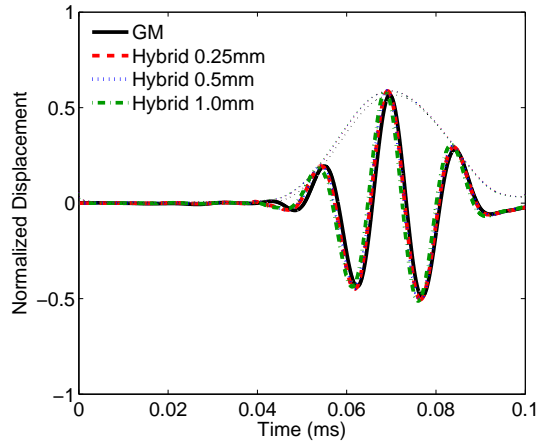


(b) 50 mm

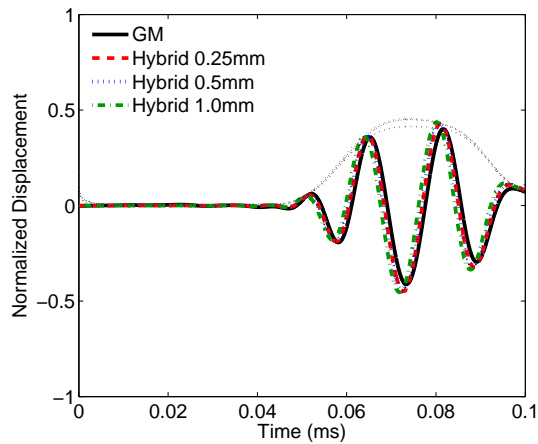


(c) 80 mm

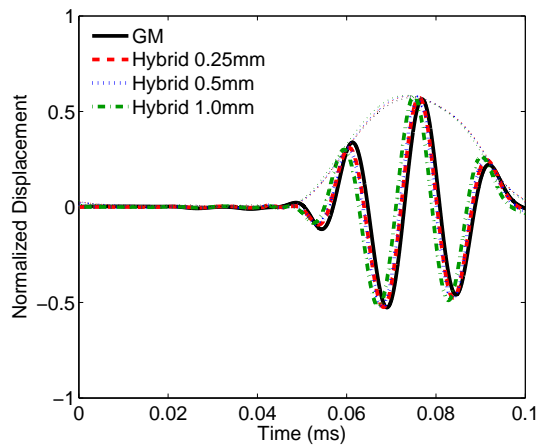
Figure 3.12: Comparison of various LISA Hybrid in-plane discretizations for an aluminum plate with a circular actuator. Locations 20, 50, and 80 mm from the actuator center are shown. The Hilbert transform envelopes are included for reference.



(a) 0 degrees

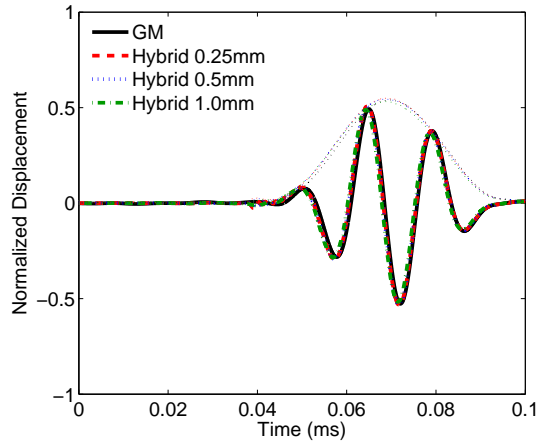


(b) 45 degrees

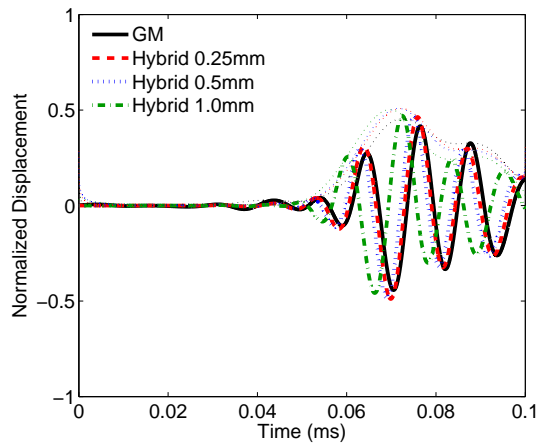


(c) 90 degrees

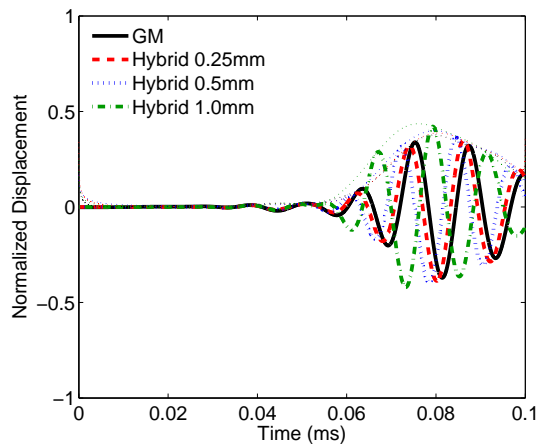
Figure 3.13: Comparison of various LISA hybrid in-plane discretizations for the cross-ply laminate with a circular actuator at a point 70 mm away from the actuator center. The 0, 45, and 90-degree directions are shown. The Hilbert transform envelopes are included for reference.



(a) 0 degrees

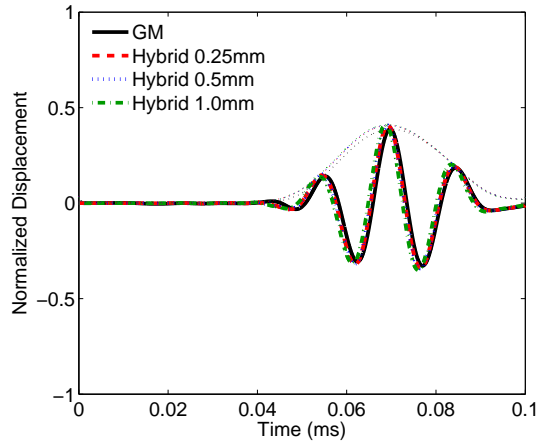


(b) 45 degrees

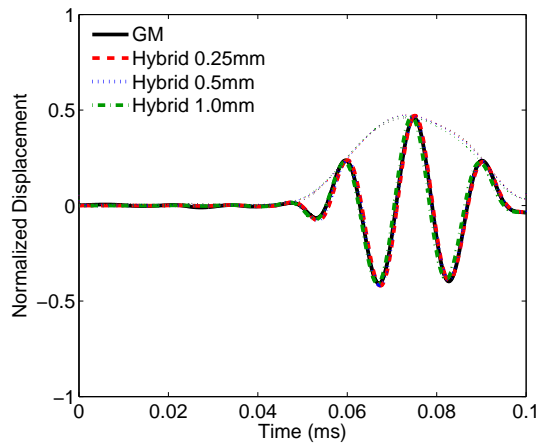


(c) 90 degrees

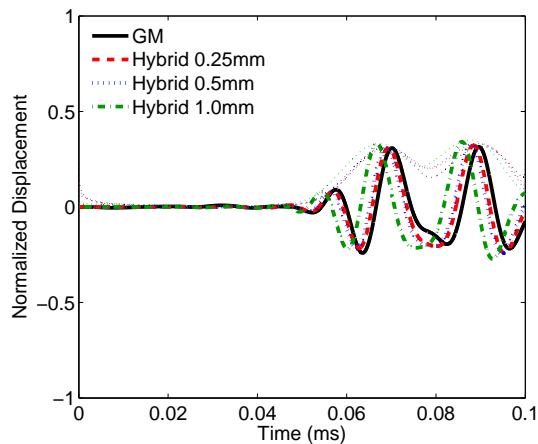
Figure 3.14: Comparison of various LISA hybrid in-plane discretizations for the unidirectional laminate with a circular actuator at a point 70 mm away from the actuator center. The 0, 45, and 90-degree directions are shown. The Hilbert transform envelopes are included for reference.



(a) 0 degrees



(b) 45 degrees



(c) 90 degrees

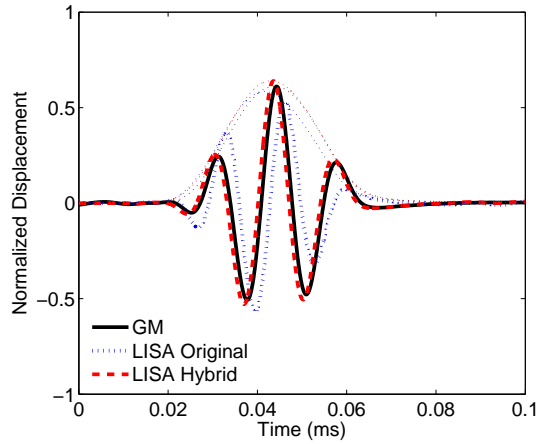
Figure 3.15: Comparison of various LISA hybrid in-plane discretizations for the quasi-isotropic laminate with a circular actuator at a point 70 mm away from the actuator center. The 0, 45, and 90-degree directions are shown. The Hilbert transform envelopes are included for reference.

as did the arrival time error of the propagating wave relative to the actual arrival time in the baseline model.

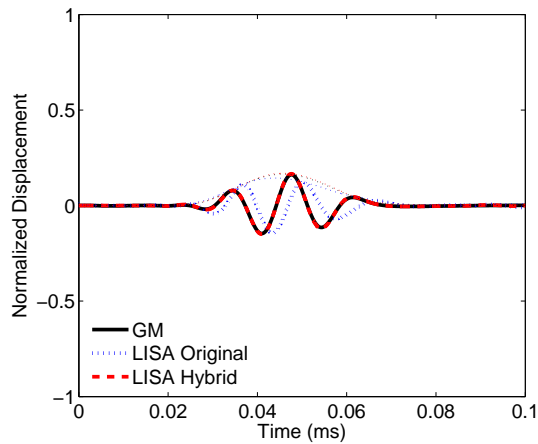
### **3.4.2 CLoVER Actuator Case**

The next actuator considered was the CLoVER transducer. For the models in this study, each sector of the actuator had an inside radius of 15 mm and an outside radius of 25 mm. Each sector occupied a 45-degree azimuthal region. For the aluminum plate, the 0-degree sector was active. Figure 3.16 shows the LISA and Global Matrix displacement time histories at points 70 mm from the center of the CLoVER profile at three different angles. As expected, the majority of the energy propagated in the direction corresponding to the active sector. The maximum amplitude of the 0-degree displacement was 3.85 and 13.9 times the amplitude of the 45 and 90-degree directions, respectively. For this case, the LISA original model produced displacement histories that were slightly out of phase with those from the Global Matrix model. Additionally, the LISA original model overpredicted the amplitudes present in the 90-degree direction, producing a maximum amplitude three times greater than the Global Matrix Method. These problems were not observed in the LISA hybrid model results.

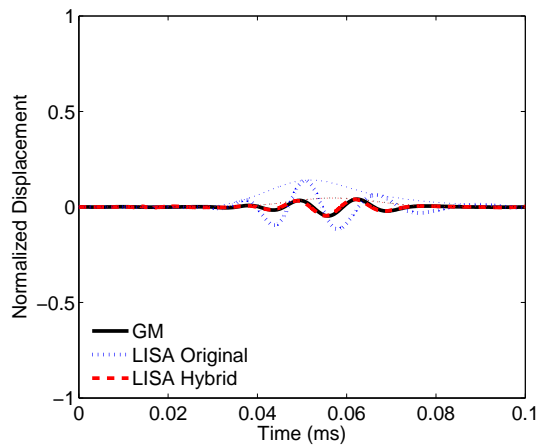
The CLoVER actuator was also modeled with the cross-ply plate, and three different active sectors were simulated. Figures 3.17-3.19 show the results when the 0, 45, and 90-degree sectors were simulated. Only one sector was simulated at a time, and the other sectors were assumed to offer no contribution. Both the LISA original and LISA hybrid models correctly showed the directionality observed when the different sectors were used, but numerous discrepancies were seen in the LISA original results when they were closely compared to those from the Global Matrix model. Conversely, for each of the CLoVER sectors on the cross-ply plate, the LISA hybrid and Global Matrix results were almost indistinguishable.



(a) 0 degrees

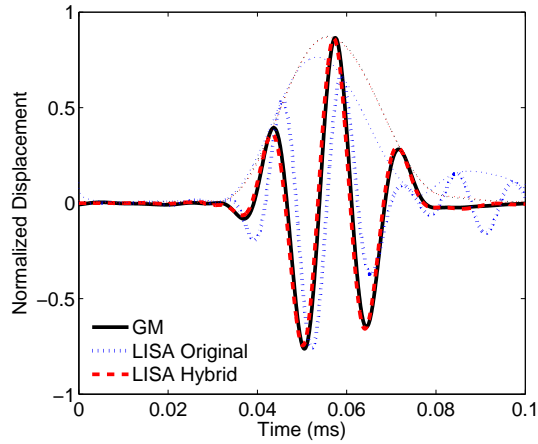


(b) 45 degrees

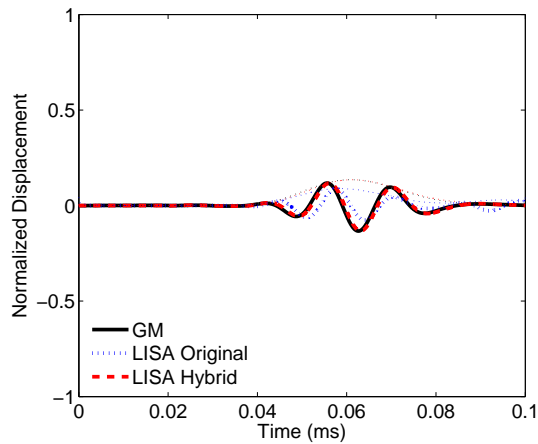


(c) 90 degrees

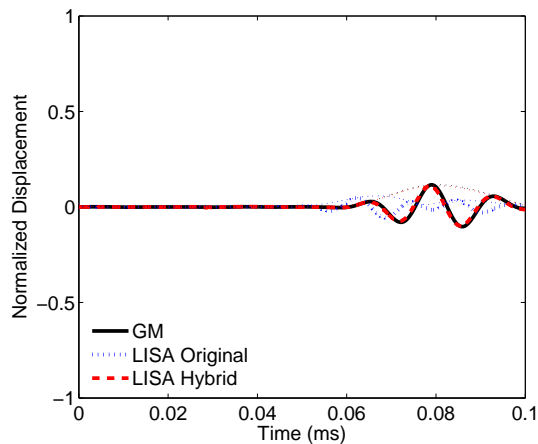
Figure 3.16: Comparison of Global Matrix, LISA original, and LISA hybrid time histories for an aluminum plate with a CLoVER actuator with the 0-degree sector active. The 0, 45, and 90-degree directions are shown for points 70 mm from the actuator center. The Hilbert transform envelopes are included for reference.



(a) 0 degrees



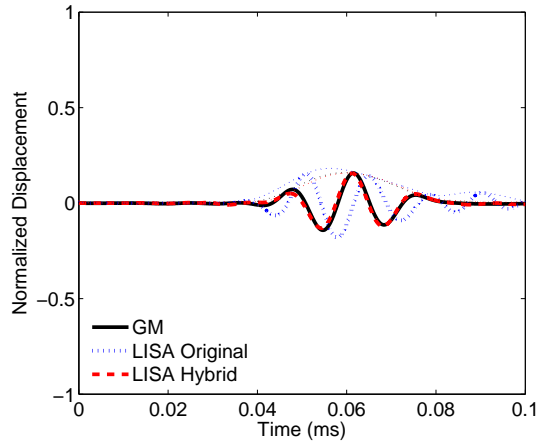
(b) 45 degrees



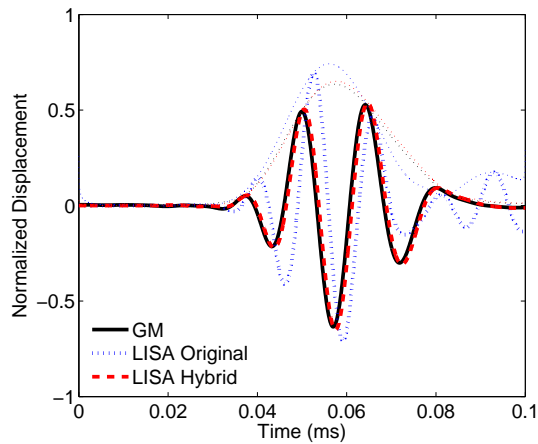
(c) 90 degrees

Figure 3.17: Comparison of Global Matrix, LISA original, and LISA hybrid time histories for a cross-ply plate with a CLoVER actuator with the 0-degree sector active. The 0, 45, and 90-degree directions are shown for points 70 mm from the actuator center. The Hilbert transform envelopes are included for reference.

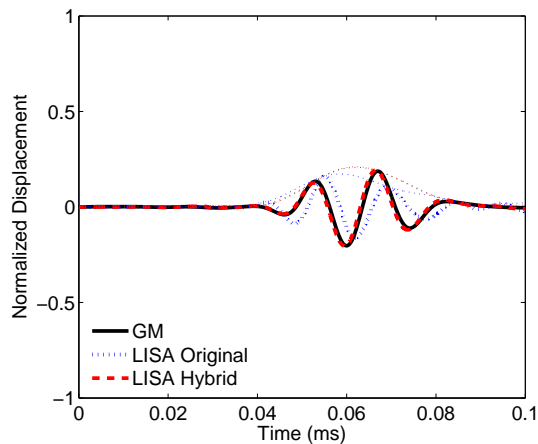




(a) 0 degrees

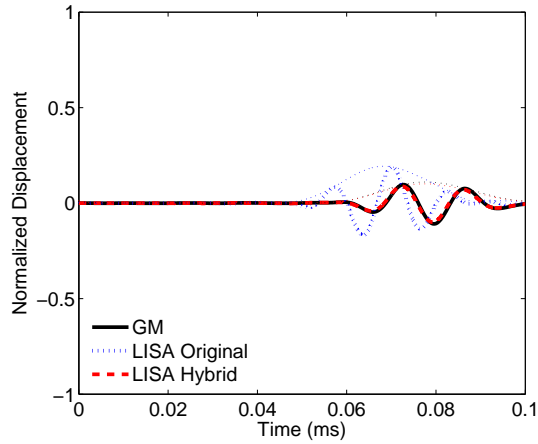


(b) 45 degrees

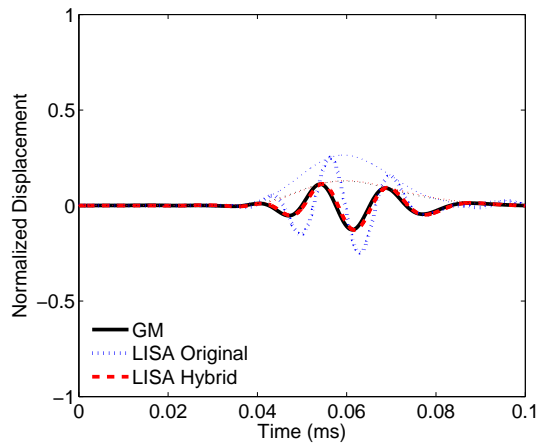


(c) 90 degrees

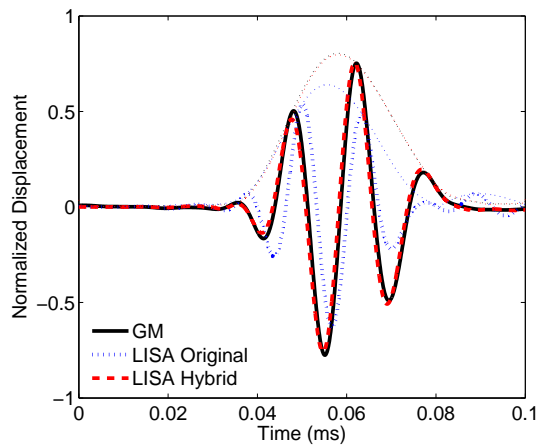
Figure 3.18: Comparison of Global Matrix, LISA original, and LISA hybrid time histories for a cross-ply plate with a CLoVER actuator with the 45-degree sector active. The 0, 45, and 90-degree directions are shown for points 70 mm from the actuator center. The Hilbert transform envelopes are included for reference.



(a) 0 degrees



(b) 45 degrees



(c) 90 degrees

Figure 3.19: Comparison of Global Matrix, LISA original, and LISA hybrid time histories for a cross-ply plate with a CLoVER actuator with the 90-degree sector active. The 0, 45, and 90-degree directions are shown for points 70 mm from the actuator center. The Hilbert transform envelopes are included for reference.

For the cross-ply plate with a CLoVER actuator, directional dependence in the results was due to both the composite configuration and the shape of the actuator itself. The field plots shown in Fig. 3.20 demonstrate the directionality in the out-of-plane displacement field produced when three different sectors are active. The figures on the left show the out-of-plane displacement observed 80  $\mu$ s after the start of the actuation pulse using the Global Matrix Method. The center figures show the LISA hybrid displacement field at the same instant in time. The figures on the right show the amplitude error of the LISA hybrid model compared to the Global Matrix results, as a percentage of the maximum amplitude in the propagating wave. As in the case of the circular actuator, the amplitude errors in the CLoVER results were consistently less than 10% of the maximum amplitude.

### 3.4.3 Square Actuator Case

Considering the previous results for the LISA original models and the actuation diagrams in Figs. 3.5 and 3.6, it is evident the previous method of specifying in-plane displacements on the plate surface was not very successful in representing either the circular or CLoVER actuators. For these cases, the Cartesian nature of the LISA grid required that the model approximate the nonlinear profile of the actuators by locating the closest nodes. There was a clear mismatch between the nodes and the actuator boundary. In this section, results for a 10-mm square piezo actuator are presented. Unlike the previous cases, the square actuator can be exactly matched by the LISA discretization, avoiding any discrepancies associated with the discretization of the actuator in LISA. The next plots compare the two models and the Global Matrix results for the four plates under consideration.

The results for the aluminum laminate with the square actuator are shown in Fig. 3.21. As previously seen in the circular actuator case, the LISA original model produced results matching the baseline case fairly well, but not as closely as the LISA hybrid model. Again, the LISA original model seemed to produce improved results at distances far from the actuator, while the LISA hybrid model was reliable at each of the distances considered.

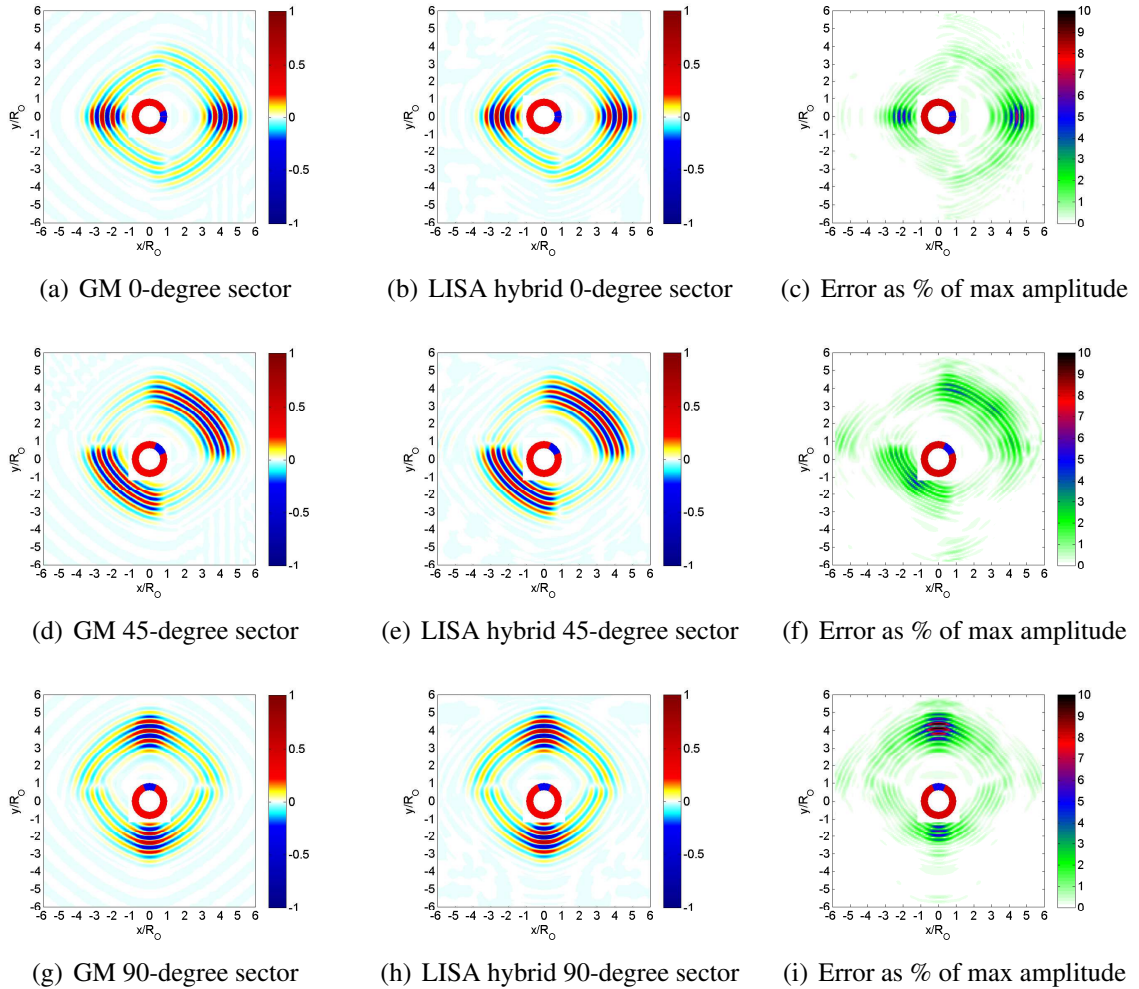
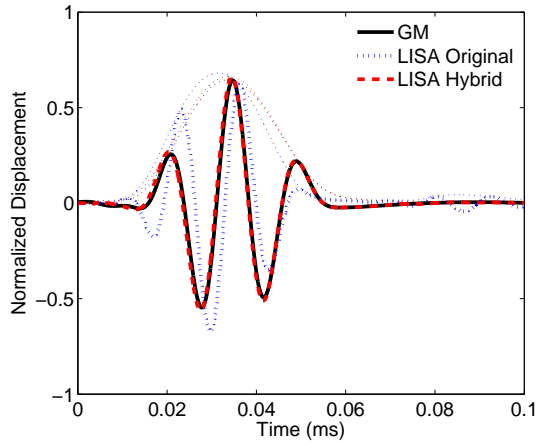


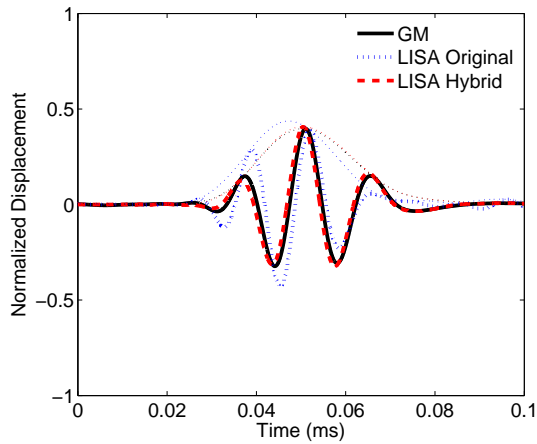
Figure 3.20: Comparison of Global Matrix and LISA hybrid results for out-of-plane displacement of a cross-ply plate at  $80 \mu\text{s}$  with various active CLoVER sectors.

For the three composite models, shown in Figs. 3.22-3.24, the LISA hybrid model clearly outperformed the LISA original model at all of the angles that were considered. The results for each of the three layup sequences showed a clear mismatch between the Global Matrix model and the LISA original model.

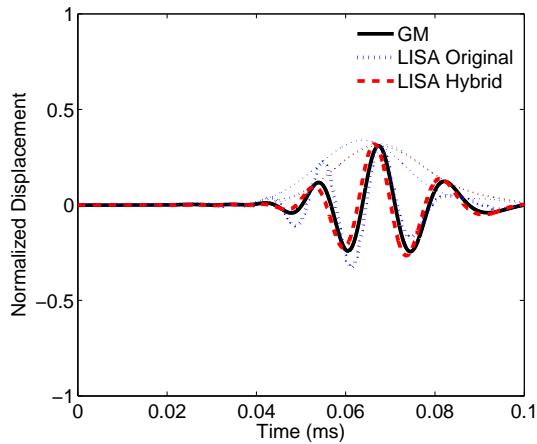
For this square actuator case, modeling the actuator profile in the LISA original model was not a challenge, since the Cartesian structure of the LISA discretization fits well with the actuator shape. However, the results showed that even with this problem not being a factor, assuming a displacement field to represent the actuator did not produce satisfactory results. Only for the aluminum plate did the LISA original model produce results that came



(a) 20 mm

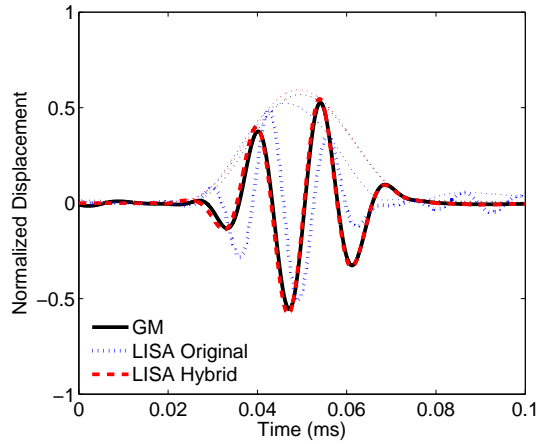


(b) 50 mm

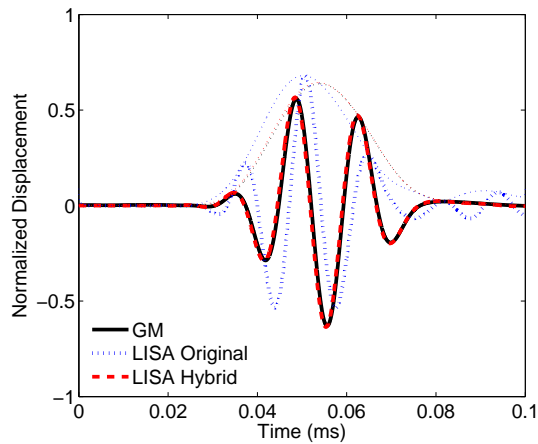


(c) 80 mm

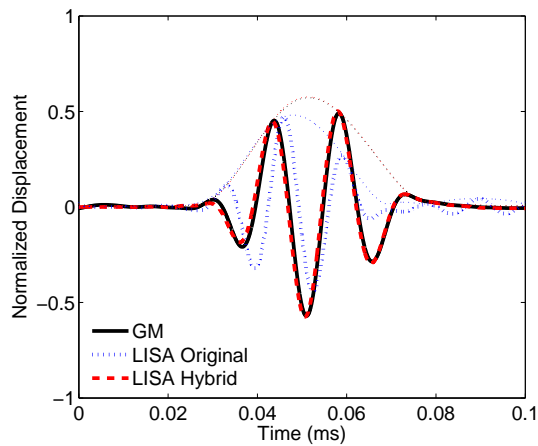
Figure 3.21: Comparison of Global Matrix, LISA original, and LISA hybrid time histories for an aluminum plate with a square actuator. Locations 20, 50, and 80 mm from the actuator center are shown. The Hilbert transform envelopes are included for reference.



(a) 0 degrees

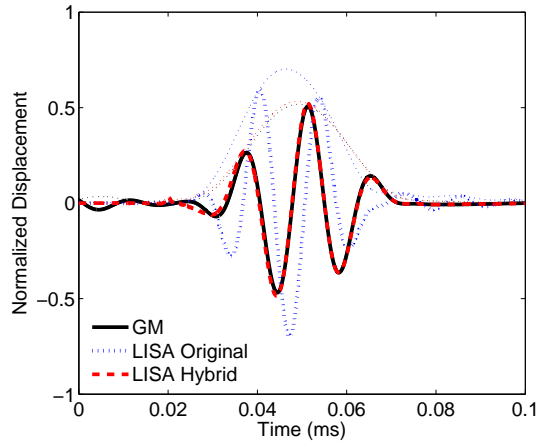


(b) 45 degrees

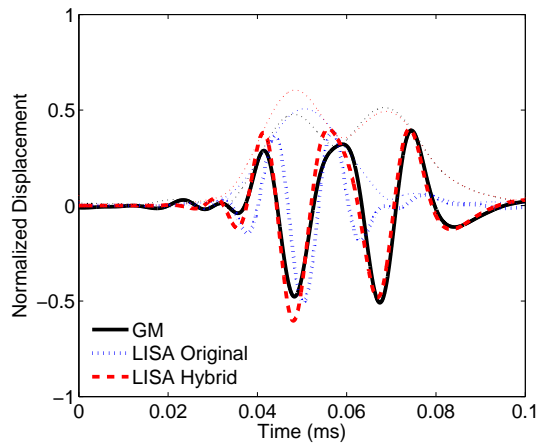


(c) 90 degrees

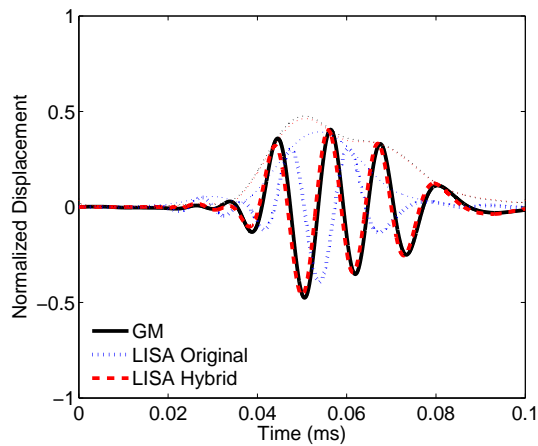
Figure 3.22: Comparison of Global Matrix, LISA original, and LISA hybrid time histories for a cross-ply plate 40mm from the square actuator center. The 0, 45, and 90-degree directions are shown. The Hilbert transform envelopes are included for reference.



(a) 0 degrees

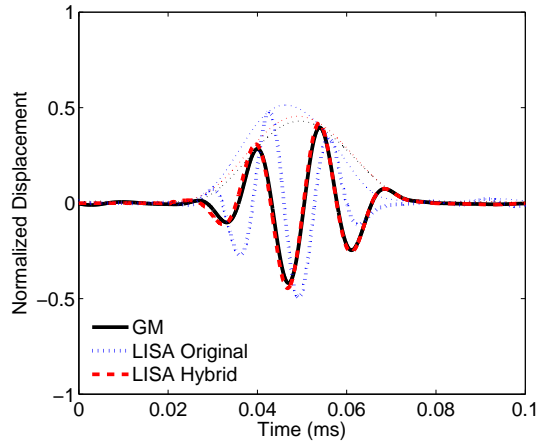


(b) 45 degrees

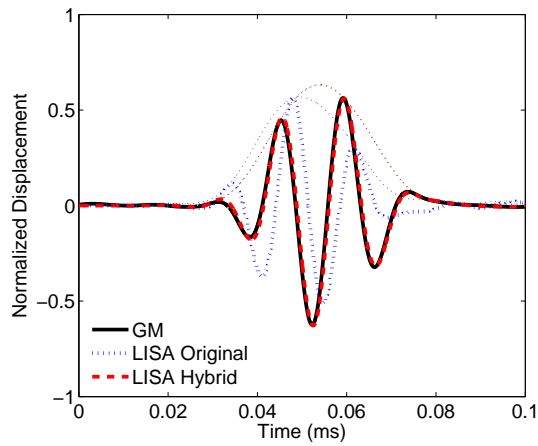


(c) 90 degrees

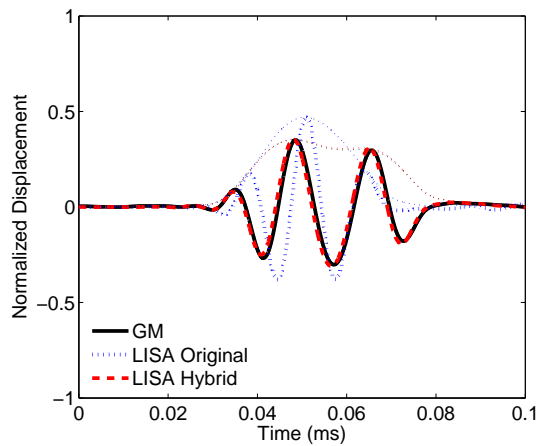
Figure 3.23: Comparison of Global Matrix, LISA original, and LISA hybrid time histories for a unidirectional plate 40mm from the square actuator center. The 0, 45, and 90-degree directions are shown. The Hilbert transform envelopes are included for reference.



(a) 0 degrees



(b) 45 degrees



(c) 90 degrees

Figure 3.24: Comparison of Global Matrix, LISA original, and LISA hybrid time histories for a quasi-isotropic plate 40mm from the square actuator center. The 0, 45, and 90-degree directions are shown. The Hilbert transform envelopes are included for reference.



close to replicating the theoretical predictions. For the composite cases considered, the use of in-plane displacements to model the actuator was not a reliable method, even when the actuator fit well within the LISA grid scheme. Therefore, the actuator representation by prescribing displacements in the actuator region provides an additional source of error.

### 3.5 Summary

This chapter introduced the LISA hybrid methodology to solve for wave generation and propagation in isotropic and composite structures. It takes advantage of the strengths of the Global Matrix Method and LISA. The Global Matrix Method was used to determine the effects of piezoelectric actuators mounted on the surface of a plate. The LISA formulation for composite plates with plies in non-principal directions was used to capture the wave propagation away from the actuator. The LISA hybrid model was used to produce displacement results for an aluminum plate and three graphite-epoxy plates (cross-ply, unidirectional, and quasi-isotropic). These results were compared with baseline results from the Global Matrix Method. In all cases, the LISA hybrid results produced more accurate time histories than previous LISA models, and the results matched those from the Global Matrix Method extremely well. A brief study on the spatial discretization used in the LISA hybrid model showed the importance of this parameter and its effect on the resulting displacement time histories. Consistent with previous work, coarse discretizations produced artificially fast propagating waves. Additionally, this work showed the influence of the azimuthal direction on the discretization effects. For all four models, a  $\frac{1}{6}t \times \frac{1}{6}t \times \frac{1}{12}t$  cell size produced results agreeing well with the baseline model for plates of thickness  $t$ , when actuated with a center frequency producing a frequency-thickness product of 112.5 kHz-mm.

Results from this work highlighted the importance of correctly modeling the actuator in numerical wave propagation simulations. The inability of the LISA original model to match the performance of the LISA hybrid model in the circular and CLoVER actuator

cases illustrated the challenge of capturing non-rectangular actuators with the Cartesian grid in LISA. However, the results from the square actuator case also showed that even when the actuator geometry can be exactly captured in the Cartesian grid, the assumption of prescribed in-plane displacements within actuator profile does not adequately describe the behavior of the laminate. This work showed that the LISA hybrid model overcame both of these challenges, and it was effective for both simple piezo wafer actuators and more complex piezocomposite actuators such as CLoVER. With the LISA hybrid model producing accurate results for the pristine plates considered in this work, the next step is to use the model to consider various types of damage likely to be seen in aerospace structures.

## CHAPTER 4

# Guided Wave Interaction with Hole Damage

This chapter considers the effects of hole damage on guided wave propagation in isotropic and composite plates using both LISA and experimental methods. While not a typical damage mode in fielded aerospace structures, holes offer a good starting point to verify LISA can properly capture the damage difference signals needed for damage identification and location. Guided wave generation from piezoceramic wafers is modeled using the LISA hybrid approach. First, holes in isotropic plates are simulated to establish LISA's ability to capture the guided wave scattering effects of various hole sizes. Next, guided wave interaction with hole damage in cross-ply composite laminates is modeled. Various hole sizes and azimuthal locations are simulated to determine the effects of varying those parameters. For both material systems, experimental results are compared with the simulations to aid in evaluating the LISA models.

## 4.1 Theoretical Formulation

### 4.1.1 Hole Modeling Strategy

Holes were represented in the LISA model using simulated air cells like those used at the plate boundaries. Cells located within the radius of the chosen hole size were given simulated air properties. Figure 4.1 shows how a hole was represented for three different in-plane discretizations. The LISA models were based on a Cartesian discretization, and

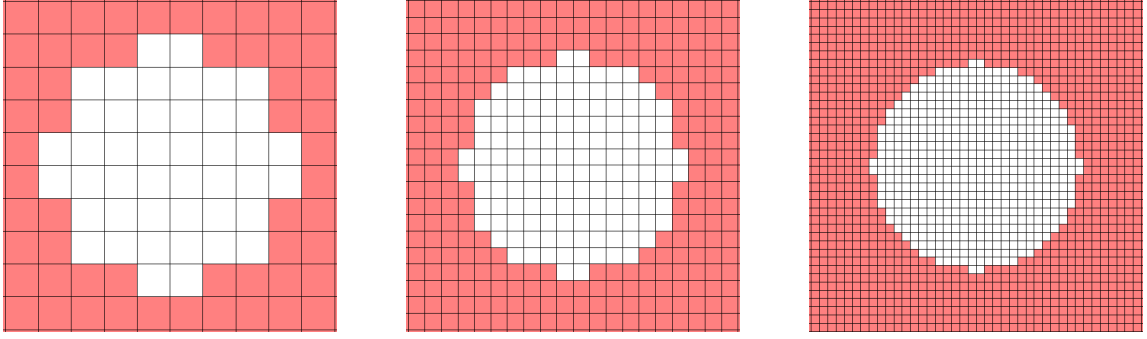


Figure 4.1: Damage models for a  $r = 2t$  hole for in-plane dimensions  $\Delta x, \Delta y = 2t/3$  (left),  $t/3$  (center), and  $t/6$  (right).

the effect of this approach is evident in the figure. Models with finer in-plane cell sizes allowed for holes with less distortion.

#### 4.1.2 Simulated Sensor Model

The in-plane interactions of the guided waves with the damaged regions were observed using a series of simulated sensors placed around the damage site. It has been shown (e. g., [46]) the voltage response  $V$  of a piezoceramic wafer sensor to be proportional to the integral of the in-plane normal strain  $\varepsilon_{ii}$  within the sensor profile:

$$V = C \int_{S_C} \varepsilon_{ii} dS, \quad (4.1)$$

where the  $C$  constant is a function of the sensor's geometric, material, and piezoelectric properties and  $S_C$  is the surface area of the sensor. The simulated sensor signal used in this dissertation was calculated by summing the in-plane normal strains for the surface nodes located within the profile of the sensor. In this sensor modeling approach, any effects of the mass of the sensor were assumed to be negligible.

## 4.2 Holes in Isotropic Plates

The first portion of this study considered the effect of holes on guided wave propagation in isotropic plates. Both through-thickness holes and half-depth holes were examined in a series of LISA simulations, and experimental results were used to validate the hole model.

### 4.2.1 Simulation Studies

For the isotropic plate scenario considered in this work, the host structure was a 3.18 mm thick aluminum plate with the material properties previously shown in Table 2.1. The simulations considered a square plate with a 6.5-mm circular piezoceramic wafer actuator bonded to the top surface at the geometric center of the plate. The plate had a side length of 700 mm. The in-plane dimensions of the plate were chosen to minimize the interference of boundary reflections in the wave propagation results. For this set of simulations, the holes were placed 125 mm from the center of the actuator. A series of sensors were modeled around the damage site at a distance of 50 mm from the center of the damage. The sensors were placed at five different angles relative to the hole, as shown in Fig. 4.2. For these models, a discretization of 0.53 mm ( $t/6$ ) was used in the thickness dimension of the plate. The in-plane discretization was set to 0.5 mm in both directions. The guided wave fields used for the simulations were produced using a 3.5-cycle Hann-modulated toneburst excitation with a center frequency of 75 kHz.

Prior to simulating the damage cases, a pristine plate was modeled to gather baseline data. Subsequently, the damage simulations were run to collect data describing guided wave interaction with the damage. Finally, the pristine and damage signals were compared to produce difference signals showing the effect of the damage.

For the isotropic case, the primary objective of the hole simulations was to characterize how increasing the radius of the hole affects the difference signal for both through-thickness and half-depth holes. Four different hole sizes ranging from  $r = 0.75t$  to  $r = 2t$  were mod-

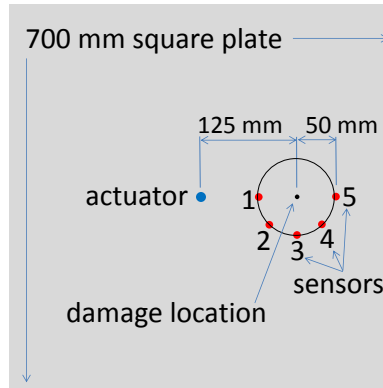
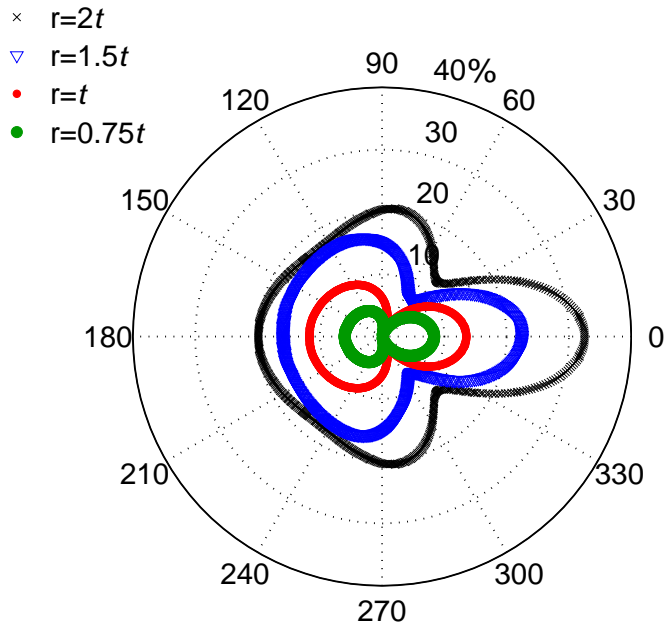


Figure 4.2: Schematic of setup for isotropic simulations.

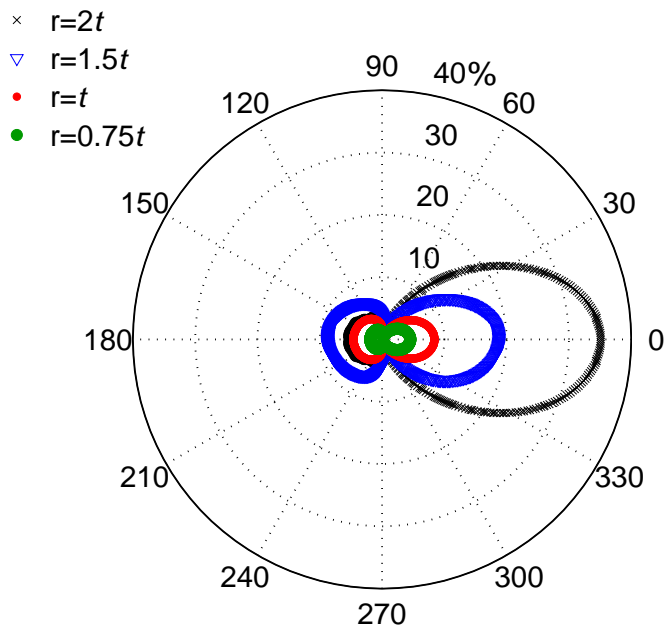
eled for each hole depth. Figure 4.3 shows how the out-of-plane difference signal varies for each hole size with respect to the observation point. In this figure, the maximum value of the out-of-plane difference signal at points 50 mm from the damage center is plotted for each azimuthal angle relative to the damage location. The results were normalized as a percentage of the maximum amplitude of the pristine signal that reached the damage site.

The simulation results for the through-thickness hole showed that for each of the hole sizes, considerable energy was reflected back toward the actuator, which is represented as the 180-degree direction in the figure. The highest difference signals, however, were found on the back side of the damage in the 0-degree direction. As the hole radius increased, the maximum difference amplitude in the 0-degree direction increased at a greater rate than the amplitude in the 180-degree direction. The 45 and 315-degree directions showed the smallest difference signal amplitudes, indicating these directions were generally the least optimal for detecting the damage.

The results for the half-depth hole scattering patterns were significantly different from those seen in through-thickness case. For all hole radii, almost no difference signal was present in the 90 and 270-degree directions. In general, the difference signals reflected back toward the actuator had a smaller amplitude than the through-thickness case. As in the through-thickness case, the maximum difference signal amplitudes were found on the back side of the half-depth holes. One particularly interesting result was seen for the largest



(a) Through-thickness Hole



(b) Half-depth Hole

Figure 4.3: Azimuthal variation of the out-of-plane difference signal's maximum amplitude for aluminum hole simulations. Results are for points 50 mm from the hole center.

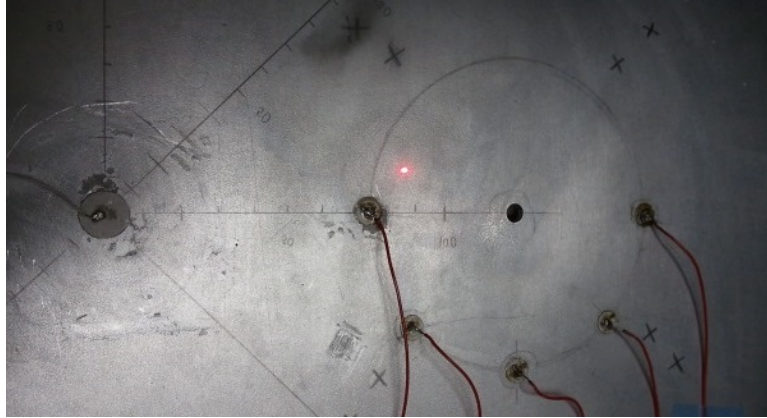


Figure 4.4: Configuration of aluminum hole experiment.

( $r = 2t$ ) hole size in the 0-degree direction. Here, the maximum amplitude of the half-depth hole difference signal was actually higher than that found in the through-thickness hole case.

#### 4.2.2 Comparison with Experimental Results

An experiment was conducted to validate the isotropic simulations using the same parameters as those used in the LISA model. The aluminum plate was instrumented with an actuator and sensors, shown in Fig. 4.4, and pristine data were recorded for the baseline case. A 15 volts peak-to-peak Hann-modulated toneburst excitation was generated using an Agilent 33220A function generator. A center frequency of 75 kHz was used like in the simulations. The responses of the five piezoceramic sensors were recorded using an Agilent DSO9254A digital oscilloscope. After the pristine sensor signals were recorded, an  $r = 1t$  through-thickness hole was drilled and another set of damage signals were recorded. Difference signals were obtained by subtracting the pristine results from the damaged results in a manner similar to that used in the simulation studies. Finally, the difference signals were post-processed using a low-pass filter to eliminate excessive noise.

A comparison of the difference signal amplitudes recorded by the simulated and experimental sensors is shown in Fig. 4.5. Each data point shows the maximum amplitude



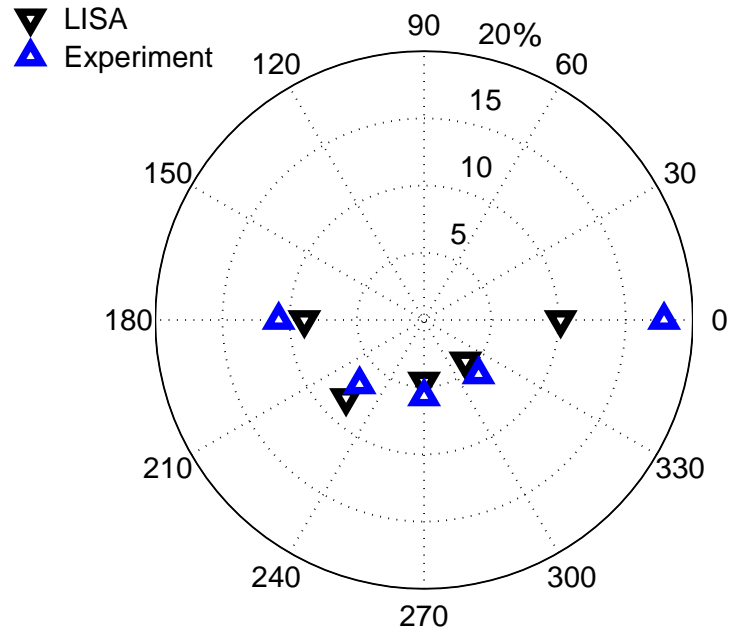


Figure 4.5: Comparison of LISA and experimental results for through-thickness hole scenario in an aluminum plate. Sensor difference signals are normalized as a percentage of the maximum pristine signal amplitude at sensor 1, which corresponds to the 180-degree direction.

of the difference signal normalized as a percentage of the maximum amplitude of the pristine signal recorded with sensor 1. The data are plotted azimuthally with respect to the sensor position, and the radial dimension indicates the normalized amplitude. A quantitative comparison of the data is shown in Table 4.1. The results for sensors 1 through 4 showed close agreement, with differences ranging from 1.1% to 1.9% of the pristine sensor 1 signal amplitude. In both the simulation and the experiment, the sensor 5 difference signal showed the largest amplitude, as expected. However, the sensor 5 results showed more variation than the others with a difference of 7.7%. The experimental difference signal at this location was larger than expected. This could be an indication that the LISA model underpredicts the difference signal at this position, or an error introduced during the experiment itself. Further studies would be needed to fully address this difference.

Table 4.1: Comparison of LISA and experimental results for through-thickness hole scenario in an aluminum plate. The maximum difference signal amplitude is shown as a percentage of the pristine signal at sensor 1.

	Sensor				
	S1	S2	S3	S4	S5
LISA %	8.9	8.2	4.6	4.4	10.2
Experiment %	10.8	6.8	5.7	5.7	17.9
Difference	1.9	1.4	1.1	1.3	7.7

Figure 4.6 shows a comparison between the time histories from the LISA simulation and the experiment. The pristine, damaged, and difference time-history signals are shown for three of the sensors. The signals were normalized relative to the maximum amplitude of the pristine signal at the sensor 1 location. Sensor 1 corresponds to the 180-degree direction relative to the damage site, and it is in the pulse-echo configuration. Sensor 5, located in the 0-degree direction, is in the pitch-catch configuration. The sensor 4 results are presented to show the behavior of the sensor in the least optimal direction for detecting the difference signal. For each of the sensors shown, the behavior of the pristine signals showed excellent agreement between the simulation and the experiment. Additionally, it can be seen that for the majority of the time history, the difference signals were much lower in amplitude than the pristine signals.

To better see the features of the difference signals, they are shown individually in Fig. 4.7. The simulation results clearly showed a number of notable features in the difference signals. For sensor 1, the major features of the difference signal included a small reflection of the  $S_0$  mode back towards the sensor followed by a much larger reflection from the  $A_0$  mode after interacting with the damage site. In the case of the sensor 5 position, a close examination of the pristine and damage signals for this sensor showed the large  $A_0$  pulse in the damage signal was slightly out of phase from the original pristine signal. The major features of the difference signal can be understood as artifacts of the wave energy slowing down as it passed around the hole. The sensor 4 difference signal had a noticeably

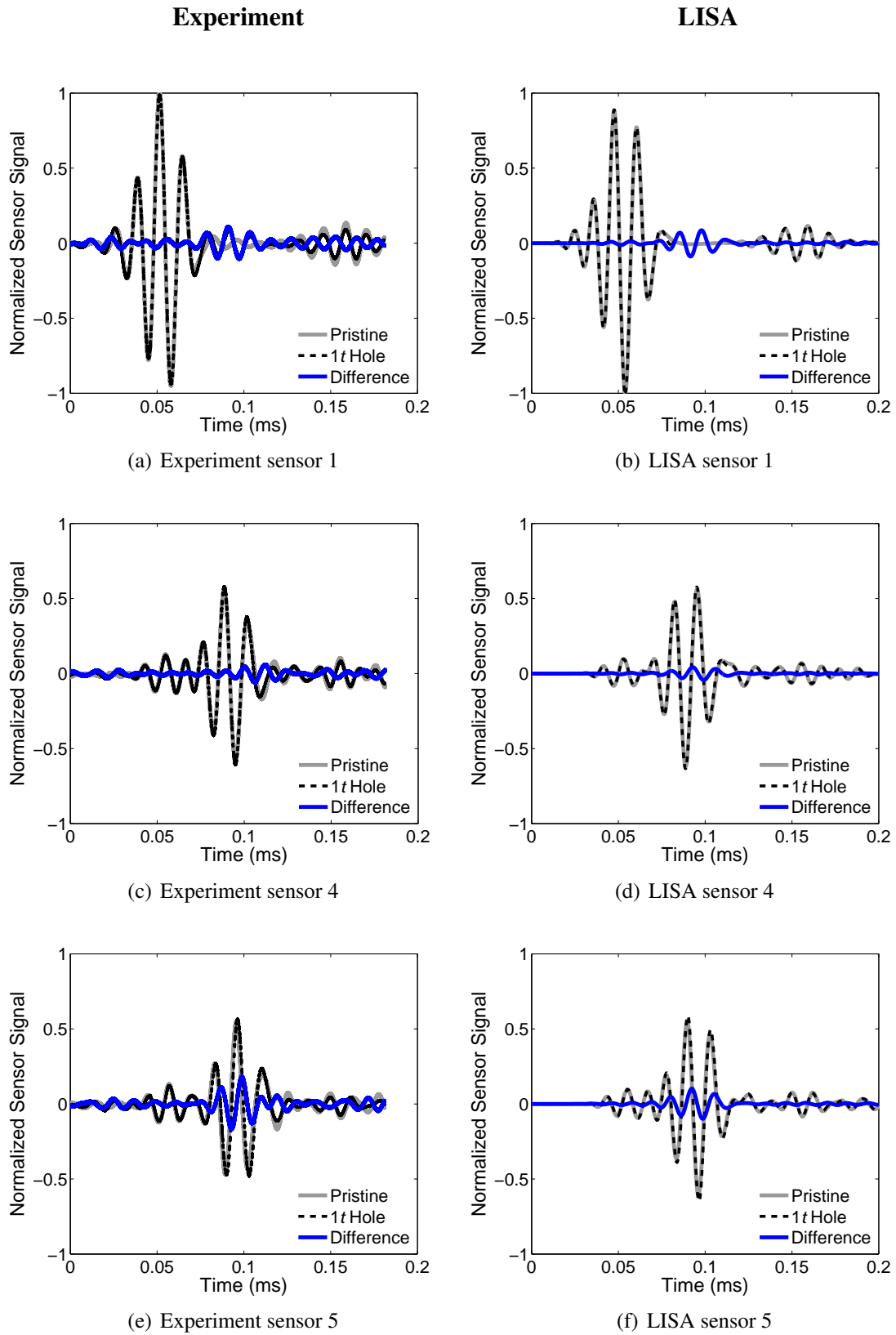


Figure 4.6: Comparison of experimental and LISA results for  $r = 1t$  hole in an aluminum plate.

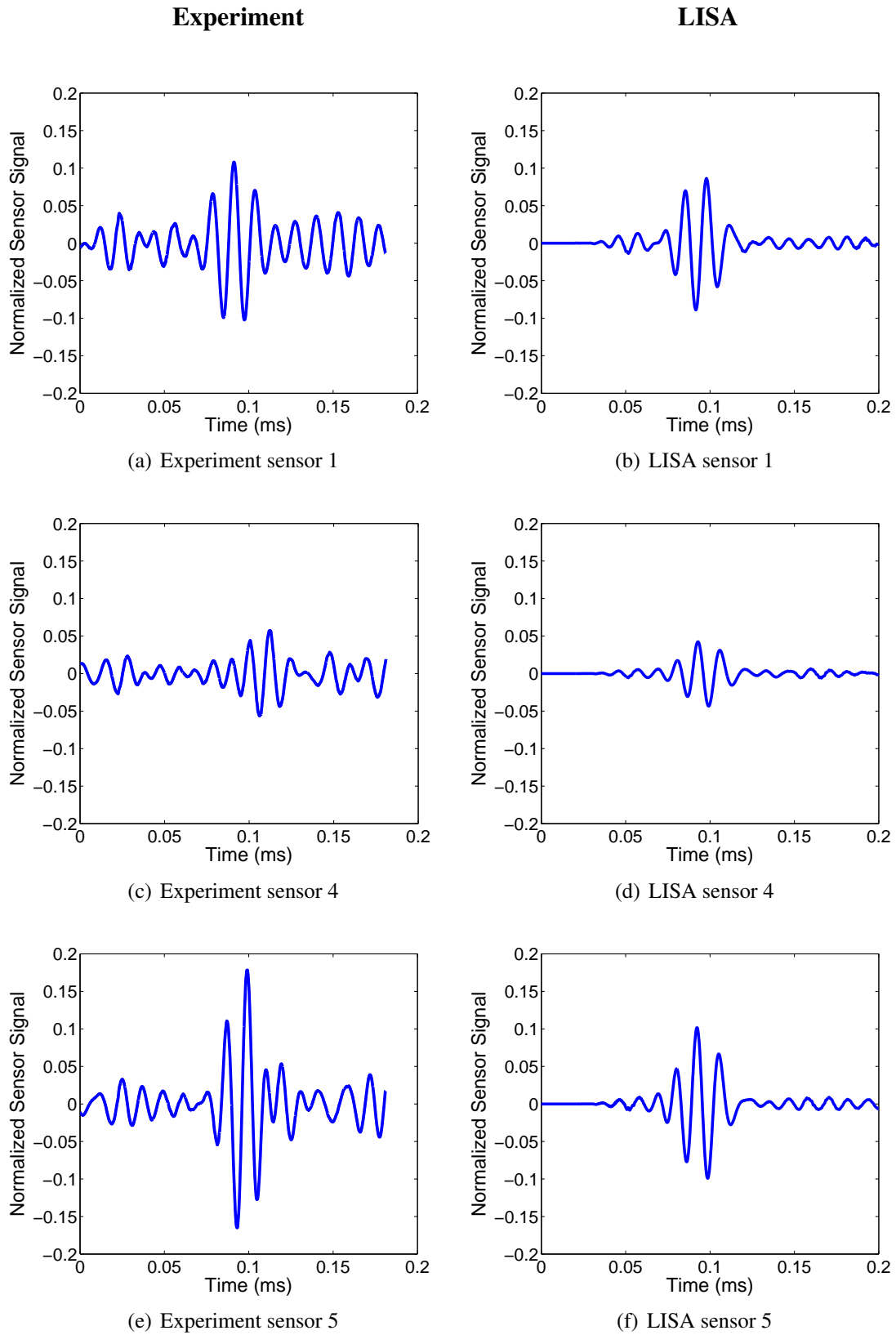


Figure 4.7: Comparison of experimental and LISA difference signals for  $r = 1t$  hole in an aluminum plate.

smaller amplitude than the other sensors, as expected. A close examination of the signals shows that in comparison to the simulation, the difference signals had a higher amplitude in the experiment relative to the amplitude of the pristine signals. The experimental sensor data showed the dominant  $A_0$  features predicted by the simulation. However, the more subtle  $S_0$  features seen in the simulation results were largely eclipsed by residual signals and noise in the experimental results. Despite these discrepancies, it is reasonable to conclude the LISA model can successfully capture the effects of the hole for the isotropic case.

## 4.3 Holes in Composite Plates

The second portion of this study focused on through-thickness and half-depth holes in composite laminates. As in the isotropic study, LISA simulations were conducted to investigate the influence of various parameters on guided wave propagation. Additionally, experiments were performed to confirm the quality of the LISA models.

### 4.3.1 Simulation Studies

For the composite case, a 12-layer cross-ply ( $[0/90]_{3S}$ ) laminate was modeled. The material system consisted of IM7 graphite fibers with a CYCOM 977-3 matrix, and the material properties were previously shown in Table 2.2. The cross-ply plate had a ply thickness of 0.125 mm and a total thickness of 1.5 mm. The actuator, sensor, and damage configuration was identical to that used in the aluminum study. The side length used in this case was 500 mm, which accomplished the previously-mentioned goal of minimizing boundary effects while also matching the dimensions of specimens used in experimental studies. The cross-ply simulations also considered three different azimuthal locations of the hole, in which the hole was located at 0, 45, and 90 degrees relative to the fiber orientation of the top layer, as shown in Fig. 4.8. The thickness-direction discretization in these models was set to match the ply thickness of the laminate, 0.125 mm. The in-plane discretization was maintained

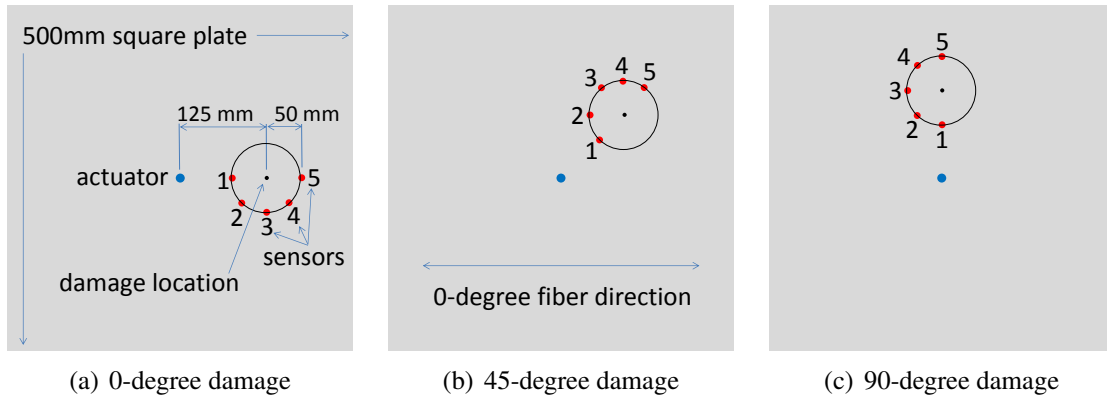
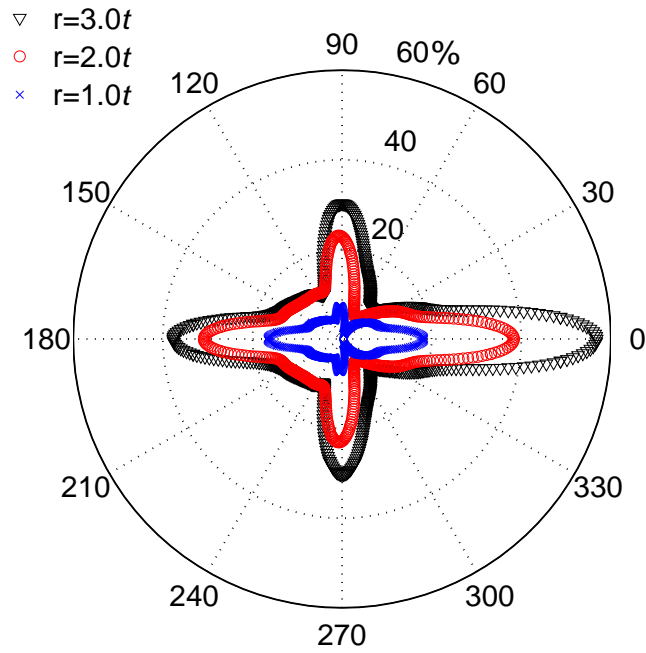


Figure 4.8: Schematics of simulation setup for cross-ply damage simulations.

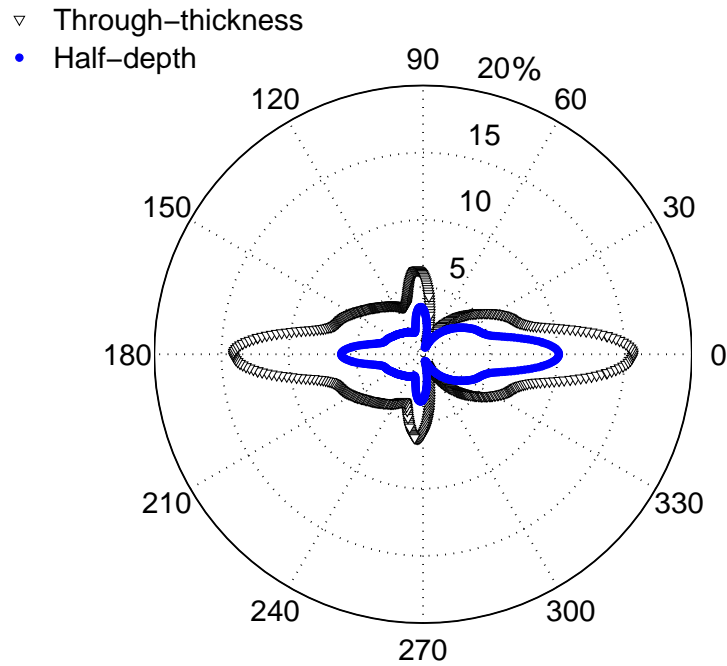
at  $0.5 \text{ mm} \times 0.5 \text{ mm}$ . As in the previous section, a 75 kHz, 3.5 cycle Hann-modulated toneburst excitation was simulated.

#### 4.3.1.1 Hole Radius Variation

Results for the cross-ply simulations were examined based on hole radius, hole depth, and azimuthal location. For the comparisons based on hole radius, through-thickness holes were placed along the 0-degree azimuth. An initial observation from the simulation results was the concentration of the difference signals in the fiber directions (0 and 90 degrees). This concentration was especially apparent as the size of the hole increased. Figure 4.9 (a) shows the difference signal scatter patterns for points 50 mm from the hole for three different hole radii. The results were normalized as a percentage of the maximum amplitude of the pristine signal when it reached the damage location. For the  $r = 1t$  hole, the energy was primarily concentrated along the 0-180 degree line. As the radius increased, the proportion of energy scattered in the 90-270 degree line increased. An additional finding was the increasing difference signal amplitude behind the hole relative to the other directions as the hole radius increased. This was consistent with the results from the isotropic case.



(a) Through-hole radius comparison



(b) Hole depth comparison

Figure 4.9: Azimuthal variation of the out-of-plane difference signal's maximum amplitude for cross-ply hole simulations. Results are for points 50 mm from the hole center for varying hole radius (a) and hole depth (b).

#### 4.3.1.2 Hole Depth Variation

Figure 4.9 (b) shows a comparison of the scatter patterns for a through-thickness and half-depth hole, both with radius  $r = 1t$ . For both hole depths, the predominance of difference signal scattering was along the fiber directions. In the half-depth hole case, the amplitudes were decreased significantly in the 0-180 degree direction, but less so in the 90-270 degree direction.

It is interesting to also compare the out-of-plane displacement fields for the two hole depths. Figure 4.10 shows a series of displacement field plots, where the top plots were taken 50 microseconds after the beginning of the actuation pulse and the bottom plots were taken at 100 microseconds. As a reference, the top two plots show the displacement field for the pristine case. The center row shows field plots of the out-of-plane difference signal for the through-thickness hole case, and the scales of these plots were adjusted to better show the results. The bottom row shows the difference signals for the half-depth hole. The axes of each of the plots were normalized by the radius of the actuator,  $R_O$ . At the 50 microsecond point in time, Fig. 4.10 (a) shows the  $A_0$  pulse had not yet arrived at the damage location. However, Fig. 4.10 (e) shows a difference signal was already present near the half-depth hole. This difference signal had a wavelength consistent with an  $A_0$  mode, and it can be attributed to a mode conversion of the  $S_0$  mode to an  $A_0$  mode. For the through-thickness hole case, this mode conversion did not occur, and no difference signal was observed. At the 100 microsecond point in time, the  $A_0$  mode had arrived at the damage location. The difference signal shown in Fig. 4.10 (d) shows the interaction of this mode with the through-thickness hole. For the half-depth hole model, the unconverted  $A_0$ - $A_0$  difference signal was present around the hole, while the mode-converted  $S_0$ - $A_0$  signal had almost reached the actuator location at the center of the plate.



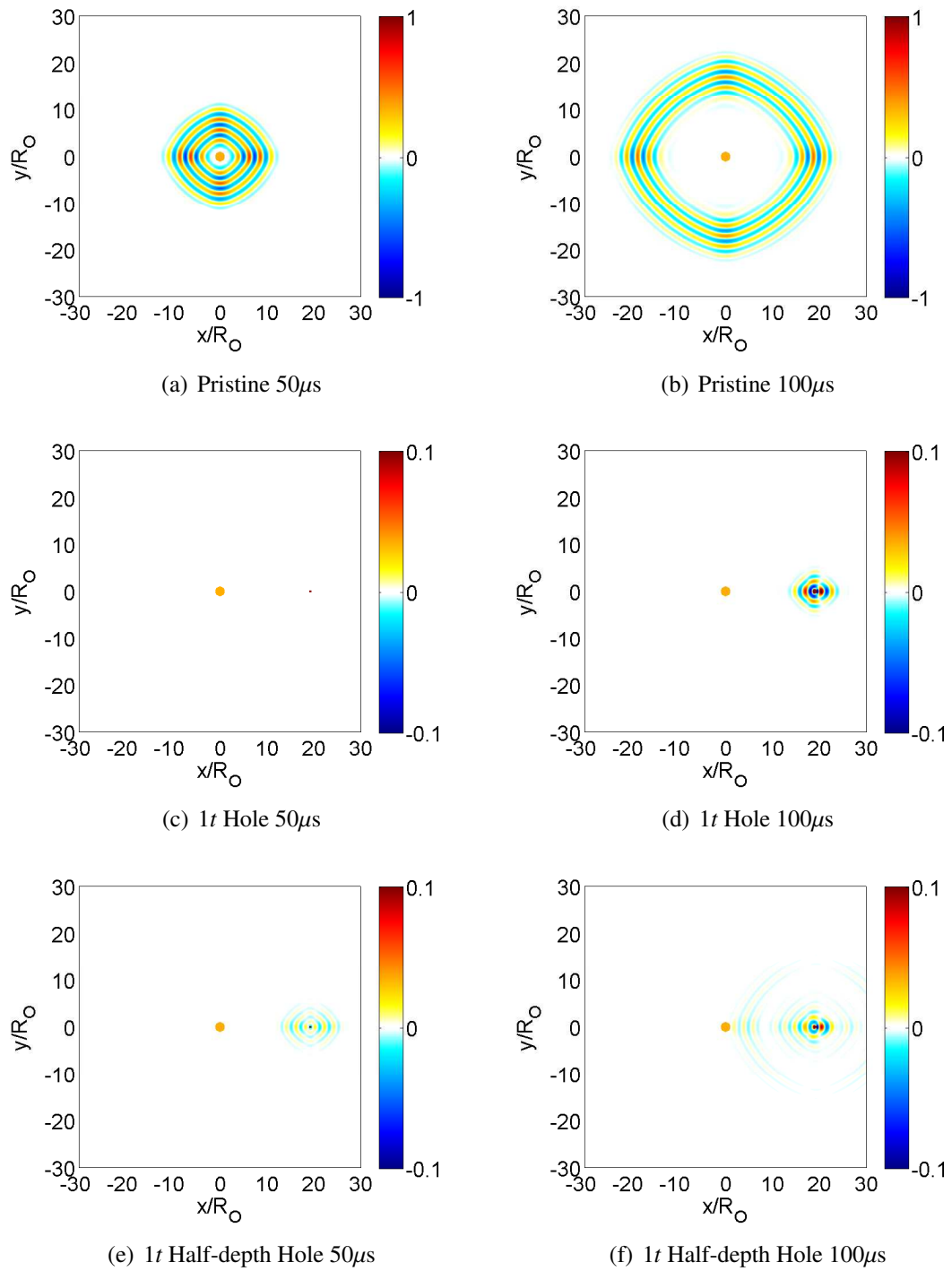
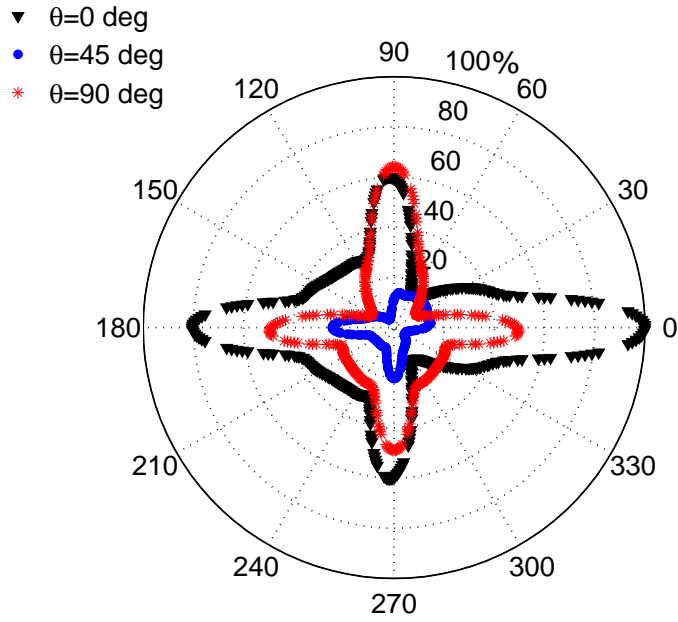


Figure 4.10: Out-of-plane displacement fields for through and half-depth holes.

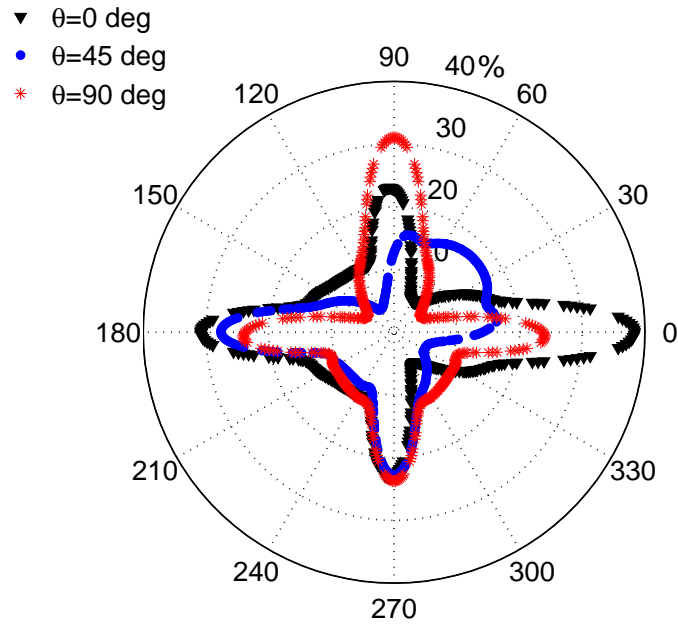
### 4.3.1.3 Hole Azimuth Variation

The effect of varying the azimuthal location of the hole was evaluated next. The holes considered for the azimuthal comparison had radius  $r = 2t$ . For this analysis, the results were normalized in two different ways. The first method normalized the results based on the maximum difference signal amplitude for the 0-degree hole, as shown in Fig. 4.11 (a). This normalization scheme allowed the results to show the differences in the difference signal amplitudes based on the amount of energy that propagated from the actuator to the hole and the amount of energy that propagated from the hole to the observed point on the plate. Under these conditions, the amplitudes for the 45-degree hole were considerably smaller than the holes located along fiber directions relative to the actuator. This presentation of the difference amplitudes was the most appropriate when considering a non-directional actuator such as the circular wafer used in the simulation. However, a second normalization method was employed to consider the results a different way. Figure 4.11 (b) shows the same data, but here the values were normalized with respect to the maximum amplitude of the pristine signal reaching the respective damage location. The results for this scheme showed the difference signal amplitudes relative to the amount of energy that actually reached the damage site. The drastic increase in the response for the 45-degree hole relative to the other hole locations using this scheme reinforced previous work [38] that recommended using directional transduction to increase guided wave amplitudes.

For the holes oriented in the 0 and 90-degree directions, the maximum difference signal amplitude was on the backside of the hole, as expected. The maximum difference signal for the 90-degree case was noticeably less than the 0-degree case, which can be attributed to the direction of the fibers in the top and bottom layers of the laminate. The 45-degree hole orientation produced a scatter pattern much different from the other two cases. In the 45-degree damage simulation, the incoming wave originated from the 225-degree direction, and the largest difference signals were focused back toward the 180-degree direction, which



(a) Azimuth comparison 1



(b) Azimuth comparison 2

Figure 4.11: Azimuthal variation of the out-of-plane difference signal's maximum amplitude for cross-ply hole simulations. Results are for points 50 mm from the hole center for (a) varying hole location normalized by maximum amplitude at 0-degree location, and (b) varying hole location normalized by max out-of-plane displacement at respective hole location.

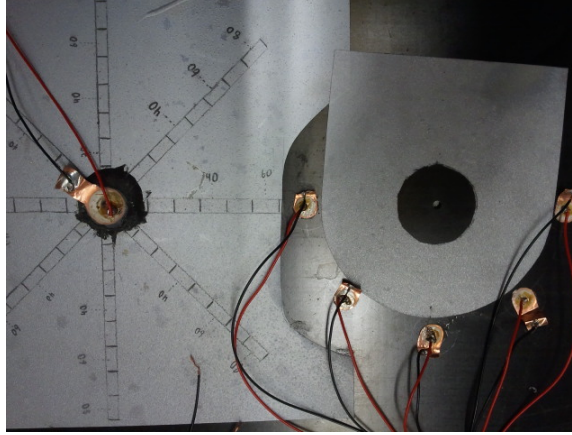


Figure 4.12: Configuration of cross-ply hole experiment.

corresponded with a fiber direction in the plate. The difference signals in both the 180 and 270-degree directions were both larger than the backside (45-degree) direction.

These simulations provided interesting insight into the placement of sensors in a composite structure and the probability of detecting damage in various locations. Considering holes aligned with the circular actuator along a fiber direction, aligned sensors in traditional pulse-echo and pitch-catch configurations produced strong difference signals, with pitch-catch sensors generally being superior. However, other directions consistently produced drastically smaller difference signals, such as the 45 and 315-degree directions. When the hole and actuator were not aligned along a fiber direction, the aligned sensors did not provide the best results.

### 4.3.2 Comparison with Experimental Data

To validate the simulation results, an experiment was conducted using a cross-ply plate with a  $r = 1t$  hole. The plate was fabricated in house using the aforementioned material system, and an autoclave was used to cure the plate. The parameters of the experiment matched the simulation case where the hole was located along the 0-degree orientation angle in the plate, as shown in Fig. 4.12. The experimental instrumentation setup was identical to that used for the isotropic study.

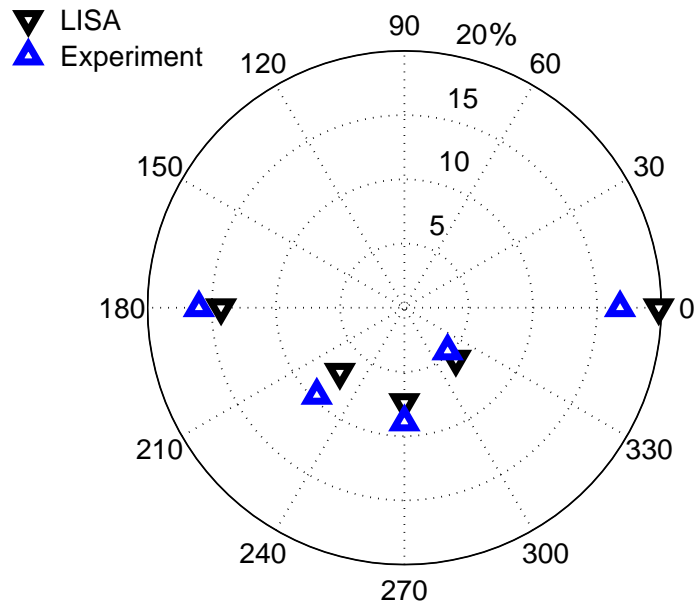


Figure 4.13: Comparison of LISA and experimental results for through-thickness hole scenario in a cross-ply laminate. Sensor difference signals are normalized as a percentage of the maximum pristine signal amplitude at sensor 1, which corresponds to the 180-degree direction.

Figure 4.13 compares the azimuthal behavior of the difference signals for the simulations and experiment. The maximum amplitudes of the sensor difference signals are plotted as a percentage of the maximum pristine signal amplitude at sensor 1. A quantitative summary of these results is included in Table 4.2. Consistent agreement was found for the five sensors, with differences ranging from 0.9% to 3% of the pristine amplitude of the sensor 1 signal. The preponderance of difference signal energy along the 0-degree fiber direction found in the experiment was well preserved by the simulation. Unlike in the aluminum case, the difference between the experimental and LISA difference signals for sensor 5 was not significantly higher than the other sensors.

Comparison of the time histories of the simulated and experimental sensor responses showed similar trends in the agreement of the results. The sensor responses for sensors

Table 4.2: Comparison of LISA and experimental results for through-thickness hole scenario in a cross-ply laminate. The maximum difference signal amplitude is shown as a percentage of the pristine signal at sensor 1.

	Sensor				
	S1	S2	S3	S4	S5
LISA %	14.3	7.1	7.4	5.7	19.8
Experiment %	16.0	9.6	8.9	4.8	16.8
Difference	1.7	2.5	1.5	0.9	3.0

1, 3, and 5 are compared in Fig. 4.14. The experimental results for the pristine, damage, and difference signals are on the top, while the LISA simulation results are on the bottom. There were some amplitude differences in the pristine signals at the sensor locations, but these can be most likely attributed to manufacturing variations in the plate. A more detailed comparison of the difference signals is included in Fig. 4.15. Examination of the difference signals within the context of the pristine signals explains much of the amplitude difference between the experimental and LISA results. For the sensor 1 location, the initial  $S_0$  portion of the pristine signal was higher in the experiment than in the simulation, and this yielded a higher amplitude reflection prior to the 0.1 ms point in the time history. The experimental pristine signal at sensor 3 had higher amplitude in both the  $S_0$  and  $A_0$  modes, and the corresponding difference signal was also higher in amplitude than in the simulation. At sensor 5, a slightly larger  $A_0$  mode in the simulation produced a slightly larger amplitude for the simulated sensor signal near the 0.14 ms point in time. The majority of the data showed good amplitude agreement during the full duration of the time history at this location.

Overall, there was excellent agreement between the simulation and the experiment for the case considered in this study. Although some discrepancies were found, the results were consistent enough to provide a high level of confidence in LISA's ability to represent guided wave interaction with this type of damage.

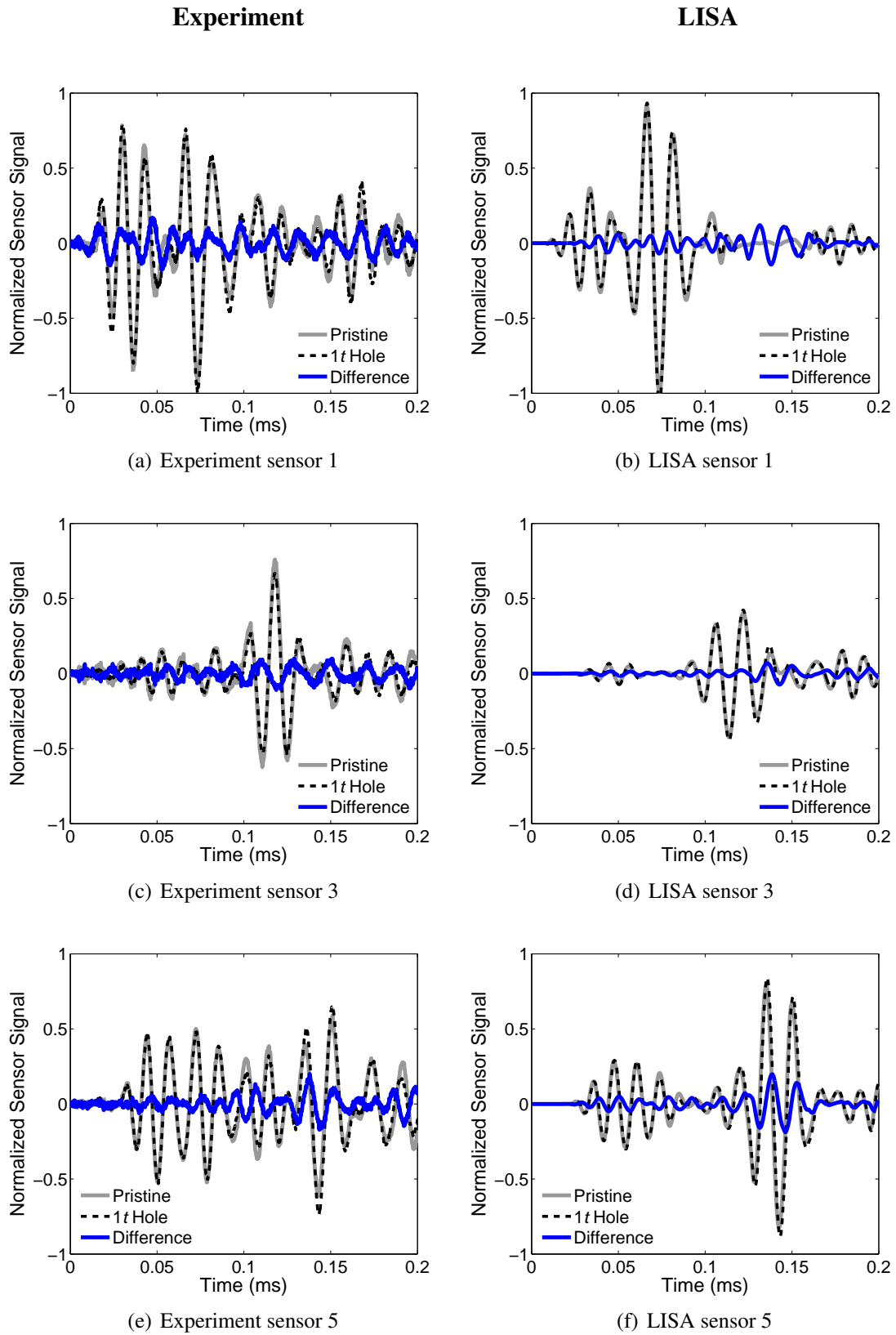


Figure 4.14: Comparison of experimental and LISA sensor results for  $r = 1t$  hole in a cross-ply laminate.

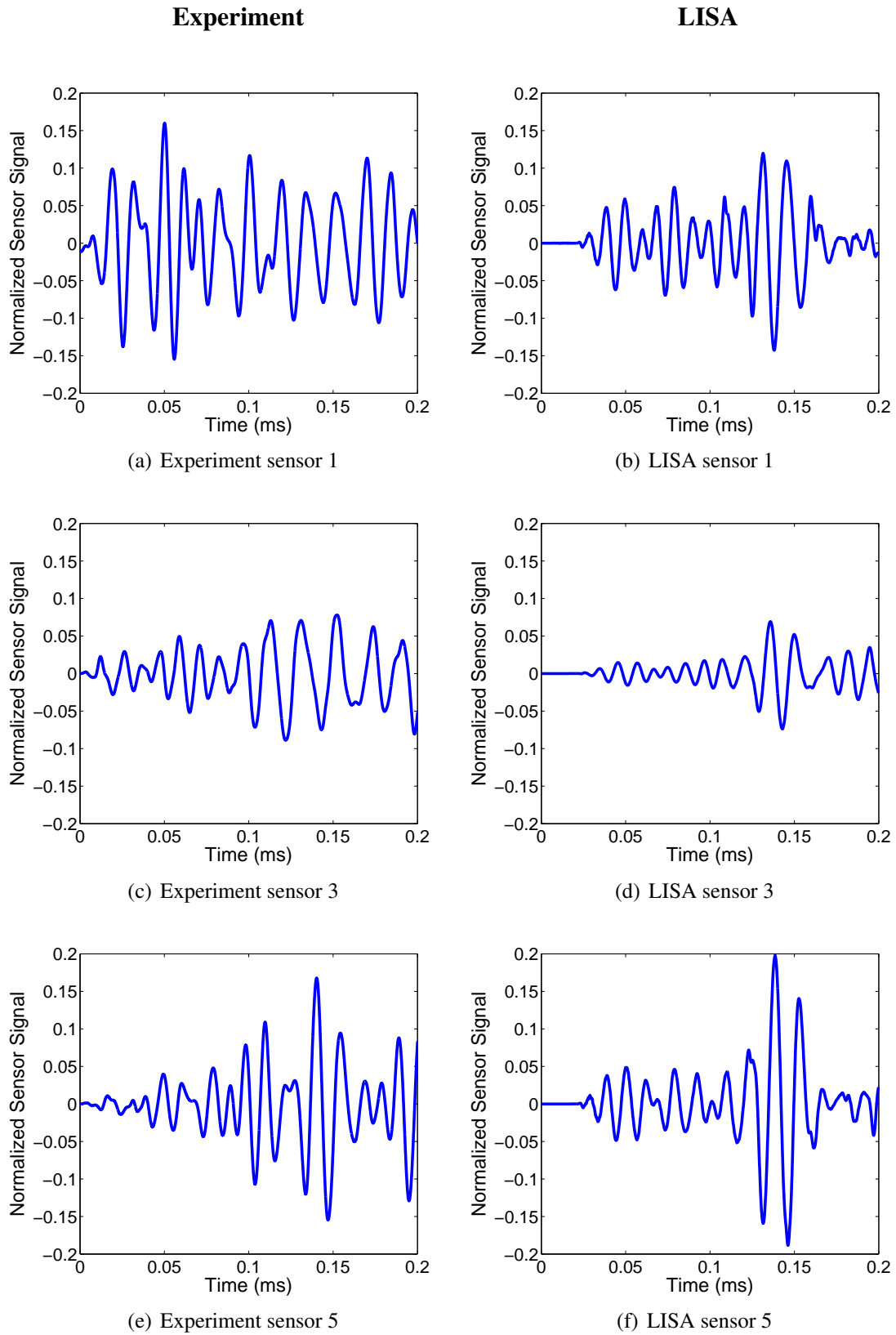


Figure 4.15: Comparison of experimental and LISA sensor difference signals for  $r = 1t$  hole in a cross-ply laminate.



## 4.4 Summary

This chapter used the LISA hybrid simulation architecture to model guided wave interaction with damage in isotropic and composite plates. First, a series of simulations considered through-thickness and half-depth holes in an aluminum plate. The azimuthal behavior of the damage difference signals was compared for holes of different radius for each hole depth. Results showed that in general, the difference signals had higher amplitude on the back side of the hole than on side facing the actuator, and this trend increased as the radius of the hole increased. Experimental results confirmed that the LISA simulation successfully captured the guided wave scattering from the holes.

Next, holes were simulated in a cross-ply laminate. Comparisons based on hole size, hole depth, and the azimuthal location of the hole were presented. Difference signal energy was highly concentrated along the fiber directions. Simulations for the half-depth hole successfully captured mode conversion effects due to partial-thickness damage. Sensors in the pitch-catch configuration relative to the actuator and damage produced higher difference signals when the damage was aligned with the actuator along a fiber direction. Results from simulations where the hole was oriented in the 45-degree azimuth showed that when the damage and actuator were not aligned with a fiber direction, sensors in the traditional pulse-echo or pitch-catch configuration did not necessarily produce the highest difference signals. Experimental data showed the LISA model was very successful in capturing the major features of the damage difference signals and representing the azimuthal behavior of the signals for the hole damage case.

## CHAPTER 5

# Guided Wave Interaction with Impact Damage

This chapter considers the effects of low-velocity impact damage in composite plates. First, a short introduction to the problem of impact damage is provided to better understand the need to examine this damage mode. The results of diagnostic inspections are provided to explain how impact damage typically manifests itself in laminated composite plates. The next section provides a series of experimental results for guided wave interaction with laboratory-produced impact damage. After analyzing guided wave behavior in the experimental specimens, the remainder of the chapter focuses on determining the best ways to model impact damage in LISA. Several candidate models are compared to determine which approaches best match the damage signals from the experiments.

## 5.1 Low-velocity Impact Damage in Composite Plates

While holes are a convenient form of damage to evaluate candidate SHM tools and better understand wave propagation, it is also necessary to understand how guided waves interact with more realistic forms of damage likely to be found in fielded composite structures. One of the most concerning damage modes is low-velocity impact, which may result from tool drops during maintenance or from other foreign object impact. What makes low-velocity impact particularly insidious is the significant internal damage it can create without producing any visually-detectable surface damage, yielding what is known as barely visible impact damage (BVID). In previous literature, there have been inconsistent definitions of

Table 5.1: HEXCEL IM7 8552 Material Properties

Property	$E_1$	$E_2$	$G_{12}$	$G_{23}$	$\nu_{12}$	$\rho$
Value	162 GPa	8.96 GPa	4.69 GPa	3.3 GPa	0.316	1580 kg/m <sup>3</sup>

what constitutes low and high-velocity impact, and it has been noted that impacts of different masses with the same kinetic energy can produce different results [140]. For the purposes of this chapter, low-velocity impacts are broadly defined as those that create sub-surface damage while creating little or no damage at the impacted surface of the composite laminate.

Low-velocity impact damage is usually a combination of multiple failure modes including delamination, fiber breakage, and matrix cracking. Previous experimental studies have shown that low-velocity impact events produce a V-shaped damage profile, with the apex of the V on the surface where the impact occurred [141, 142]. In order to better understand the characteristics of the impact damage in the composite laminates used in this chapter, a series of diagnostic tests were performed. Cross-ply ( $[0/90]_{3S}$ ) composite plate specimens were fabricated in house using IM7 graphite fibers with a HEXCEL 8552 matrix. The properties for this material system are shown in Table 5.1, and a photograph of a representative specimen is shown in Fig. 5.1. For each of the specimens, a drop-weight

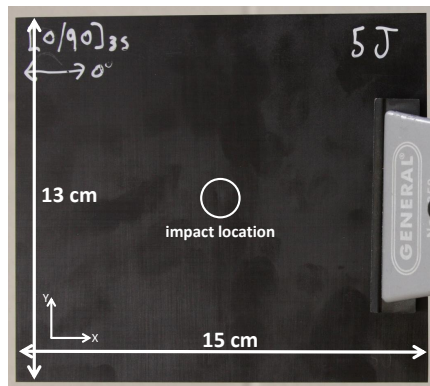


Figure 5.1: Impact specimen.

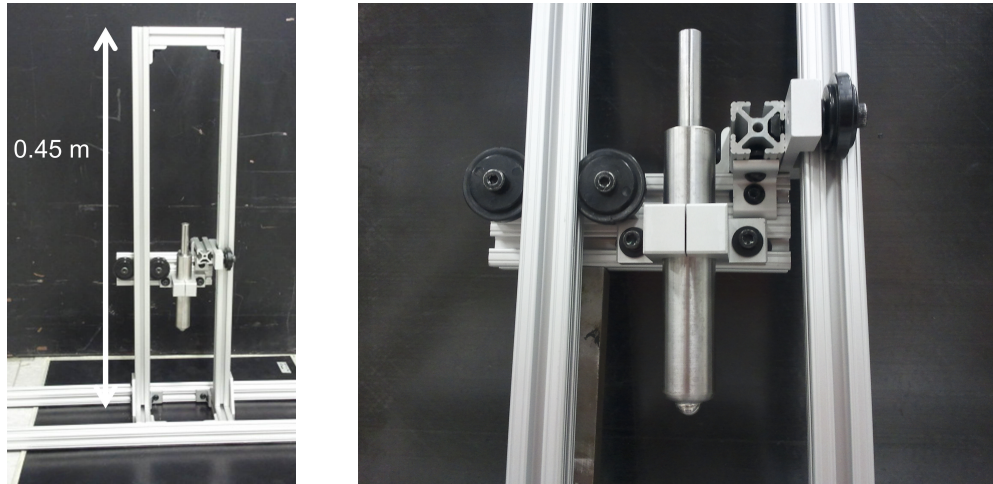
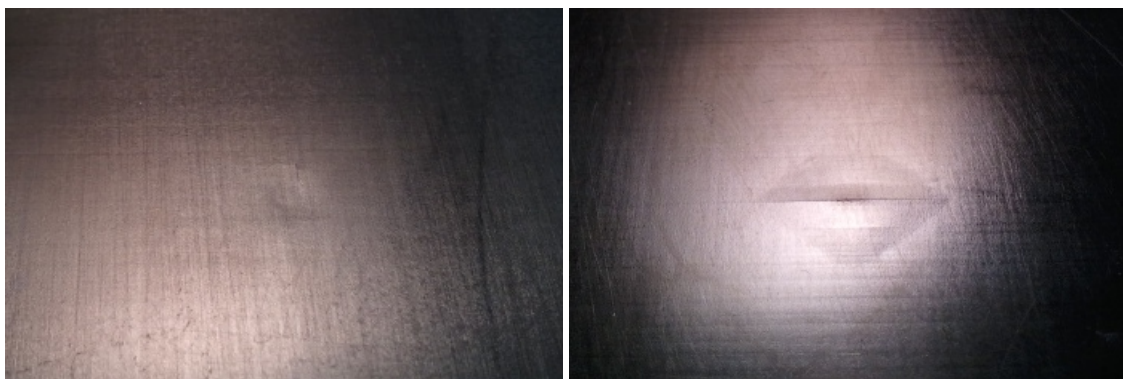


Figure 5.2: Drop-weight impactor.

impact was applied using the impactor shown in Fig. 5.2. In this fixture, the tip of the impactor was a steel ball with a 12.7-mm diameter. Desired amounts of impact energy were applied by dropping the impactor from different heights above the surface of the specimen. In Fig. 5.3, the front and back side of a damaged specimen are shown after a 5-J impact. The impact resulted in a barely-visible dent on the front side of the specimen. On the back side of the specimen, more extensive damage was visible. A long matrix crack ran along



(a) Front (impacted) side of specimen.

(b) Back side of specimen

Figure 5.3: Surface features from 5-J impact.

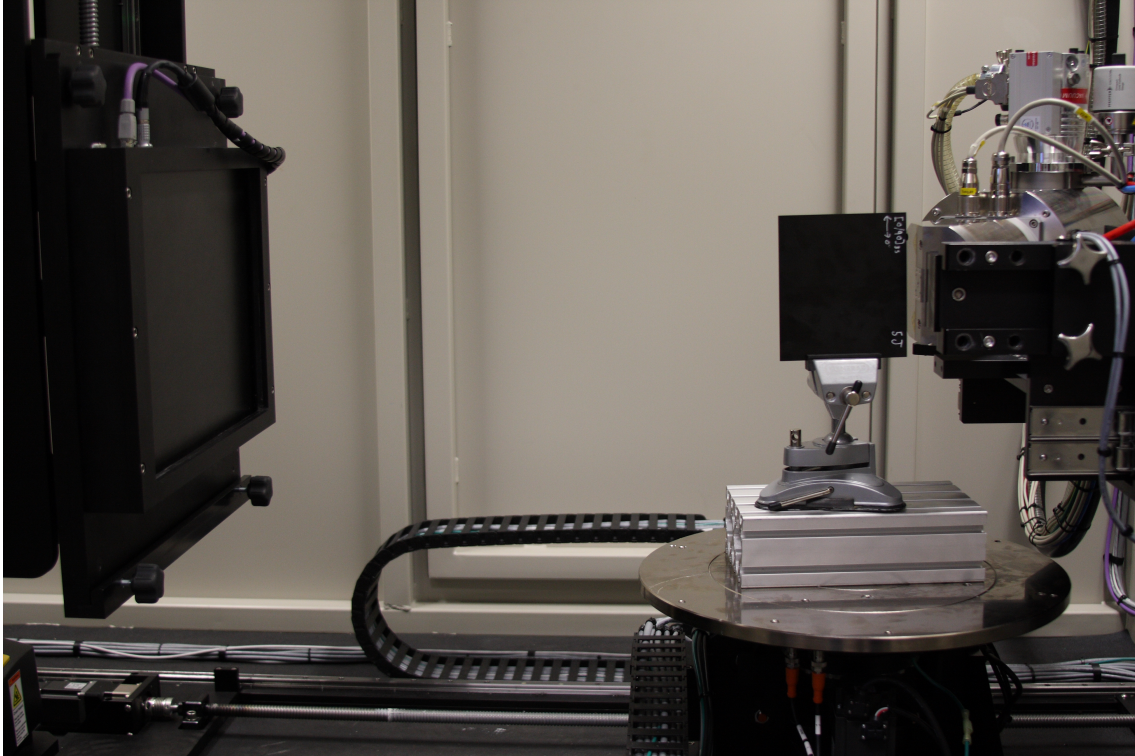


Figure 5.4: Impact damage specimen in CT system at the University of Texas, Arlington.

the fiber direction of the bottom lamina, and a diamond-shaped damage pattern around this crack was also visible.

After the impact damage was created, the specimens were inspected using a North Star Imaging X5000 Computed Tomography (CT) X-ray system at the University of Texas, Arlington. The X-ray system had a voxel resolution of  $0.37 \times 10^{-3}$  inches ( $9.4 \times 10^{-3}$  mm). Figure 5.4 shows one of the specimens mounted in the CT system. For each specimen, a series of cross-sectional scans were produced showing how any existing damage progresses in different directions. The next few figures show the results for the 5-J impact specimen.

The first series of cross-sectional scans, shown in Fig. 5.5, captured the in-plane profile of the damage region at various depths in the through-thickness direction. Each scan covered a rectangular region with dimensions  $28 \text{ mm} \times 20 \text{ mm}$ . The scan in the upper left corner is at the top surface of the plate, and the impact dent is clearly visible. As the scans

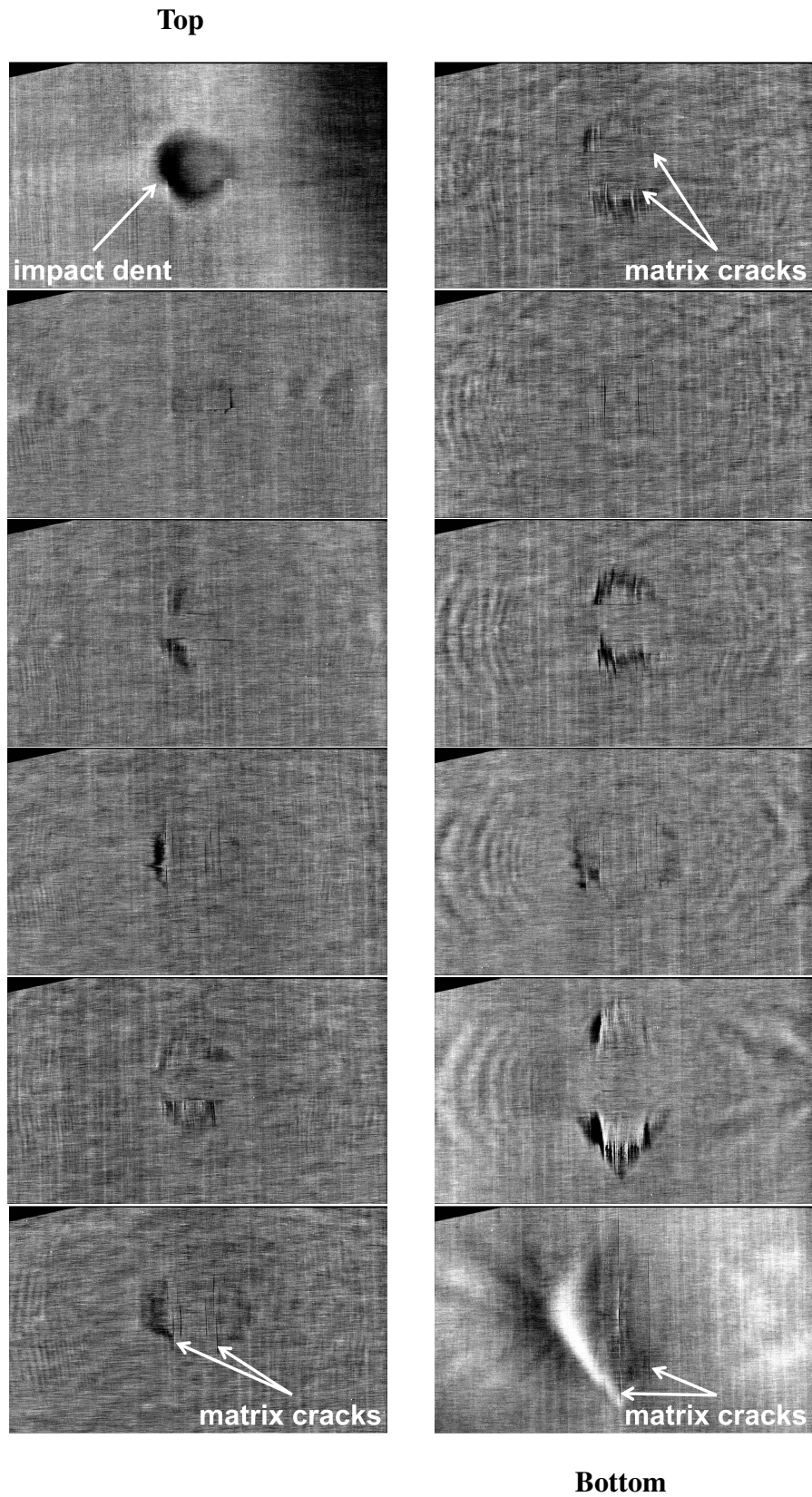


Figure 5.5: In-plane views of impact damage at various depths through specimen.

move down the left column and then down the right column, the depth gradually increases, and the size of the damage region increases. This was the expected result based on previous studies. In many of the scans, distinct matrix cracks running along the fiber directions were visible, which gave the damage a rectangular profile in the center of the damaged region. The final scan in the lower right corner showed the large matrix crack on the bottom surface of the plate along with the diamond-shaped surface damage.

The next series of scans, shown in Fig. 5.6, represent cross sections in the X-Z plane of the specimen. The five scans are equally spaced in the Y direction and range from  $\pm 1.8$

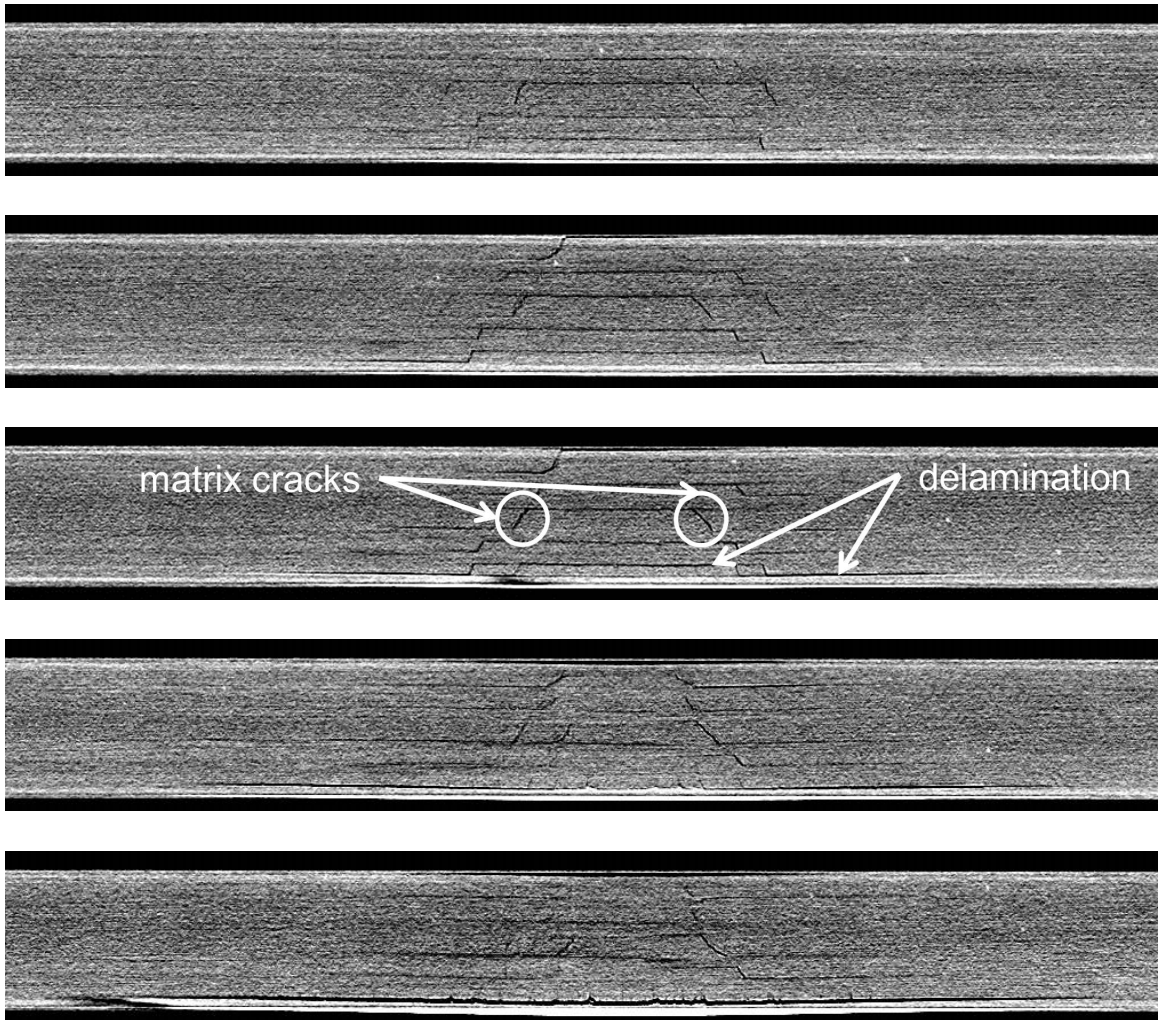


Figure 5.6: Section views in X-Z plane.

mm from the damage center. In this orientation, the fibers in the top and bottom lamina are running along the length of the picture, while the fibers in the middle two lamina are running in and out of the page. The matrix cracks are the most visible damage feature in these images, and the inverted V pattern is very evident. In addition to the matrix cracks, delaminations are clearly visible—especially near the damage center.

A similar series of cross-sectional scans for the Y-Z plane of the specimen is shown in Fig. 5.7. Here, the fibers in the top and bottom lamina are running in and out of the page, while the fibers in the middle two lamina are running along the length of the picture. These scans are equally spaced in the X direction and range from  $\pm 1.8$  mm from the damage center. The inverted V pattern is noticeable in these images as well. The distinct matrix cracks are in the opposite lamina from the previously shown X-Z plane scans. The long matrix crack seen on the bottom surface of the specimen in Fig. 5.3 (b) is clearly seen in each of the Y-Z section scans shown here. Significant delaminations are also visible, with the largest delamination appearing between the bottom two lamina.

## **5.2 Experimental Characterization of Guided Wave Interaction with Impact Damage**

A series of experiments were performed to obtain data needed to better understand how Lamb waves interact with impact damage. For these experiments, cross-ply  $([0/90]_{3S})$  plates were fabricated using the HEXCEL IM7-8553 material system. As in the hole damage experiments, damage sites in the 0, 45, and 90-degree orientation were instrumented with five sensors around each damage location, as previously shown in Fig. 4.8. The excitation parameters used for these impact damage sensor experiments were identical to those used in the hole damage experiments.

In addition to the sensor measurements, a Polytec scanning laser vibrometer was used to record out-of-plane motion. For the laser vibrometer measurements, the Agilent 33220A



function generator was used to generate the Hann-modulated toneburst at 75 kHz, this time at 0.5 V p-p. The excitation signal was passed through a Krohn-Hite 7500 amplifier to increase the signal to 50 V p-p. The laser vibrometer recorded the out-of-plane motion at a series of specified scan points surrounding the damage site. Retroreflective tape was

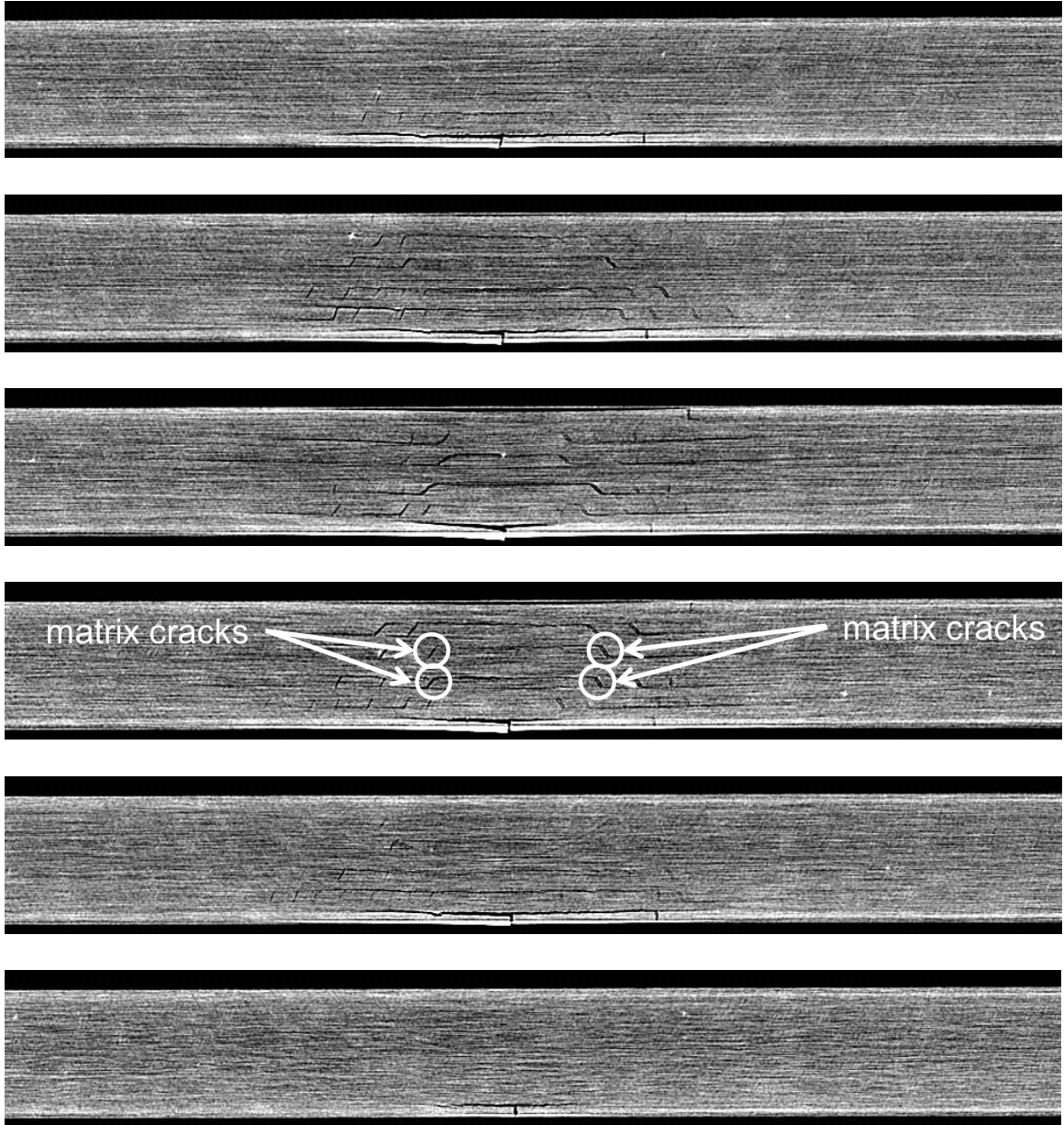


Figure 5.7: Section views in Y-Z plane.

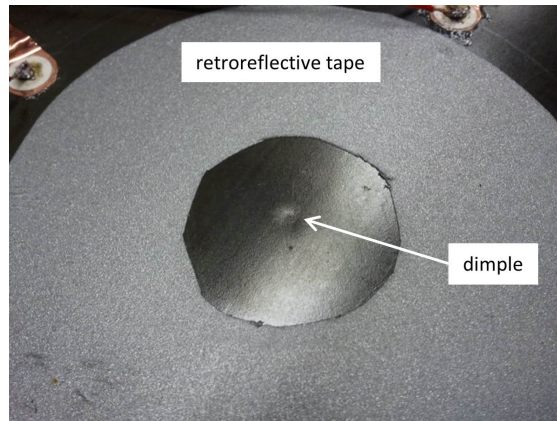


Figure 5.8: Impact dent on surface of composite plate.

attached to the plate in the area surrounding the damage site to increase the strength of the reflection back to the laser vibrometer during the experiment.

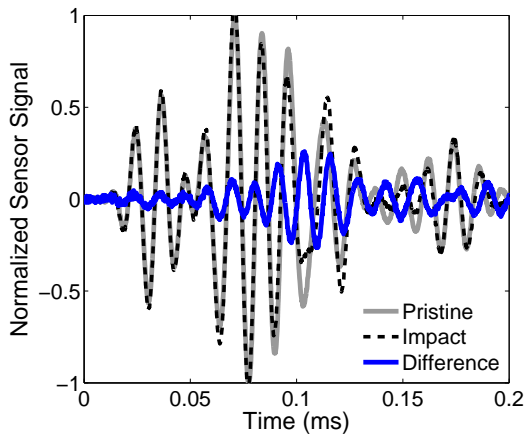
It should be noted that in these experiments, the measurements were taken on the side of the plate where the impact occurred. In a realistic situation, it is likely the sensors will be attached to the surface of the plate on the interior of the structure, placing them on the side opposite the impact.

The first stage in each experiment involved collecting data for the undamaged plate. Once the pristine data were recorded, the drop-weight impactor was used to apply an impact to the plate. For these experiments, the 5-J impact energy resulted in barely-visible dimples on the impacted surfaces of the plates, as seen in Fig. 5.8. Unlike in the case of the impact-damage specimen, no damage was observed on the back side of the plates. It is likely that the impact imparted on the plates had slightly lower energy than the specimen, resulting in less backside damage. Even though the height used for the drop-weight procedure was the same for both cases, it is possible that friction in the impactor resulted in a lower impact velocity for the impact on the plates used in these experiments. Once the impacts were applied, post-damage measurements were taken for comparison with the pristine signals using both the sensors and the laser vibrometer. As in the hole experiment, a low-pass filter was used during post-processing to eliminate noise in the difference signals.

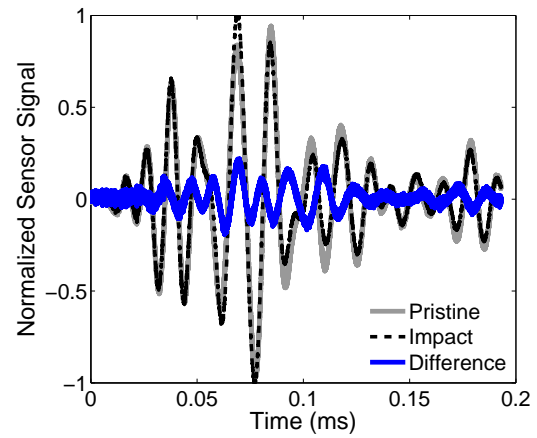
### **5.2.1 Sensor Results for 0-degree Damage Site**

The first impact damage experiments considered damage located in the 0-degree orientation relative to the fiber direction of the top and bottom lamina. For this case, two separate experiments were conducted, and the results for both are included in this section. Figure 5.9 shows the sensor results for sensors 1, 2, and 3, while Fig. 5.10 shows the results for sensors 4 and 5. In these figures, the pristine, damage, and difference signals are included for each sensor location. Each signal was normalized with respect to the maximum amplitude of the pristine signal recorded using sensor 1. In general, the signals for each location were quite similar between the two experiments, and notable differences in the pristine signals arriving at each respective sensor location can largely be attributed to expected variation between the two composite plate specimens.

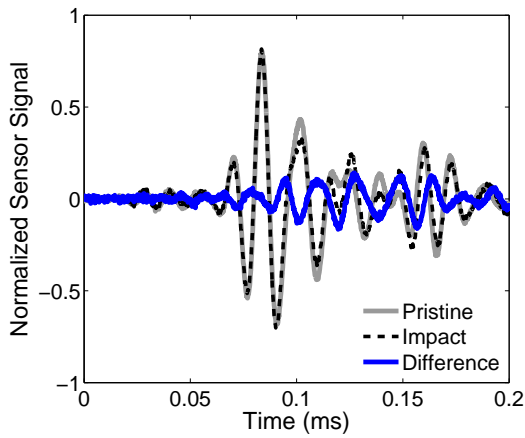
Figures 5.11 and 5.12 show additional views of the difference signals obtained after subtracting the pristine signals from the damage signals. Several notable results are worth mentioning. The strongest difference signals were obtained using sensors 1 and 5, which were located in the pulse-echo and pitch-catch orientations, respectively. Of these two sensor locations, sensor 1 produced the largest signal in both of the experiments. Strong signals were also obtained using sensor 2. The amplitudes of the sensor 1 and 2 signals indicated that the impact damage region produced substantial reflections back toward the actuator location at the center of the plate. As was previously seen in the hole damage experiment, the weakest difference signals were recorded using sensor 4.



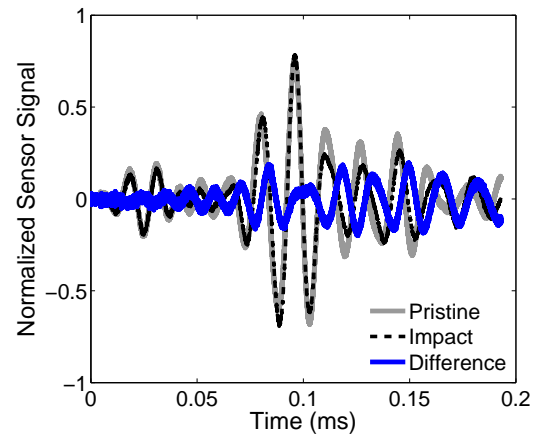
(a) Sensor 1 Plate 1



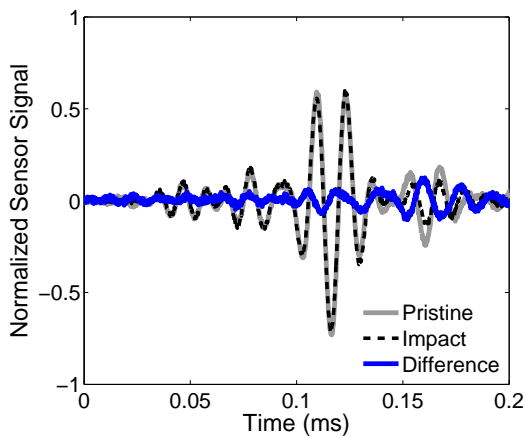
(b) Sensor 1 Plate 2



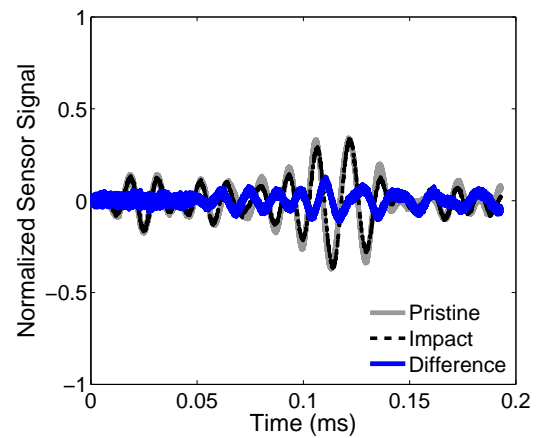
(c) Sensor 2 Plate 1



(d) Sensor 2 Plate 2



(e) Sensor 3 Plate 1



(f) Sensor 3 Plate 2

Figure 5.9: 5-J impact damage in cross-ply laminate: sensor signals at 0-degree damage location.

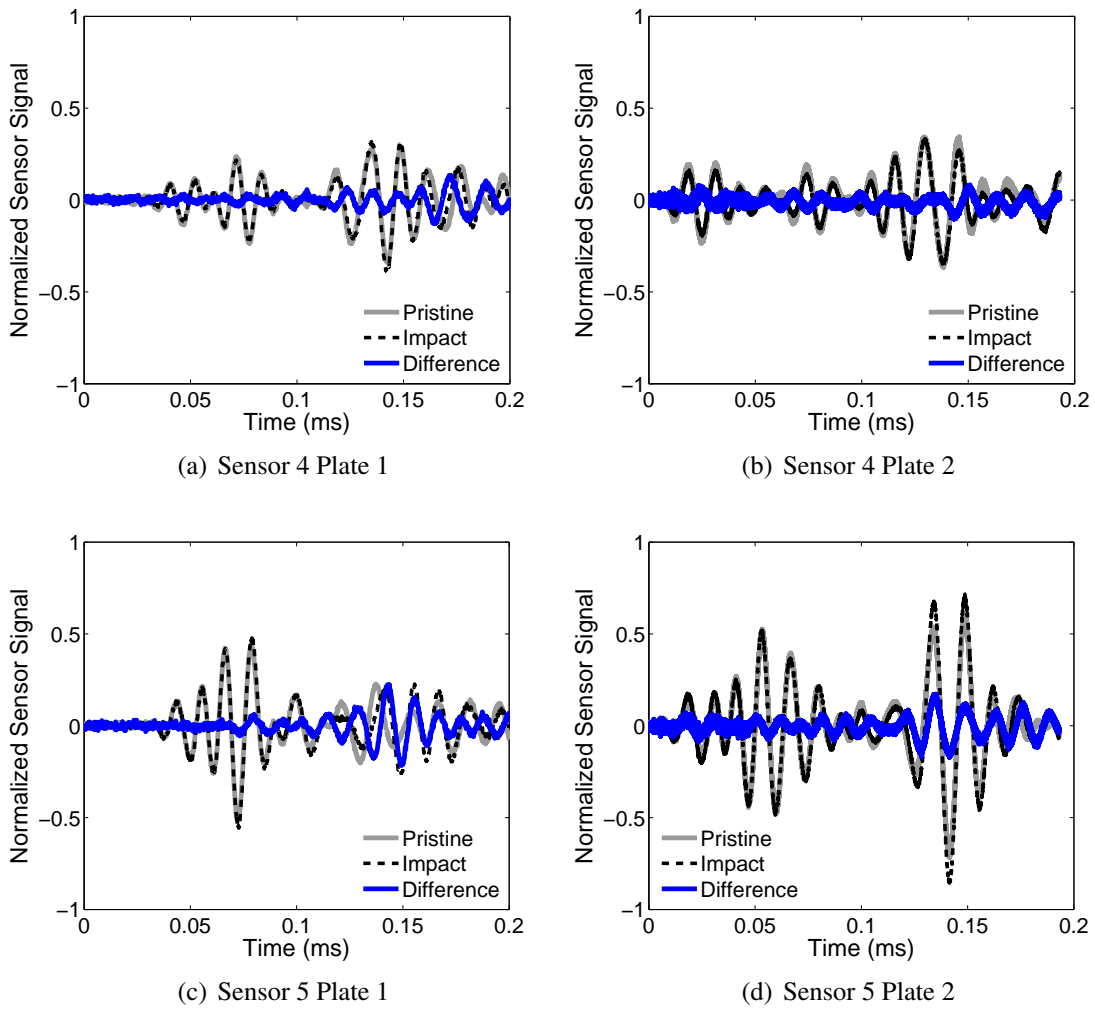


Figure 5.10: 5-J impact damage in cross-ply laminate: sensor signals at 0-degree damage location.

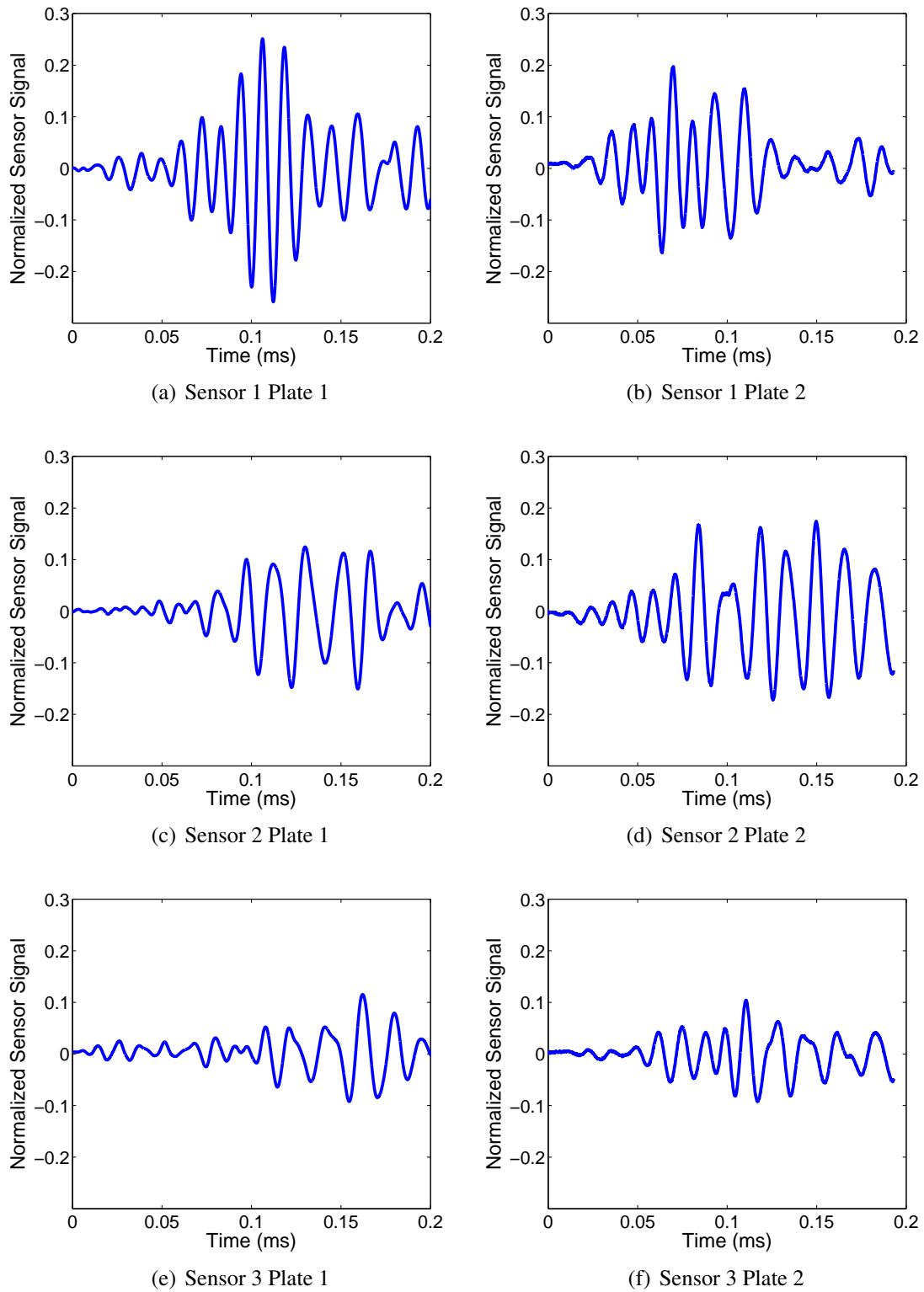


Figure 5.11: 5-J impact damage in cross-ply laminate: sensor difference signals at 0-degree damage location.

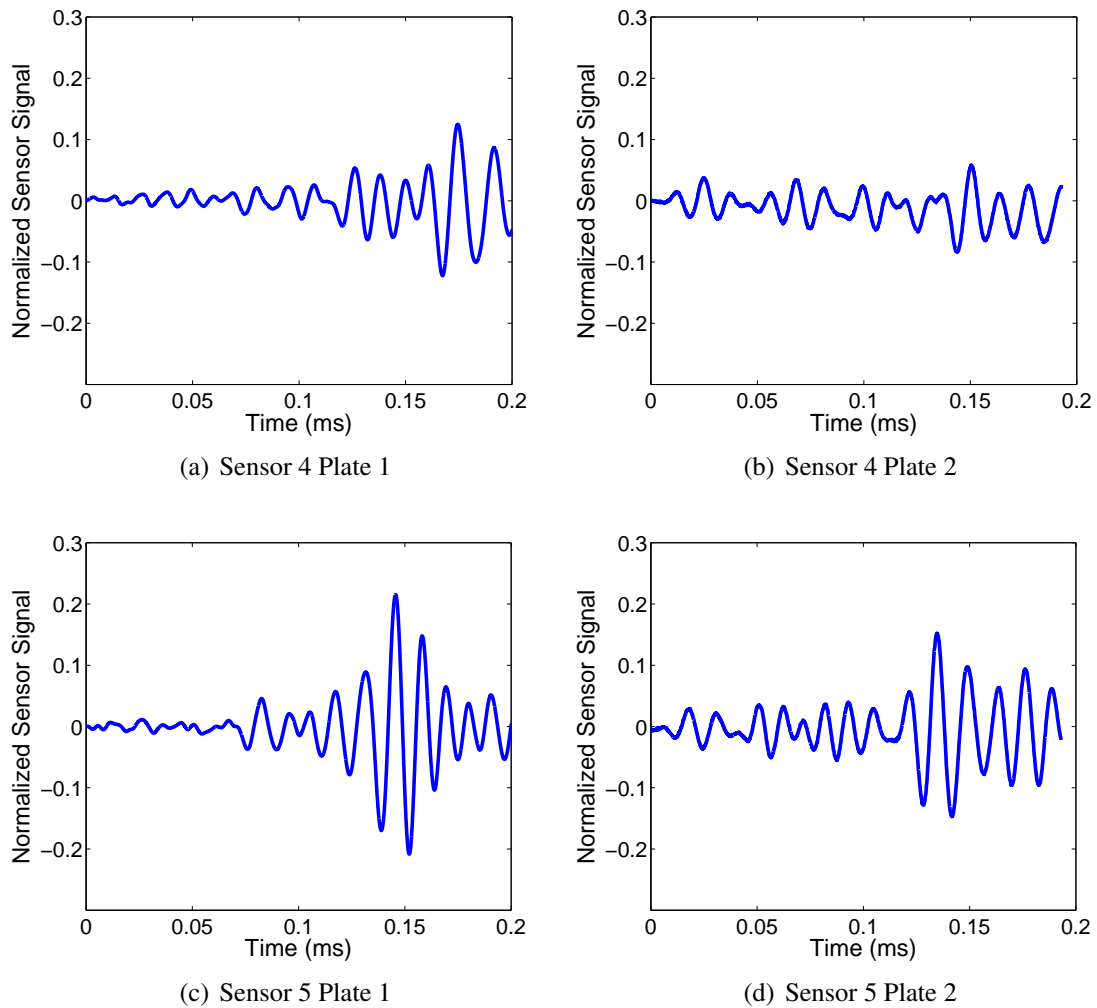


Figure 5.12: 5-J impact damage in cross-ply laminate: sensor difference signals at 0-degree damage location.

### **5.2.2 Sensor Results for 45-degree Damage Site**

The pristine, damage, and difference signal results for damage located at the 45-degree location are shown in Fig. 5.13. The results were normalized with respect to the maximum amplitude of the pristine signal at the sensor 1 location. The difference signals are also included for each sensor in Fig. 5.14. At this damage location, the maximum amplitudes of the difference signals obtained at sensors 1, 2, and 3 were relatively similar. The sensor 4 location recorded the smallest difference signals, while sensor 5 produced the largest difference signals.

### **5.2.3 Sensor Results for 90-degree Damage Site**

The sensor results for impact damage at the 90-degree site are shown in Figs. 5.15 and 5.16. Like the 0-degree results, the largest difference signal in the 90-degree case was recorded using sensor 1, which corresponded to the pulse-echo configuration. A large difference signal was also observed at sensor 5. Interestingly, sensor 4 observed a difference signal higher than that of sensors 2 and 3, unlike in the other damage cases. While it is possible this was an effect of the different fiber orientation, it seems more likely that the impact damage manifested itself differently in this case due to variability in the impact procedure. Future experiments should be conducted to see if this result is repeatable or if the sensor 4 result is lower in other trials as expected.



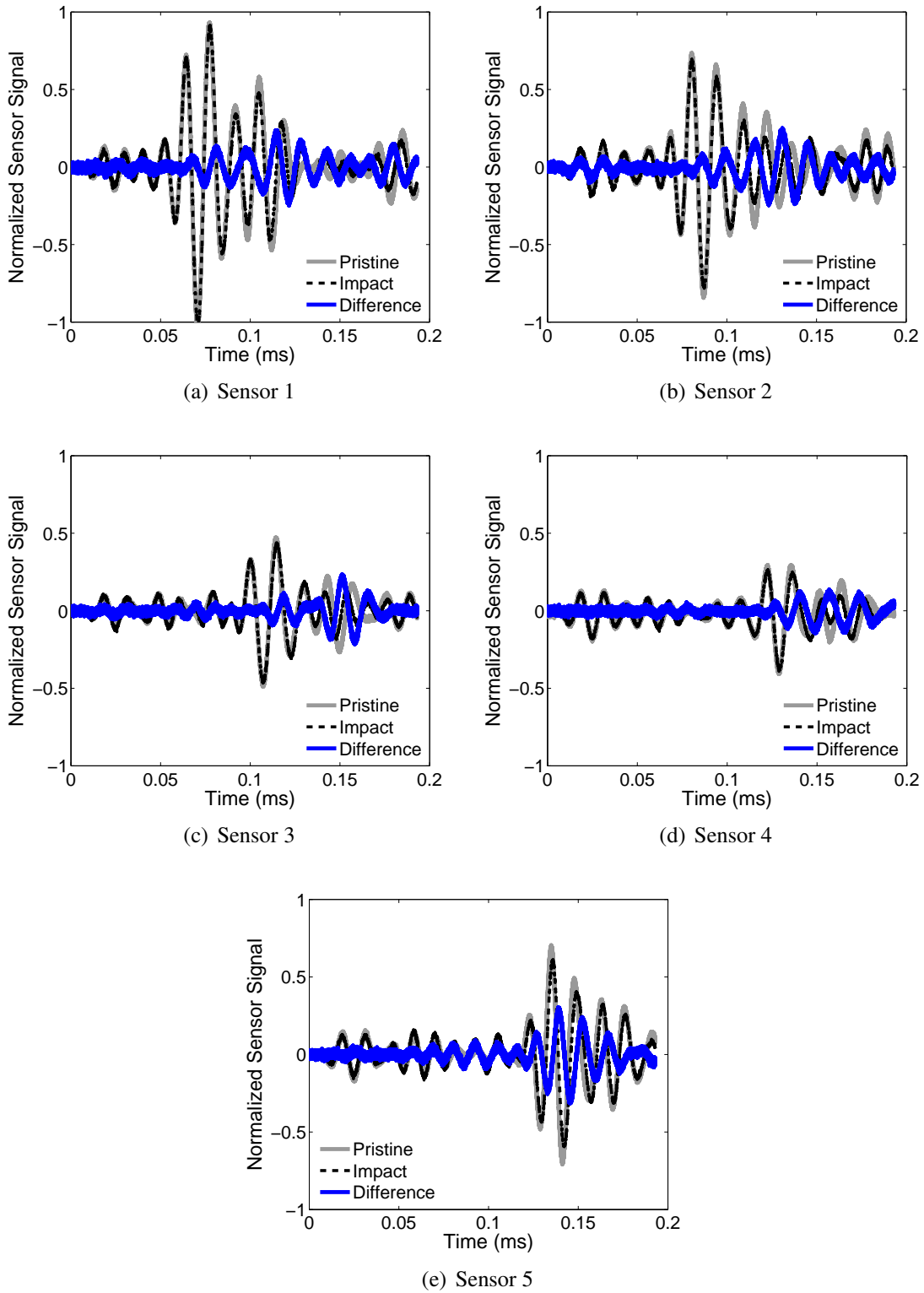


Figure 5.13: 5-J impact damage in cross-ply laminate: sensor signals at 45-degree damage location on plate 2.

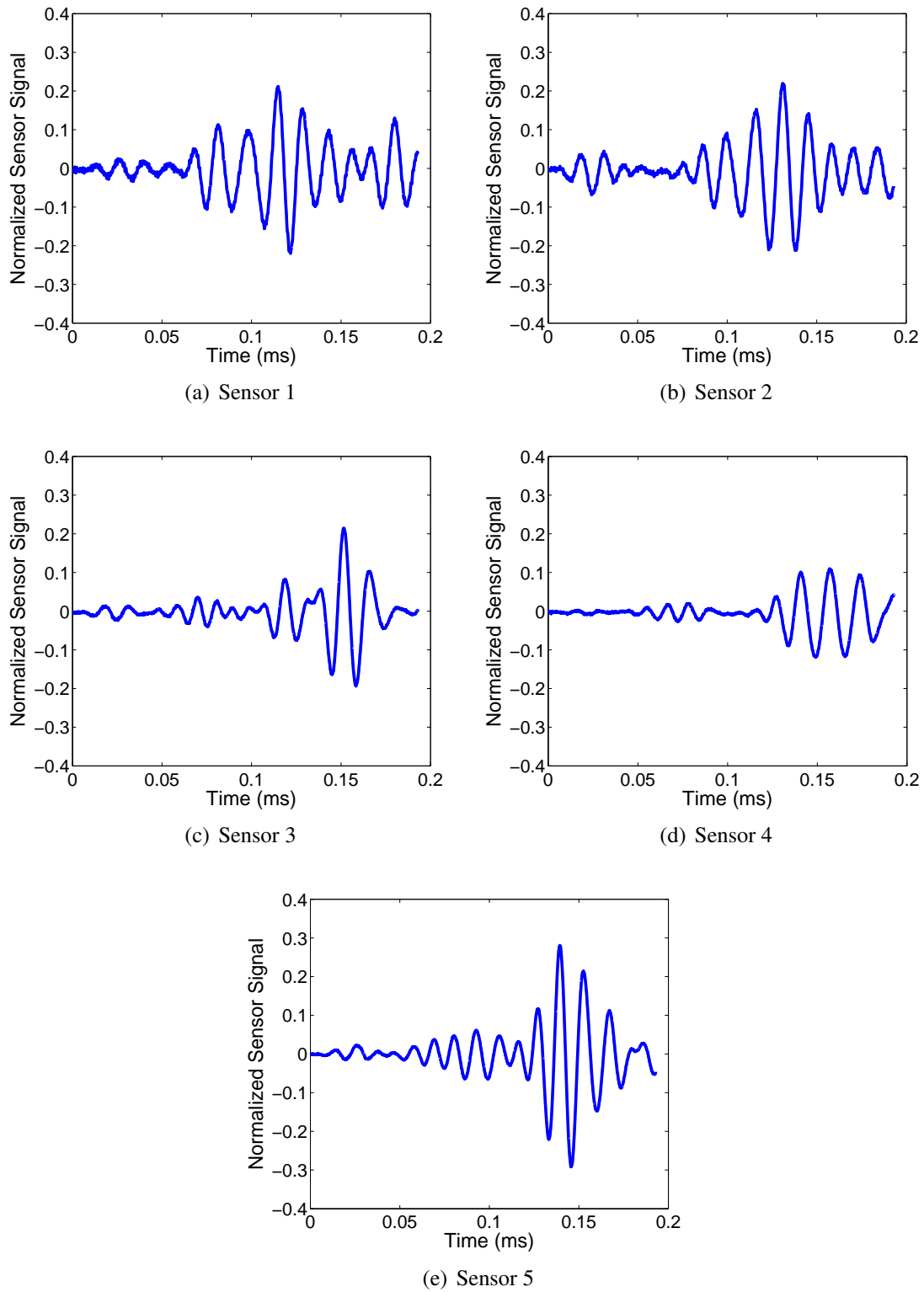


Figure 5.14: 5-J impact damage in cross-ply laminate: sensor difference signals at 45-degree damage location on plate 2.

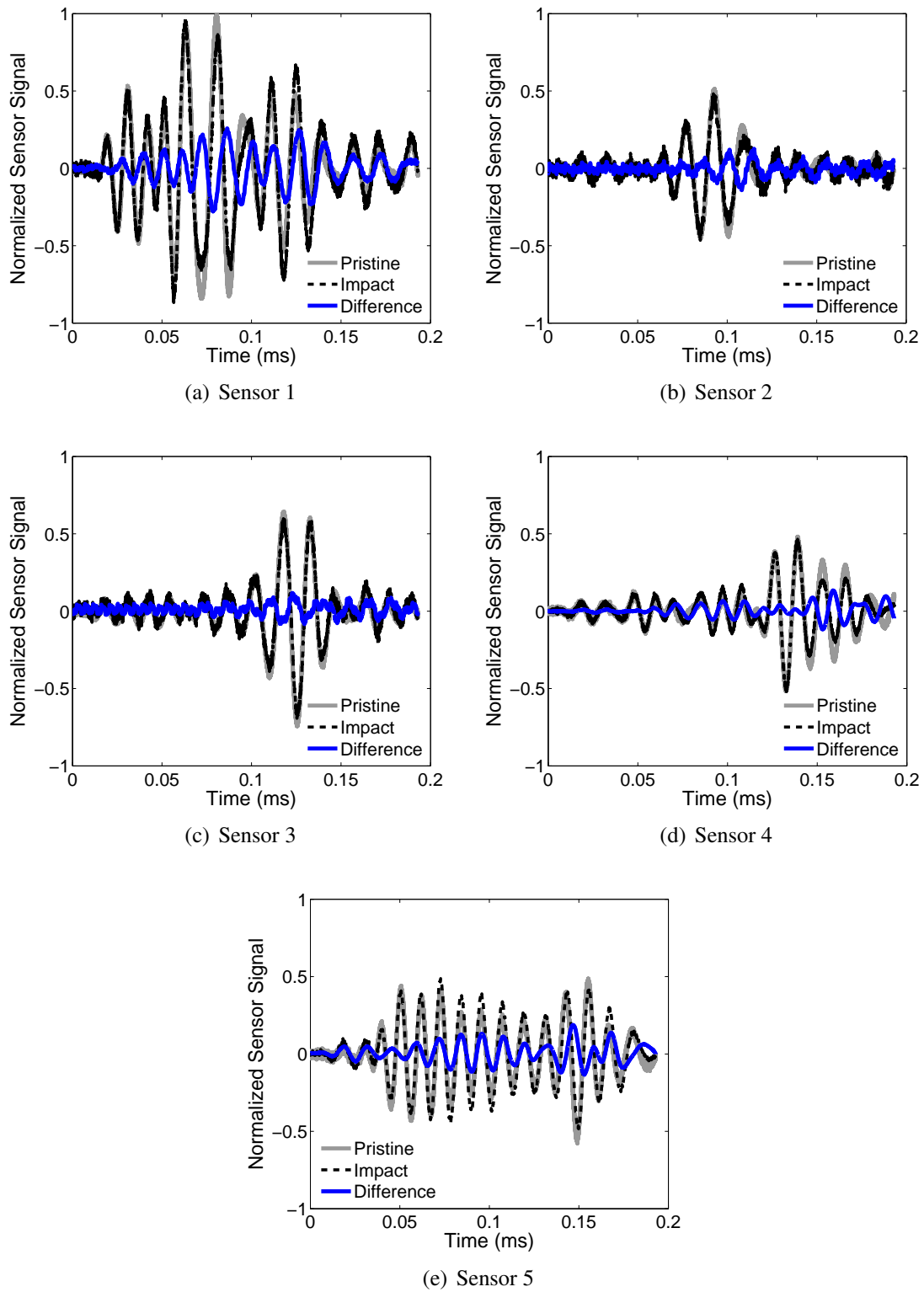


Figure 5.15: 5-J impact damage in cross-ply laminate: sensor signals at 90-degree damage location on plate 2.

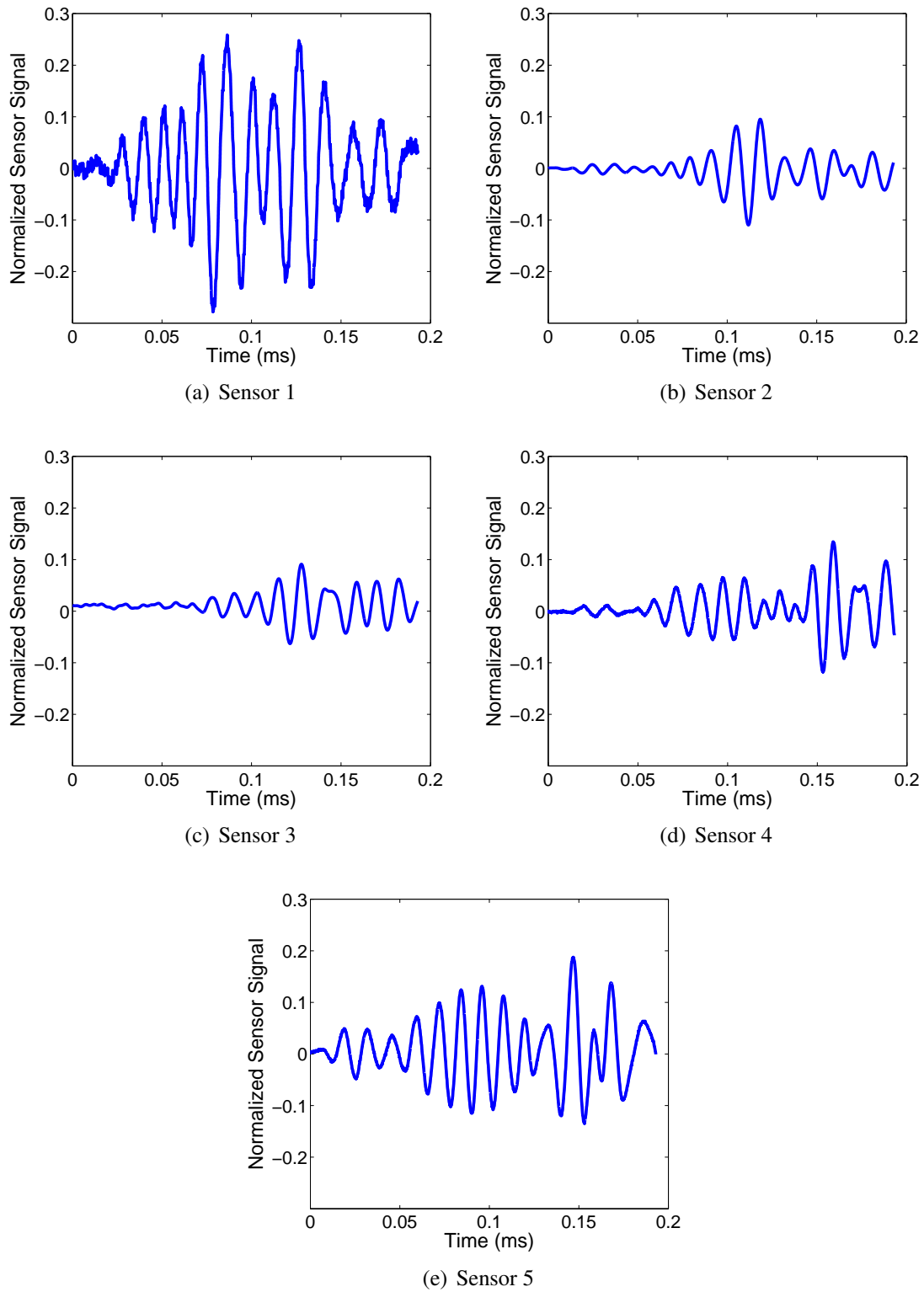


Figure 5.16: 5-J impact damage in cross-ply laminate: sensor difference signals at 90-degree damage location on plate 2.

## 5.2.4 Laser Vibrometry Results

The laser vibrometer was used to capture the out-of-plane behavior of the area surrounding each damage site. As with the sensor measurements, laser readings were taken both before and after the impact event to allow for a baseline subtraction technique to form a difference signal. From a practical standpoint, obtaining reliable laser vibrometer results was much more challenging than in the case of the PZT sensors.

During the 0-degree damage experiments, the plate was supported on two of its edges below the laser vibrometer, as previously shown in Fig. 2.14. For the first experiment, using plate 1, only one set of pristine data was taken before the impact, and one set of damage data was taken after the impact. Post-processing of the data revealed a much larger difference signal on the back side of the damage (0-degree direction) than what was expected after considering the sensor results. In the laser vibrometer experiment, the maximum amplitude of the difference signal was almost 40% of the pristine value in the 180-degree direction, while the maximum amplitude was only 25% in the plate 1 sensor experiment. While these values are not guaranteed to be equal, it was expected that they correlate better. For this reason, more care was taken during the 0-degree experiment on plate 2. For this plate, three sets of pristine data were taken. After each scan, the plate was moved and repositioned to align the scan points. Once all three pristine data sets were recorded, the plate was damaged with the 5-J impact. Three sets of damage data were collected in the same manner. After all the data were obtained, each of the three sets of pristine data was used with each of the three sets of damage data to obtain nine sets of difference signals for each scan point. The maximum values of the nine difference signals at each scan point were then averaged.

For the 45 and 90-degree experiments, the plate was hung from a wall-mounted fixture for the laser vibrometer measurements, as shown in Fig. 5.17. It was hypothesized that hanging the plate would allow for a more repeatable placement when the plate was moved between measurements. To further mitigate against alignment errors, four sets of measurements were taken both before and after the damage was applied. After each set of pristine

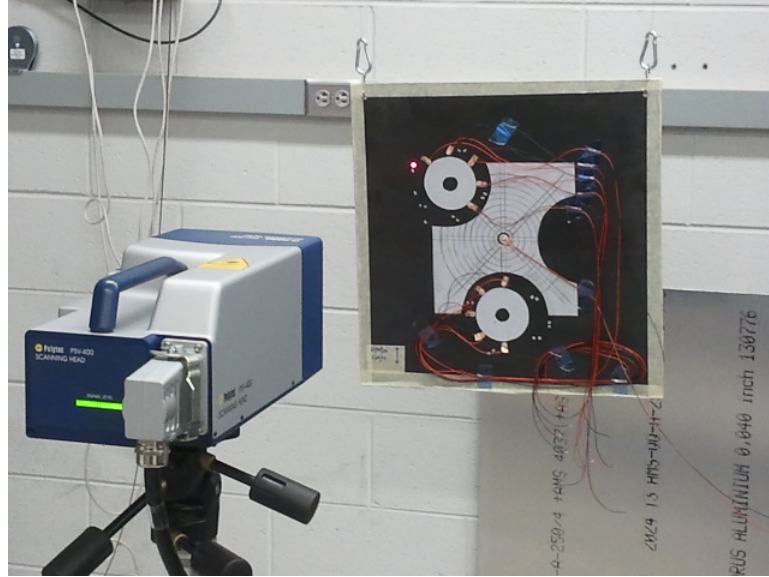
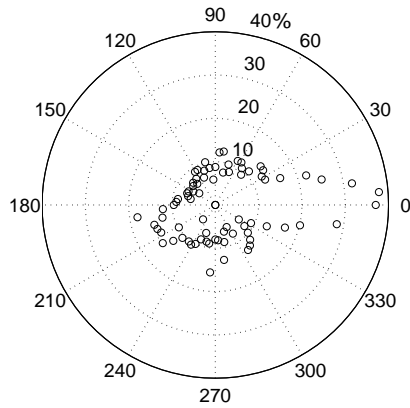


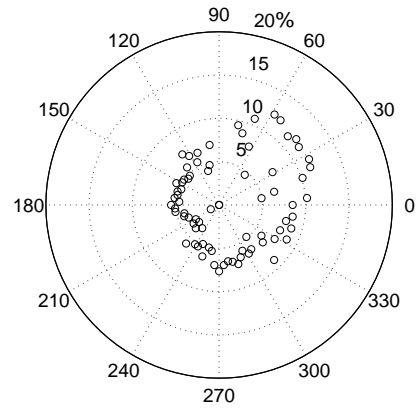
Figure 5.17: Hanging-plate setup used for laser vibrometer experiments during impact damage study.

data was taken, the plate was moved and then hung again. After the pristine data were recorded, the plate was damaged with the 5-J impact. The damaged data sets were then recorded, and the plate was repositioned in between each set. When the plate was returned to the hanging position after each scan, it was still difficult to ensure a perfect alignment of the laser scan points from before the impact. In a similar process to the 0-degree experiment, each of the four pristine data sets was used with each of the four damage data sets to produce 16 sets of difference signals. The maximum values of the 16 difference signals at each point were averaged to produce a final amplitude value at each point.

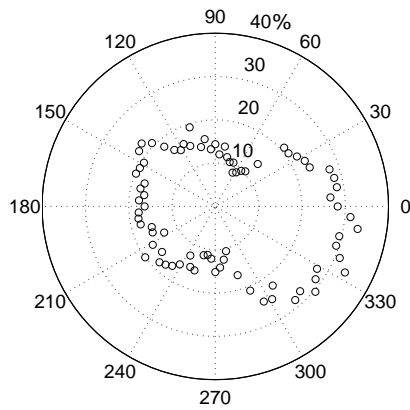
In each of the four experiments, the scan points were located along a circle 40 mm from the center of the damage site. Figure 5.18 shows the azimuthal variation of the difference signal for each damage site, where the average value of the maximum amplitude of the difference signal is plotted for each scan point location. In each plot, the 180-degree azimuth represents the direction back towards the actuator, while the 0-degree direction is on the back side of the damage. The data were normalized with respect to the maximum value of the pristine signal at the scan point located in the 180-degree direction. Several notable



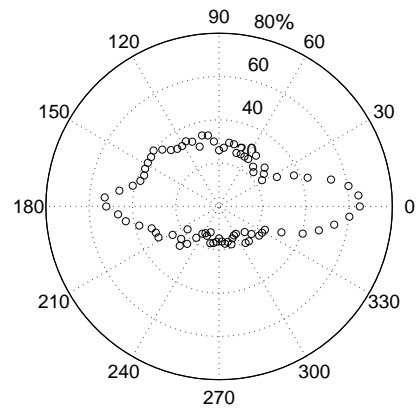
(a) 0-deg Plate 1



(b) 0-deg Plate 2



(c) 45-deg Plate 2



(d) 90-deg Plate 2

Figure 5.18: Azimuthal variation of out-of-plane difference signals from laser vibrometry experiments for the three impact damage sites. Results are normalized as a percentage of the pristine amplitude in the 180-degree direction with respect to each damage site.

results can be seen in the figures. Even though the sensor results for the two 0-degree experiments were reasonably close, the difference signal amplitudes recorded with the laser vibrometer varied widely between the two cases. The first experiment had a maximum difference signal of nearly 40% of the pristine amplitude, while in the second experiment the maximum amplitude was less than 15%. Another discrepancy between the two 0-degree experiments was the direction of the maximum difference signal amplitude. In the first experiment, the maximum amplitude was in the 0-degree direction, while in the second experiment the 45-degree direction had the largest signals.

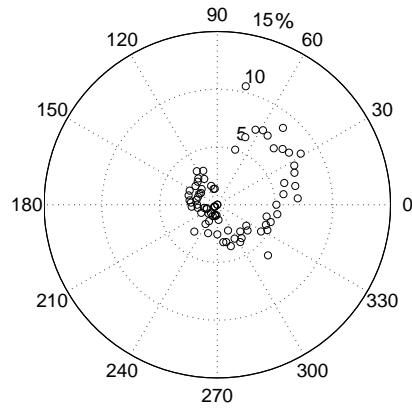
In the 45-degree experiment, the maximum difference signal was on the back side of the damage. A subtle steering effect was visible where increased amplitudes were seen in 45, 135, 225, and 315-degree directions relative to the direction of the incident wave. In general, the amplitude of the difference signals was consistent with those recorded in the sensor data.

One unexpected result was the magnitude of the difference signals in the 90-degree case. Whereas the sensor results predicted similar maximum amplitudes for the difference signals at the three damage sites, the 90-degree laser vibrometer results predicted amplitudes significantly larger than found in the other two damage sites.

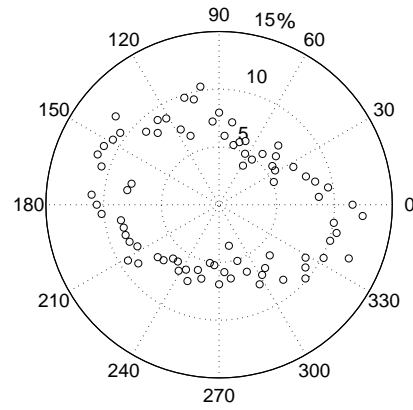
For the three experiments using plate 2 where multiple data sets were recorded, there was considerable variability between the calculated difference signals. Figure 5.19 shows how the standard deviation of the difference signal amplitudes varied with the azimuth of the scan point. The range of standard deviation values is included in Table 5.2. The amount of variation was itself highly dependent on the azimuthal position of the observation point. In general, the directions with the highest damage difference signals also had the highest variation in the difference signal.

Due to the variability of the laser vibrometry results, they were not used further in this chapter. They are included here for completeness and to show general trends only, and further studies should be carried out to determine more reliable procedures for data

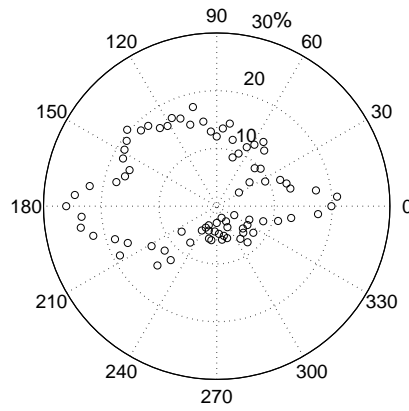




(a) 0-deg Plate 2



(b) 45-deg Plate 2



(c) 90-deg Plate 2

Figure 5.19: Azimuthal variation of the standard deviation of the out-of-plane difference signals from laser vibrometry experiments for the three impact damage sites. Results are normalized as a percentage of the pristine amplitude in the 180-degree direction with respect to each damage site.

Table 5.2: Comparison of standard deviation values for 5-J impact damage laser vibrometry experiments at 0, 45, and 90 degrees. SD values are reported as a percentage of the pristine signal amplitude in the respective cases' 0-degree azimuth.

Damage site	0 degrees	45 degrees	90 degrees
Max SD %	10.5	12.5	26.1
Min SD %	0	3.7	2.2
Average SD %	3.3	7.9	12.6

collection. Evaluations of numerical results in the remainder of the chapter were confined to sensor measurements where the experimental data were judged to be more reliable.

### 5.3 Simulation of Impact Damage

Compared to holes, modeling impact damage in composites is much more difficult. The levels of discretization in most numerical wave propagation models do not allow for small matrix cracks and delaminations to be modeled in detail. For this reason, most studies have used a homogenization approach, such as stiffness reduction, to account for the damaged region. In most of these studies, however, the basis for the choice of homogenized properties and the size of the modeled damage region have not been well justified. The objective of this section is to create a more data-driven impact damage model and to examine possible strategies for representing impact damage based on their effect on guided wave propagation.

The first task in modeling the damage was to define the size and shape of the damage region in both the in-plane and through-thickness directions. The impact damage model developed in this section is based on the 5-J impact case, and the diagnostic inspections included earlier in this chapter provided a sound starting point for defining the spatial extents of the model. It should be noted here that modeling different impact energies would require alteration of the dimensions used in this section. Figure 5.20 illustrates how the damage was represented in the through-thickness direction. Three damage regions were defined,

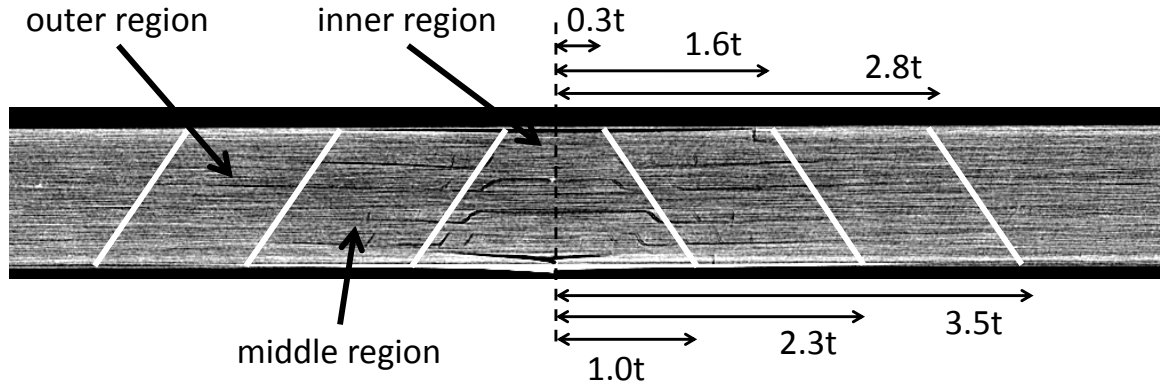


Figure 5.20: Side view of impact damage model for a cross-ply graphite-epoxy laminate subjected to 5-J impact.

with each region having increasing in-plane dimensions as the through-thickness distance from the impact site increases. The angle of the damage region was chosen to closely match the angle of the matrix cracking seen in the region below the impact site. The inner region below the impact site contains the majority of the damage visible in the diagnostic images. The middle and outer regions contain progressively less damage, but they still have some combination of delamination and matrix cracking. The in-plane dimensions of each of these regions are shown in Fig. 5.20, and the overall shape of each region is further explained using Fig. 5.21. The inner region can be understood as a square-shaped inverted pyramid. The choice of a square region for the inner region was largely defined by the dominant matrix cracks running along the fiber directions on the outer boundaries of the region. The middle and outer regions can be viewed as inverted cones. The squares and circles shown in the figure show the extents of each region for the top and bottom surfaces of the plate, and the through-thickness view is included to scale as a reference.

The next few sections describe various strategies for modeling the impact damage. Damage was modeled in the 0-degree direction in each case, unless otherwise specified. In each section, the primary method of comparing the models among themselves and comparing the models to experimental results is to examine the maximum amplitude of the sensor

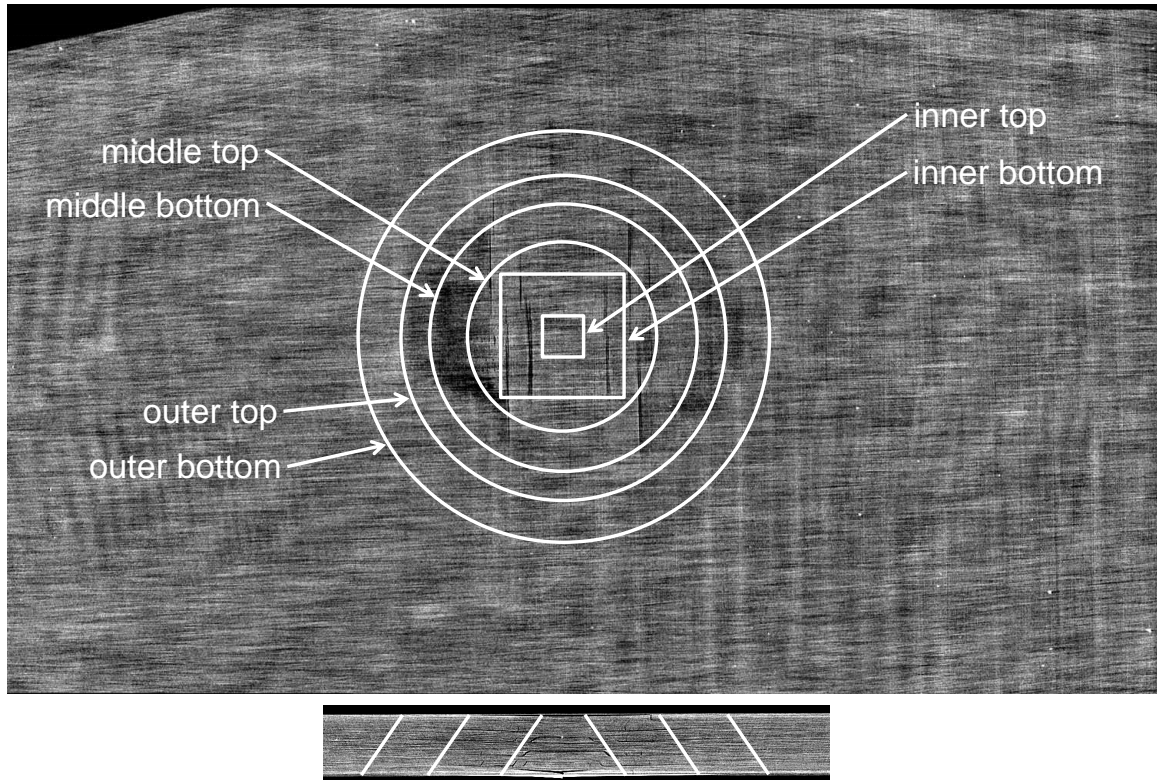


Figure 5.21: Comparison of top and side views of impact damage model for a cross-ply graphite-epoxy laminate subjected to 5-J impact.

difference signals, which have been normalized with respect to the maximum amplitude of the pristine signal at the sensor 1 location. In each figure, these values are plotted azimuthally based on the sensor location. For each sensor location, two experimental values from the two different 0-degree impact experiments are plotted.

Additionally, the maximum values of the out-of-plane difference signals from the simulations are plotted as a reference on each figure. The out-of-plane data correspond to points located 50 mm from the center of the damage region, and they were normalized with respect to the maximum amplitude of the pristine signal for the point in the 180-degree direction. In general, there is no guarantee that the out-of-plane difference signal amplitude, which is a velocity-based measurement, corresponds to the sensor difference signal amplitude, which is a strain-based measurement. However, the following figures will show a fairly

good correlation between the two amplitudes for the simulations. Because the out-of-plane difference signals were more easily calculated over the full azimuthal region surrounding the damage site, the out-of-plane data give a good idea of the overall shape of the scatter pattern in regions where sensors were not modeled.

### 5.3.1 Reduction of Stiffness Properties

The first set of simulations reduced each of the six elastic constants ( $E_{11}$ ,  $E_{22}$ ,  $E_{33}$ ,  $G_{12}$ ,  $G_{13}$ ,  $G_{23}$ ) in a specified region of the damage model. Results when the inner region elastic properties were reduced to a certain percentage of their original values are shown in Fig. 5.22. The sub-figures show the effect of reducing these properties to 30%, 20%, and 10% of the original values. As the stiffnesses were reduced, the amplitude of the difference signal from sensor 5 (0-degree direction) increased considerably, and it approached the values seen in the experiments. However, almost no reflection in the direction of the actuator was observed in any of the models, and sensor 1 (180-degree direction) amplitude remained far below the experimental values. Additionally, the amplitude of sensors 2 and 3 were considerably smaller than the experimental values.

A second and related set of models reduced the stiffness properties in both the inner and middle regions surrounding the damage site. The amount of reduction was the same for the two regions. The effects of these damage models on the guided wave propagation are shown in Fig. 5.23. Expanding the area in which the stiffness was reduced resulted in considerably higher difference signals for sensor 5. In fact, reducing the properties to less than 50% of the original values resulted in difference signals that exceeded those seen in both experiments. Although a 50% reduction in stiffness produced good results at sensors 4 and 5, the simulation did not produce high enough difference signals reflecting back toward the actuator.

At this point in the analysis, it would have been possible to reduce the outer region elastic properties along with the inner and middle region properties. However, it was likely

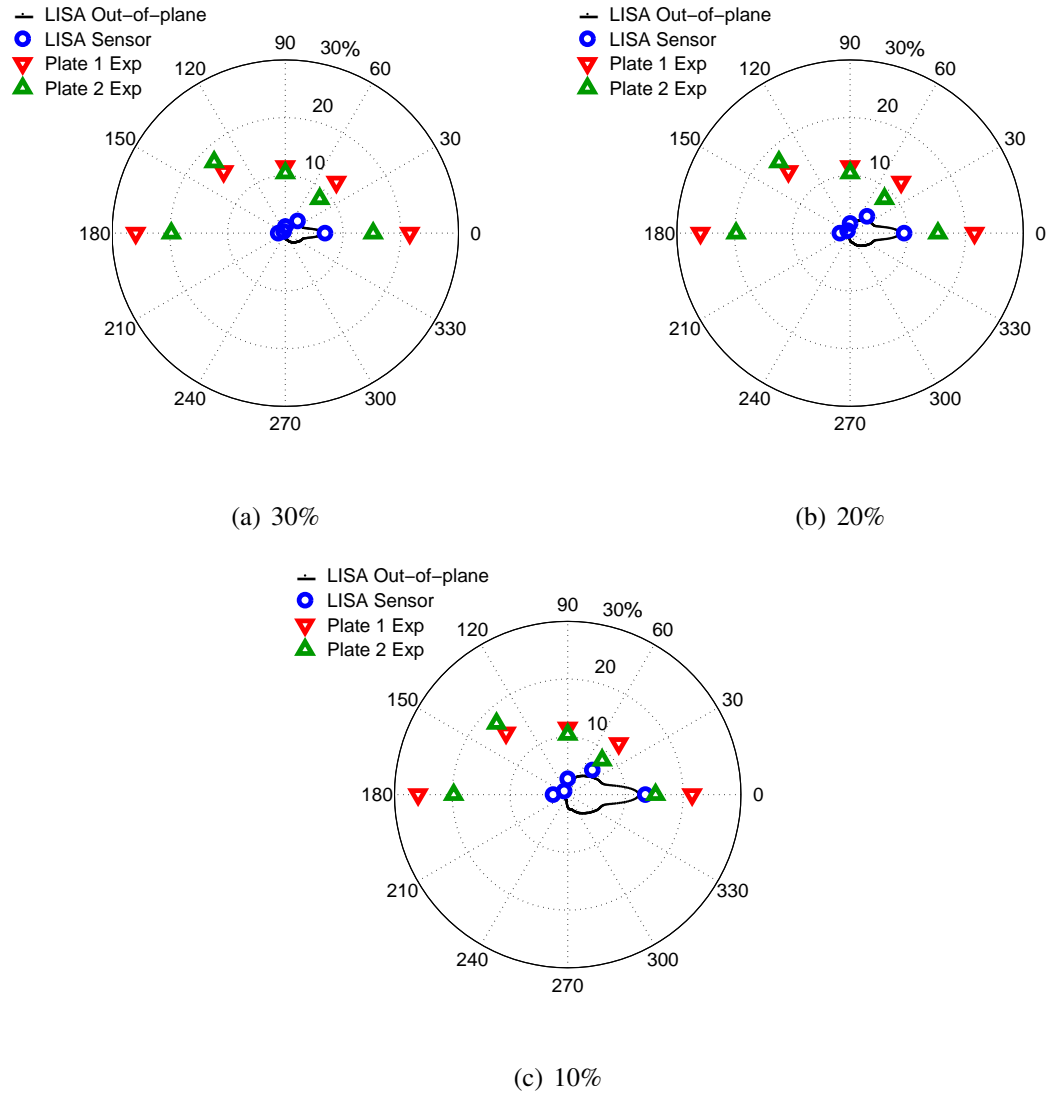


Figure 5.22: Effect of reducing inner region stiffness properties to given percentage of original values.

this would further increase the sensor 5 difference signals while still having little effect on the sensor 1 signals. Perturbations of the outer region properties are addressed later in this section, but the next step in this analysis focused on adjusting a different set of parameters.

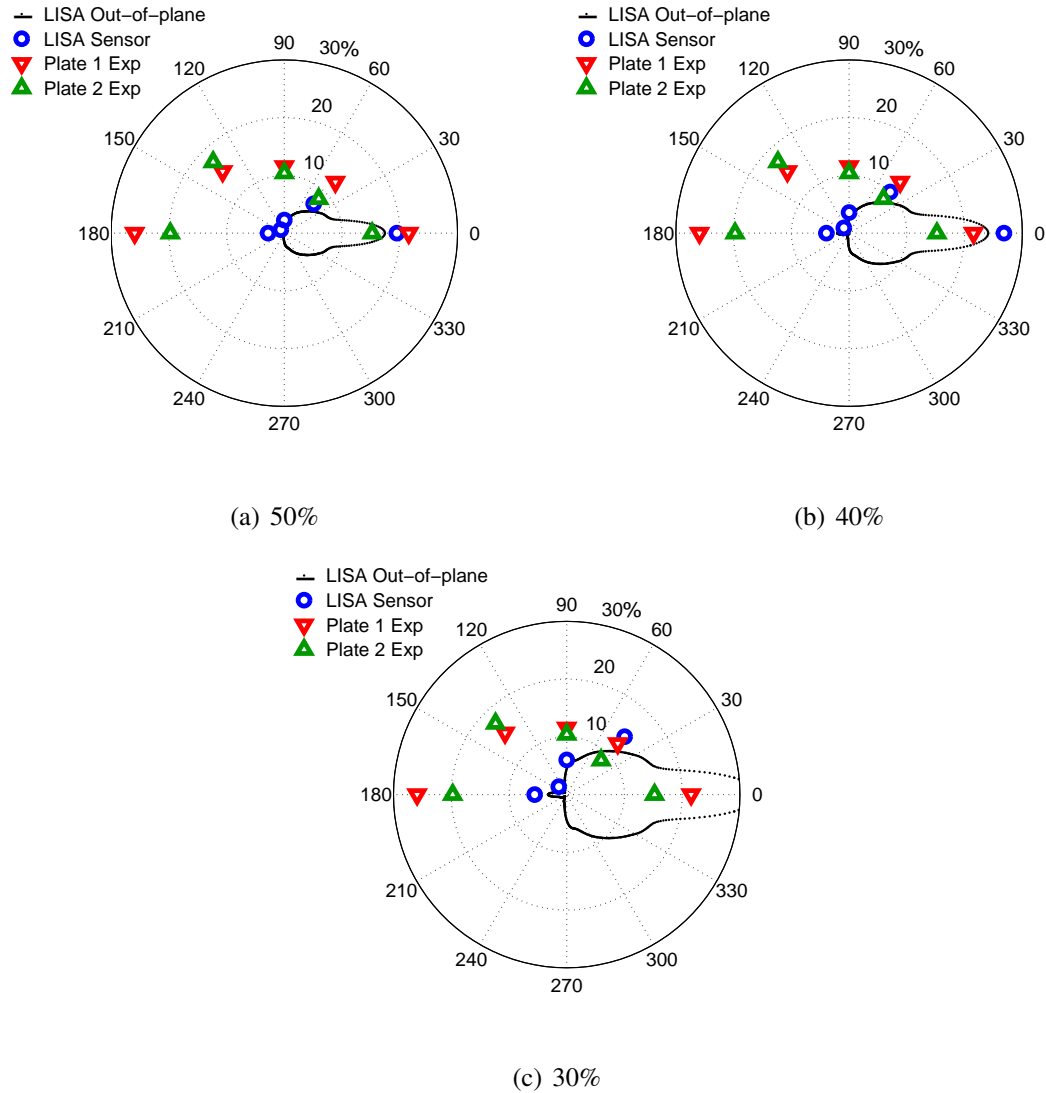


Figure 5.23: Effect of reducing inner and middle region stiffness properties to given percentage of original values.

### 5.3.2 Reduction of Stiffness and Density

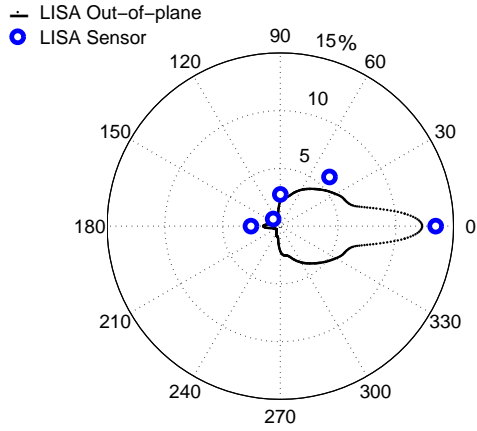
Because stiffness reductions alone did not capture the correct scatter pattern for the difference signal energy, the next sets of models considered the effect of reducing both the stiffness properties and the density of the damaged regions. This should not be taken as a statement that impact damage creates a density change in the actual plate. Rather, this technique is based on the knowledge that a density change, such as that found at the in-

terface between the material cells and air cells at the edge of a hole, can create a strong reflection. Considering the CT scan images previously presented, it is very likely that each of the matrix cracks presents an interface that reflects energy back toward the direction of an incident wave. In aggregate, the matrix cracks present in the damaged area create a reflection similar to that of a hole. The attempt in this section was thus to create a model that simulated the same effects as the impact damage site, even if a density change was not strictly justifiable on physical grounds.

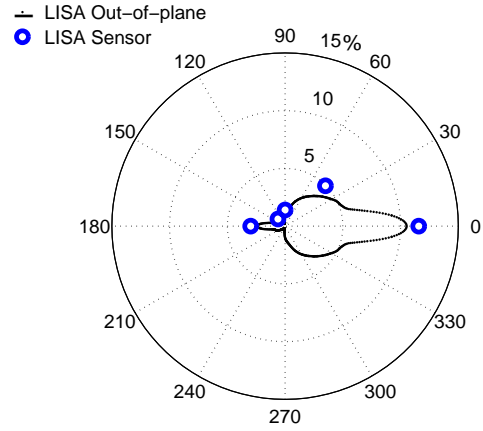
First, the inner region stiffnesses were reduced to 10% of the original values and the density of the inner region was reduced to a percentage of its original value. Figure 5.24 shows the simulation data for these cases. As the density was reduced in the inner region, the amplitude of the difference signal on the back side of the damage gradually reduced, but the signal on the front side of the damage increased. Additionally, more difference signal energy was seen in the transverse (90-270 degree) fiber direction with larger density reductions. While none of the models captured the correct difference signal magnitudes, a better combination of front and back side energy scattering was produced.

The next set of models started with both the stiffness and density properties reduced to 10% of their original values in the inner region of the model, and the stiffness properties of the middle region were then reduced. The results shown in Fig. 5.25 show that the difference signal reflected back to sensor 1 increased from around 5% of the pristine signal value to nearly 10% as the stiffness values in the middle region were reduced from 100% to 50% of their original values. In contrast, the difference signal on the back side of the damage site at sensor 5 increased from around 5% to just over 20% of the pristine value. The amplitude of the difference signal in the transverse fiber direction, captured by sensor 3, did not change significantly for this set of models. In the final model of the set of simulations, shown in sub-figure (f), the sensor 4 and 5 values correspond well with the actual values. The amplitudes of the other sensor signals were still not large enough, but they were an improvement over the previous cases.

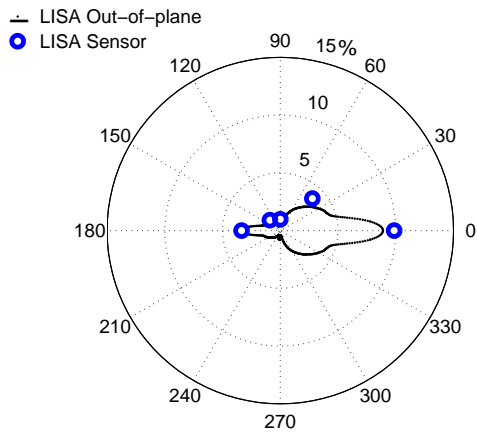




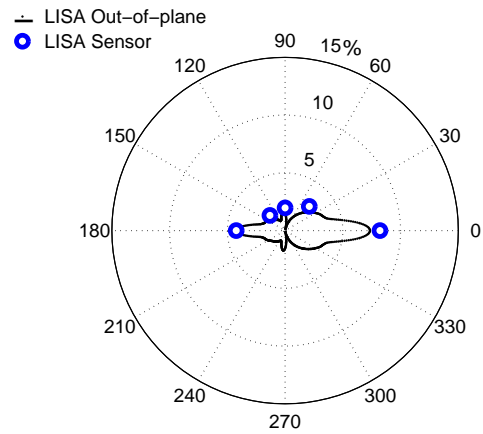
(a) 100%



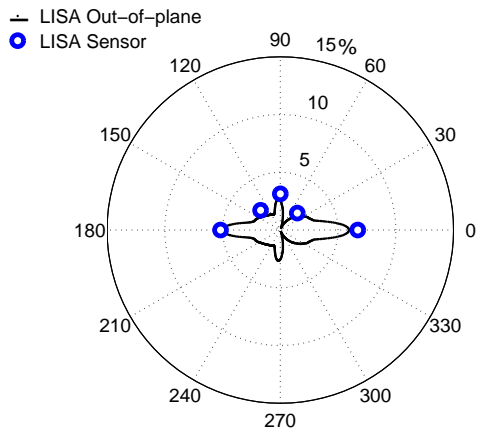
(b) 80%



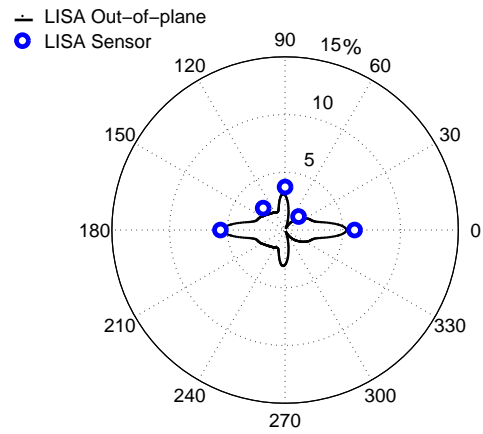
(c) 60%



(d) 40%



(e) 20%



(f) 10%

Figure 5.24: Effect of reducing inner region density to given percentage of original value. Inner region stiffness values are set to 10% of original values.

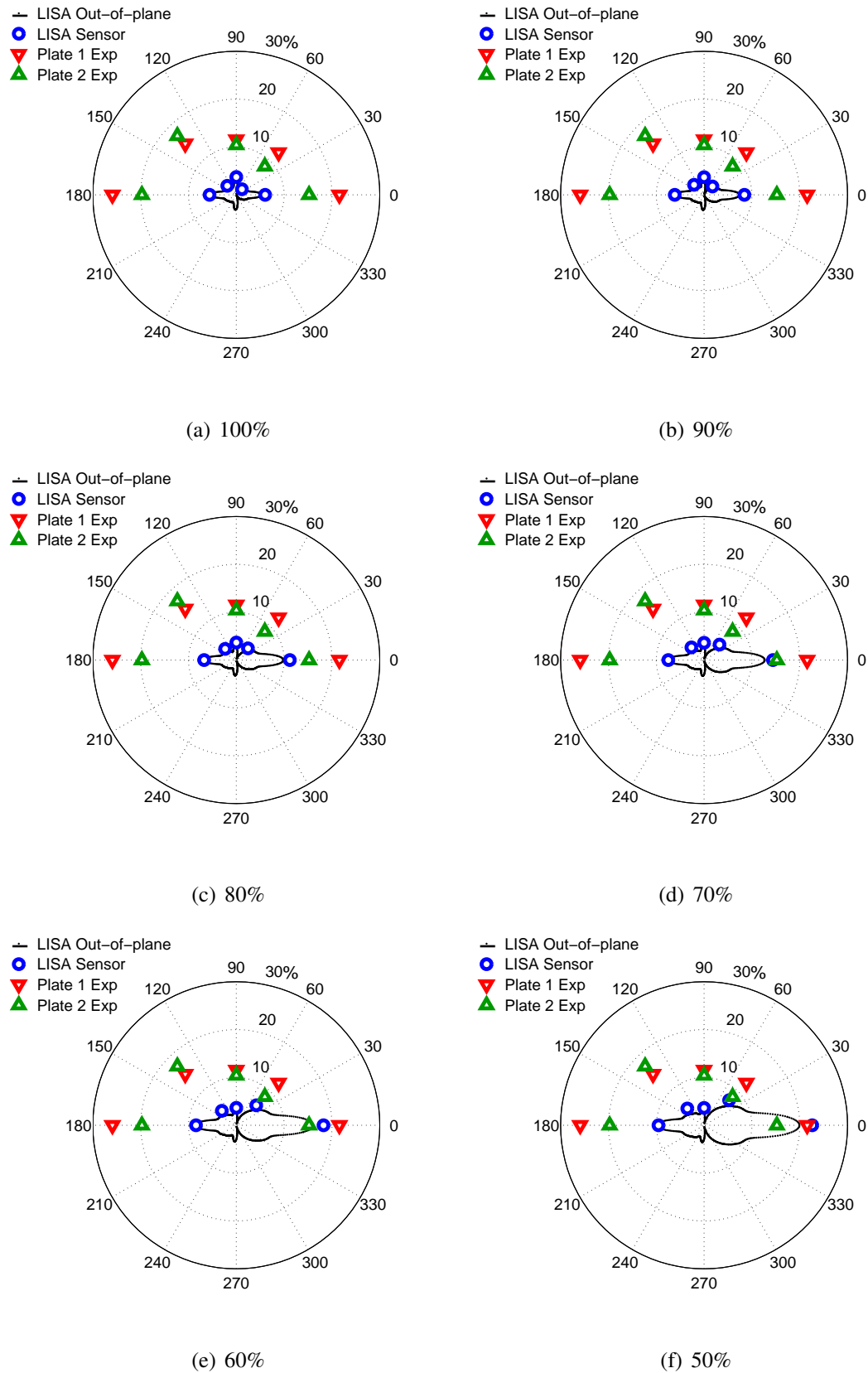


Figure 5.25: Effect of reducing middle region stiffness to given percentage of original value. Inner region stiffness and density values are set to 10% of original values.

The effect of an outer region stiffness reduction was examined next. From the diagnostic images, it was apparent that any damage in this region was considerably lower in severity than in the interior regions, so only small stiffness reductions were considered. Both the inner stiffness and density were reduced to 10%, and the middle stiffness values were reduced to 50%. Figure 5.26 shows results for the cases where the outer stiffness values were set to 100%, 90%, and 80% of the original values. For the sensor 5 location, even small reductions in outer region stiffness had large effects on the difference signal amplitudes. The effect on the other sensors was minimal.

The final parameter to be examined was the value of the density in the middle region. The starting point for these simulations was the final simulation from the previous set, where the outer region stiffness values were reduced to 80% of the original values. In Fig. 5.27, a few noticeable trends are present. As the middle density is reduced, the difference signal energy seems to shift where the sensor 5 amplitude decreases and the sensor 3 amplitude increases. The amplitude found at sensor 1 also increased, but not to the same degree as sensor 3.

In order to better understand the influence of each of the parameters considered in these simulations, a sensitivity study was conducted next where each parameter was individually changed. The baseline case was set to a model where the inner, middle, and outer stiffness properties were reduced to 20%, 50%, and 80% of the original values, respectively. The inner, middle, and outer density values were set to 90%, 60%, and 20% of the original value, respectively. Separate models were then run where each parameter was perturbed by 10% on either side of the baseline value. In addition to the density and stiffness values, the dimensions of the damage regions were also varied. The four dimensional parameters that were changed were the radius of the inner region of the top surface, the radius of the inner region at the bottom surface, the radius of the middle region at all through-thickness locations, and the radius of the outer region at all through-thickness locations. The baseline values for the radius of the inner region at the top and bottom surfaces of the plate were

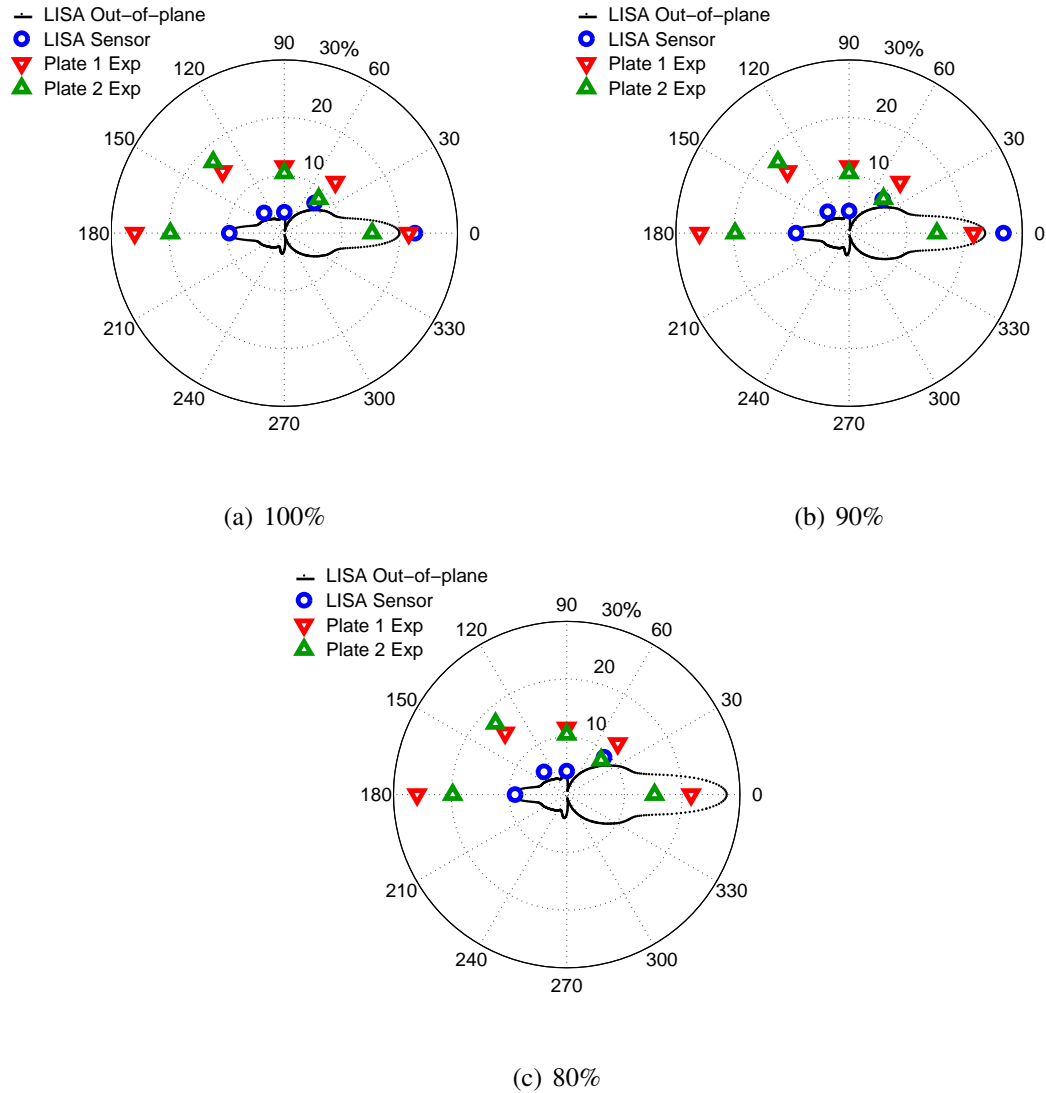
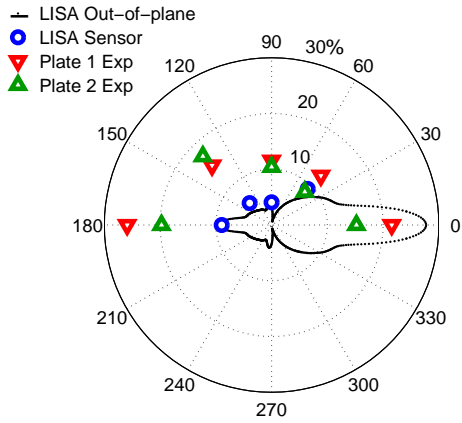
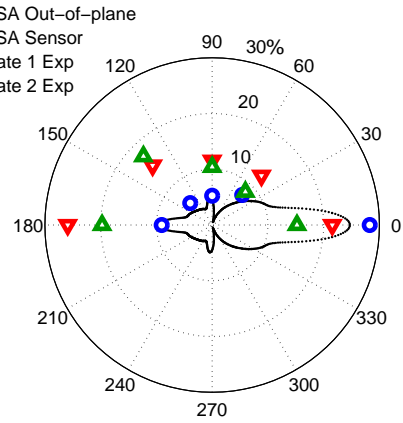


Figure 5.26: Effect of reducing outer region stiffness to given percentage of original value. Inner region stiffness and density values are set to 10% of original values. Middle region stiffness values are set to 50% of original values.

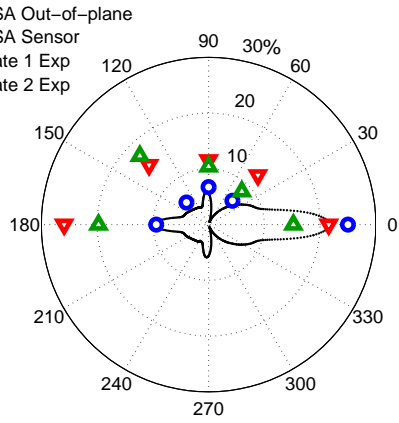
0.3 $t$  and 1.0 $t$ , respectively. The baseline value for the radius of the middle region was set to be 1.3 $t$  greater than the radius of the inner region at each through-thickness location. The baseline value of the radius of the outer region was set to be 2.5 $t$  greater than the radius of the inner region at each through-thickness location.



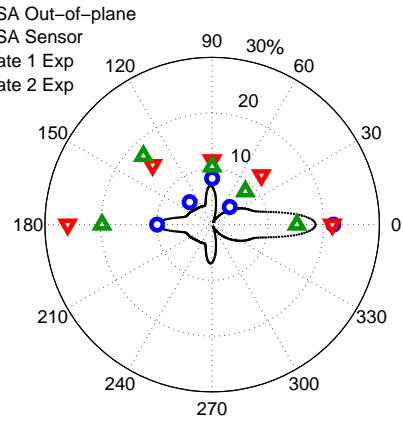
(a) 100%



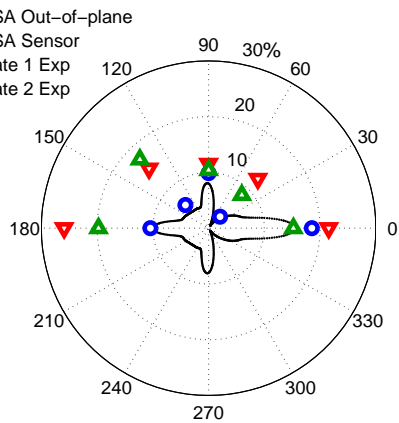
(b) 90%



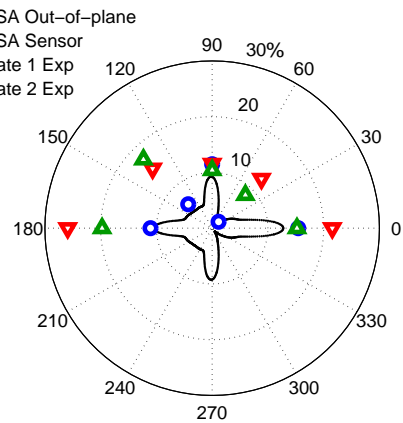
(c) 80%



(d) 70%



(e) 60%



(f) 50%

Figure 5.27: Effect of reducing middle region density to given percentage of original value. Inner region stiffness and density values are set to 10% of original values. Middle region stiffness values are set to 50% of original values. Outer region stiffness values are set to 80% of original values.

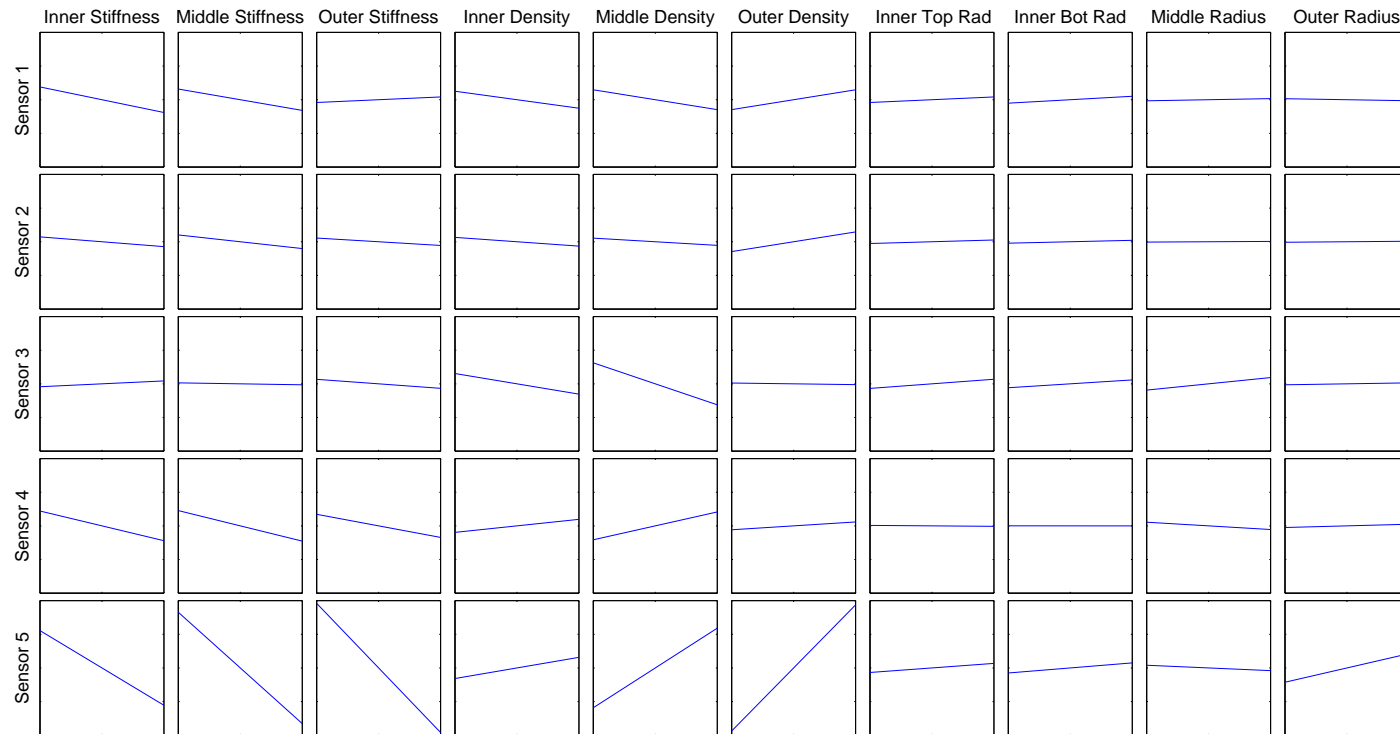


Figure 5.28: Results of impact damage model sensitivity study. Each block represents a parameter change of 10% on either side of the baseline value. Blocks with a negative slope show an increase in the difference signal when the given property is reduced in value.

Figure 5.28 shows the results of the study in graphical form. Moving from left to right along the x-axis of each block represents a 20% increase in the value of the applicable parameter. The y-axis shows the effect of that increase on the value of the maximum difference signal amplitude for a given sensor. For example, the block on the top left corner of the figure shows that an increase in the value of the stiffness in the inner region decreases the value of the sensor 1 difference signal, while a stiffness reduction increases the difference signal amplitude.

It should be noted that when a particular parameter was varied more than 10% on each side of the baseline value, the value of the difference signal amplitudes did not change linearly. The trends in this sensitivity study thus should only be applied to small perturbations away from the baseline case.

Using the information gained in the sensitivity study and in the previous models, numerous simulations were run to capture the effects of possible combinations of parameter changes. Figure 5.29 shows the results from the simulations that best matched the experimental results. To quantify the effectiveness of the simulations, a metric was calculated for each that took the average value of the difference between the simulated sensor amplitude and the average amplitude of the experimental sensor reading. The numerical results are included in Table 5.3.

Table 5.3: Selected impact damage simulation models in LISA (stiffness and density reductions). Error is measured as the average value of the difference between the simulated and experimental difference signal amplitude for the five sensors, measured as a percentage of the pristine signal at sensor 1. Baseline dimensions were used in all models.

Model	Stiffness %			Density %			Error %
	Outer	Middle	Inner	Outer	Middle	Inner	
1	100	30	10	100	50	10	5.3
2	90	40	10	100	60	10	5.9
3	100	40	10	100	70	10	6.3
4	80	50	10	100	60	10	6.3

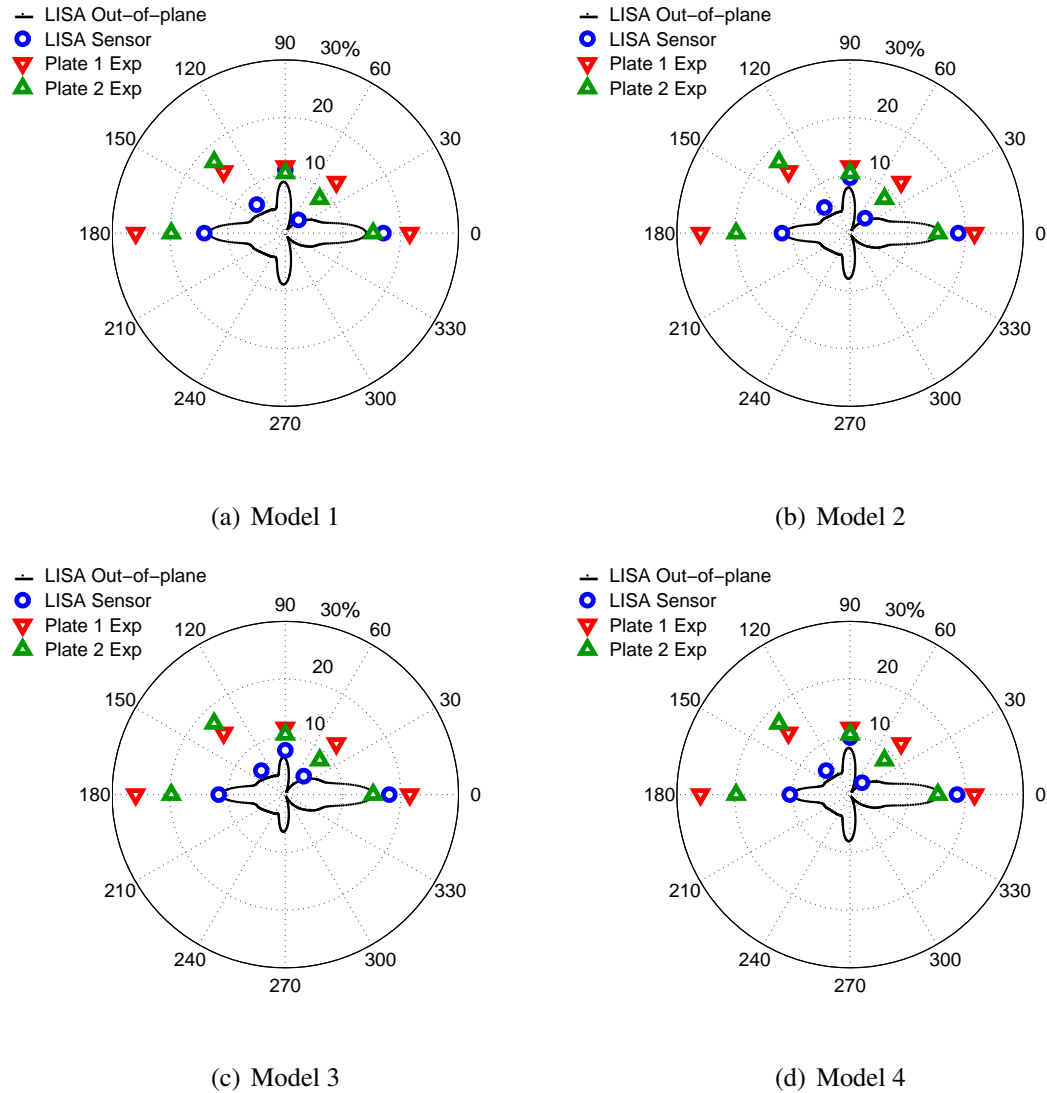


Figure 5.29: Best matching impact damage models using stiffness and density reductions.

### 5.3.3 Simulated Delamination with Stiffness and Density Reductions

The final group of simulations added an additional feature to the impact damage model. In the diagnostic imagery, a large delamination was visible between the bottom two lamina that spanned most, if not all, of the inner and middle regions of the damaged area. This delamination was simulated here as a void region in the thickness range of the second lamina from the bottom. The void spanned both the inner and middle damage regions, and



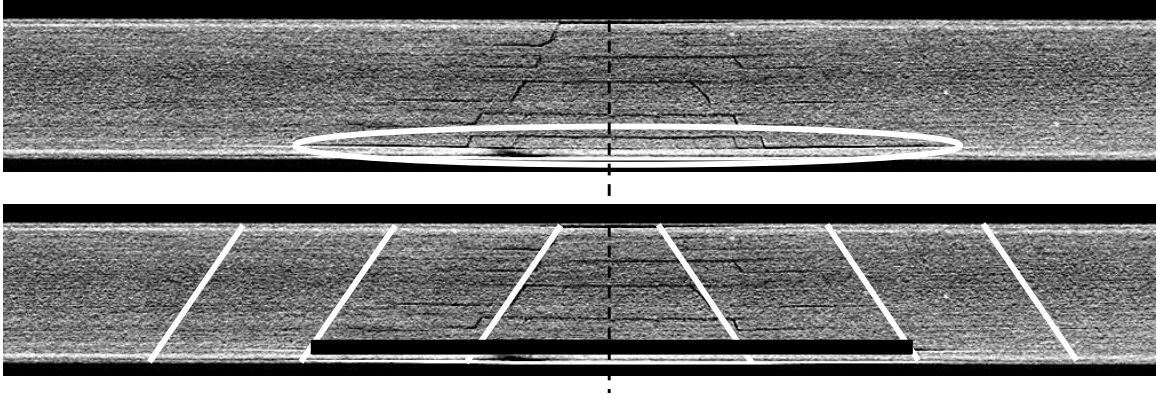


Figure 5.30: Side view of impact damage model with simulated delamination. The large delamination between the bottom two layers is circled in the top image. The location of the void region in the model is indicated by the black rectangle.

simulated air properties were used which were identical to those used at the plate boundary.

A schematic of the impact region with the simulated delamination is shown in Fig. 5.30.

This void region was added to the models previously summarized in Table 5.3. The results for these models are shown in Fig 5.31, and a numerical summary of the results is presented in Table 5.4. The addition of the simulated delamination improved the quality of the previous simulations in each of the cases, as indicated by a reduction of the error metric

Table 5.4: Selected impact damage simulation models in LISA (stiffness and density reductions with simulated delamination). Error is measured as the average value of the difference between the simulated and experimental difference signal amplitude for the five sensors, measured as a percentage of the pristine signal at sensor 1. Baseline dimensions were used in all models.

Model	Stiffness %			Density %			Error %
	Outer	Middle	Inner	Outer	Middle	Inner	
1	100	30	10	100	50	10	4.3
2	90	40	10	100	60	10	5.1
3	100	40	10	100	70	10	5.3
4	80	50	10	100	60	10	5.5

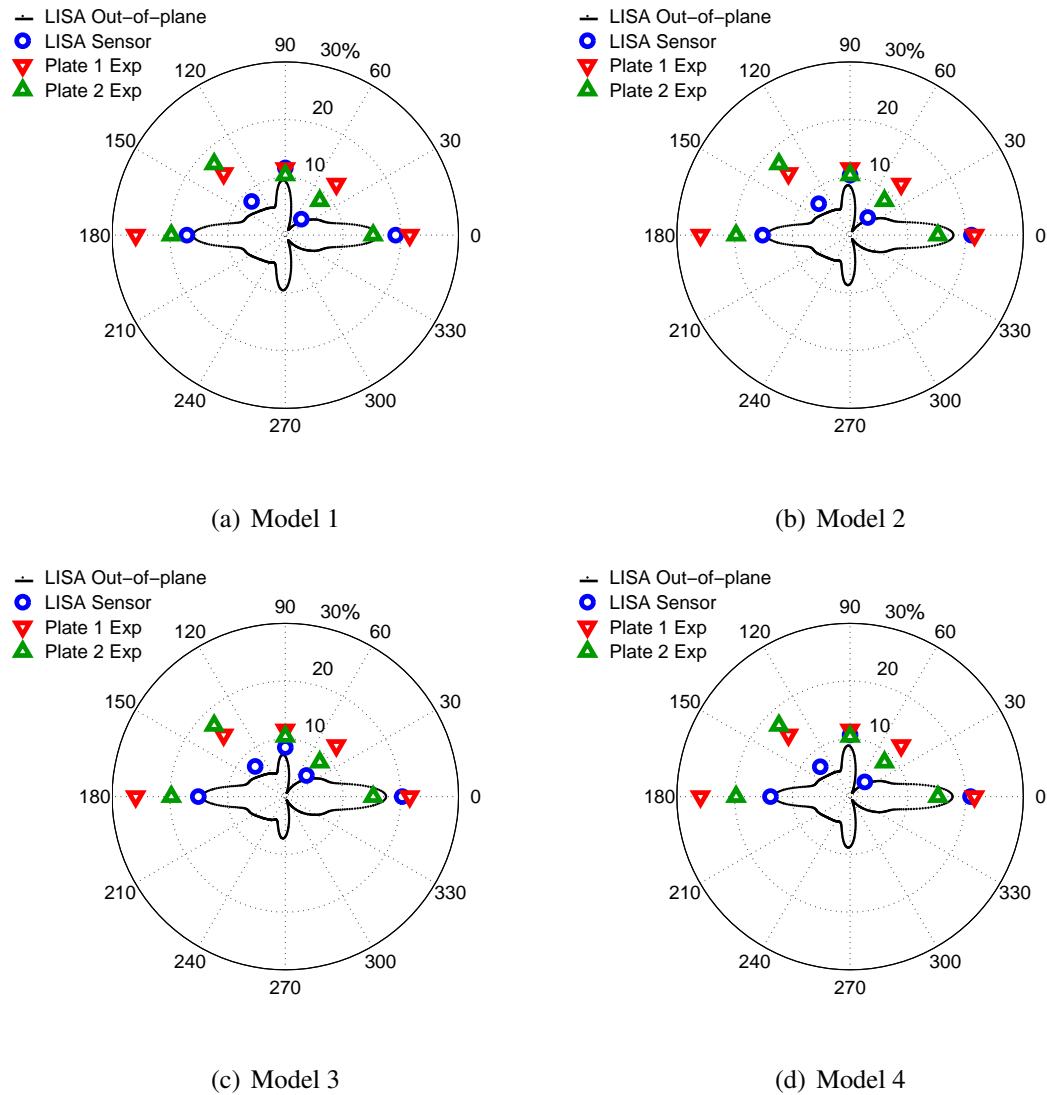


Figure 5.31: Best matching impact damage models using simulated delamination along with stiffness and density reductions.

previously introduced for the models. For selected Model 1, for example, the average sensor error reduced from 5.3% to 4.3% of the pristine signal at sensor 1.

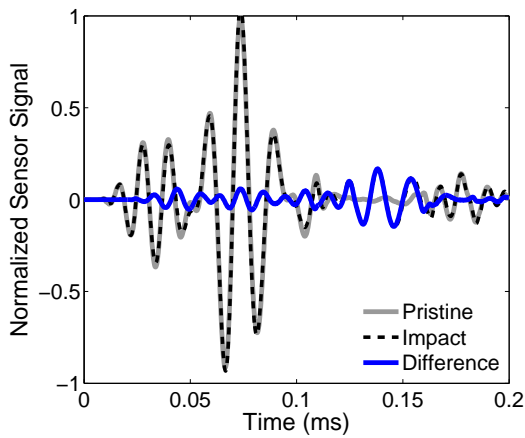
### 5.3.4 Analysis of Simulation Results for Impact Damage Located at 0-degrees

The combination of simulated delamination and property reduction summarized as Model 1 in Table 5.4 was selected as the most successful model. A numerical comparison of the sensor results for this model is included in Table 5.5. For each sensor, the maximum amplitude of the difference signal from the simulation is shown with the average value of the sensor signal from the two 0-degree experiments. The bottom row shows the difference between the two results for each sensor. Sensors 3 and 5 matched the best, with errors less than 1% of the value of the pristine sensor 1 signal. The model was least successful matching the amplitude of sensor 2, with an error of 8.1%.

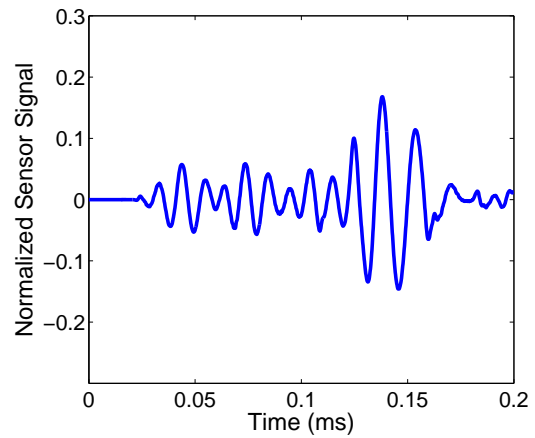
To better understand the performance of the model and the sources of some of the errors, further comparison of the simulated and experimental time histories was conducted next. Figure 5.32 shows a comparison of the signals from sensor 1. In general, there was good agreement between the pristine signals from the simulation and the two experiments. The simulation and both experimental signals showed the passage of the initial  $S_0$  mode starting at 0.01 ms followed by the larger  $A_0$  mode starting at 0.05 ms. The sub-figures on the right side compare the damage difference signals between the simulation and the experiments. These signals show that even though the best impact model was able to come close to predicting the correct maximum amplitude, it still did not capture all of the features of the

Table 5.5: Comparison of selected LISA impact model with average experimental results for damage at 0-degree location. The maximum difference signal amplitude is shown as a percentage of the pristine signal at sensor 1.

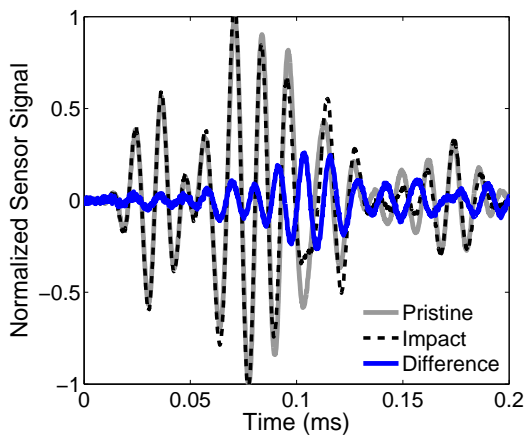
	Sensor				
	S1	S2	S3	S4	S5
LISA %	17.1	8.2	11.6	3.9	19.2
Experiment %	22.8	16.3	11.0	10.5	18.4
Difference	5.7	8.1	0.6	6.6	0.8



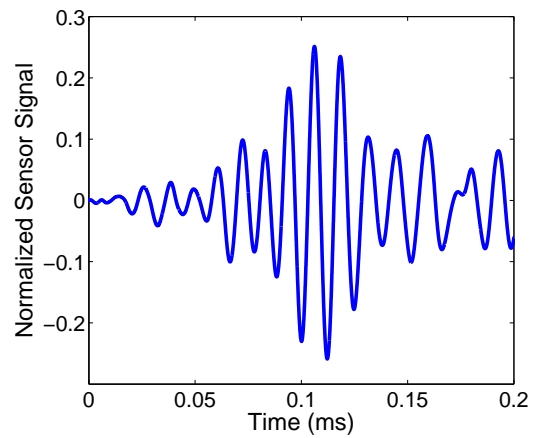
(a) LISA



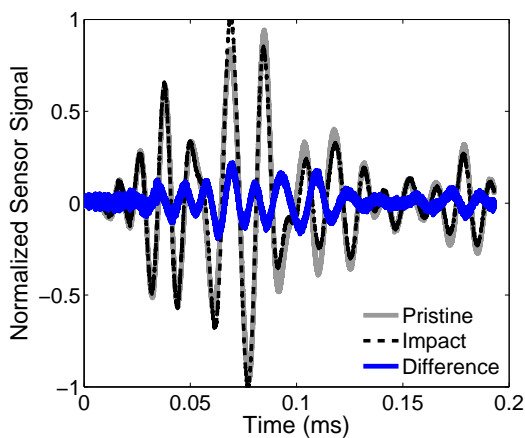
(b) LISA difference signal



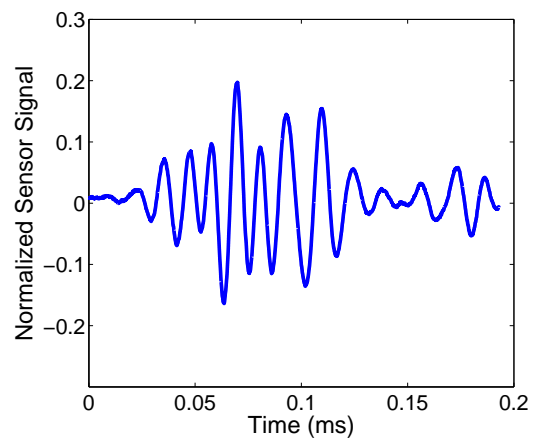
(c) Plate 1 experiment



(d) Plate 1 experiment difference signal



(e) Plate 2 experiment



(f) Plate 2 experiment difference signal

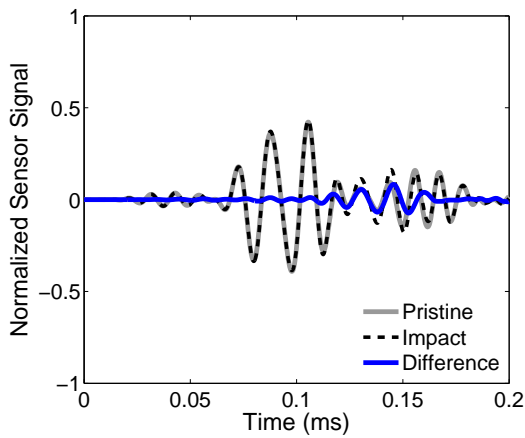
Figure 5.32: Comparison of selected LISA simulation with results from 5-J impact experiments for sensor 1.

difference signal properly. The simulated difference signal contained four major features. First, the reflection of the unconverted  $S_0$  mode from the damage site appeared at the sensor at around 0.025 ms. The next feature in the time history was a reflection representing an  $S_0$ - $A_0$  mode conversion starting at around 0.05 ms. Third, the  $A_0$ - $S_0$  mode conversion appeared at the sensor near the 0.09 ms point. Finally, the unconverted  $A_0$  reflection reached the sensor starting at around 0.12 ms. An examination of the experimental difference signal from plate 1 showed that each of these features was present in that signal as well, but the magnitudes were considerably different between them. In the simulation, the largest amplitude was found in the unconverted  $A_0$  reflection. In the plate 1 experiment, the largest amplitude came from the  $A_0$ - $S_0$  mode conversion. In the plate 2 experiment, the four major components of the time signal were also present. However, the largest amplitude was generated by the  $S_0$ - $A_0$  mode conversion. The  $A_0$ - $S_0$  mode conversion also produced a large amplitude.

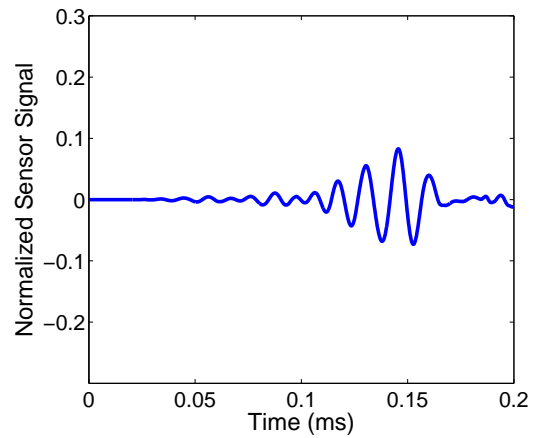
Another interesting comparison can be made with the sensor 2 time history results, shown in Fig. 5.33. The difference signals on the right hand side show a consistent large amplitude section arriving at the sensor just before 0.15 ms. However, the experimental amplitude from each experiment was significantly larger than that seen in the simulation. This discrepancy can be partly explained by considering the pristine signals on the left side of the figure. The simulation underpredicted the magnitude of the pristine signal reaching sensor 2 in the experiments, and it is reasonable that the lower pristine signal resulted in a lower amplitude reflection.

Of the five sensors, the impact damage model was most successful in capturing the behavior of the sensor 5 signals, shown in Fig. 5.34. In both the simulation and the experiments, the major feature of the difference signal was the slight delay of the unconverted  $A_0$  mode in reaching sensor 5 after passing through the damaged region.

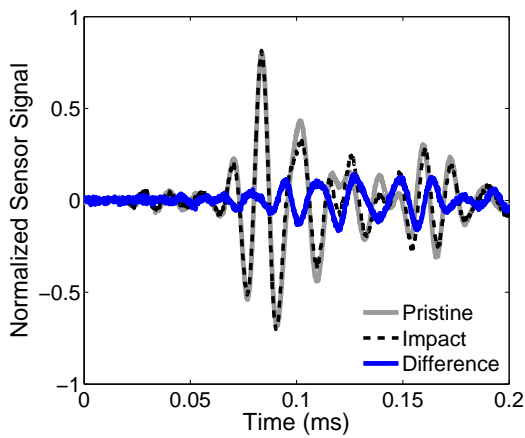
Overall, the most notable deficiency of the impact damage model was its inability to properly capture the amplitude of the unconverted and mode converted portions of the dif-



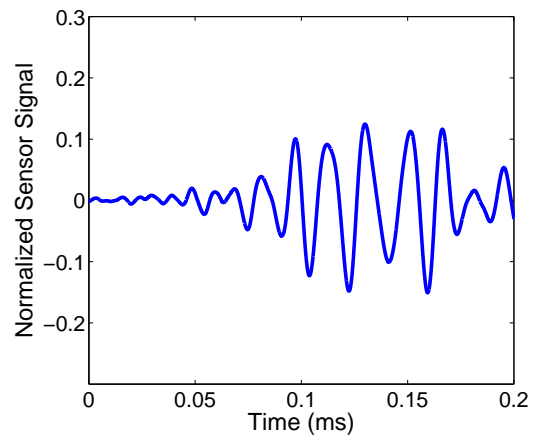
(a) LISA



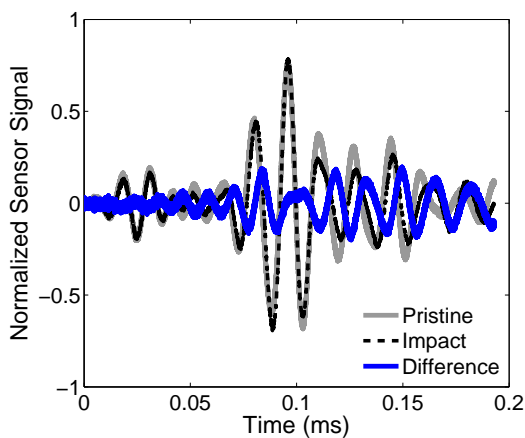
(b) LISA difference signal



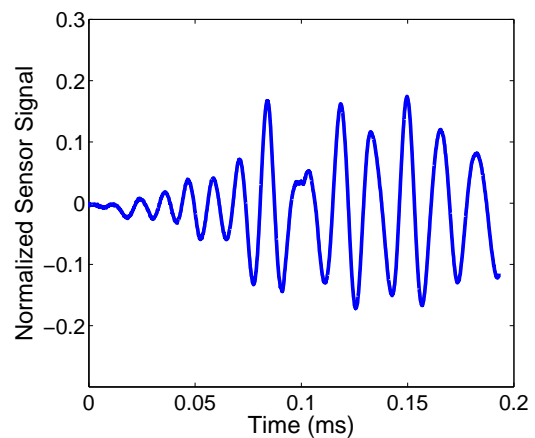
(c) Plate 1 experiment



(d) Plate 1 experiment difference signal

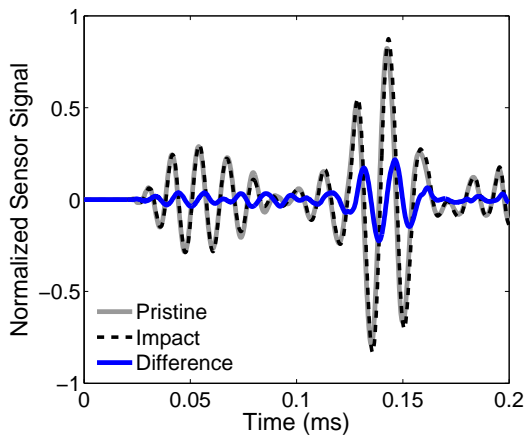


(e) Plate 2 experiment

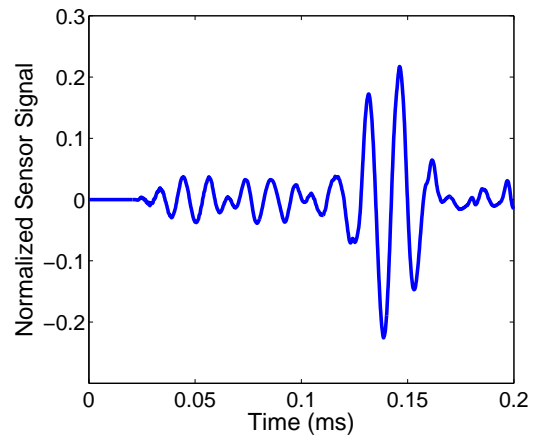


(f) Plate 2 experiment difference signal

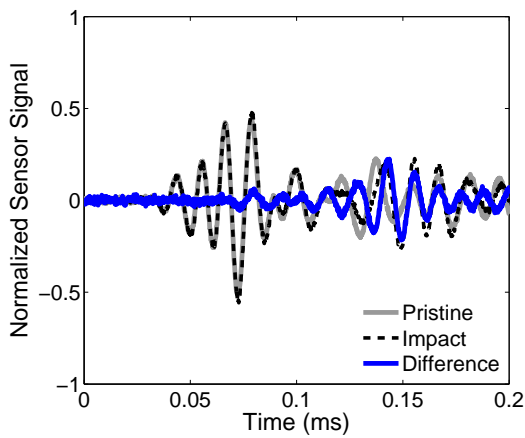
Figure 5.33: Comparison of selected LISA simulation with results from 5-J impact experiments for sensor 2.



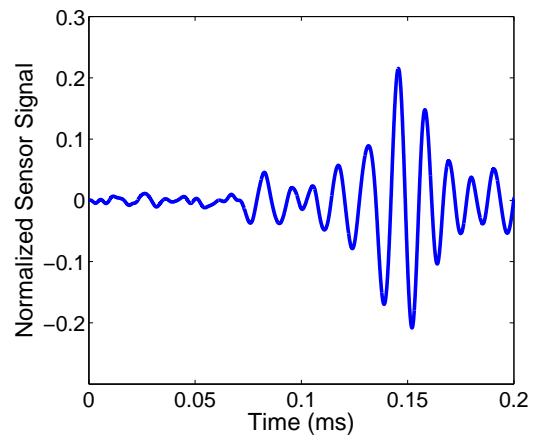
(a) LISA



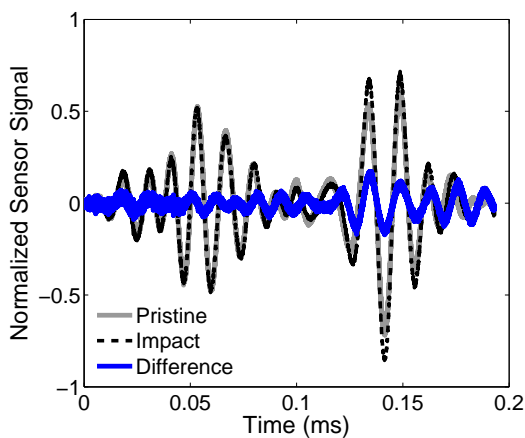
(b) LISA difference signal



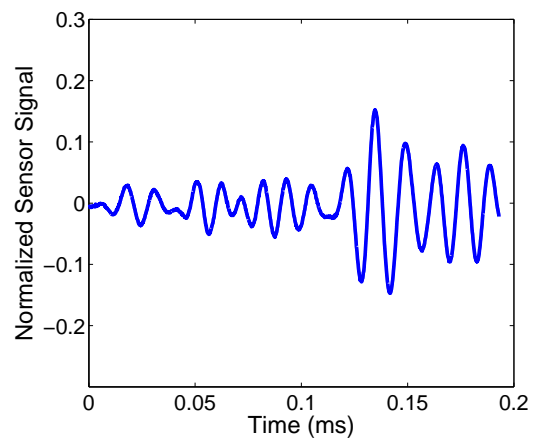
(c) Plate 1 experiment



(d) Plate 1 experiment difference signal



(e) Plate 2 experiment



(f) Plate 2 experiment difference signal

Figure 5.34: Comparison of selected LISA simulation with results from 5-J impact experiments for sensor 5.

ference signal that were reflected back toward the sensor 1 position. The combination of simulated delamination and property reduction used in the model evidently did not completely capture the interaction between the incident wave and the distributed damage beneath the impact site. It is possible that each small matrix crack produces mode-converted reflections that were not produced to the same level with the homogenized damage model used here. It is also possible that the higher amplitudes of the mode conversions were due to nonlinear effects of the delaminations that were not considered in the LISA model. Despite this drawback, the results showed that a model of this type captured much of the guided wave behavior. This model should be a useful starting point for future studies needing to model composite impact damage.

### **5.3.5 Comparison of Experimental and Simulation Results for Damage Located at 45 and 90 Degrees**

The final comparisons between the simulation and experiments consider the two other damage sites. Using the same Model 1 parameters for the damage as done in the previous section, Fig. 5.35 shows the sensor results for the 45 and 90-degree damage locations. In the 90-degree case shown on the right, there is good agreement for sensors 3 and 5, but significant discrepancies in the amplitude of sensors 1, 2, and 4. The experiment showed a reflection back toward sensor 1 that was almost twice as large as that predicted by the LISA model, even with the addition of the simulated delamination.

In the 45-degree case, there was generally poor agreement between the simulation and the experiment. With the exception of sensor 4, the maximum recorded difference signals did not match well. The amplitude of the experimental difference signals was much higher than that of the simulation, in general. It is possible that some manufacturing variation in this region of the plate resulted in more severe damage during the 5-J impact. It should also be noted that secondary impacts after the initial impact were not prevented in any of the experiments in this study. It is possible a secondary impact created a larger damage



area than that seen in the other experiments, which artificially increased the size of the difference signal. A final possibility that should be considered is that the Cartesian grid may affect the results. When the damage is located at the 45-degree site, the waves arriving at the center of the damage in the simulation travel along the diagonals of the cells. It is possible this changes the way the pristine waves interact with the interfaces of the damage in the LISA model. These should be topics of future study.

## 5.4 Summary

This chapter presented a thorough analysis of guided wave interaction with low-velocity impact damage in a cross-ply laminate. First, X-ray CT scans were used to characterize the sub-surface damage present after a cross-ply graphite-epoxy laminate was subjected to a 5-J impact. These revealed a noticeable V-shaped impact damage region containing numerous small matrix cracks and delaminations. Next, guided-wave experiments for damage located at 0, 45 and 90 degrees relative to the top fiber direction were presented. Sensor results indicated large difference signal amplitudes in the 0 and 180-degree directions relative to

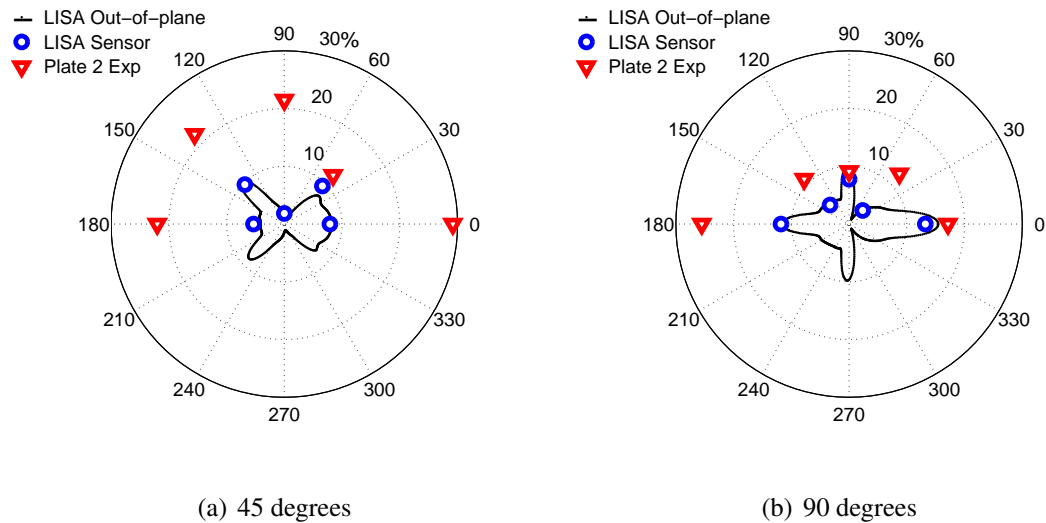


Figure 5.35: Impact damage models for damage at 45 and 90 degrees.

the direction of the incident wave. Laser vibrometry experiments were also conducted, but the results showed large amounts of variation that need to be addressed before the technique can be used reliably.

The final section of the chapter explained the formulation of a LISA impact damage model. Information from the X-ray images was used to define the size of the damage model. The effects of altering the elastic properties of the damaged region and the density of the region were studied. It was found that solely reducing elastic properties did not produce sufficient reflection back toward the actuator. Reducing the density in the damaged region helped to produce damage difference signals with amplitudes closer to experimental results for the 0-degree case. The addition of a void region simulating a large delamination further improved the performance of the model. Comparison of sensor signals from a selected LISA model with experimental results showed the model was able to simulate the signals on the back side of the damage very accurately, with an error in the difference signal amplitude of less than 5% of the average experimental value. The most notable deficiency of the model was the predicted amplitude of the mode conversions reflected back toward the actuator, which was smaller than those seen in the experiments.

## CHAPTER 6

# Damage Location and Characterization Using Matching Pursuit and a LISA Library

This chapter introduces a guided wave signal analysis tool based on chirplet matching pursuit and LISA. First, the fundamentals of matching pursuit are described, and the general process for decomposing guided wave time signals is reviewed. Next, a new algorithm is presented that uses a library of LISA simulations to locate and characterize damage in a host plate structure. This algorithm is then demonstrated for a 1-D scenario involving hole damage in both aluminum plates and composite laminates. Experimental sensor results in both material systems are used to reinforce the capability of the method. The remainder of the chapter applies the algorithm to locate hole damage in a 2-D scenario, focusing on the cross-ply laminate. Graphical results are presented showing the ability of the new algorithm to predict the location of hole damage using signals from a combination of actuators and sensors.

### 6.1 Theoretical Background

#### 6.1.1 Matching Pursuit Decomposition

Matching pursuit is a process to decompose signals into a linear combination of waveforms from a pre-defined dictionary. It was originally proposed by Mallat and Zhang [130], and

it has shown promise in the analysis of guided wave signals. The process of decomposing a signal using matching pursuit is iterative, and a typical iteration  $m$  involves first projecting each time-frequency atom  $k$  in the dictionary containing  $i$  atoms onto the current residual signal  $R^{m-1}$ . For the first iteration, the residual signal is the original guided wave signal. The best matching atom  $k_{i_m}$  is chosen as the one which maximizes the value of the projection,

$$k_{i_m} = \arg \max_{k_i \in D} \left| \langle R^{m-1}, k_i \rangle \right| \quad (6.1)$$

where the inner product is defined as:

$$\langle f_1, f_2 \rangle = \int_{-\infty}^{\infty} f_1(t) f_2(t) dt \quad (6.2)$$

Once the best atom has been identified, the next residual is calculated,

$$R^m = R^{m-1} - \langle R^{m-1}, k_{i_m} \rangle k_{i_m} \quad (6.3)$$

and the next iteration is begun. With enough iterations, a signal can be completely reconstructed. In practice, it is often the case that only a small number of iterations are needed to capture the important features of a guided wave signal. Noisy signals are easily cleaned by simply stopping the process before enough iterations occur to capture the noise.

### 6.1.2 Choice of Waveform Dictionary

In their original paper, Mallat and Zhang proposed using a dictionary of Gaussian-modulated time-frequency atoms defined as:

$$k_{(l,u,\omega)}(t) = \frac{1}{\sqrt{l}} g\left(\frac{t-u}{l}\right) e^{i\omega(t-u)} \quad (6.4)$$

where  $u$  is the time center of the atom and  $\omega$  is the frequency center. The parameter  $l$  represents the dilation of the Gaussian window  $g$ , which is defined as:

$$g(t) = 2^{1/4} e^{-\pi t^2} \quad (6.5)$$

Figure 6.1 shows the behavior of a typical atom of this type. The time history is shown on the left, and a spectrogram of the signal is shown on the right. From the spectrogram, the stationary time-frequency behavior of the atom is apparent, as the frequency at which the peak energy occurs for each time is equal to the center frequency of the atom. Unfortunately, this stationary time-frequency behavior can be problematic for guided wave analysis, since Lamb waves are dispersive in nature.

Gribonval [135] introduced an alternative waveform dictionary based on Gaussian-modulated chirplets. In this dictionary, an additional parameter  $c$  is introduced for the chirp rate of the atom, and the dictionary is defined as:

$$k_{(l,u,\omega,c)}(t) = \frac{1}{\sqrt{l}} g\left(\frac{t-u}{l}\right) e^{i(\omega(t-u) + \frac{c}{2}(t-u)^2)} \quad (6.6)$$

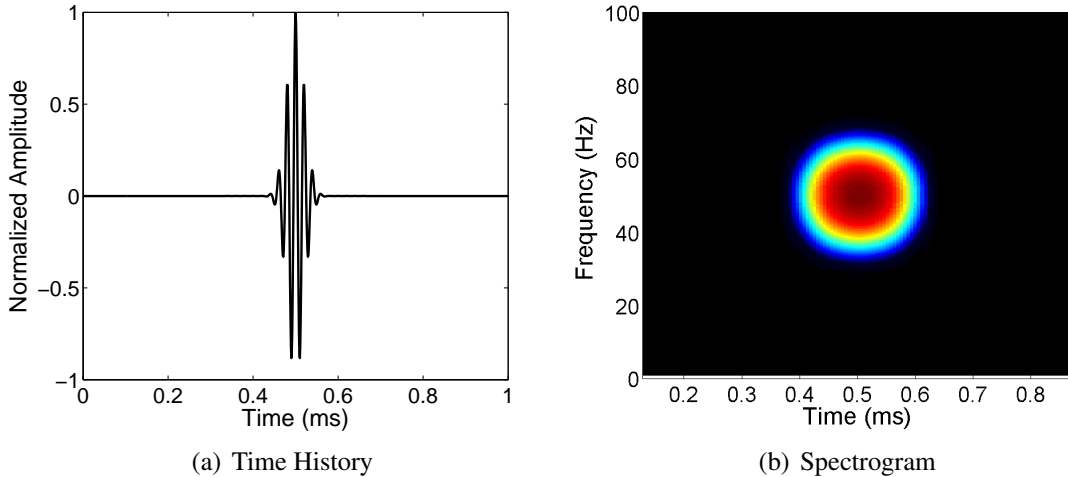


Figure 6.1: Stationary Gaussian-modulated atom.

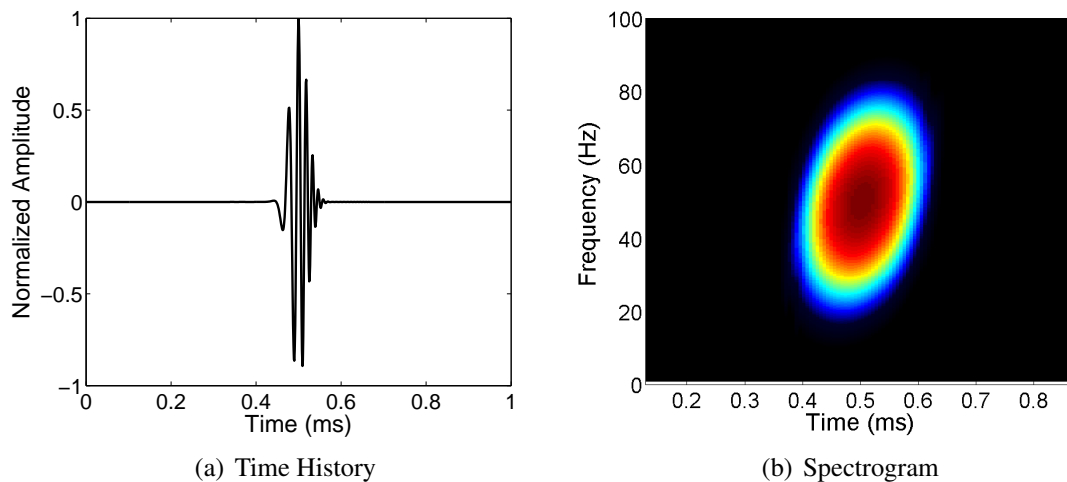


Figure 6.2: Gaussian chirplet atom.

Figure 6.2 shows the behavior of a chirplet atom. The spectrogram on the right side of this figure shows the non-stationary time-frequency behavior. This chirplet dictionary is better suited for guided wave analysis, since the atoms can account for the frequency dispersion commonly found in guided wave signals. Atoms with higher chirp rates display larger amounts of dispersion, and these atoms produce better matches to guided wave signals containing highly dispersive modes.

## 6.2 Matching Pursuit Algorithm Development

The literature review in Chapter 1 highlighted several recent implementations of matching pursuit methods. The following algorithm is based on the foundation set by Raghavan and Cesnik [136], who introduced the idea of using chirplet matching pursuit along with a library of candidate damage sites to locate damage in simulated or experimental signals. In that work, the scenario assumed a collocated actuator-sensor pair attached to an isotropic structure. Damage was assumed to act as a point scatterer, and an analytical approach was used to develop a library of possible damage signals at known locations, time centers, and frequency centers. The procedure introduced in this chapter improves on the previous work

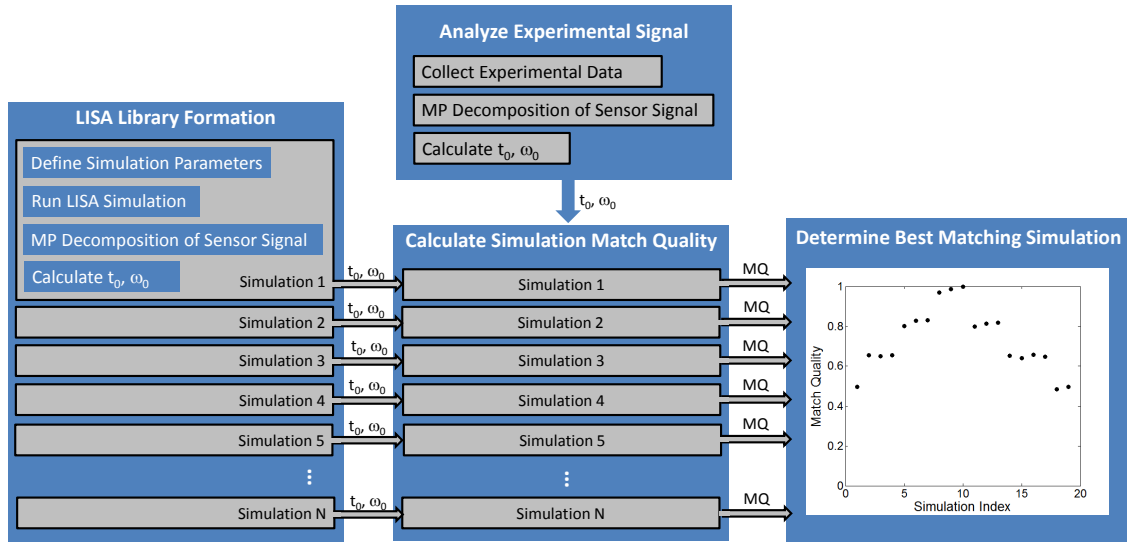


Figure 6.3: Matching pursuit algorithm flow chart.

by removing the restriction that the actuator and sensor be collocated, and it also allows for analysis of composite laminates with no additional complexity.

A block diagram of the new algorithm is shown in Fig. 6.3. The first major step in the process is to populate a library of possible damage signals using a series of LISA simulations. This step is a major departure from previous methods, and it eliminates the need to assume that damage sites act as point scatterers. Any damage modes that can be accurately modeled in LISA can be included in the damage library. Each simulation is based on specified parameters including damage location and size. Desired sensor locations can be simulated in the same manner as described in Chapter 4. For each simulation, the damage difference signals for each sensor are decomposed using chirplet matching pursuit. The matching pursuit procedure was implemented using the LastWave 3.1 signal processing software, which is available as freeware [143]. An example result for the matching pursuit decomposition is shown in Fig. 6.4, where the original sensor signal is shown along with the first atom returned by the decomposition. For this algorithm, the time and frequency centers of the matched atoms, defined as  $t_0$  and  $\omega_0$  respectively, are the primary data extracted during the decomposition process.

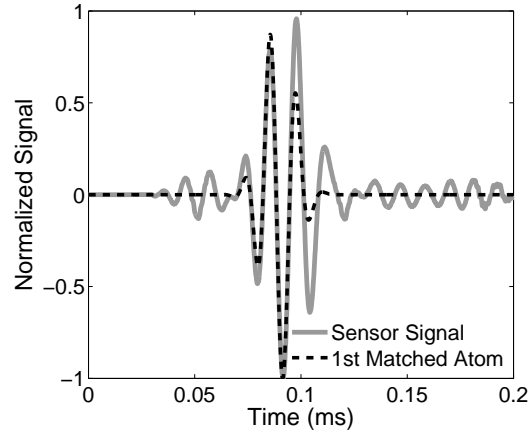


Figure 6.4: First matched atom for an example damage difference signal.

Once the damage library is complete, a damage difference signal from an experiment or simulation is collected, and it is analyzed using matching pursuit decomposition. The time and frequency centers of the matched atom are recorded. These are passed, along with the time and frequency centers from each simulation in the damage library, to the next step in the process.

The next step is to determine how well each simulated damage case represents the damage captured in the actual difference signal using the parameters obtained in the matching pursuit decomposition. For each simulation, the match error is quantified using:

$$Match\ Error = \frac{|t_0^{Sim} - t_0^{Exp}|}{t_0^{Exp}} W + \frac{|\omega_0^{Sim} - \omega_0^{Exp}|}{\omega_0^{Exp}} (1 - W) \quad (6.7)$$

The  $t_0^{Exp}$  and  $\omega_0^{Exp}$  terms represent the time and frequency centers of the matched atom from the actual difference signal, such as one obtained in an experiment. The  $t_0^{Sim}$  and  $\omega_0^{Sim}$  terms are the time and frequency centers of the matched atom from the library simulation currently under consideration. The parameter  $W$  is a weighting factor used to determine how much to consider the difference in frequency centers relative to the difference in time centers. It was determined that using  $W = 0.25$  produced good results for the cases consid-



ered in this study. Once the match error for each damage library simulation is calculated, it is converted to a match quality,  $MQ$ , metric, i. e.,

$$MQ(j) = 1 - \frac{MatchError(j)}{Max(MatchError)} \quad (6.8)$$

where a match quality value of 1 for simulation  $j$  indicates a perfect match between the actual difference signal and the difference signal from simulation  $j$ . The final step in the algorithm is to compare the match quality of each possible damage simulation to determine which one matches best. The parameters of the best matching simulation can then be reported as the best characterization of the actual damage.

In this study, only the first matched atom from each matching pursuit decomposition was used in the algorithm. This atom corresponded to the unconverted  $A_0$  portion of the difference signal from each simulated sensor. This algorithm, however, can be extended to take into account the remaining matched atoms, which would capture the unconverted  $S_0$  mode as well as any mode conversions that are present. Including these additional matched atoms in the match quality calculations should further improve the ability of the algorithm to identify the simulation best matching the experimental damage.

### 6.3 Matching Pursuit Algorithm: 1-D Scenario

The first analyses using the matching pursuit algorithm focused on locating and characterizing hole damage where the actuator, sensors, and damage were always aligned. A schematic showing the configuration of the actuator and sensors as well as the possible damage locations is shown in Fig. 6.5. The location of the damage in the library simulations was allowed to vary along a line connecting the actuator, sensor 1, and sensor 2. The hole location varied from 80 mm from the actuator center to 170 mm from the actuator center in 5 mm increments. Additionally, the hole radius was allowed to vary at each location. Holes in both aluminum and cross-ply plates were considered. For the isotropic

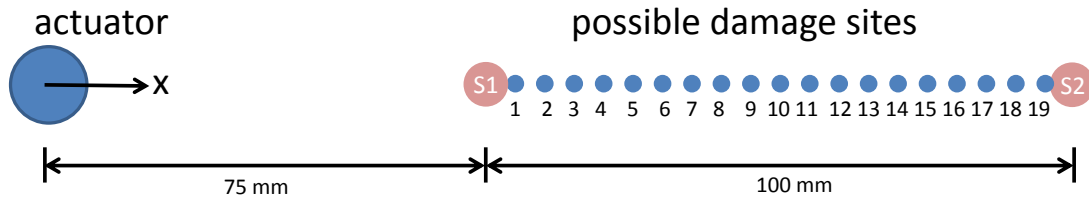
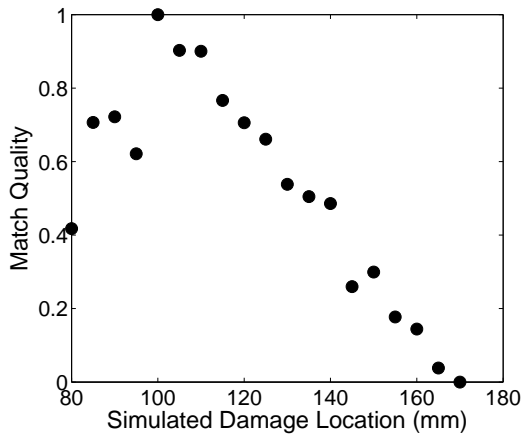


Figure 6.5: Possible damage locations in matching pursuit damage library (1-D analysis).

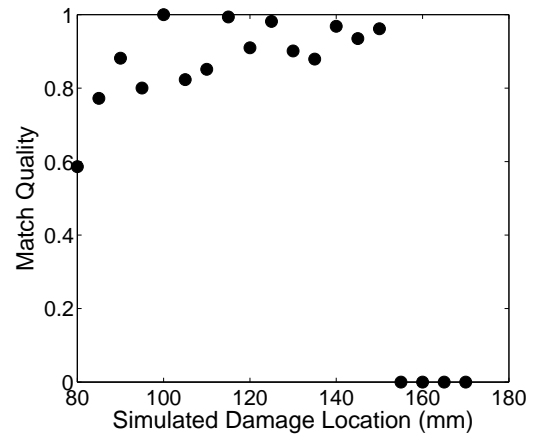
case, a 700-mm square aluminum host plate with 3.18-mm thickness was modeled. For the cross-ply case, a  $[0/90]_{3S}$  laminate constructed with the CYCOM IM7/977-3 material system was used as the host structure. The laminate was a 500-mm square with a thickness of 1.5 mm. Both cases modeled the guided waves generated by a 12.8-mm diameter piezoceramic disc subject to a 3.5-cycle Hann-modulated toneburst with 75-kHz center frequency. The actuator was assumed to be surface mounted at the geometric center of the plate. The sensors were modeled as piezoceramic discs with a diameter of 7.5 mm.

### 6.3.1 Identification of Hole Location

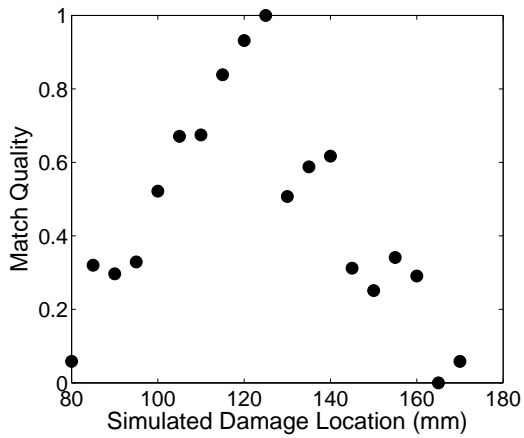
In the first stage of the 1-D analysis, the library of possible damage simulations was restricted to those where the through-thickness hole damage had radius  $r = 1t$ . The signals representing the actual damage location were taken from one of the simulations, and the algorithm was run to determine if it could identify the correct damage simulation. In these three trial cases, the actual damage locations were at  $x = 100$  mm,  $x = 125$  mm, and  $x = 150$  mm. Damage difference signals from the two sensors shown in Fig. 6.5 were used to identify the location of the actual damage. Graphical representations of the matching results for the three simulated damage locations in the aluminum plate are shown in Fig. 6.6. In each of the figures, the match quality of each damage library simulation is plotted with respect to the simulated damage location. The left column shows the results of the algorithm when



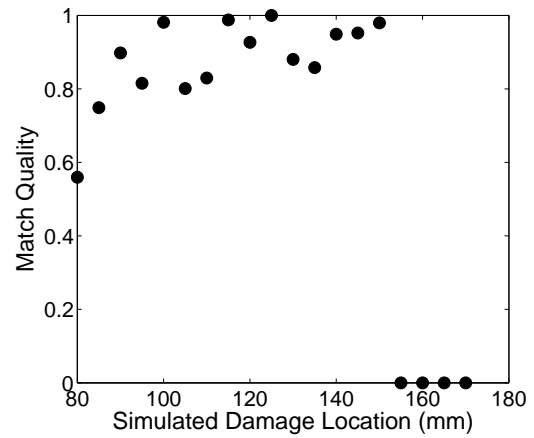
(a) Damage at  $x = 100$  mm - Sensor 1



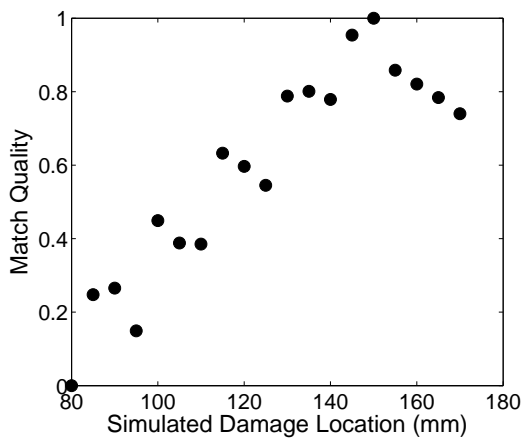
(b) Damage at  $x = 100$  mm - Sensor 2



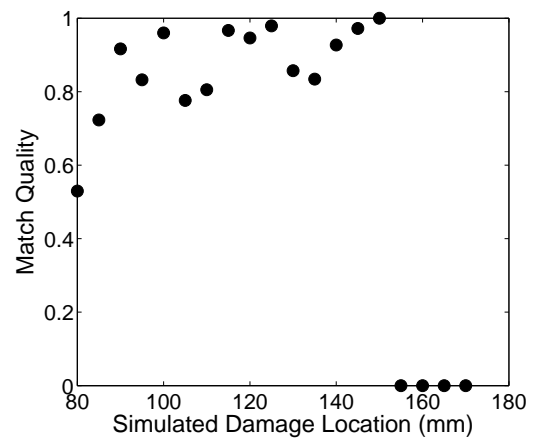
(c) Damage at  $x = 125$  mm - Sensor 1



(d) Damage at  $x = 125$  mm - Sensor 2



(e) Damage at  $x = 150$  mm - Sensor 1



(f) Damage at  $x = 150$  mm - Sensor 2

Figure 6.6: Matching pursuit algorithm location results for hole damage in an isotropic plate at various damage sites (1-D analysis).

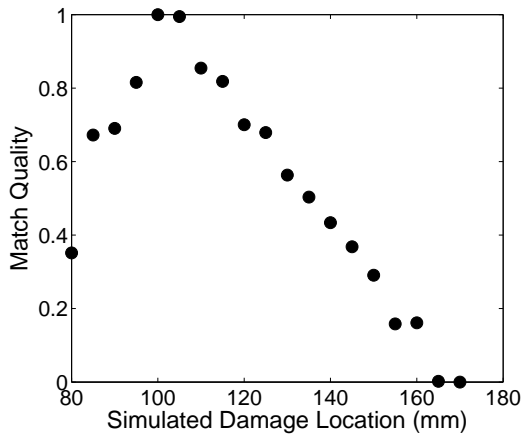
data from sensor 1 were used to locate the hole. The right column shows the results when the sensor 2 data were used.

For these three locations, the algorithm correctly identified the simulation corresponding to the actual damage location when information from sensor 1 was used. The algorithm was less successful in clearly identifying the correct damage location using the information from sensor 2. Because the algorithm relies heavily on the value of the time center of the actual and library atoms, the sensor arranged in a pulse-echo configuration relative to the actuator and damage locations performed better than the sensor located in a pitch-catch configuration. In the sensor 2 case, the damage difference signals reached the sensor at nearly the same time regardless of the damage location, so there was not much differentiation between the different library simulations. For sensor 1, the difference signals were primarily reflections from the damage site, and these arrived at the sensor at different times for each damage location.

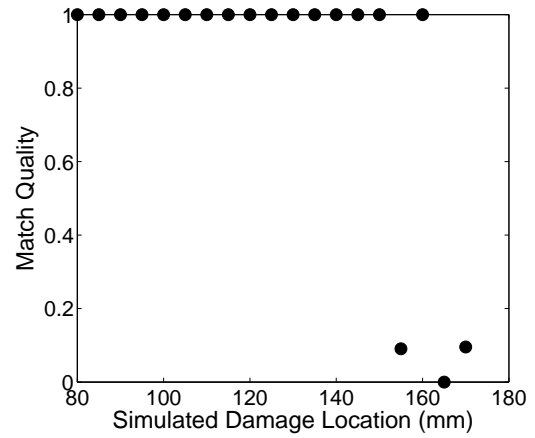
Similar trials were conducted to determine if the algorithm could locate hole damage in the cross-ply laminate. The actual damage locations were again set to  $x = 100$  mm,  $x = 125$  mm, and  $x = 150$  mm, and graphical results were produced to show how well each simulation matched the actual damage case. The results are shown in Fig. 6.7. As in the isotropic case, the matching pursuit algorithm was able to correctly identify the location of the hole damage in each of the three trial locations using the sensor 1 data. The results using the sensor 2 data did not provide a useful location prediction, as was previously seen.

### **6.3.2 Variation of Hole Size**

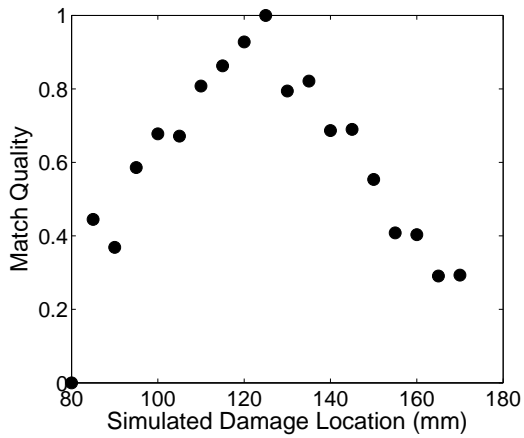
The next phase of the 1-D analysis restricted the location of the actual damage to  $x = 125$  mm, but the radius of the through-thickness hole was allowed to vary. For the aluminum case, the hole radius varied from  $r = 0.5t$  to  $r = 2t$  in  $0.25t$  increments for the damage library simulations. The damage difference signal used as the actual result was set to the



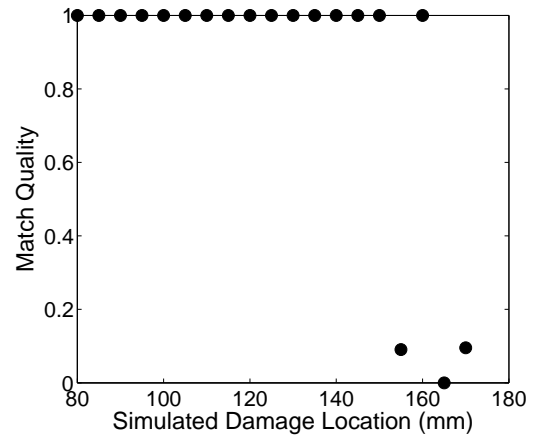
(a) Damage at  $x = 100\text{ mm}$  - Sensor 1



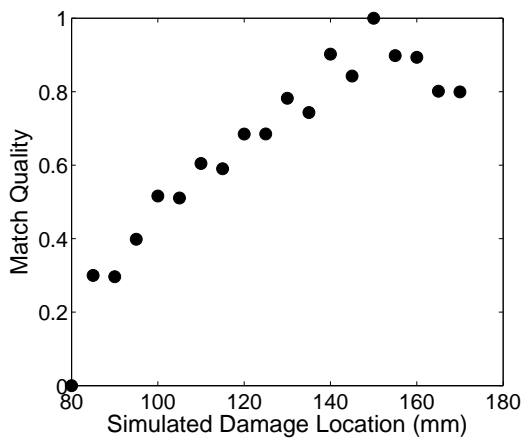
(b) Damage at  $x = 100\text{ mm}$  - Sensor 2



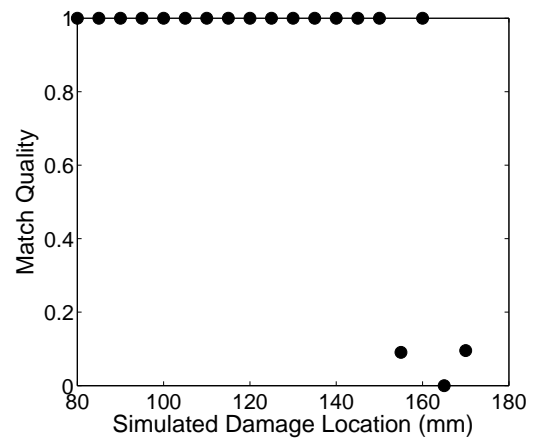
(c) Damage at  $x = 125\text{ mm}$  - Sensor 1



(d) Damage at  $x = 125\text{ mm}$  - Sensor 2



(e) Damage at  $x = 150\text{ mm}$  - Sensor 1



(f) Damage at  $x = 150\text{ mm}$  - Sensor 2

Figure 6.7: Matching pursuit algorithm location results for hole damage in a cross-ply laminate at various damage sites (1-D analysis).

case where the damage radius was  $r = 0.5t$ ,  $r = 1t$ , and  $r = 1.5t$  in three different tests of the algorithm. The best results were again obtained using the information from sensor 1, and the results for this sensor are shown in the left column of Fig. 6.8. In each of the three tests, the algorithm correctly predicted the simulation that matched the actual damage size. Results when data from sensor 2 were used are shown in the right column of Fig. 6.8. With sensor 2 information, the algorithm correctly identified the size of the  $r = 0.5t$  and  $r = 1t$  holes. The results were more ambiguous for the  $r = 1.5t$  case, where the simulations for  $r = 1.25t$  and  $r = 1.75t$  were also identified as good matches.

A similar series of steps were taken to determine if the algorithm could identify the damage size for holes in the cross-ply laminate. For the damage library simulations, the hole radius varied from  $r = 0.5t$  to  $r = 3t$  in  $0.5t$  increments. Three trial cases were run with damage sizes  $r = 1t$ ,  $r = 2t$ , and  $r = 3t$ . The match quality results using sensors 1 and 2 are shown in Fig. 6.9. For the case where  $r = 1t$ , data from both sensors produced a correct match for the hole size. This was also true for the case where  $r = 3t$ . In the case where the hole had radius  $r = 2t$ , the sensor 2 data produced a correct match, but the sensor 1 data predicted both the  $r = 1.5t$  and the  $r = 2t$  simulations as perfect matches.

Two observations are notable for the hole variation trials. First, unlike the hole location trials, the sensor 2 data produced correct matches in most cases. The second observation is that the algorithm sometimes produced ambiguous results for the size identification, where hole sizes close to the actual size were also reported as good matches. This result stems from the fact that for a given hole location, the damage difference signals were best represented with atoms with the same time center but slightly different frequency centers. In cases where ambiguous size identification results were produced, the frequency centers of the best matched atoms for two adjacent hole sizes were nearly identical, resulting in similar match quality results.

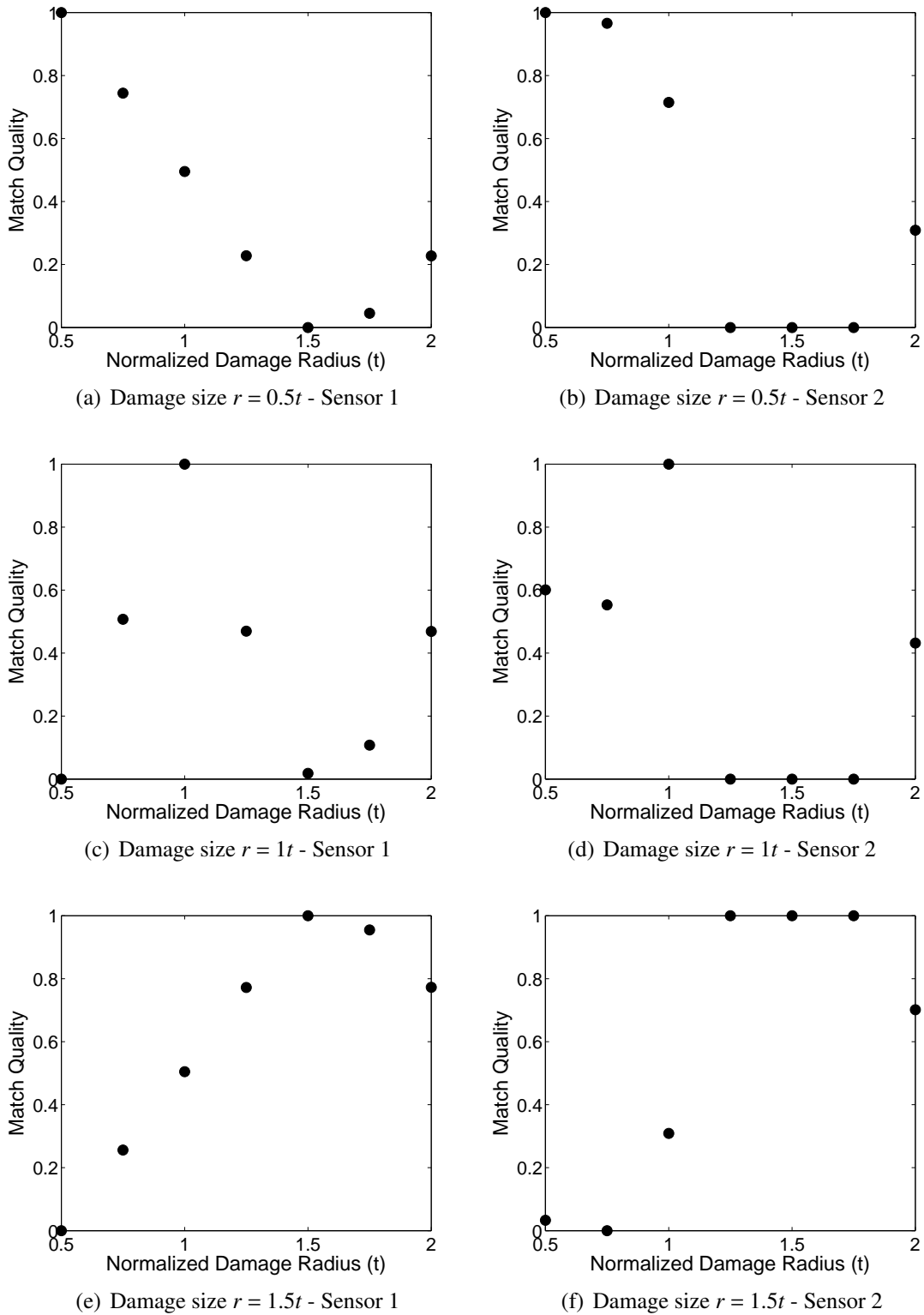


Figure 6.8: Matching pursuit algorithm size identification results for hole damage in an isotropic plate with varying radius (1-D analysis).

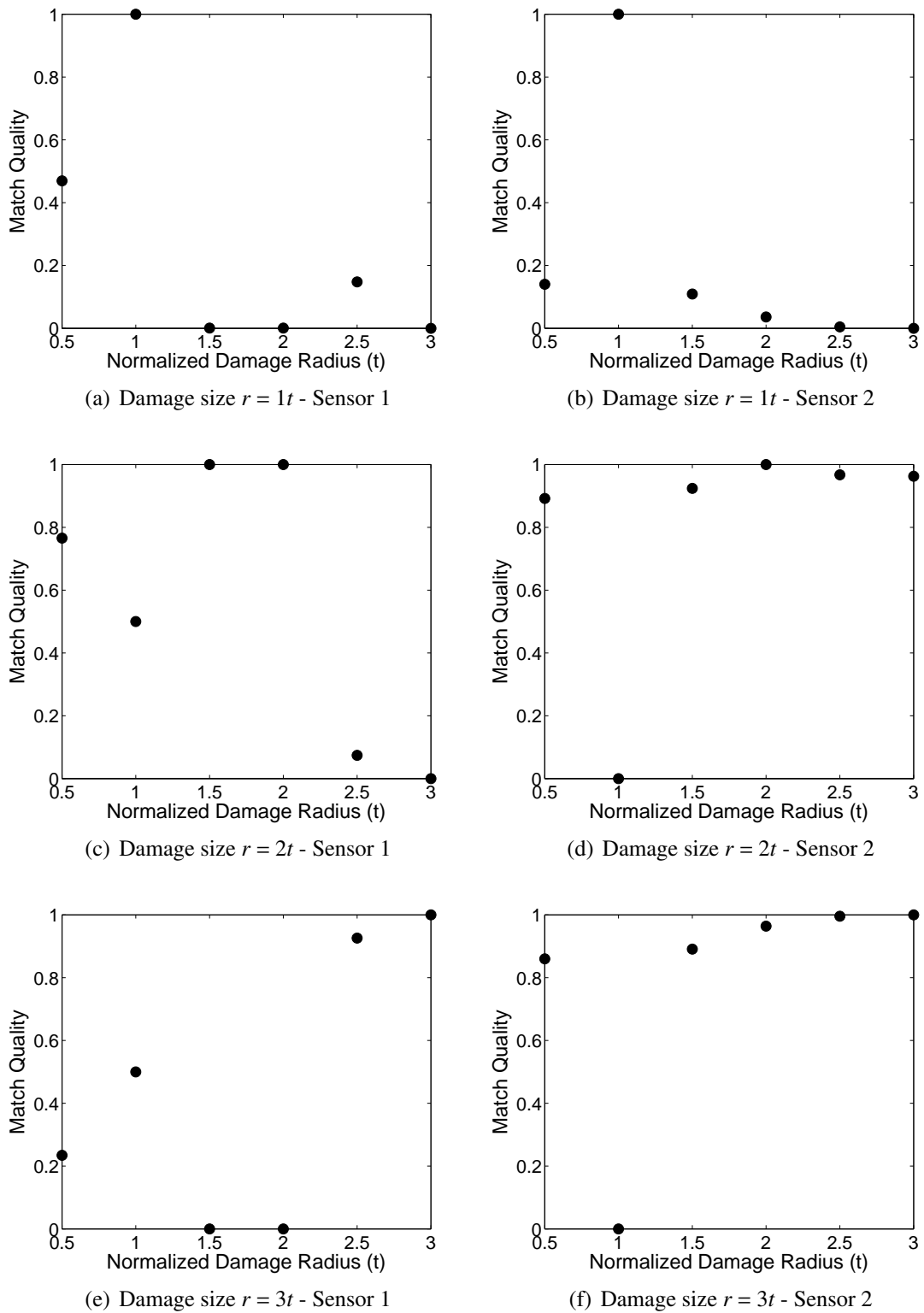


Figure 6.9: Matching pursuit algorithm size identification results for hole damage in a cross-ply laminate with varying radius (1-D analysis).



### 6.3.3 Variation of Hole Size and Location

The third phase of the 1-D analysis considered a damage library where three possible hole sizes existed for each possible damage location in the aluminum plate. The hole radii  $r = 0.5t$ ,  $r = 1t$ , and  $r = 2t$  were included in the library. Various combinations of hole size and location were then assigned as the actual damage case, and the algorithm produced graphical matching results for each case. Only the sensor 1 data were used in this phase of the analysis. Figure 6.10 shows these results for nine simulated damage signals. In the figures, higher predicted match qualities are represented by darker regions in the figure, with a value of 1.0 indicating a perfect match. The actual parameters of the damage are annotated for each case. To better understand the performance of the algorithm, numerical results were also produced to quantify how well the hole location and hole size were identified. The predicted value for the location of the hole in each case was calculated using a weighted average of the locations corresponding to the two best matching library simulations:

$$x_{predicted} = \frac{\sum_{j=1}^2 (x_{sim}(j))(MQ(j))}{\sum_{j=1}^2 MQ(j)} \quad (6.9)$$

A similar calculation was performed to calculate the predicted radius of the hole. The results for the 9 simulations in Fig. 6.10 are shown in Table 6.1. In each case, the damage location was identified within 5 mm of the actual location. The correct hole size was identified in all but one trial.

### 6.3.4 Robustness to Noise

The previous three subsections used simulated damage difference signals to represent the true damage, which did not contain noise expected in real-world scenarios. To demonstrate the algorithm's ability to deal with noisy signals, Gaussian white noise with a signal-to-noise ratio of 175 dB was added to the damage difference signal from sensor 1 for the case

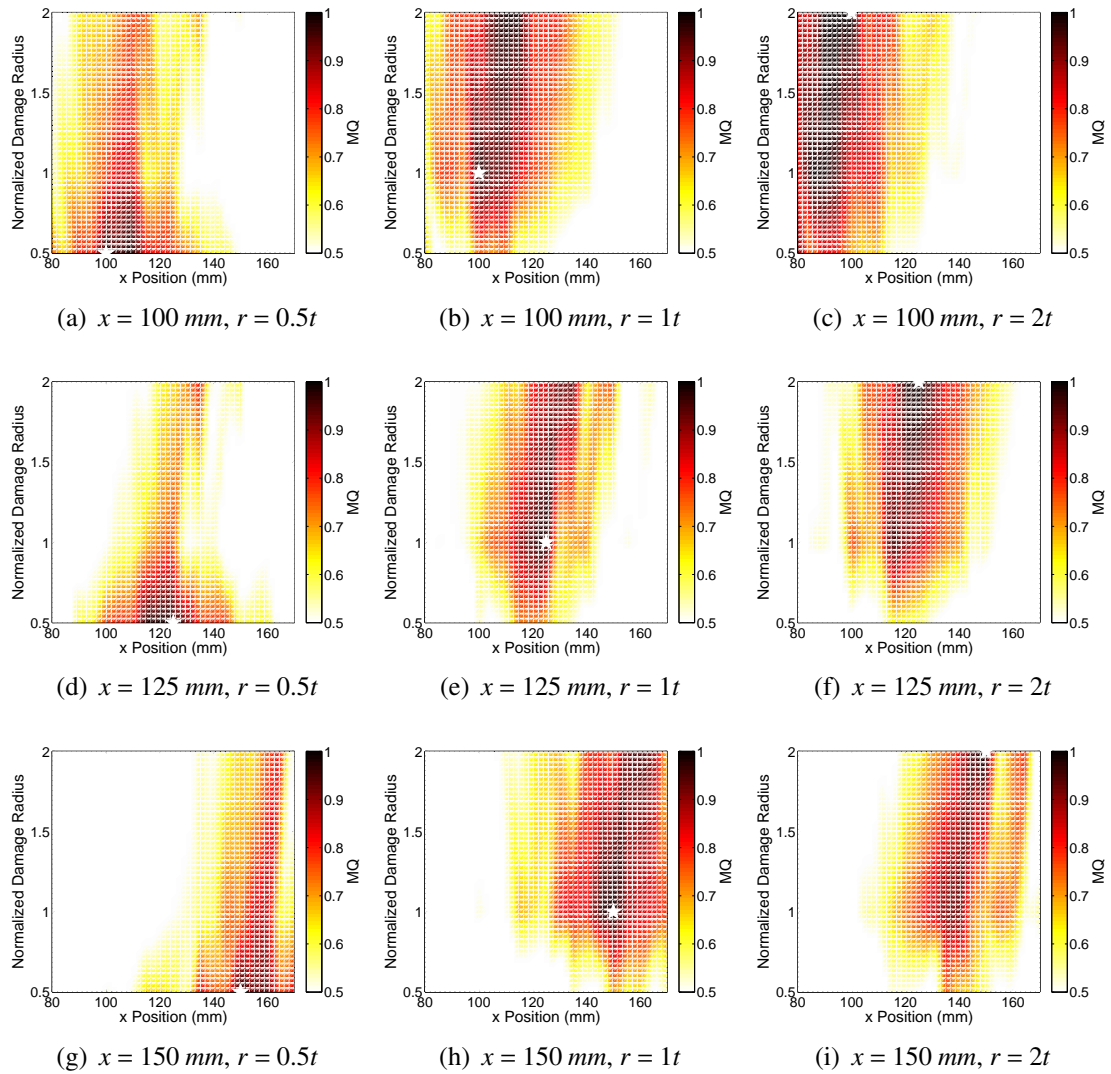


Figure 6.10: Matching pursuit algorithm damage identification results for hole damage in an aluminum plate (1-D analysis, sensor 1 only).

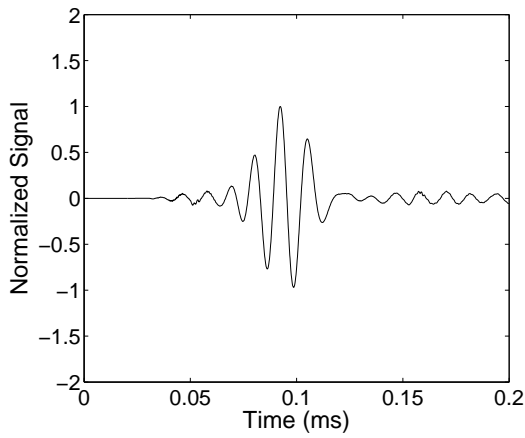
Table 6.1: Damage characterization results for 1-D matching pursuit algorithm with variable hole size and hole location. All values are measured in mm.

Trial	$x_{actual}$	$x_{predicted}$	$x_{error}$	$r_{actual}$	$r_{predicted}$	$x_{actual}$
1	100	105.0	5.0	0.5	0.5	0
2	100	105.0	5.0	1.0	1.5	0.5
3	100	97.5	2.5	2.0	2.0	0
4	125	122.5	2.5	0.5	0.5	0
5	125	122.6	2.4	1.0	1.0	0
6	125	122.5	2.5	2.0	2.0	0
7	150	154.9	4.9	0.5	0.5	0
8	150	147.5	2.5	1.0	1.0	0
9	150	147.6	2.4	2.0	2.0	0

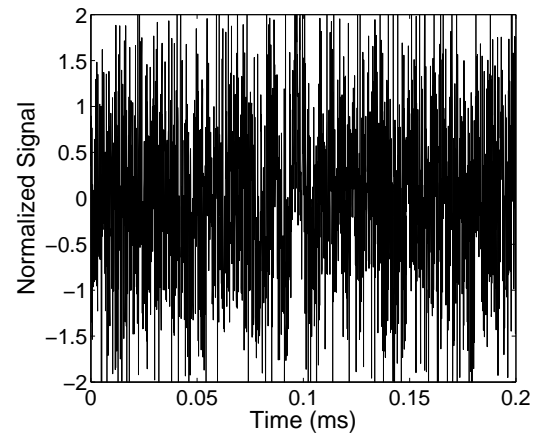
where an  $r = 1t$  hole was located at  $x = 125$  mm. In Fig. 6.11, sub-figures (a) and (b) show the original difference signal and the difference signal with the noise added. When both of these difference signals were used in the matching pursuit algorithm, the resulting matched atoms were almost identical, as shown in sub-figures (c) and (d). While the shape of the atoms was slightly different, their time and frequency centers were almost a perfect match. The location matching results using the original and noisy signals are included in sub-figures (e) and (f). Although the match quality was not as strong, the correct damage location was predicted when the noisy signal was used. Because the matching pursuit algorithm compares the characteristics of the matched atoms and not the damage difference signals themselves, even noisy signals can produce useful information, as long as the noise is uncorrelated. For correlated noise, a significant loss in match quality is likely.

### 6.3.5 Experimental Validation

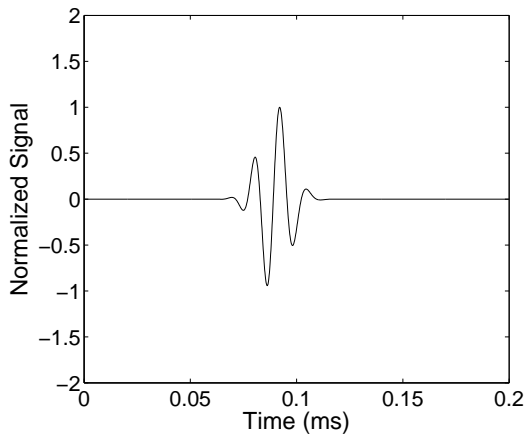
The final phase in evaluating the matching pursuit algorithm for the 1-D scenario was to use experimental results for the actual damage difference signals. For this analysis, the experimental data came from the hole experiments described in Chapter 4. For both the aluminum plate and the cross-ply laminate, a through-thickness hole with radius  $r = 1t$  was



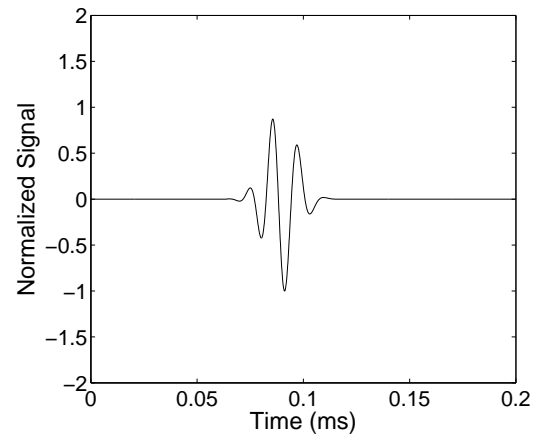
(a) Original sensor 1 difference signal



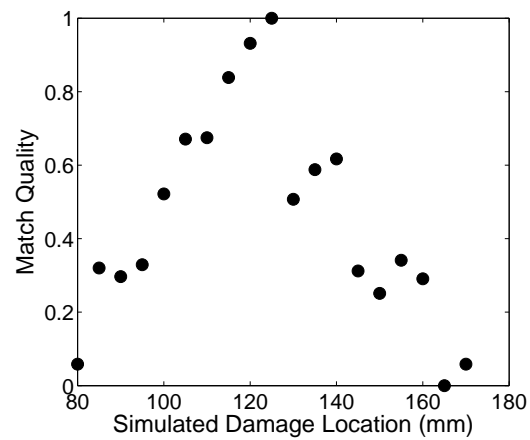
(b) Difference signal with added noise



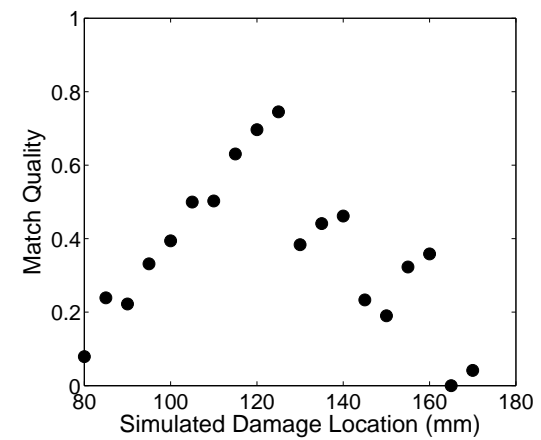
(c) First matched atom for original signal



(d) First matched atom for noisy signal



(e) Matching results with original signal



(f) Matching results with noisy signal

Figure 6.11: Matching pursuit algorithm performance with a noisy sensor signal (isotropic plate with  $r = 1t$  hole at 125 mm from the actuator center).

located at  $x = 125$  mm relative to the actuator center. The actuator and sensor configurations were identical to those described in Chapter 4, but for the present analysis only the sensor 1 data were used.

The results for the aluminum plate experiment are shown in Fig. 6.12. When considering only hole location, the algorithm predicted the hole damage to be best matched with the simulation with damage at 120 mm. When hole size was the only parameter, the correct hole size of  $r = 1t$  was successfully predicted. Figure 6.12 (c) shows a graphical depiction

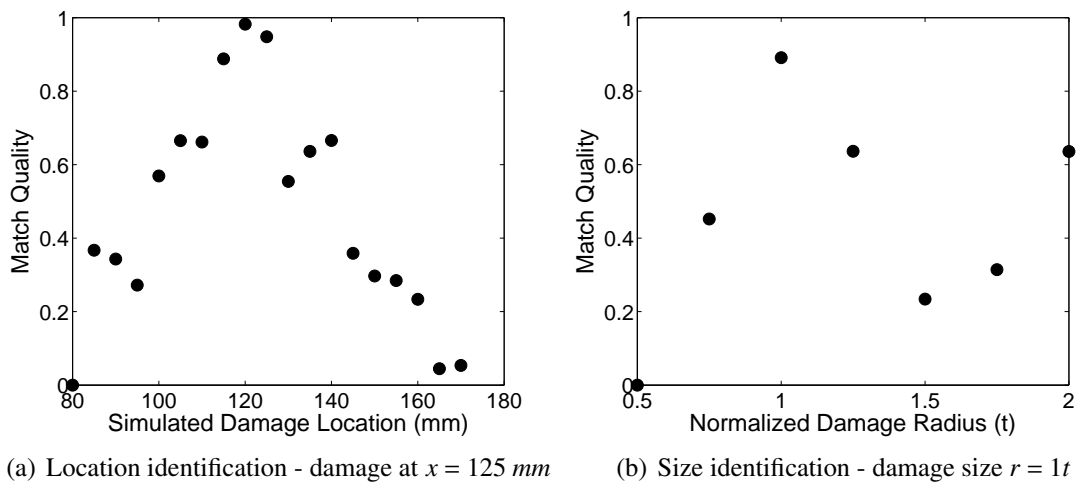


Figure 6.12: Matching pursuit algorithm characterization of experimental hole damage in an aluminum plate. Actual damage size of  $r = 1t$  located at  $x = 125$  mm (1-D analysis, sensor 1 only).

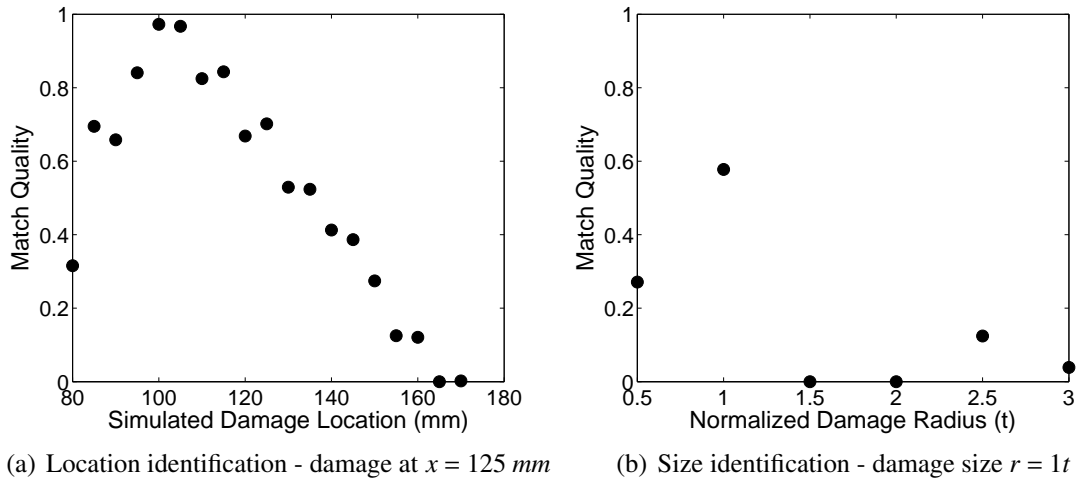


Figure 6.13: Matching pursuit algorithm experimental damage characterization for a cross-ply laminate (1-D analysis, sensor 1 only).

of the results obtained when using the combined library containing three possible sizes for each location. When Eq. 6.9 was used to determine an overall location prediction based on the two best matching simulations, the hole was predicted to be located at 122.5 mm, which is 2.5 mm from the actual location.

Results for the cross-ply laminate are shown in Fig. 6.13. In this case, there was more substantial error between the algorithm's location prediction and the actual damage location. The algorithm identified the simulations with damage at  $x = 100 \text{ mm}$  and  $x = 105 \text{ mm}$  as the best matches, which was 20-25 mm from the actual damage location. An analysis of the sensor signals from the experiment and the simulations showed that the arrival times of the pristine signals correlated well between the experiment and the  $x = 125 \text{ mm}$  damage simulation. However, the damage difference signal in the experiment arrived sooner than what was predicted in the simulation. It is possible that the process of drilling the hole introduced some internal damage in the laminate that extended closer to the sensor, resulting in an early arrival of the damage difference signal. For the hole size identification analysis, the algorithm was able to successfully predict the size of the hole from the six possible sizes in the damage library.

## 6.4 Matching Pursuit Algorithm: 2-D Scenario

The next step in evaluating the matching pursuit algorithm involved extending the library of possible damage locations to a 2-D region. This analysis concentrated on  $r = 1t$  through-thickness hole damage in the cross-ply laminate, and proper location of the hole damage was the primary focus. A schematic showing the location of the actuator, sensors, and possible damage locations is included in Fig. 6.14. For this scenario, two possible actuator locations were simulated. Five sensors were modeled around each actuator. For each possible damage site, simulations were conducted when each actuator was active. Based on the previous conclusion that sensors in the pitch-catch configuration were not optimally placed for this matching pursuit algorithm, only the sensors immediately surrounding the respective actuator were active during the simulations.

### 6.4.1 2-D Analysis Using a Single Sensor

The first stage in the 2-D analysis of the algorithm was to evaluate its location capabilities when only data from sensor 1, resulting from A1 actuation, were used. The results for this scenario are shown in Fig. 6.15. In each of the sub-figures, the darker areas represent locations for which the algorithm predicted a closer match to the actual damage difference signal. The active sensor and actuator positions are also shown on the figures. With only the data from the single sensor, the algorithm produced mixed results. Figure 6.15 (a) shows one of the best cases, where the damage was located at the coordinates (80, 20) with respect to actuator A1, measured in millimeters. For this hole location, the algorithm produced a very accurate location even with only one sensor. A moderately successful result can be seen in Fig. 6.15 (b), which corresponds to a damage location of (120, 60) mm. Here, the algorithm correctly predicted the simulation corresponding to the damage location as the best match, but there were other locations that produced close matches as well. Finally, results for damage located at (50,90) mm are included in Fig. 6.15 (c). The algorithm

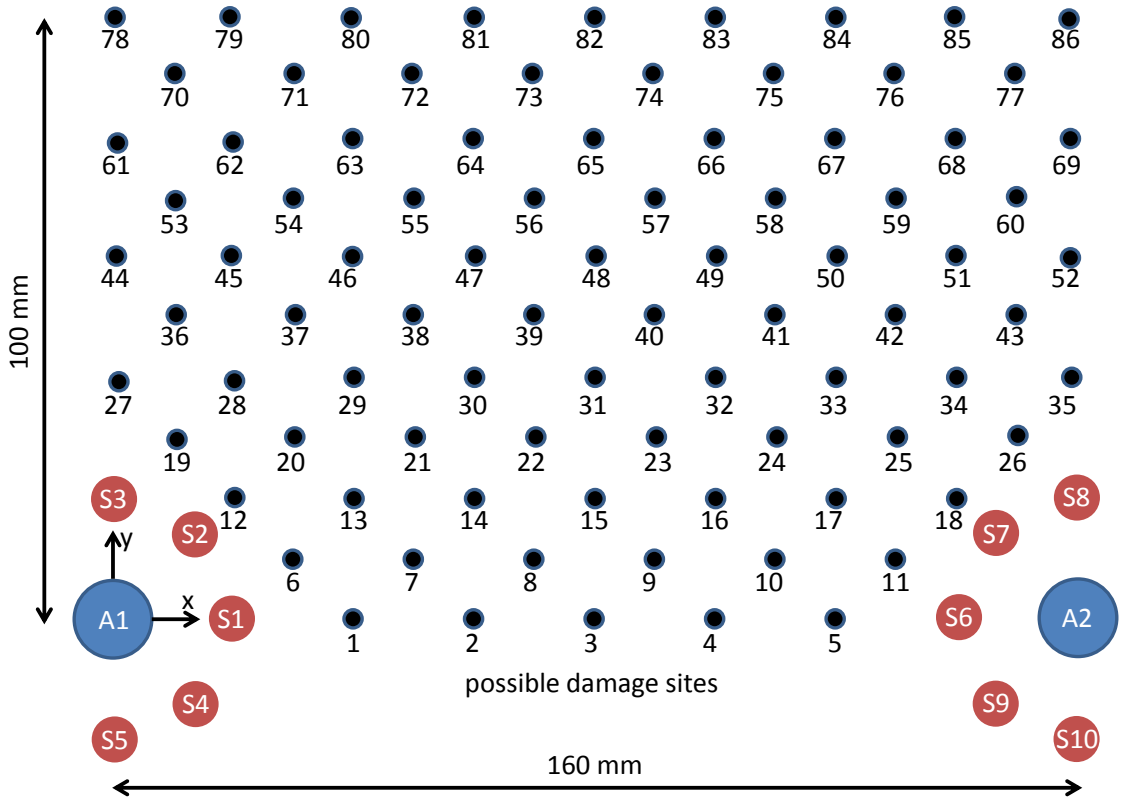


Figure 6.14: Schematic for 2-D matching pursuit analysis showing actuator positions (A1, A2), sensor configuration (S1, S2, ..., S10), and possible locations included in damage library.

indicated that numerous simulations were close matches to the actual damage signal, and the locations for the damage in these simulations formed a large area. In this case, using only one sensor did not provide satisfactory results.

A numerical comparison of these three models was obtained by calculating a predicted location for the damage based on the 4 simulations with the highest reported match quality. The predicted  $x$  position was calculated using:

$$x_{predicted} = \frac{\sum_{j=1}^4 (x_{sim}(j))(MQ(j))}{\sum_{j=1}^4 MQ(j)} \quad (6.10)$$



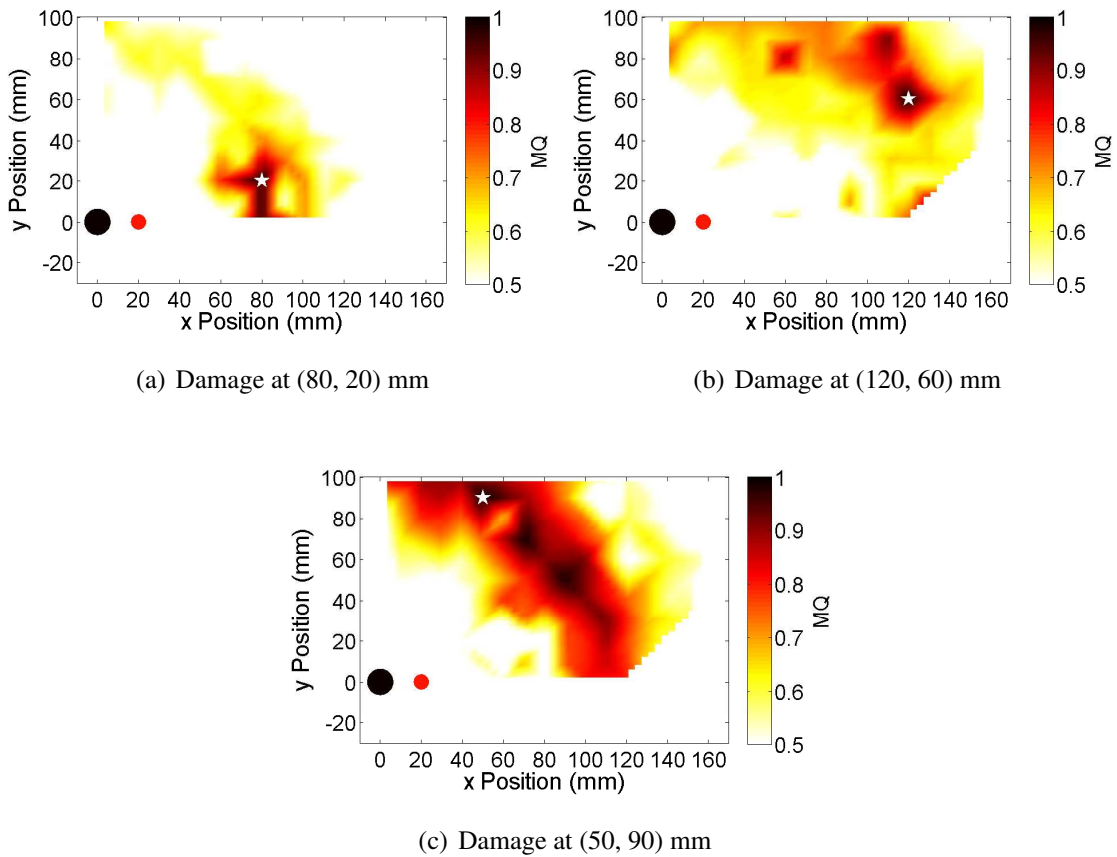


Figure 6.15: Matching pursuit algorithm damage location results for a cross-ply laminate using only sensor S1 (2-D scenario).

A similar equation was used to calculate the predicted y position. The results for the three trials shown in Fig. 6.15 are included in Table 6.2.

Table 6.2: Matching pursuit algorithm damage location results for a cross-ply laminate using only sensor S1 (2-D scenario).

Trial	Actual Location (mm)	Predicted Location (mm)	Error (mm)
1	(80, 20)	(77.5, 16.4)	4.3
2	(120, 60)	(105.3, 60.7)	14.7
3	(50, 90)	(79.4, 60.6)	41.5

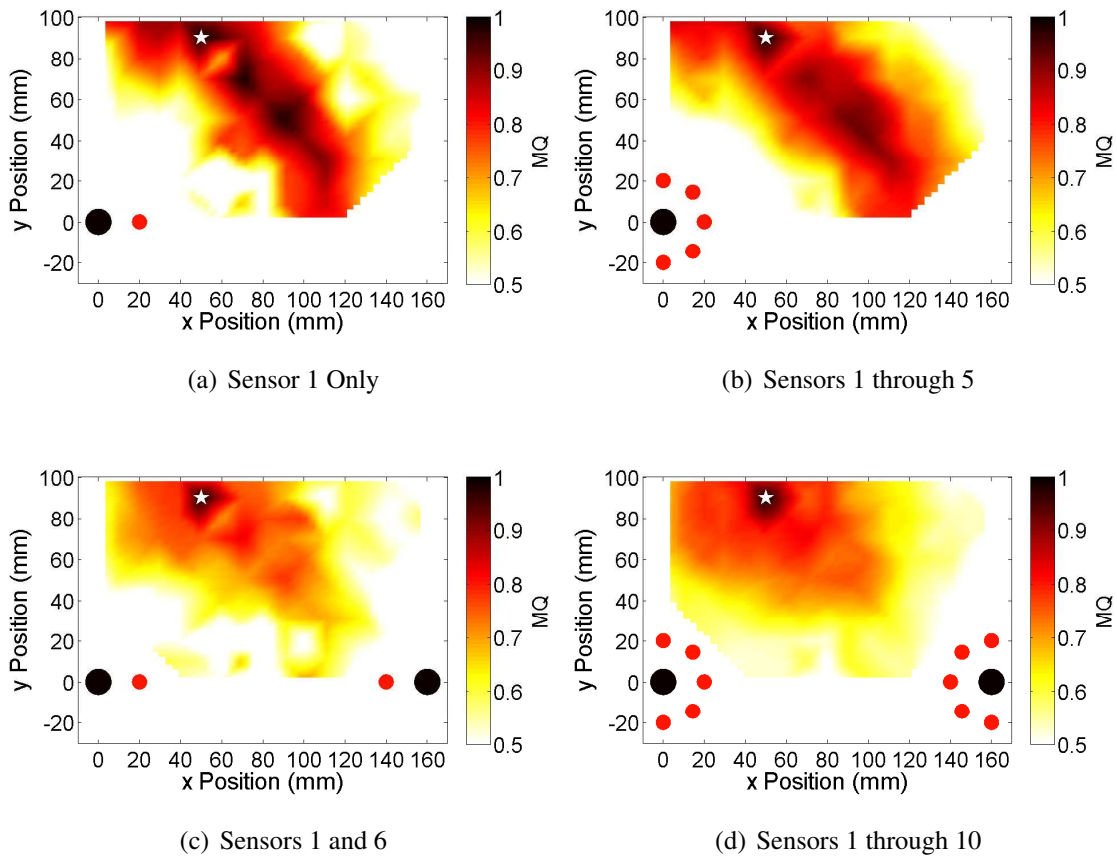


Figure 6.16: Improvement in matching pursuit algorithm location results for a cross-ply laminate when data from multiple sensors are used (2-D scenario with hole at (50, 90) mm).

## 6.4.2 Effect of Using Multiple Sensor and Actuator Locations

Because one sensor alone did not reliably locate the damage in all cases, additional sensors were added to the algorithm to aid in locating the damage. This involved running the matching pursuit algorithm individually for each sensor, and then averaging the results of each of the sensors included in the analysis.

The effect of including multiple sensors in the algorithm is illustrated in Fig. 6.16 for damage located at (50, 90) mm. The previously shown case where only sensor S1 was used is shown again in sub-figure (a). In sub-figure (b), results are shown for the algorithm when each of the five sensors (S1-S5) surrounding actuator A1 were used. It is evident in this

Table 6.3: Improvement in matching pursuit algorithm location results for a cross-ply laminate when data from multiple sensors are used (2-D scenario with hole at (50, 90) mm).

Case	Predicted Location (mm)	Error (mm)
A1/S1	(79.4, 60.6)	41.5
A1/S1-S5	(77.0, 63.0)	38.2
A1/S1; A2/S6	(61.8, 78.2)	16.7
A1/S1-S5; A2/S6-S10	(54.7, 85.3)	6.6

figure that many of the incorrect damage locations have lightened in intensity, indicating their match quality has diminished. A different approach was to include both actuators with only one sensor associated with each, as shown in sub figure (c). In this case, actuator A1 was used with sensor S1, and actuator A2 was used with sensor S6. Even better results were obtained when both actuators and each of their corresponding sensors were used. In sub-figure (d), the results are for the case where sensors S1 through S5 were used for actuator A1 excitation and sensors S6 through S10 were used for actuator A2 excitation. When the results for all 10 sensors were averaged, an accurate location was reported without any regions of conflicting matches. Table 6.3 shows how the predicted hole location improved in accuracy as the number of actuators and sensors increased. It is notable that adding a second actuator/sensor pair had a much more significant effect on location accuracy than increasing the number of sensors used with a particular actuator from 1 to 5.

Damage location results from the analysis of four additional damage sites are included in Fig. 6.17. All 10 sensors were used in each of these cases, and in each case the matching pursuit algorithm was able to locate the hole damage to within 4 mm when considering the four best-matching simulations. Numerical results are shown in Table 6.4.

### 6.4.3 Location of Holes Not Included in Damage Library

In each of the scenarios included to this point in the 2-D analysis, the actual damage location corresponded to a location captured by one of the damage library simulations. Because

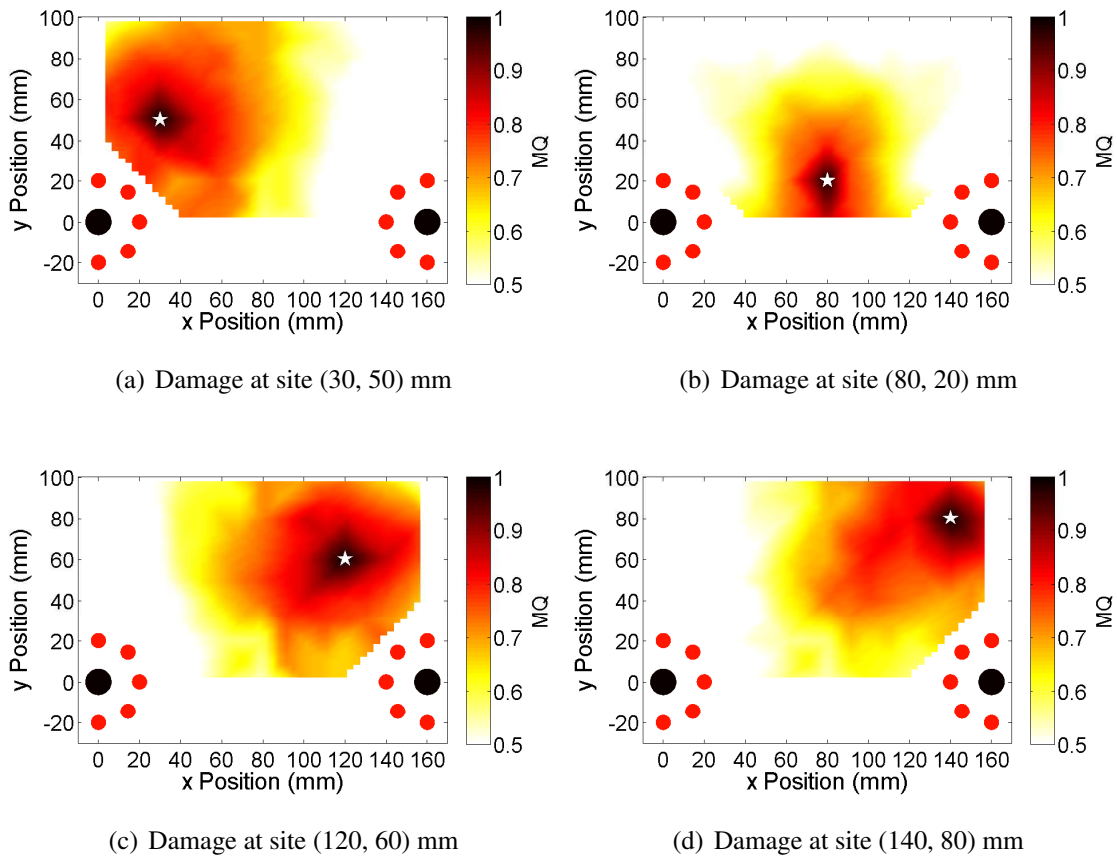


Figure 6.17: Matching pursuit algorithm location results for a cross-ply laminate at various damage sites when all 10 sensors are used (2-D scenario).

of this, each set of location results contained one location that was a perfect match. This section considers a few cases where the actual damage signal comes from a hole location not included in any of the library simulations. Ideally, the matching pursuit algorithm

Table 6.4: Matching pursuit algorithm location results for a cross-ply laminate at various damage sites when all 10 sensors are used (2-D scenario).

Trial	Actual Location (mm)	Predicted Location (mm)	Error (mm)
1	(30, 50)	(32.4, 52.3)	3.4
2	(80, 20)	(82.3, 17.2)	3.6
3	(120, 60)	(119.9, 59.9)	0.2
4	(140, 80)	(142.5, 77.5)	3.6

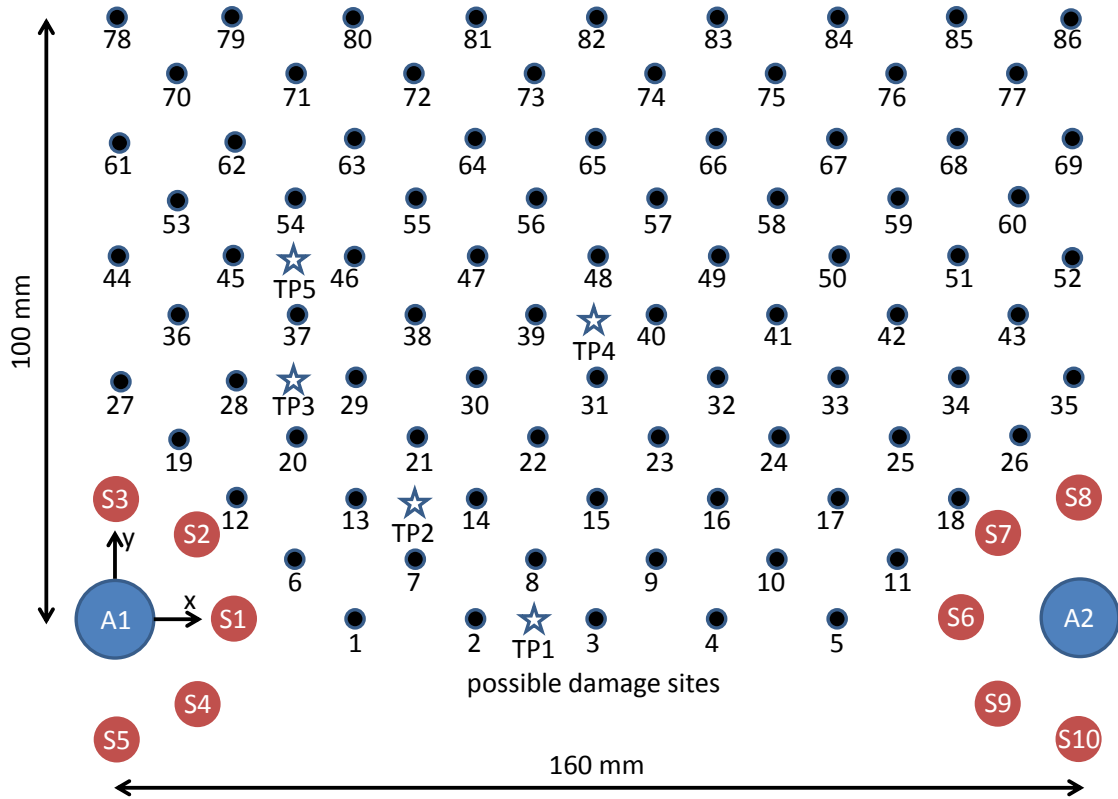


Figure 6.18: Location of non-collocated simulated test points (TP1-TP5) for 2-D analysis.

should identify the damage library simulations that are closest to these new damage points as the most likely matches for the damage. Figure 6.18 shows the location of the new damage points. LISA simulations were run to obtain the damage difference signals for each of the sensors for each of these damage locations. Each of these new difference signals were then used as the actual difference signals in the algorithm. The graphical location results for these cases are shown in Fig. 6.19, and a numerical comparison is included in Table 6.5. For the cases considered, the location error ranged from 0.1 mm to 14.6 mm.

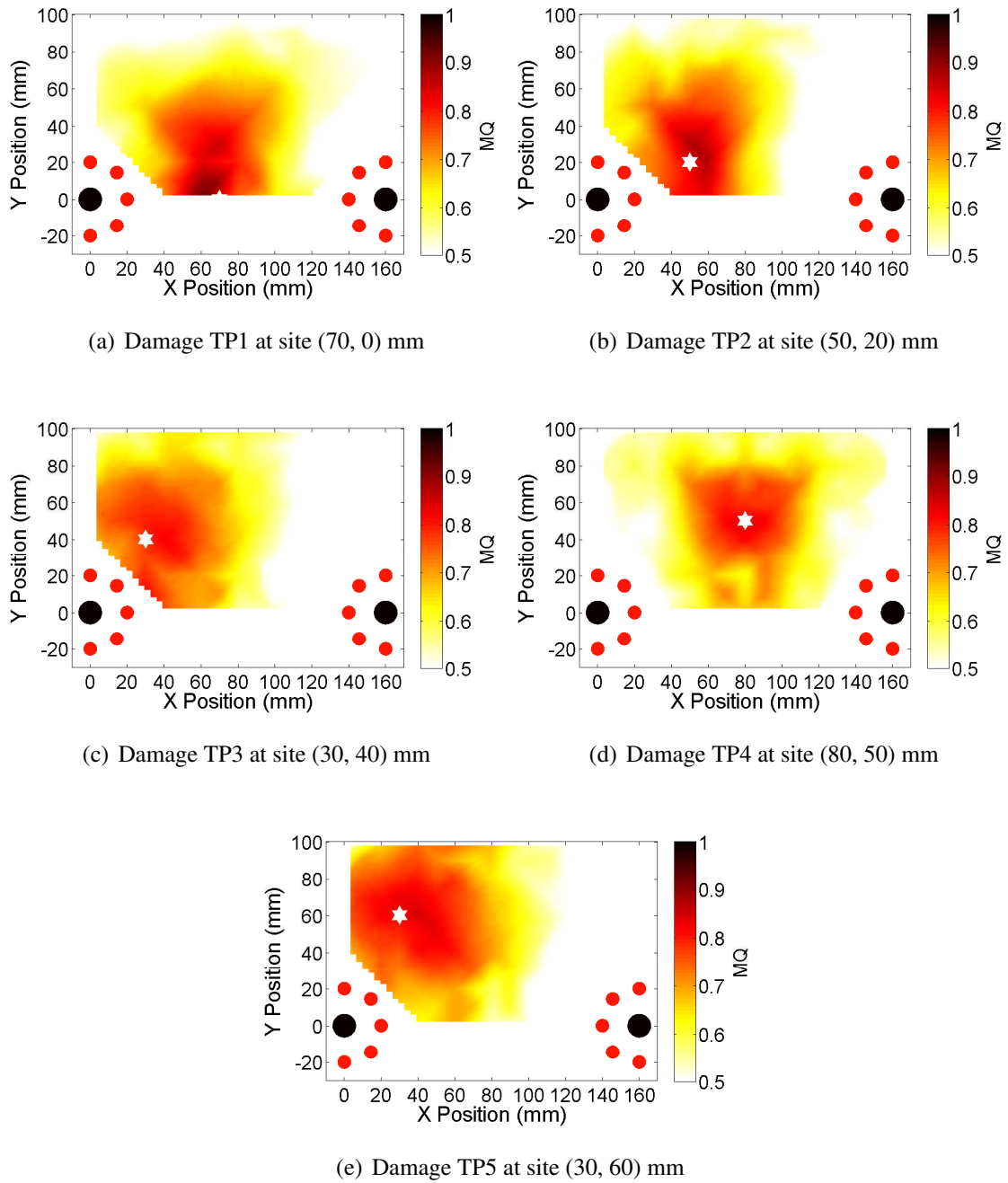


Figure 6.19: Matching pursuit algorithm location results for a cross-ply laminate with damage at non-simulated locations (2-D scenario).

Table 6.5: Matching pursuit algorithm location results for a cross-ply laminate with damage at non-simulated locations (2-D scenario).

Trial	Actual Location (mm)	Predicted Location (mm)	Error (mm)
TP1	(70, 0)	(65.0, 14.6)	14.6
TP2	(50, 20)	(57.4, 22.5)	7.6
TP3	(30, 40)	(37.5, 32.4)	10.7
TP4	(80, 50)	(80.0, 49.9)	0.1
TP5	(30, 60)	(35.1, 60.0)	5.1

## 6.5 Summary

This chapter described a new damage characterization tool for guided wave SHM based on matching pursuits and LISA. Results from the 1-D scenario showed the algorithm's ability to predict the correct location of hole damage and the correct hole size in trial cases involving isotropic plates and cross-ply laminates. The algorithm was shown to be useful even in the case of excessive noise, and it was able to closely identify the location of experimental hole damage in an aluminum plate. It was determined that data from a sensor in the pulse-echo configuration were better suited to locating damage than data from a sensor in the pitch-catch configuration. It is expected that if both sensors are used, the location accuracy results will fall in the middle of the two individual sensor cases, since the data from the pitch-catch sensor will add uncertainty to the location prediction.

Demonstration of the algorithm in a 2-D scenario for a cross-ply laminate further reinforced its damage location capability. A sparse array of possible hole damage locations were included in the library of damage simulations. Results showed that using information from multiple sensors improved the location prediction, and including information from sensors associated with multiple actuators further improved the accuracy of the prediction. The algorithm was able to closely predict the location of simulated hole damage even when the exact hole location was not contained in the library of possible damage sites, with location errors ranging from 0.1 mm to 14.6 mm for the cases considered.

## CHAPTER 7

### Concluding Remarks

This chapter concludes the dissertation by reviewing the important conclusions and contributions. First, the dissertation is summarized and important conclusions are reiterated. Next, the key contributions of this dissertation are highlighted. Finally, recommendations for future work are offered.

#### 7.1 Summary

The work contained in this dissertation included theoretical, numerical, and experimental efforts to advance the state of the art in the field of guided wave structural health monitoring. The first portion of the dissertation used the Global Matrix Method to develop accurate wave propagation time histories. It was shown that both inward and outward propagating waves are present in the general solution for wave propagation in laminates with transversely isotropic lamina. Previous methods to isolate the inward wave and produce displacement time histories for the isotropic case were successful, but attempts to do the same for cross-ply laminates left artifacts of the inward wave. An updated solution method was presented, showing that when properly executed, the Global Matrix Method produces very accurate displacement solutions.

The next major effort in the dissertation developed the LISA hybrid simulation framework. Examination of previous LISA implementations showed that modeling actuators



using prescribed displacement methods based on *ad-hoc* assumptions did not produce solutions that match well with semi-analytical results. This was true even for square actuators where representing the shape of the actuator in the Cartesian grid was not a challenge. Wave propagation results from the LISA hybrid model matched well with theoretical results for isotropic, unidirectional, cross-ply, and quasi-isotropic laminates. A discretization study showed that a cell size of  $\frac{1}{6}t \times \frac{1}{6}t \times \frac{1}{12}t$  was sufficient, while coarser cell sizes produced artificially fast group velocities.

The next two chapters employed the LISA hybrid model to characterize damage in plate-like structures. First, the effect of holes on guided wave propagation was investigated using both simulations and experimental results. Both isotropic plates and cross-ply laminates were considered. For through-thickness holes in the isotropic case, the highest damage difference signals were seen on the back side of the hole. The smallest difference signals were present 45 degrees from that direction. For the composite case, results indicated the difference signal energy followed the predominant fiber directions. Results for damage located in the 45-degree direction relative to the top fiber direction showed that sensors in traditional pulse-echo and pitch-catch were not necessarily in the best place to capture the largest difference signals. The simulations also demonstrated that the LISA model properly captured mode conversions seen frequently in damage that is not uniform through the thickness, such as a half-depth hole.

After studying holes, the second focus of the LISA simulation studies was low-velocity impact damage. Specimens that were damaged with a drop-weight impact device were inspected using an X-ray CT scan, and diagnostic images of the damage showed a combination of matrix cracking and delamination as the two primary damage modes. The information from these images was used to develop a model of the impact damage in LISA. A parameter study of this LISA model showed that changing stiffness and density values in various regions changed the behavior of the damage difference signals observed in the model. It was also found that adding a void layer as a rough representation of a large de-

lamination increased the accuracy of the model. Comparison of the LISA impact damage model with experimental results showed a good overall agreement in the amplitudes of the difference signals. An in-depth comparison of the time histories showed one major deficiency of the LISA model was its inability to capture the amplitude of the  $A_0$ - $S_0$  and  $S_0$ - $A_0$  mode conversions that reflect back toward the actuator.

With LISA's ability to model guided wave interactions with damage mostly demonstrated, the model was then used as the backbone of a novel damage characterization tool based on the matching pursuit method. The new algorithm used the matching pursuit method to decompose damage difference signals into a set of usable parameters. A LISA library of damage signals was formed, and sample difference signals from simulations and experiments were compared to the library to characterize the location and size of the damage. A match quality metric based 75% on the difference in frequency centers and 25% on the difference in time centers showed good results. Studies with a 1-D scenario showed the algorithm was successful in locating and sizing damage when using a sensor in the pulse-echo configuration. Sensors in the pitch-catch configuration did not produce accurate location results. Results of a 2-D study showed significant benefits in using multiple actuators with several associated sensors. The 2-D algorithm closely identified the location of simulated damage even when the exact location wasn't captured in the damage library

## 7.2 Key Contributions

This dissertation included several key contributions to advance the state of the art, which are briefly summarized below. This work:

- Formulated a new method to perform the 2-D Fourier inversions needed to calculate displacement time histories using the Global Matrix Method. The procedure corrects for the presence of non-physical inward propagating waves in the general solution.

- Developed the LISA hybrid model to accurately capture actuation behavior of piezoelectric actuators. The model correctly captures the tractions applied by surface-mounted actuators, eliminates the need to make *ad-hoc* assumptions about prescribed displacements, and eliminates difficulties involved with discretizing non-rectangular actuators in a Cartesian grid.
- Produced the first experimentally-verified evaluation of LISA hole damage simulations. Quantified the agreement between the damage difference signals recorded by experimental and simulated sensors. Advantages and disadvantages of particular sensor locations were highlighted.
- Developed and evaluated a LISA damage model based on experimental investigation of laboratory-produced impact damage. Demonstrated that in numerical models, reduction of elastic properties alone does not accurately represent the effects of impact damage on guided wave propagation.
- Introduced a new matching pursuit algorithm that uses a library of LISA simulations to characterize damage. Experimentally verified the algorithm for a 1-D scenario, and demonstrated the algorithm in a 2-D scenario using simulated damage signals.

### **7.3 Recommendations for Future Work**

Based on the results of this dissertation, there are several key areas that warrant attention in future research efforts.

- The time needed to run the LISA simulations that were developed and employed in this study needs to be reduced. The LISA formulation naturally lends itself to parallelization, but the versions of the code used for this study only scratch the surface of that potential. Parallel computing solutions that utilize graphics processing cards have become increasingly popular, and applying these to make the LISA codes more

efficient would be a wise path forward. Decreasing the time cost of the individual simulations would allow for more comprehensive parametric studies.

- Reduced computational time would facilitate another important next step, which is to model smaller composite damage features such as individual matrix cracks and delaminations. Currently, the level of discretization needed to keep the simulation size tractable prevents the formation of a fine mesh around these damage types. A related research direction would be the formulation of a multi-scale version of LISA that allows for regions of finer discretization in regions of simulated damage.
- Delamination was simulated in this dissertation as a void region spanning the thickness of one layer. A future direction for LISA development should focus on a more rigorous model to capture the effects of delamination. Previous finite element efforts have developed ways to release nodes along a delaminated interface. It may be possible to use a similar technique in LISA. It may also be possible to model a delaminated interface as a series of springs between nodes. These options should be considered. Additionally, it is known that delaminations produce nonlinear effects, and the feasibility of developing a nonlinear LISA formulation should be investigated.
- This dissertation highlighted several difficulties when using laser vibrometer experiments along with a baseline subtraction method to form damage difference signals. Future studies should develop better ways to ensure a precise alignment between the scan points for the pristine and post-damage measurements. Different options to support the plate should be explored. If placement of the plate cannot be done more reliably, it may be possible to adjust the scan points themselves within the user interface environment. The ability to use the laser vibrometer to capture out-of-plane motion is valuable, and reducing the experimental variability in the measurements would be an important step forward.

- The impact damage studies in this dissertation considered only cross-ply laminates. There are no guarantees that the impact damage features identified in the CT imagery would appear in the same way in other laminates (uni-directional and quasi-isotropic, for example). The LISA impact damage model developed in this dissertation should be evaluated with other laminates, and it should be refined to better capture the damage features present in those cases.
- The LISA models and experiments presented in this dissertation agreed well in many cases. However, there were a few times where the results showed discrepancies that do not have clear causes. In the aluminum hole experiment, the sensor 5 difference signal was considerably higher than that predicted by the simulation. The impact damage experiment for the 90-degree location showed a higher-than-expected difference signal amplitude at sensor 4 compared to the other sensors. Most notably, the difference signal amplitude for the 45-degree impact damage experiment was significantly higher than in the LISA model. Additional experiments should be conducted to determine if these anomalies can be reproduced.
- The studies in this dissertation focused on laminated composite plates, but many realistic structures are based on sandwich construction with foam or honeycomb cores. Some previous work exists that applies LISA to sandwich panels, but considerable study is needed to refine these models. From a damage modeling standpoint, techniques to capture delamination between the face sheet and core material need to be developed for LISA.
- The matching pursuit algorithm presented in this dissertation can be advanced in a few important ways. First, it would be advisable to continue the experimental validation of the algorithm, especially for the 2-D scenario covered in this work. Another logical step forward is the incorporation of the CLoVER actuator into the matching pursuit scheme. The arrangement of actuator and sensors used in the 2-D scenario

could easily be replaced by a single CLoVER, where each sector could be used as a sensor and actuator in a rotating manner. Finally, the algorithm should be extended to use more than the first matched atom from each matching pursuit decomposition. This extension should enable more accurate identification of the correct damage parameters, and it will also enable the identification of multiple damage sites affecting an experimental difference signal.

## APPENDIX A

### Eigenvectors for Global Matrix Method

The formulation of the displacement and stress eigenvectors used in the Global Matrix Method is included here as a reference. These eigenvectors are based on those found in Refs. [59] and [62]. The stiffness matrix for a transversely isotropic lamina is represented as:

$$\mathbf{S} = \begin{bmatrix} S_{11} & S_{12} & S_{13} & 0 & 0 & 0 \\ S_{12} & S_{22} & S_{23} & 0 & 0 & 0 \\ S_{13} & S_{23} & S_{33} & 0 & 0 & 0 \\ 0 & 0 & 0 & S_{44} & 0 & 0 \\ 0 & 0 & 0 & 0 & S_{55} & 0 \\ 0 & 0 & 0 & 0 & 0 & S_{66} \end{bmatrix} \quad (\text{A.1})$$

Then, the squares of the bulk wave velocities are represented as:

$$\begin{aligned} a_1 &= S_{22}/\rho \\ a_2 &= S_{11}/\rho \\ a_3 &= (S_{12} + S_{55})/\rho \\ a_4 &= (S_{22} - S_{23})/2\rho = S_{44}/\rho \\ a_5 &= S_{55}/\rho \end{aligned} \quad (\text{A.2})$$

As explained in Chapter 2, harmonic excitation is assumed,

$$\mathbf{u} = \mathbf{C}e^{-i(\xi_1 x_1 + \xi_2 x_2 + \zeta x_3 - \omega t)} \quad (\text{A.3})$$

which allows for the formation of the Christoffel equation:

$$\begin{bmatrix} S_{11}\xi_1^2 + S_{55}(\xi_2^2 + \zeta^2) & (S_{12} + S_{55})\xi_1\xi_2 & (S_{12} + S_{55})\xi_1\zeta \\ (S_{12} + S_{55})\xi_1\xi_2 & S_{55}\xi_1^2 + S_{22}\xi_2^2 + S_{44}\zeta^2 & (S_{23} + S_{44})\xi_2\zeta \\ (S_{12} + S_{55})\xi_1\zeta & (S_{23} + S_{44})\xi_2\zeta & S_{55}\xi_1^2 + S_{44}\xi_2^2 + S_{22}\zeta^2 \end{bmatrix} \begin{bmatrix} u_1 \\ u_2 \\ u_3 \end{bmatrix} = \rho\omega^2 \begin{bmatrix} u_1 \\ u_2 \\ u_3 \end{bmatrix} \quad (\text{A.4})$$

The three pairs of solutions for the through-thickness wavenumber are given by,

$$\begin{aligned} \zeta_1^2 &= -\xi_2^2 + b_1 \\ \zeta_2^2 &= -\xi_2^2 + b_2 \\ \zeta_3^2 &= -\xi_2^2 + (\omega^2 - a_5\xi_1^2)/a_4 \end{aligned} \quad (\text{A.5})$$

where the  $b_1$  and  $b_2$  constants are found from:

$$\begin{aligned} b_1 &= -\left(\frac{\beta}{2\alpha}\right) - \sqrt{\left(\frac{\beta}{2\alpha}\right)^2 - \frac{\gamma}{\alpha}} \\ b_2 &= -\left(\frac{\beta}{2\alpha}\right) + \sqrt{\left(\frac{\beta}{2\alpha}\right)^2 - \frac{\gamma}{\alpha}} \\ \alpha &= a_1 a_5 \\ \beta &= (a_1 a_2 + a_5^2 - a_3^2)\xi_1^2 - \omega^2(a_1 + a_5) \\ \gamma &= (a_2\xi_1^2 - \omega^2)(a_5\xi_1^2 - \omega^2) \end{aligned} \quad (\text{A.6})$$



The displacement eigenvectors can then be formed as,

$$\begin{aligned}
\mathbf{e}_1 &= \begin{bmatrix} i\xi_1 q_{11} & i\xi_2 q_{21} & i\zeta_1 q_{21} \end{bmatrix}^T \\
\mathbf{e}_2 &= \begin{bmatrix} i\xi_1 q_{12} & i\xi_2 q_{22} & i\zeta_2 q_{22} \end{bmatrix}^T \\
\mathbf{e}_3 &= \begin{bmatrix} 0 & i\zeta_3 & i\xi_2 \end{bmatrix}^T \\
\mathbf{e}_4 &= \begin{bmatrix} i\xi_1 q_{11} & i\xi_2 q_{21} & -i\zeta_1 q_{21} \end{bmatrix}^T \\
\mathbf{e}_5 &= \begin{bmatrix} i\xi_1 q_{12} & i\xi_2 q_{22} & -i\zeta_2 q_{22} \end{bmatrix}^T \\
\mathbf{e}_6 &= \begin{bmatrix} 0 & -i\zeta_3 & i\xi_2 \end{bmatrix}^T
\end{aligned} \tag{A.7}$$

where the  $q_{ij}$  terms are represented as:

$$\begin{aligned}
q_{11} &= a_3 b_1 \\
q_{12} &= a_3 b_2 \\
q_{21} &= \omega^2 - a_2 \xi_1^2 - a_5 b_1 \\
q_{22} &= \omega^2 - a_2 \xi_1^2 - a_5 b_2
\end{aligned} \tag{A.8}$$

At this point, it is possible to form the complete displacement and stress eigenvector matrices  $Q_{ij}^m$  for each lamina using the following formulas:

$$\begin{aligned}
Q_{11}^m &= \begin{bmatrix} \mathbf{e}_1^m & \mathbf{e}_2^m & \mathbf{e}_3^m \end{bmatrix} \\
Q_{12}^m &= \begin{bmatrix} \mathbf{e}_4^m & \mathbf{e}_5^m & \mathbf{e}_6^m \end{bmatrix} \\
Q_{21}^m &= \begin{bmatrix} -\rho a_5 \xi_1 \zeta_1 (q_{11} + q_{21}) & -\rho a_5 \xi_1 \zeta_2 (q_{12} + q_{22}) & \rho a_5 \xi_1 \xi_2 \\ -2\rho a_4 \xi_2 \zeta_1 q_{21} & -2\rho a_4 \xi_2 \zeta_2 q_{22} & \rho a_4 (\xi_2^2 - \zeta_3^2) \\ \mu_1 & \mu_2 & 2\rho a_4 \xi_2 \zeta_3 \end{bmatrix} \\
Q_{22}^m &= \begin{bmatrix} \rho a_5 \xi_1 \zeta_1 (q_{11} + q_{21}) & \rho a_5 \xi_1 \zeta_2 (q_{12} + q_{22}) & \rho a_5 \xi_1 \xi_2 \\ 2\rho a_4 \xi_2 \zeta_1 q_{21} & 2\rho a_4 \xi_2 \zeta_2 q_{22} & \rho a_4 (\xi_2^2 - \zeta_3^2) \\ \mu_1 & \mu_2 & -2\rho a_4 \xi_2 \zeta_3 \end{bmatrix}
\end{aligned} \tag{A.9}$$

with:

$$\begin{aligned}\mu_1 &= \rho \left[ (a_5 - a_3) \xi_1^2 q_{11} - (a_1 - 2a_4) \xi_2^2 q_{21} - a_1 \zeta_1^2 q_{21} \right] \\ \mu_2 &= \rho \left[ (a_5 - a_3) \xi_1^2 q_{12} - (a_1 - 2a_4) \xi_2^2 q_{22} - a_1 \zeta_1^2 q_{22} \right]\end{aligned}\tag{A.10}$$

## APPENDIX B

### Global Matrix Forcing Terms for CLoVER

The final actuator type considered in this dissertation is the Composite Long-range Variable-direction Emitting Radar. An example of it is shown in Fig. B.1. This actuator has not previously been incorporated into the Global Matrix Method, and determination of the transformed forcing vector needed to accomplish this is a more lengthy process. However, a strategy for representing the tractions from a CLoVER sector was developed by Salas and Cesnik [37] to facilitate an exact isotropic solution, and that process can be adapted to produce the forcing terms needed for the Global Matrix Method. For a given CLoVER sector, the components of the forcing vector can be represented as,

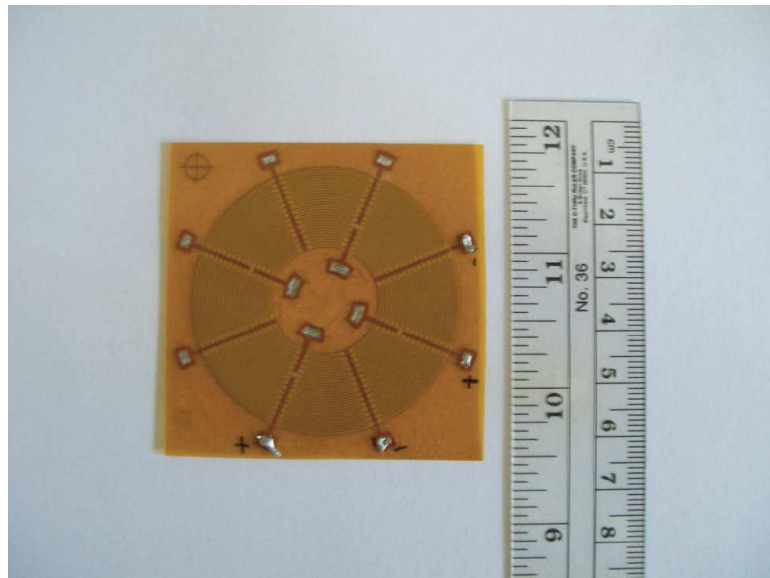


Figure B.1: CLoVER actuator.

$$\begin{aligned}
F_1 &= \int_0^{2\pi} \int_0^{\infty} [u(\theta - \theta_L) - u(\theta - \theta_R)][\delta(r - R_I) - \delta(r - R_O)] \cos(\theta) e^{iKr \cos(\theta - \Gamma)} r dr d\theta \\
F_2 &= \int_0^{2\pi} \int_0^{\infty} -[u(\theta - \theta_L) - u(\theta - \theta_R)][\delta(r - R_I) - \delta(r - R_O)] \sin(\theta) e^{iKr \cos(\theta - \Gamma)} r dr d\theta
\end{aligned} \tag{B.1}$$

where  $\theta_L, \theta_R$  represent the azimuthal boundaries of the sector of interest and  $R_I, R_O$  are its radial boundaries. The  $u()$  term is the Heaviside step function and  $\delta()$  is the Dirac delta function. The integrals in Eq. B.1 do not have a closed-form solution, but it is possible to use a Fourier series representation of the forcing terms to circumvent this difficulty:

$$F_j = \sum_{M=-\infty}^{\infty} c_M^{(j)} e^{iM\Gamma} (-i)^M 2\pi [R_O J_M(KR_O) - R_I J_M(KR_I)] \quad j = 1, 2 \tag{B.2}$$

In Eq. B.2, the  $c_M$  terms are Fourier coefficients that must be calculated for each direction and each term of the series. The formulas for these coefficients can be found in Ref. [37]. In that work, it is also noted that satisfactory results can be obtained while only including the first 150 positive and negative terms of the Fourier series.

## APPENDIX C

### Implementation of Global Matrix Method

The theoretical background for the Global Matrix Method was presented in Chapter 2. This appendix provides some of the practical knowledge needed to develop displacement time histories, and it includes the procedures for building the complete displacement files used in the LISA hybrid method described in Chapter 3. A block diagram showing the data flow between the various programs is shown in Fig. C.1. This diagram is for the case of a circular actuator, and the process for a rectangular actuator is virtually identical. The process for the CLoVER case is shown later in this appendix. The complete procedure uses a combination of FORTRAN and MATLAB scripts, and each of these are explained here.

#### C.1 Description of Global Matrix Input File

A single input file (`GlobalMatrix_InputFile.txt`) is used to specify the parameters for each of the three FORTRAN scripts used in the Global Matrix procedure. The file contains 17 entries along with one additional entry for each layer of the laminate. The contents of the file are as follows:

- **Mode:** This entry specifies whether the calculations are for the  $A_0$  (value of 1) or  $S_0$  mode (value of 2).

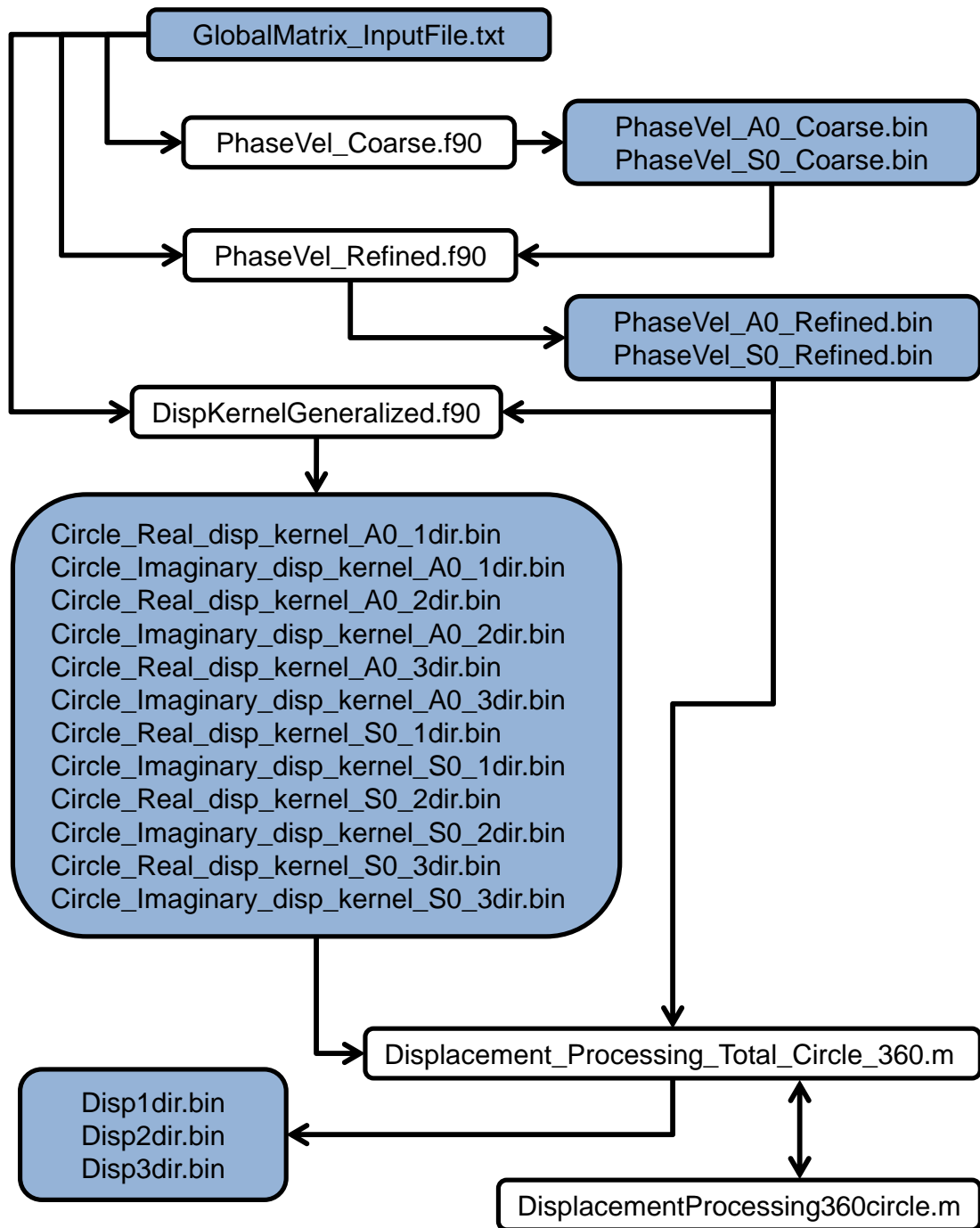


Figure C.1: Global Matrix process for a circular actuator.

- Actuator Type: This entry is set to 1 for a circular actuator, 2 for a rectangular actuator, and 3 for a CLoVER actuator.
- Rectangular Actuator Length: This is the first of two dimensions needed if a rectangular actuator is being considered. The length is measured in meters.
- Rectangular Actuator Width: Measured in meters.
- Coarse Search Parameter: This parameter is used in the coarse phase velocity calculations.
- Refined Search Parameter: This parameter is used in the refined phase velocity calculations.
- Start Value: This is an initial guess for the coarse phase velocity calculations.
- $E_1$ : Elastic modulus along the fiber direction for the lamina (Pa).
- $E_2$ : Elastic modulus transverse to the fiber direction for the lamina (Pa).
- $\nu_{12}$ : Poisson's ratio value.
- $\nu_{23}$ : Poisson's ratio value.
- $G_{12}$ : Shear modulus value (Pa).
- Density: Density of bulk material in  $\text{kg/m}^3$ .
- Thickness: Total thickness of the plate in meters.
- Angular Resolution: This sets the angular resolution of the phase velocity calculations, measured in degrees. A resolution of 0.1 degrees was used in this dissertation, and coarser angular resolution resulted in errors in the calculated displacement time histories.

- Frequency Resolution: This sets the frequency resolution of the phase velocity calculations, measured in kHz. A resolution of 0.1 kHz worked well in the studies contained in this dissertation.
- Number of Layers
- Layer Orientations: Measured in degrees.

## C.2 Coarse Calculation of Phase Velocities

The first major section of the Global Matrix Method involves the calculation of the admissible phase velocities for the laminate. The procedure implemented in this dissertation uses two FORTRAN scripts to do these calculations: `PhaseVel_Coarse.f90` and `PhaseVel_Refined.f90`. The first set of calculations uses the `PhaseVel_Coarse.f90` source code. Before this program is run, it must be compiled using a suitable makefile with a FORTRAN compiler. This makefile ensures the appropriate libraries from the LAPACK linear algebra library are included in the executable.

This coarse calculation is designed to generate an initial guess for the admissible phase velocity for the laminate in the 0-degree direction at each desired frequency. A block diagram of this program is shown in Fig. C.2. In this figure, the processes is shown for the case of the  $A_0$  mode. This program must be run for both fundamental modes if both modes are to be included in the displacement solution. The first steps in the program define each of the variables to be used and load the needed values from the input file. An output file is also opened to allow for data recording later in the program.

The main program contains two nested loops. It loops through a defined frequency range, which includes the frequencies expected to be present in the excitation of the plate. This loop progresses through the frequency range according to the frequency resolution defined in the input file. For each frequency, the program then loops through a specified



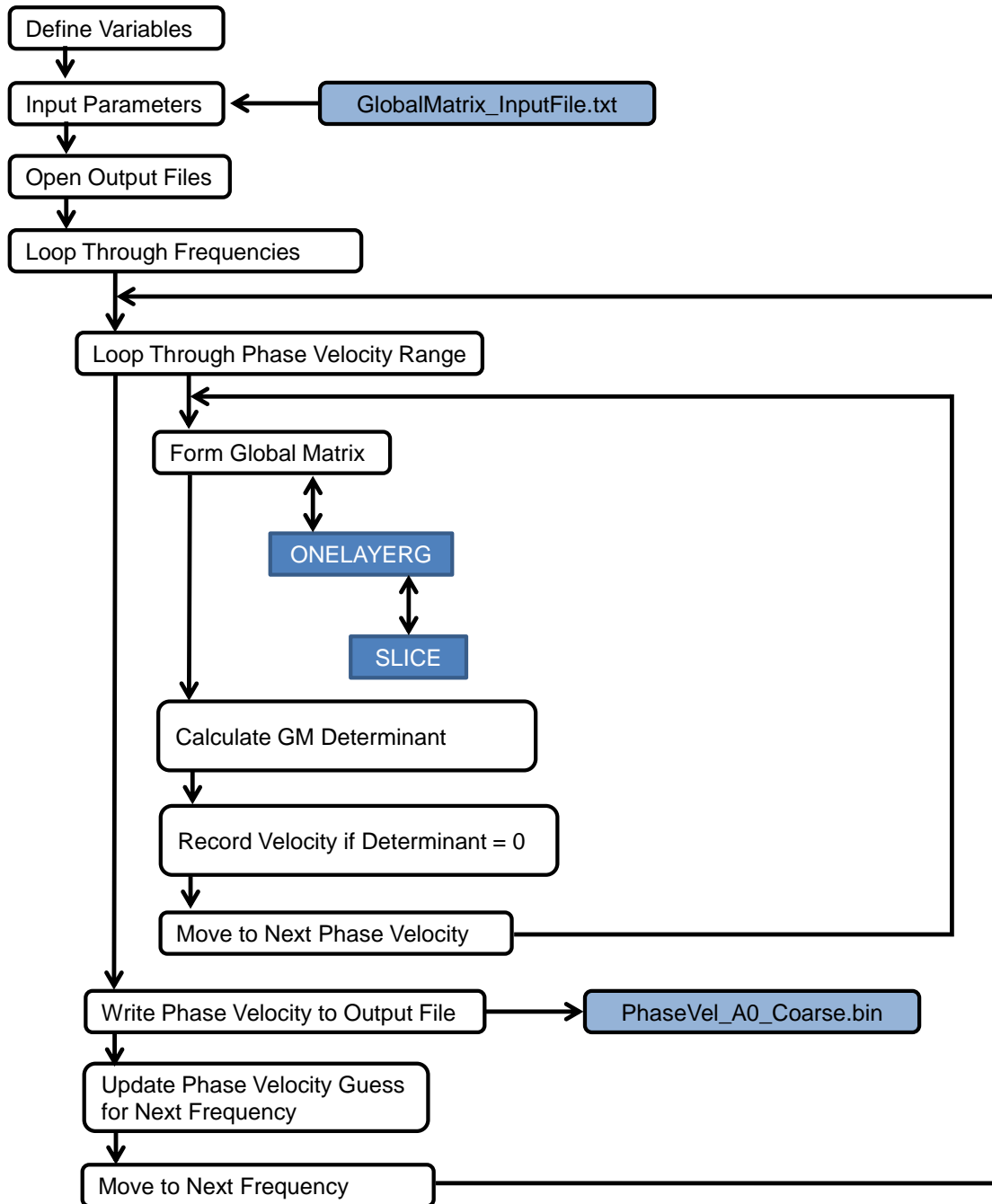


Figure C.2: Block diagram of coarse phase velocity program (PhaseVel\_Coarse.f90).

range of possible phase velocities. This range of velocities is initially defined using the start value and the coarse search parameter from the input file.

At each possible phase velocity, the program assembles the Global Matrix for the laminate corresponding to that velocity. Two subroutines aid in this process. The `ONELAYERG` subroutine assembles a series of submatrices that are defined using the `SLICE` subroutine. The `SLICE` subroutine calculates the contribution of each individual lamina to the Global Matrix, and the `ONELAYERG` subroutine then arranges these into the appropriate positions in the Global Matrix.

After the Global Matrix is formed, the next section of the program uses LU decomposition to calculate the determinant of the Global Matrix. This program uses a zero-crossing approach to determine the admissible phase velocities for the laminate. If the current phase velocity under consideration moves the determinant from a positive value to a negative value (or vice-versa), the program records that phase velocity as a good approximation to the admissible phase velocity for the current frequency.

Once all applicable phase velocities have been considered at a given frequency, the recorded value for the coarse prediction is written to the output file. This value is also set as the initial guess for the next frequency in the loop. The program moves to the next frequency and the process continues until a coarse phase velocity prediction has been obtained for each frequency.

### **C.3 Refined Calculation of Phase Velocities**

The second program used in the phase velocity calculations is called `PhaseVel_Refined.f90`. It must be compiled using a similar makefile to the coarse program, and it uses the same input file. A block diagram of the program is shown in Fig. C.3 for the  $A_0$  case. The  $S_0$  case is identical, except the `PhaseVel_A0_Coarse.bin` and `PhaseVel_A0_Refined.bin` filenames change to `PhaseVel_S0_Coarse.bin` and Pha-

seVel\_S0\_Refined.bin, respectively. The first section of the program defines each of the variables and reads parameters from the input file. It then reads the phase velocities from the coarse prediction. The output file is opened next to prepare for the refined phase velocity calculations.

The main portion of the program contains three nested loops. As in the coarse program, it loops through the defined frequency range according to the specified frequency resolution. The refined program then loops through the entire angular range in increments as specified by the angular resolution in the input file. For the analysis included in this dissertation, it was found that an angular resolution of 1 degree was too coarse, and it resulted in inaccuracies in the displacement solutions. A resolution of 0.1 degrees was sufficient for the analysis. At each of the angles, the program then loops through the range of possible phase velocities.

For each frequency, the initial guess for the phase velocity in the 0-degree azimuth is taken from the coarse phase velocity prediction. The phase velocity range is then defined by the refined search parameter from the input file. The program runs through the phase velocity range, builds the Global Matrix, and records the values of any determinant zero crossings just as in the coarse program. For this program, the resolution of the phase velocity range is significantly smaller than in the coarse program. This ensures the phase velocity calculations achieve the needed level of accuracy. After completing these steps for the first azimuthal angle, the program moves to the next angle. The phase velocity solution for the first angle is written to the output file and then used as the initial guess for the next angle.

Once the phase velocities for each azimuthal angle at the current frequency have been determined, the program moves to the next frequency. The initial guess for next frequency comes from the coarse phase velocity file. This process continues until refined phase velocity solutions are obtained for each angle at each frequency.

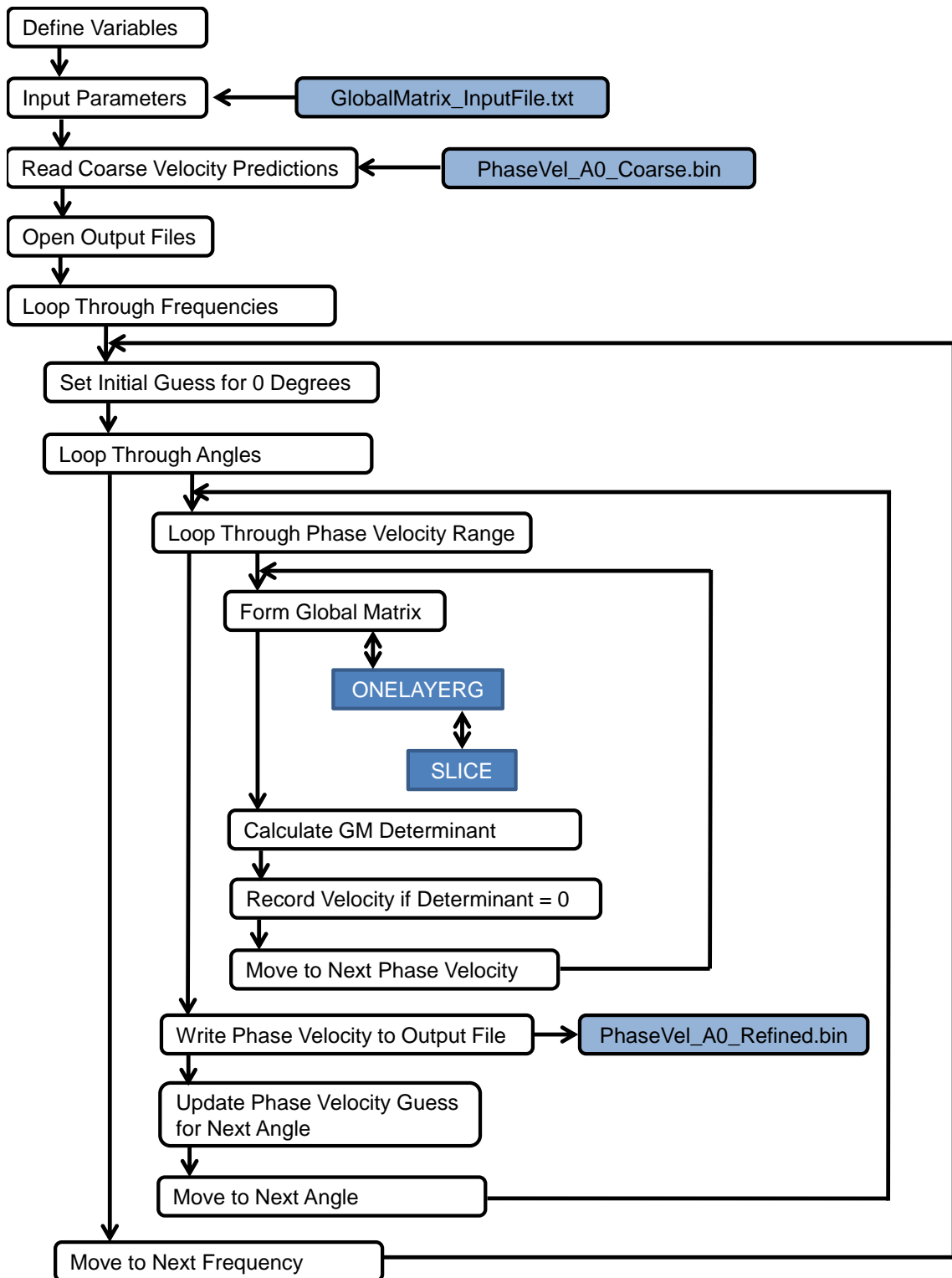


Figure C.3: Block diagram of refined phase velocity program (PhaseVel\_Refined.f90).

## C.4 Calculation of Displacement Kernels

The third FORTRAN program used in the Global Matrix process is called `DisplacementKernelGeneralized.f90`. The block diagram for the  $A_0$  case of this program is included as Fig. C.4. The purpose of this program is to form the integrand contained in Eq. 2.14. Specifically, the displacement kernel can be understood to be the fraction portion of the integrand, which is shown in Eq. 2.11. The program begins with variable definitions and the reading of the input file. Additionally, the refined phase velocities are read and stored for future use.

The program loops through the frequency range for the simulation. At each frequency, it then loops through the angular range. At each subsequent combination of angle and frequency, the first step in the process is to specify the two in-plane traction components that go into the forcing vector of the Global Matrix equation in Eq. 2.8. As explained in Chapter 2, these must be represented in the wavenumber domain. Next, the Global Matrix is formed. The admissible phase velocity for the angle/frequency combination is used in this step. The `ONELAYERG` and `SLICE` subroutine are also called in the same manner as in the phase velocity programs.

Once the Global Matrix is formed, the next steps in the program solve for the displacement constants in Eq. 2.8. The procedure used is based on Cramer's rule, but the implementation in this program contains one slight difference. The denominator of the integrand in Eq. 2.12 contains the determinant of the Global Matrix, which is a direct result of the application of Cramer's rule. However, application of the residue formula changes this denominator to be the derivative of the determinant with respect to the global radial wavenumber, as shown in Eq. 2.14. To facilitate this, the program calculates this derivative for the current angle and frequency and then moves on with Cramer's rule. The end result is the solution for the complete set of displacement constants.

Once the displacement constants are determined, the program performs the matrix multiplication shown in Eq. 2.9 to calculate the displacement kernel. This calculation is per-

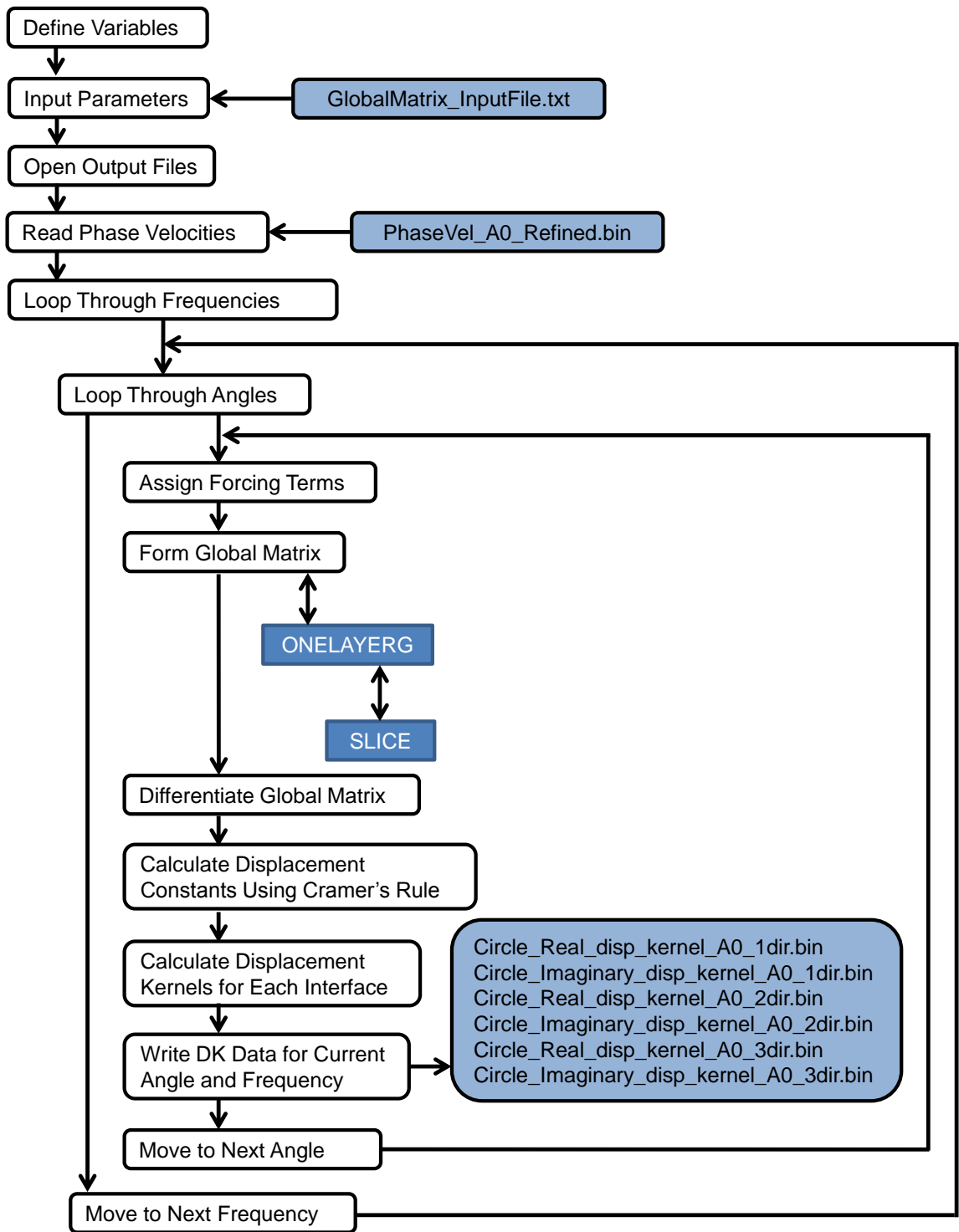


Figure C.4: Block diagram of displacement kernel program (DisplacementKernelGeneralized.f90).

formed for each layer interface, which allows for the displacement at each of the interface locations to be calculated later in the Global Matrix procedure. When the kernels for each interface at the current angle and frequency are determined, they are written to the output files. It should be noted here that the displacement kernels have complex values, and the real and imaginary parts are separated and written to different files. The program continues until all azimuthal angles have been considered at each frequency in the specified range.

For the case of the CLoVER actuator, a preprocessing step is needed before the displacement kernel calculations can be accomplished. As explained in Chapter 2, the traction components for the CLoVER must be represented with a Fourier series solution to be written in the wavenumber domain. These components must be calculated in a separate MATLAB routine and then read into the displacement kernel program. Figure C.5 shows how these steps fit into the overall Global Matrix procedure for the CLoVER case.

## **C.5 Inversion to Spatial and Time Domains**

The displacement kernels calculated in the previous section represent the displacements of the plate in the wavenumber and frequency domain. To build the displacement time history, a series of Fourier inversions must now be implemented. These are accomplished using the `Displacement_Processing_Total_Circle_360.m` MATLAB script for the circular actuator, and similar programs exist for the square and CLoVER actuators. The block diagram for this script is shown in Fig. C.6. The end product of this program is the complete set of displacement time histories needed for the LISA hybrid program.

The program starts by defining the in-plane locations of each of the boundary points for the cut-out region in the LISA hybrid model. It then defines the parameters of the actuation pulse used with the actuator. Next, the phase velocities and displacement kernels are read and stored for future use. As shown in the block diagram, this program uses both the  $A_0$  and

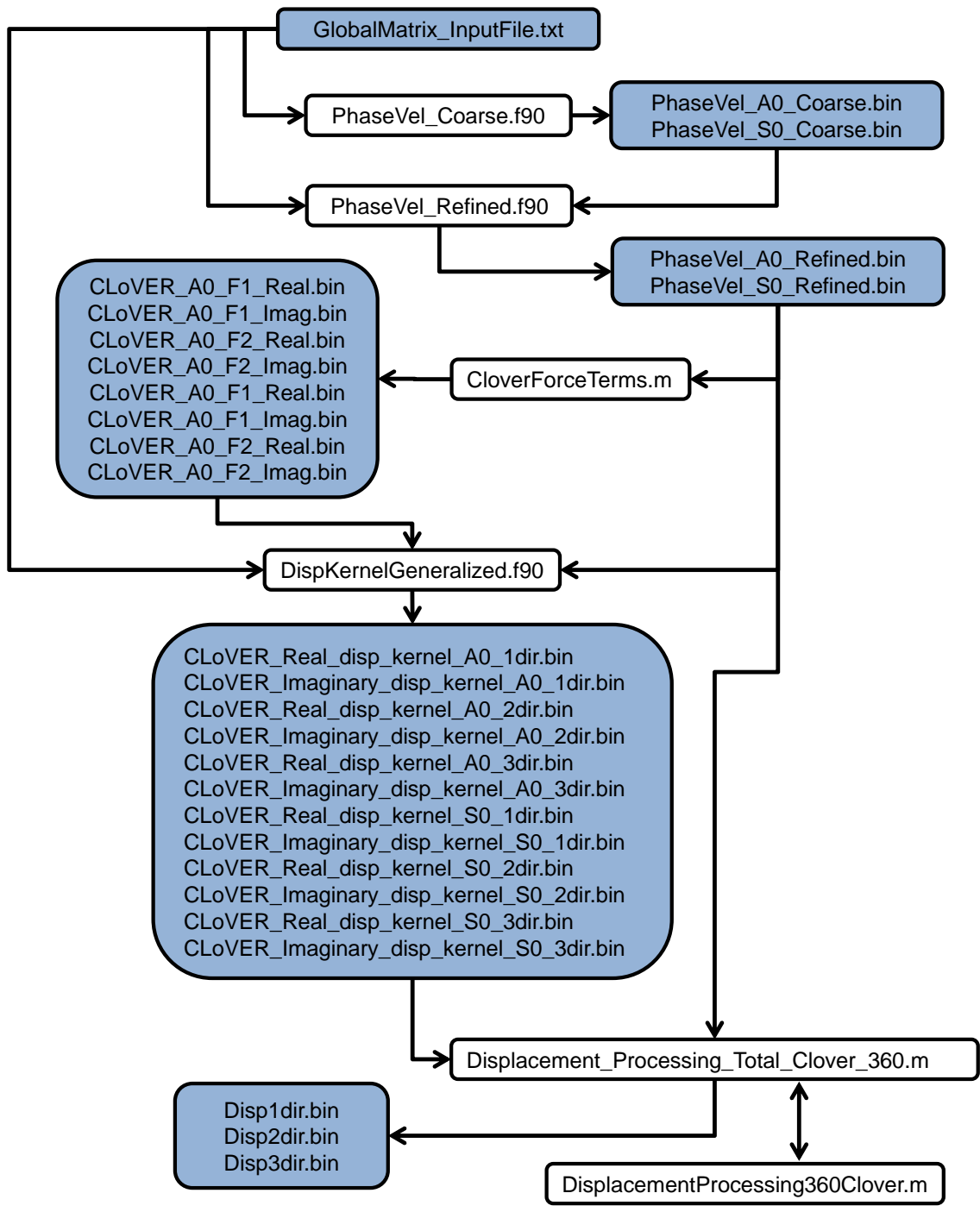


Figure C.5: Global Matrix process for a CLoVER actuator.



$S_0$  velocities and displacement kernels to build time histories that contain the contributions from both modes.

The remainder of the program contains two main loops. It loops through each interface in the laminate. For each interface, it then loops through each of the specified boundary points. For each point, the first step is to convert the Cartesian coordinates to polar coordinates. Once the polar coordinates are known, it is possible to carry out the Fourier inversion that moves the displacement information from the wavenumber domain to the spatial domain. This portion of the program implements the updated inversion method that was explained in Chapter 2. For the given point, the program loops over each of the frequencies contained in the actuation profile. At each point and frequency, a MATLAB function called `DisplacementProcessing360Circle.m` evaluates the inversion formulas contained in Eqs. 2.28 and 2.29 using numerical integration. It then produces the corrected signal in the spatial and frequency domain using Eq. 2.30. This corrected signal is known as the displacement harmonic for the given point and frequency.

The remaining step needed to produce the displacement time history is to complete the last Fourier transform moving the signal from the frequency domain to the time domain. This is implemented in two steps in the program. First, the frequency content of the displacement signal is obtained by multiplying each of the displacement harmonics by the Fourier transform of the excitation signal. Then, numerical integration is used to evaluate the Fourier inversion formula, which results in the time history signal for the given point and interface.

This process continues until displacement time histories are known for each boundary point at each interface. The final portion of the program arranges these time histories and writes them to the output files so they can be read by the LISA hybrid program.

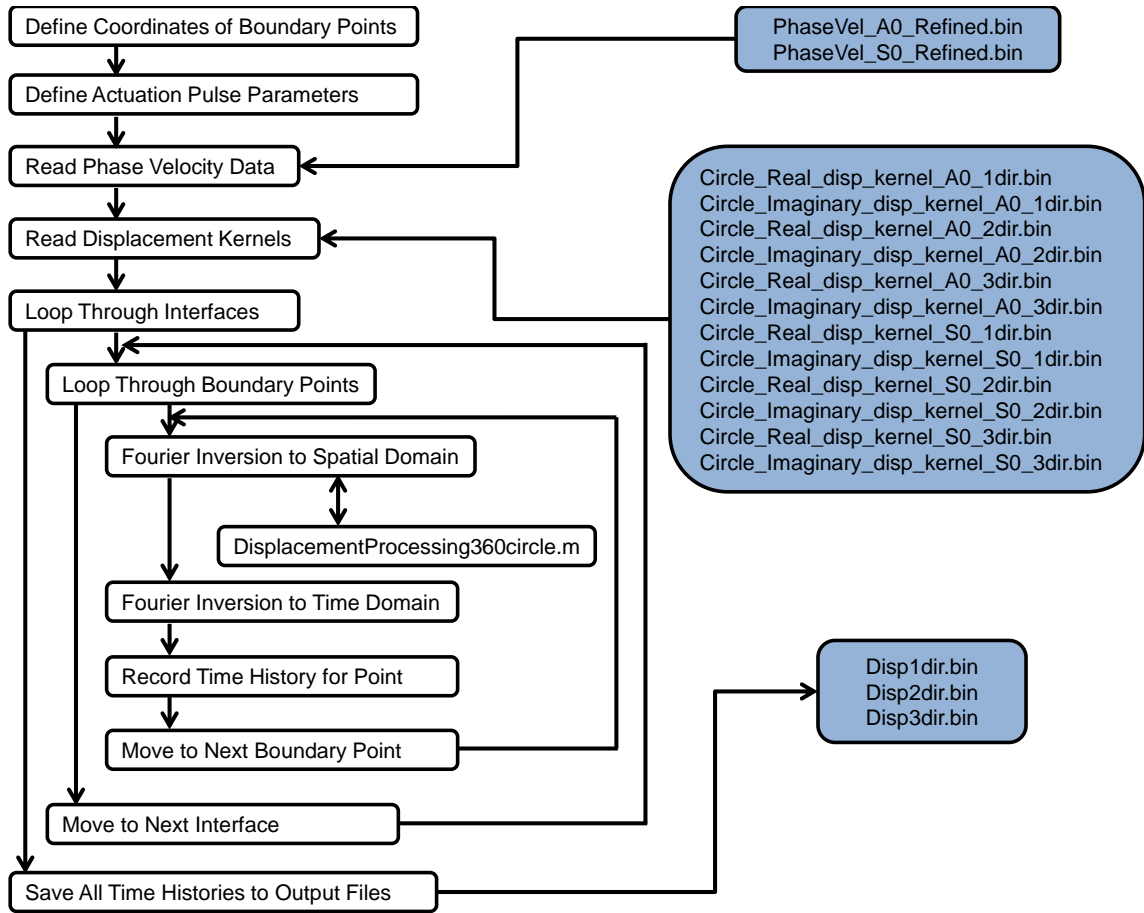


Figure C.6: Block diagram for Fourier inversion program.

## APPENDIX D

### Implementation of LISA Hybrid Program

This appendix provides an overview of the LISA hybrid code. The code is written in FORTRAN 95, and the source code must be compiled using a suitable FORTRAN compiler. The compiler must support OPENMP protocols for code parallelization. A block diagram showing an overview of the program is included as Fig. D.1.

#### D.1 Initialization Steps

The various steps needed to initialize the program are depicted in Fig. D.2, and they are described next.

##### D.1.1 Variable Definition

The first portion of the code defines each of the variables used in the program, which is standard procedure in the FORTRAN language.

##### D.1.2 Input Parameters

The main input file for the program is LISA.Input.Parameters.txt. The file contains 13 input parameters for the program:

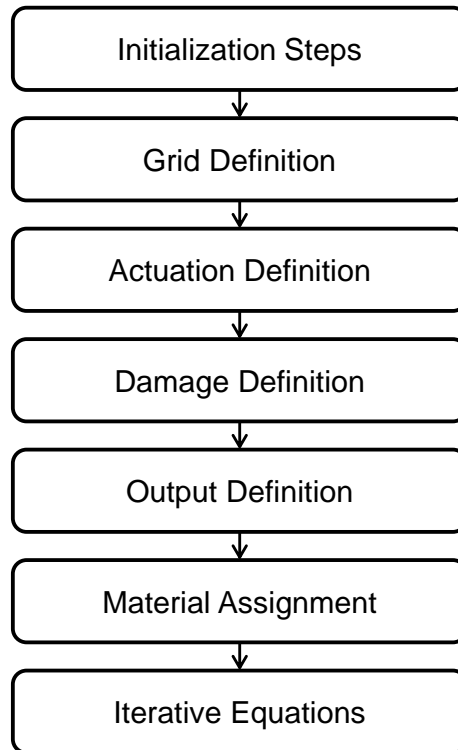


Figure D.1: Block diagram of LISA hybrid program.

- Number of Layers in the Model: This includes the number of lamina in the plate model plus an additional layer of simulated air cells on the top and bottom surfaces of the plate.
- Air Cells in Lateral Directions: This parameter is almost always set at 2, indicating two simulated air cells along the lateral edges of the plate model.
- Total Model Run Time: Measured in seconds.
- Time Step Size: Measured in seconds.
- Discretization in X Direction: Measured in meters.
- Discretization in Y Direction: Measured in meters.

- Discretization in Z Direction: Measured in meters. This is the nominal through-thickness discretization for the model. This value is only used to verify that the CFL number is within limits. The discretization of each individual layer is taken as an input parameter later in the grid definition stage.
- Offset Distance: This parameter is used for the LISA hybrid actuation to specify the half-length of one of the sides of the square cut-out region surrounding the actuator. Measured in meters.
- Actuation Profile: This variable is used for prescribed displacement actuation to specify the actuator setup. A value of 1 is used for a top actuator only. A value of 2 is used for top and bottom actuators with  $A_0$  actuation. A value of 3 is used for top and bottom actuators with  $S_0$  actuation.
- Damage Type: This parameter specifies the type of damage included in the LISA model. It takes a value of 0 for no damage, 1 for hole damage, 2 for impact damage, and 3 for impact damage with simulated delamination.
- Hybrid Status: This parameter determines which type of actuation is used. It takes a value of 1 for prescribed displacement actuation and 2 for hybrid actuation.
- Center Frequency: This parameter specifies the frequency of actuation in Hz for the prescribed displacement actuation.
- Circular Actuator Radius: This parameter specifies the radius of the circular actuator for prescribed displacement actuation. Measured in meters.

### **D.1.3 Verify Time Step**

Care should be taken when specifying the total model run time and the desired time step in the input file to ensure an integer number of time steps are requested. However, the

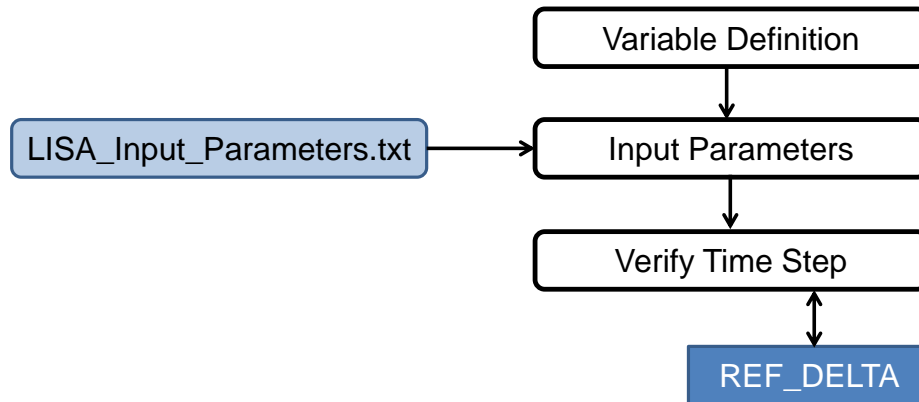


Figure D.2: Block diagram of LISA hybrid initialization steps.

code includes a subroutine REF\_DELTA that double-checks these values and adjusts them if needed.

## D.2 Grid Definition

The next major section of the program defines the Cartesian grid used in the LISA model.

### D.2.1 Read Dimensions From Input File

This section reads the layer thicknesses and discretizations from the Material\_Dimensions.txt file. Each row in the input file specifies the dimensions of a layer in the model as well as its material, orientation angle, and through-thickness discretization.

### D.2.2 Define Nodal Coordinates

After reading the information for each layer, the program arranges the thickness and discretization information into a series of array variables that are used throughout the re-

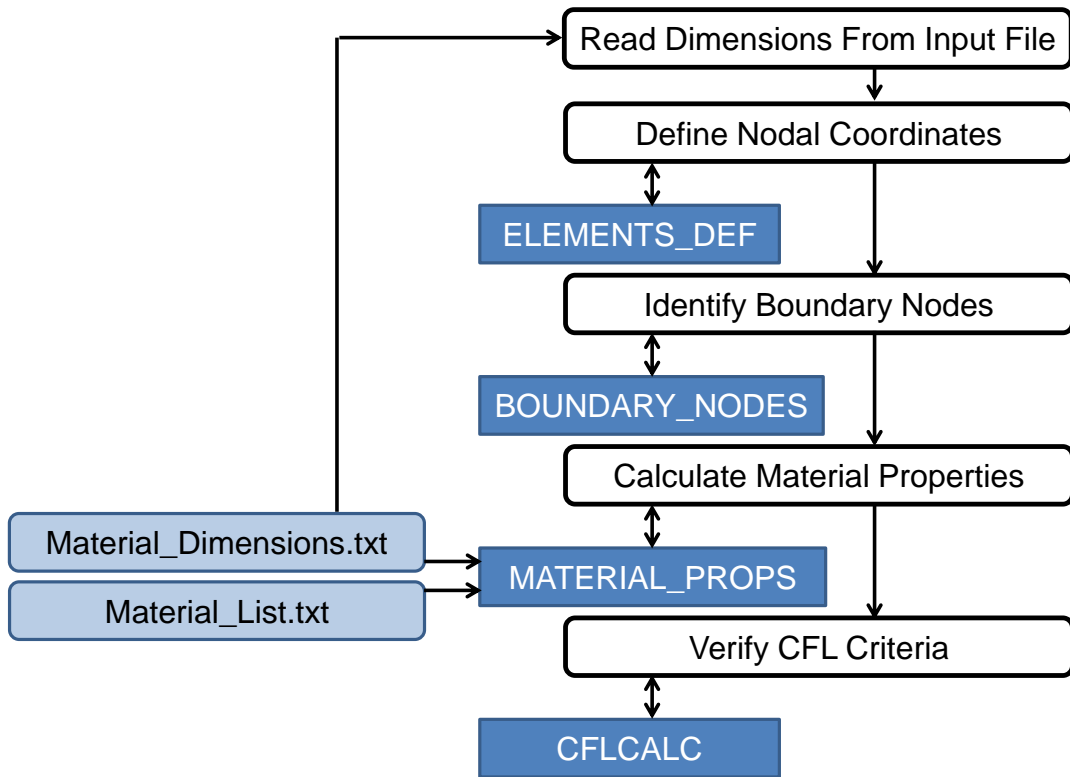


Figure D.3: Block diagram of LISA grid definition steps.

remainder of the program. The number of nodes in each direction is calculated using the previously read information. Next, the `ELEMENTS_DEF` subroutine determines the coordinates of each node and stores the information in an array for future reference.

### D.2.3 Identify Boundary Nodes

The next portion of the program uses the `BOUNDARY_NODES` subroutine to identify the nodes that are on the edge of the plate model. The program marks these nodes as boundary nodes that are to remain at a fixed position throughout the duration of the simulation.

## **D.2.4 Calculate Material Properties**

The MATERIAL\_PROPS subroutine first reads from the Material\_Dimensions.txt file to determine the material and orientation angle for each of the layers in the model, including the air layers on the top and bottom surfaces of the plate. Next, the subroutine reads material property information from the Material\_List.txt file. In this file, each row corresponds to a possible material for the model, and each column contains one of the applicable material properties. Once all the properties are read from the file, the remainder of the subroutine calculates the material properties for each layer based on its orientation angle and material.

## **D.2.5 Verify CFL Criteria**

The CFLCALC subroutine is used to verify the CFL number for the model is less than one. It uses the previously calculated material properties to calculate the maximum bulk wave velocity for the model, and it then uses this along with the spatial discretization and time step to calculate the CFL number.

## **D.3 Actuation Definition**

This program supports two possible types of actuation: LISA hybrid and prescribed displacements. As explained in Chapter 3, the prescribed displacements method has some serious drawbacks, but in some cases it may be useful to use it. Based on the chosen actuation type as specified in the input file, this section of the program defines the needed actuation properties for the simulation. For both actuation methods, the first step in this section of the program is to specify the initial displacement for all nodes in the model to be zero.



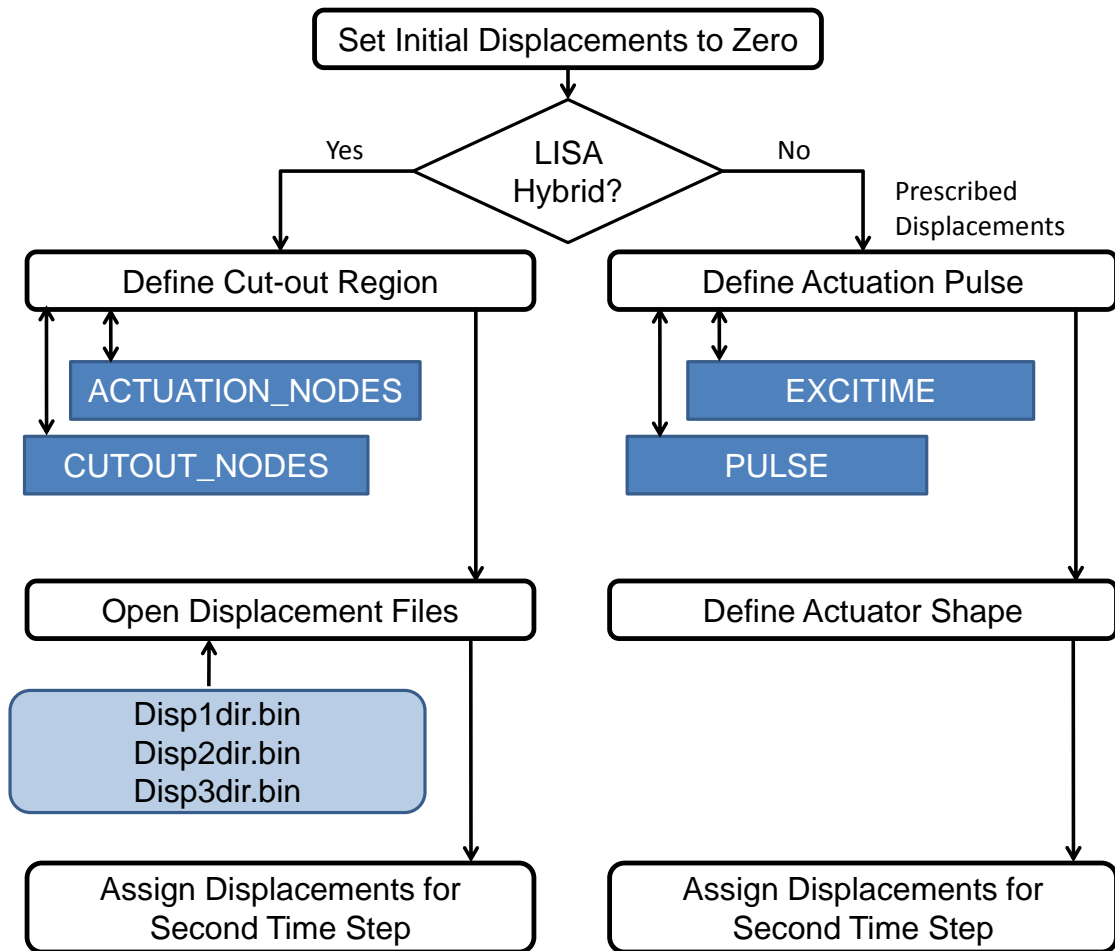


Figure D.4: Block diagram of LISA actuation definition steps.

### D.3.1 LISA Hybrid Actuation

#### D.3.1.1 Define Cut-out Region

The first step for the LISA hybrid actuation is to identify the nodes used for the cut-out region. The ACTUATION\_NODES subroutine determines and tabulates the nodes located on the cut-out boundary. These are the nodes where the Global Matrix displacement time

histories are applied. The CUTOUT\_NODES subroutine identifies and tabulates the nodes that are located inside of the cut-out boundary.

### **D.3.1.2 Open Displacement Files**

At this point the program opens the three binary files that contain the Global Matrix displacement time histories. These files specify the three displacement components for each node on the cut-out boundary at each time step. The files remain open for the remainder of the program, and the values are read at each time step.

### **D.3.1.3 Assign Displacements for Second Time Step**

The displacements corresponding to the second time step are then read from the displacement input file and applied to the nodes on the cut-out boundary.

## **D.3.2 Prescribed Displacements Actuation**

### **D.3.2.1 Define Actuation Pulse**

For the case of prescribed displacements, the EXCITIME subroutine defines the number of time steps in the actuation pulse. Then, the PULSE subroutine is used to define the properties of the actuation pulse based on the center frequency in the input file. This subroutine specifies the Hann-modulated toneburst signal used for the actuation in this dissertation.

### **D.3.2.2 Define Actuator Shape**

The next portion of the code determines which nodes are included in the circular actuator region.

### **D.3.2.3 Assign Displacements for Second Time Step**

The displacements for the second time step are then assigned for the actuator nodes. The values of the excitation are scaled base on the position of the node.

## **D.4 Damage Definition**

This section of the program reads in the parameters for the chosen damage type. Typical input parameters include the in-plane coordinates of the damage center, the radius of the damage, and the depth of the damage. For impact damage, the input file contains the information needed to specify the radius of the damage at each through-thickness location.

## **D.5 Output Definition**

### **D.5.1 Define Recording Locations**

The LISA simulation produces four sets of displacement output files to be used for various post-processing activities.

- **Radial Displacement Traces:** The simulation produces three sets of output files to show how the out-of-plane displacement time histories change along a radial line that extends from the actuator. The three lines are in the 0, 45, and 90-degree directions.
- **Movie Data Files:** A data file is produced for each component of displacement. The displacements are recorded at a sampling of points on the top surface of the plate, and they are recorded at specified time intervals. These files can be used to produce animations of the displacement fields for the plate.
- **Damage Area Displacements:** This group of output files records the displacements on the top surface of the plate in the region immediately surrounding the damage

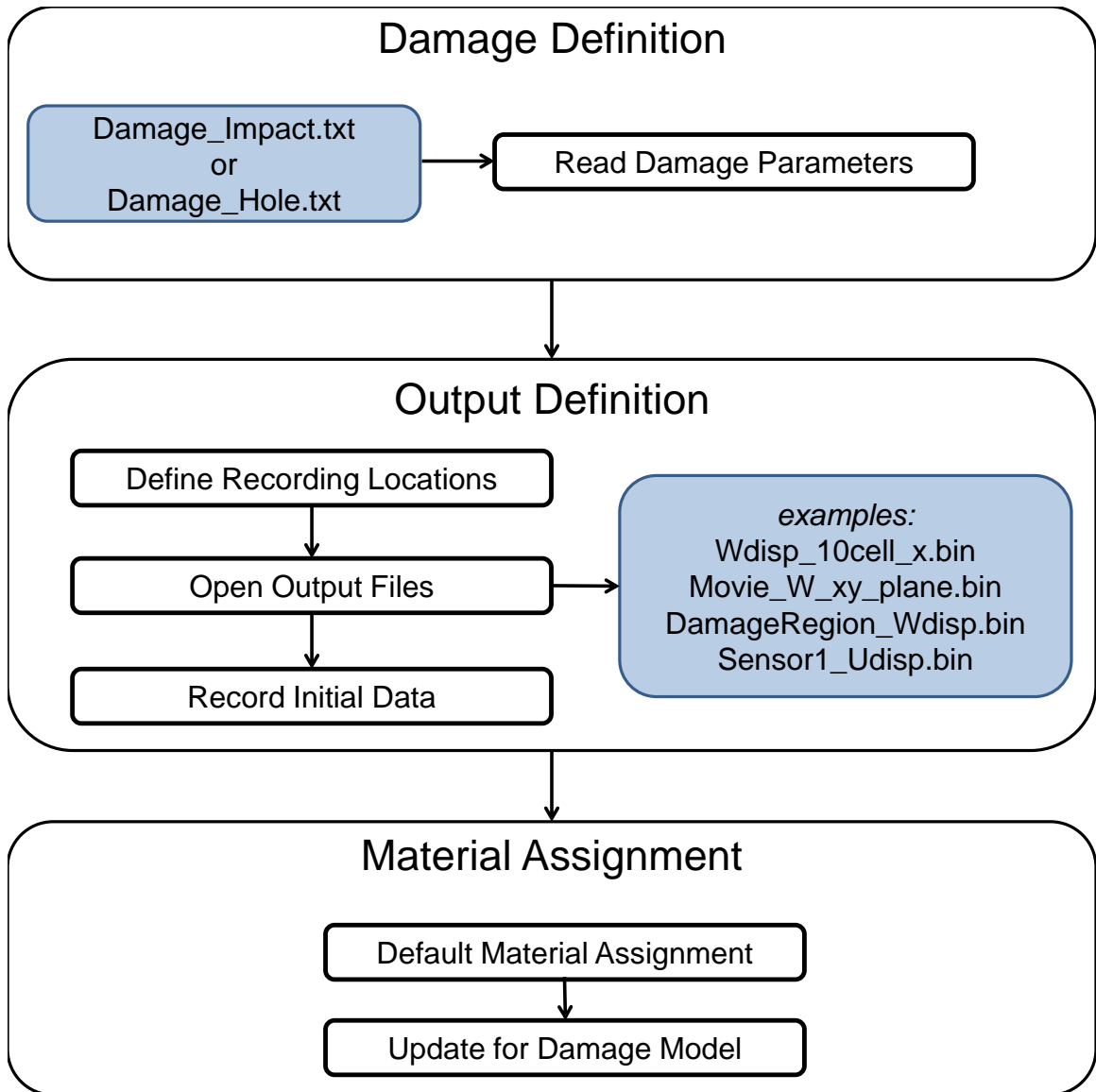


Figure D.5: Block diagram of LISA damage definition, output definition, and material assignment sections.

location. These are useful when examining how different damage features affect the guided wave propagation.

- **Simulated Sensor Data:** These output files record the in-plane displacements in five regions of the plate corresponding to the location of the sensors.

## **D.5.2 Open Output Files**

After the applicable nodes are defined for each of the four output sets, the output files are opened to prepare for data recording.

## **D.5.3 Record Initial Data**

Based on the recording instructions, the displacements for the first two time steps are written to the output files.

## **D.6 Material Assignment**

Prior to starting the simulation, the materials for each of the nodes' neighbors are identified and tabulated. This process can be completed outside of the time-marching loop, since the materials do not change with time. By saving a material identifier for each neighbor rather than all the material properties themselves, considerable memory is conserved.

### **D.6.1 Default Material Assignment**

First, the default materials are identified based on the construction of the laminate. For each node, an 8-position array is formed to identify a material number for each neighbor cell.

### **D.6.2 Update for Damage Model**

Once the default materials are assigned, any necessary changes are made to account for the chosen damage model. For hole damage, this involves changing applicable material assignments to the simulated air material. For impact damage, this involves changing applicable cells to a material assignment that reflects some type of reduced property.

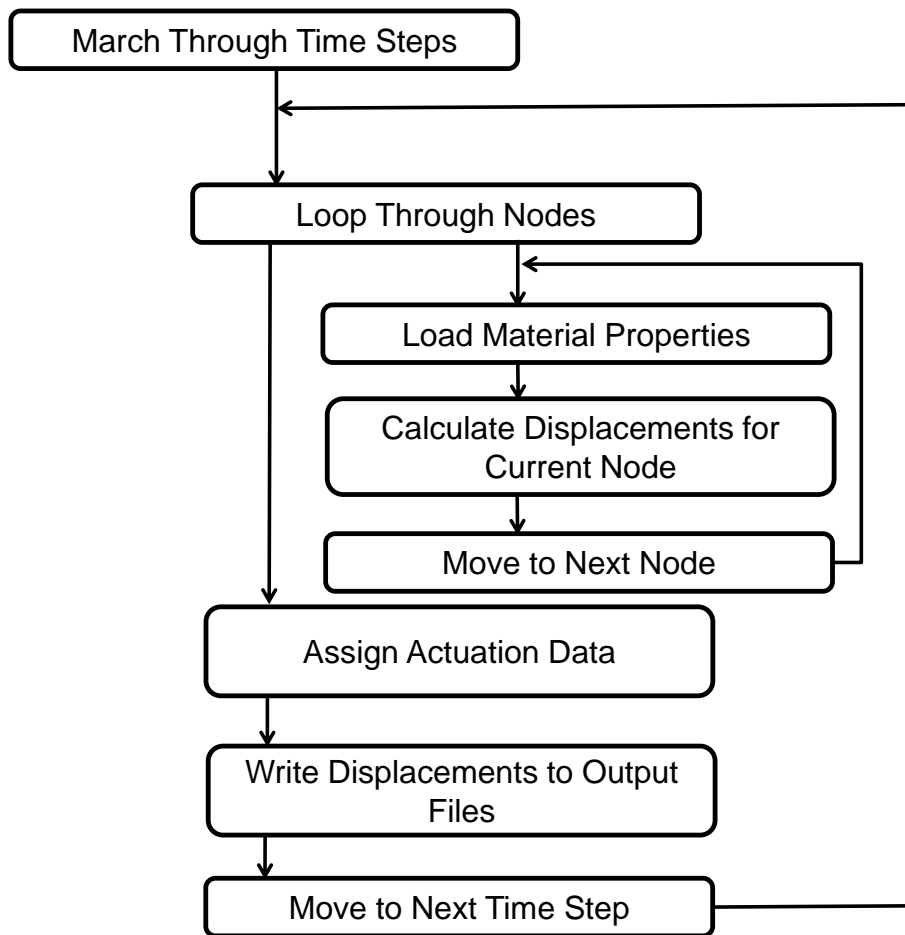


Figure D.6: Block diagram of LISA iterative equation section.

## D.7 Iterative Equations

This section of the program contains iterative calculations that form the core of the LISA simulation. It involves marching through each time step and calculating three displacement components for each node at the current time step.

### **D.7.1 Load Material Properties**

For the given node, the previously formed array that identifies the neighbor cells' materials is used to ensure the correct material properties are used in the iterative equations.

### **D.7.2 Calculate Displacements for Current Node**

The three iterative equations are then used with the loaded material properties to calculate the three displacement components for the given node at the current time step. The equations also reference the displacement values for the node's neighbor nodes at the previous two time steps, which have been stored in memory.

### **D.7.3 Assign Actuation Data**

After the iterative equations for each node at the current time step are complete, the actuation values are assigned for the time step. This involves referencing the displacement input files for the LISA hybrid actuation or using the calculated excitation profile for the prescribed displacement actuation.

### **D.7.4 Write Displacements to Output Files**

The final step for the current time step is to write the displacement data to the output files based on the recording instructions. Once this is complete, the program moves to the next time step and repeats the cycle.

## APPENDIX E

### Comments on 2-D Fourier Inversion

In Chapter 2, an updated method was presented to carry out the 2-D inverse Fourier transform used to move from the wavenumber domain to the spatial domain during the employment of the Global Matrix Method. First, an original wave solution was developed which contained both an inward and outward propagating wave:

$$u_i^O(r, \theta, X_3, \omega) = \sum_{\hat{K}} \frac{\tau_0}{4\pi} \int_0^{2\pi} \frac{\Psi_i(\hat{K}, \Gamma, X_3, \omega)}{\Delta'(\hat{K}, \Gamma, \omega)} \hat{K} e^{-i\hat{K}r \cos(\theta - \Gamma)} d\Gamma \quad (\text{E.1})$$

Subsequently, a correction signal was produced by including an additional cosine term in the integrand of the inversion integral:

$$u_i^C(r, \theta, X_3, \omega) = \sum_{\hat{K}} \frac{\tau_0}{4\pi} \int_0^{2\pi} \frac{\Psi_i(\hat{K}, \Gamma, X_3, \omega)}{\Delta'(\hat{K}, \Gamma, \omega)} \hat{K} e^{-i\hat{K}r \cos(\theta - \Gamma)} \cos(\theta - \Gamma) d\Gamma \quad (\text{E.2})$$

This correction signal reversed the sign of the inward wave, as shown in Fig. E.1. When the correction signal was added to the original signal, the inward wave was canceled, leaving only the desired outward propagating wave:

$$u_i^{\text{corrected}} = \frac{u_i^O + u_i^C}{2} \quad (\text{E.3})$$



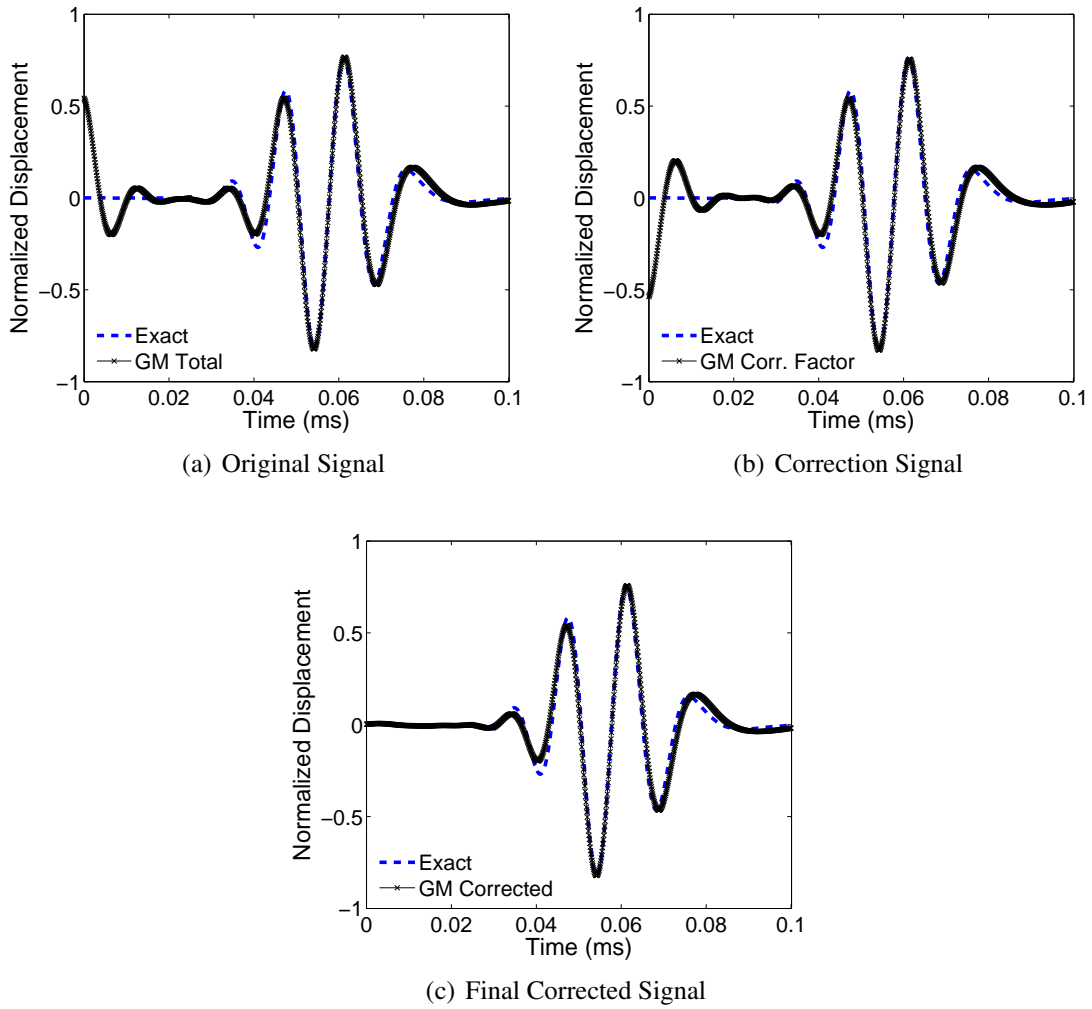


Figure E.1: Correction procedure for displacement time history at 60 mm location. Results are for a circular actuator on an aluminum laminate.

The purpose of this appendix is to provide some background detail on the genesis of the cosine term added to the integrand in the correction signal.

## E.1 Development of Correction Signal

The initial attempts at producing a correct displacement signal began with a previous formulation that was outlined in Chapter 2. In that formulation, the limits of integration used in Eq. E.1 were altered to ensure the coefficient of  $\hat{K}$  in the complex exponential remained

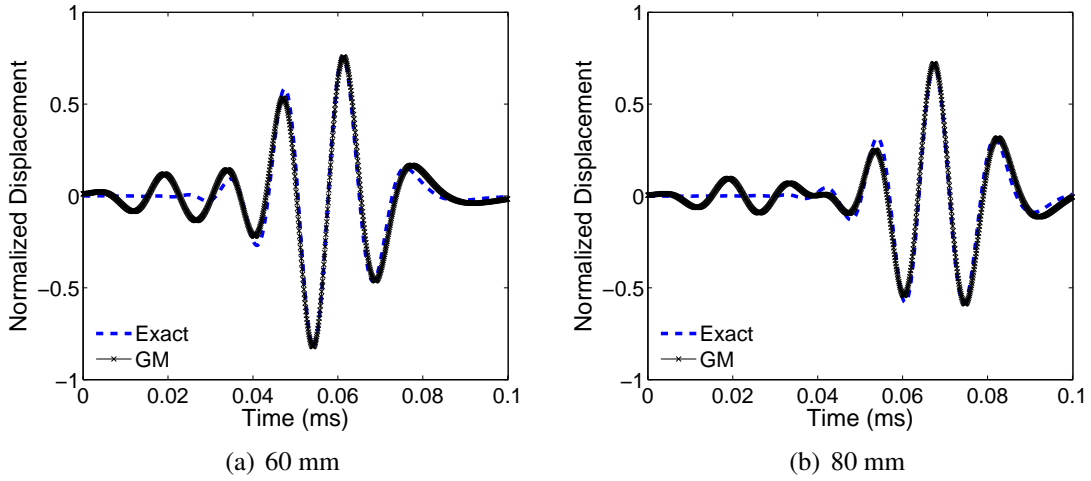


Figure E.2: Displacement time histories for an aluminum laminate at 60 and 80 mm, showing the artifact present in the previous solution.

positive over the entire domain of integration:

$$u_i(r, \theta, X_3, \omega) = \sum_{\hat{K}} \frac{\tau_0}{2\pi} \int_{\theta - \frac{\pi}{2}}^{\theta + \frac{\pi}{2}} \frac{\Psi_i(\hat{K}, \Gamma, X_3, \omega)}{\Delta'(\hat{K}, \Gamma, \omega)} e^{-i\hat{K}r \cos(\theta - \Gamma)} \hat{K} d\Gamma \quad (\text{E.4})$$

The goal of this formulation was to avoid integrating over azimuthal wavenumbers which resulted in an inward propagating wave. This technique eliminated most of the inward wave, but it left an artifact in the time history. The presence of this artifact is shown in Fig. E.2 for points 60 and 80 mm from the actuator. Further investigation of this formulation considered the results when the limits of integration were switched to include the previously avoided azimuthal wavenumbers:

$$u_i(r, \theta, X_3, \omega) = \sum_{\hat{K}} \frac{\tau_0}{2\pi} \int_{\theta + \frac{\pi}{2}}^{\theta - \frac{\pi}{2}} \frac{\Psi_i(\hat{K}, \Gamma, X_3, \omega)}{\Delta'(\hat{K}, \Gamma, \omega)} e^{-i\hat{K}r \cos(\theta - \Gamma)} \hat{K} d\Gamma \quad (\text{E.5})$$

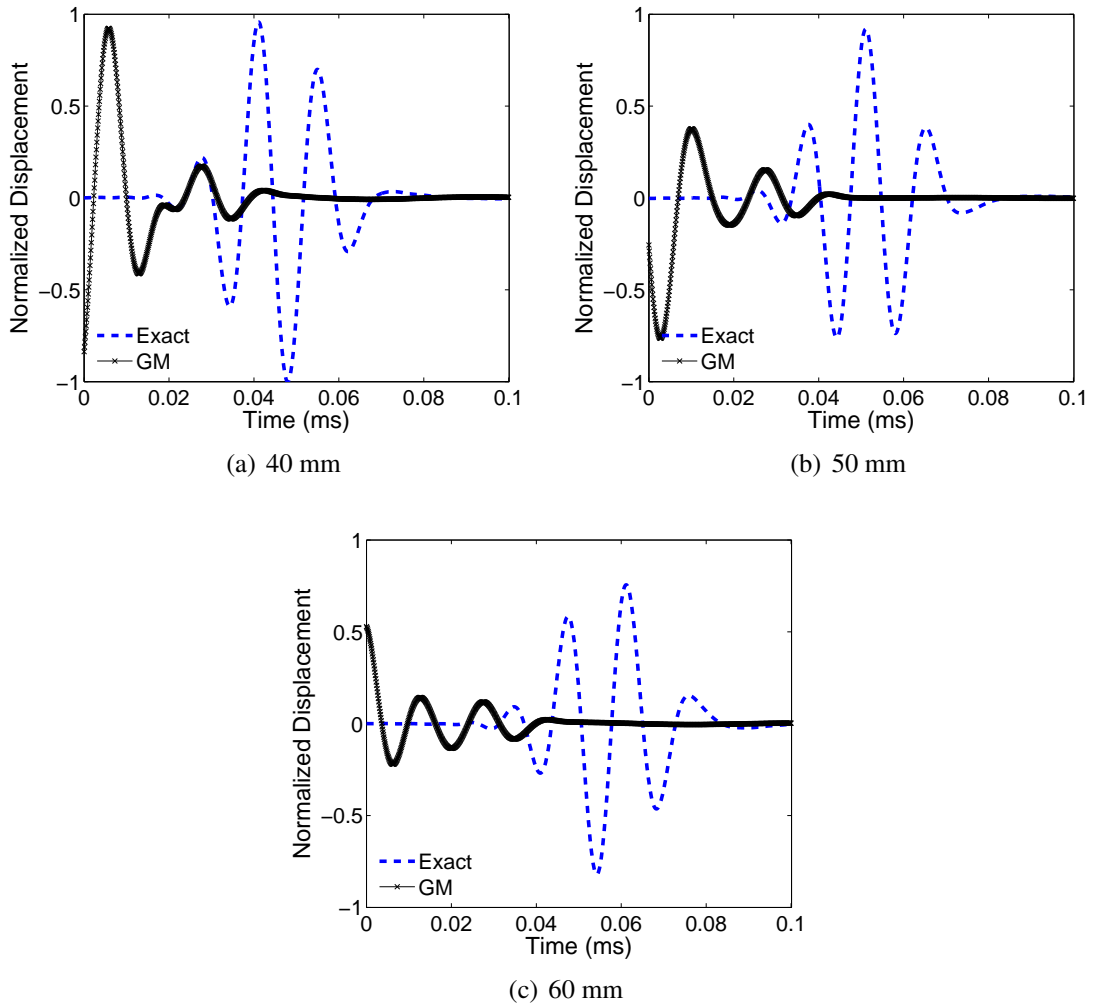


Figure E.3: Inward propagating wave solution for an aluminum laminate at 40, 50, and 60 mm, showing the artifact present in the previous solution.

As expected, using these limits resulted in the inward wave instead of the outward wave. However, the previously mentioned artifact in the time history was also present, as shown in Fig. E.3.

Additional studies were conducted to determine the source of the artifact found in the displacement time histories. Initially, the limits of integration were changed to determine how they affect the presence of the artifact. Focusing on the solution defined by Eq. E.4, the azimuthal span of the limits of integration was narrowed to determine if a smaller region

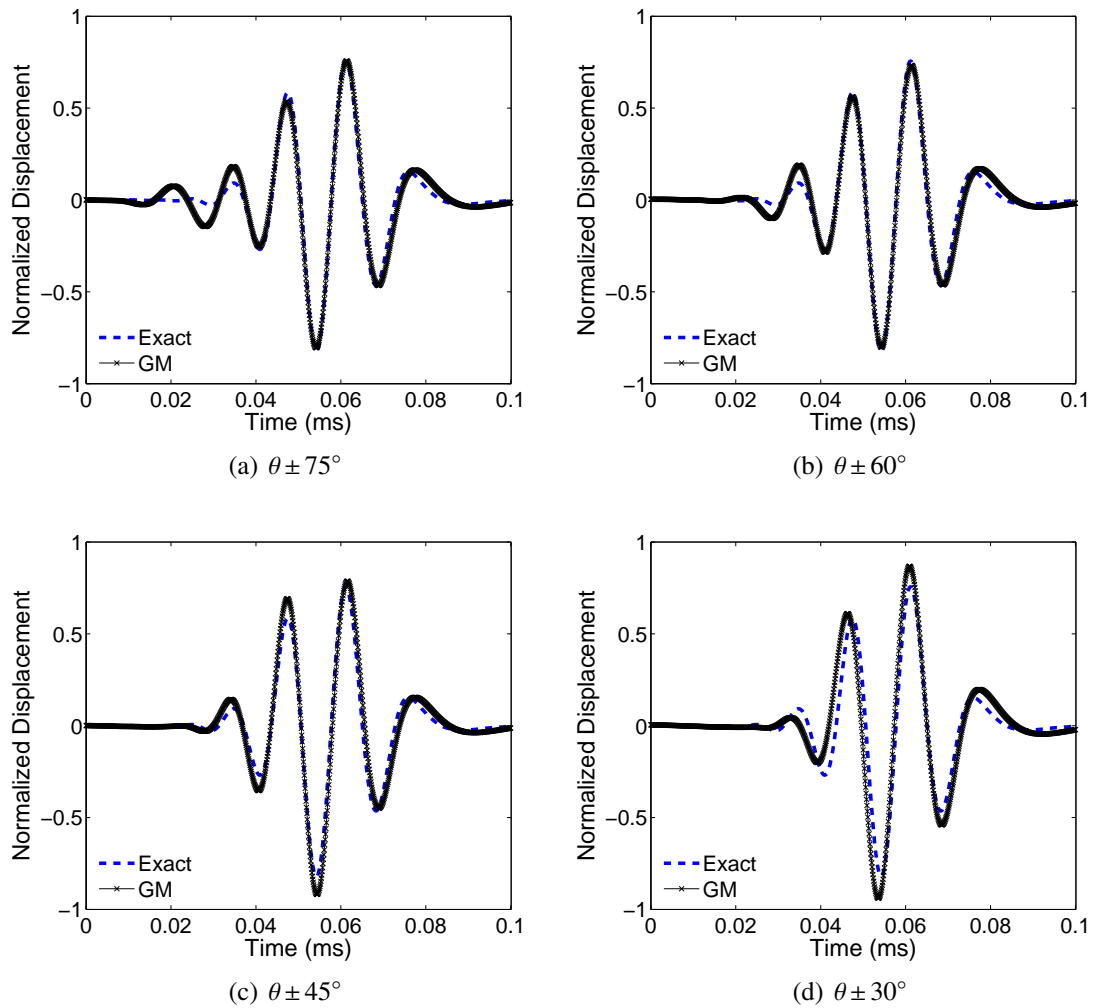


Figure E.4: Displacement time histories for an aluminum laminate at 60 mm, showing the effect of further reducing the region of integration.

of integration resulted in a signal without the displacement artifact. The results indicated that by reducing the limits to a smaller span around the angle of interest  $\theta$ , the size of the artifact decreased. However, reducing the span of integration also resulted in the distortion of the outward wave solution when too much of the original span was excluded. These results are shown in Fig. E.4. It was also determined that the results of reducing the limits of integration were not consistent as the distance from the actuator changed. For the point 60 mm from the actuator, shown in Fig. E.4 (c), integrating from  $\theta \pm 45^\circ$  produced a good

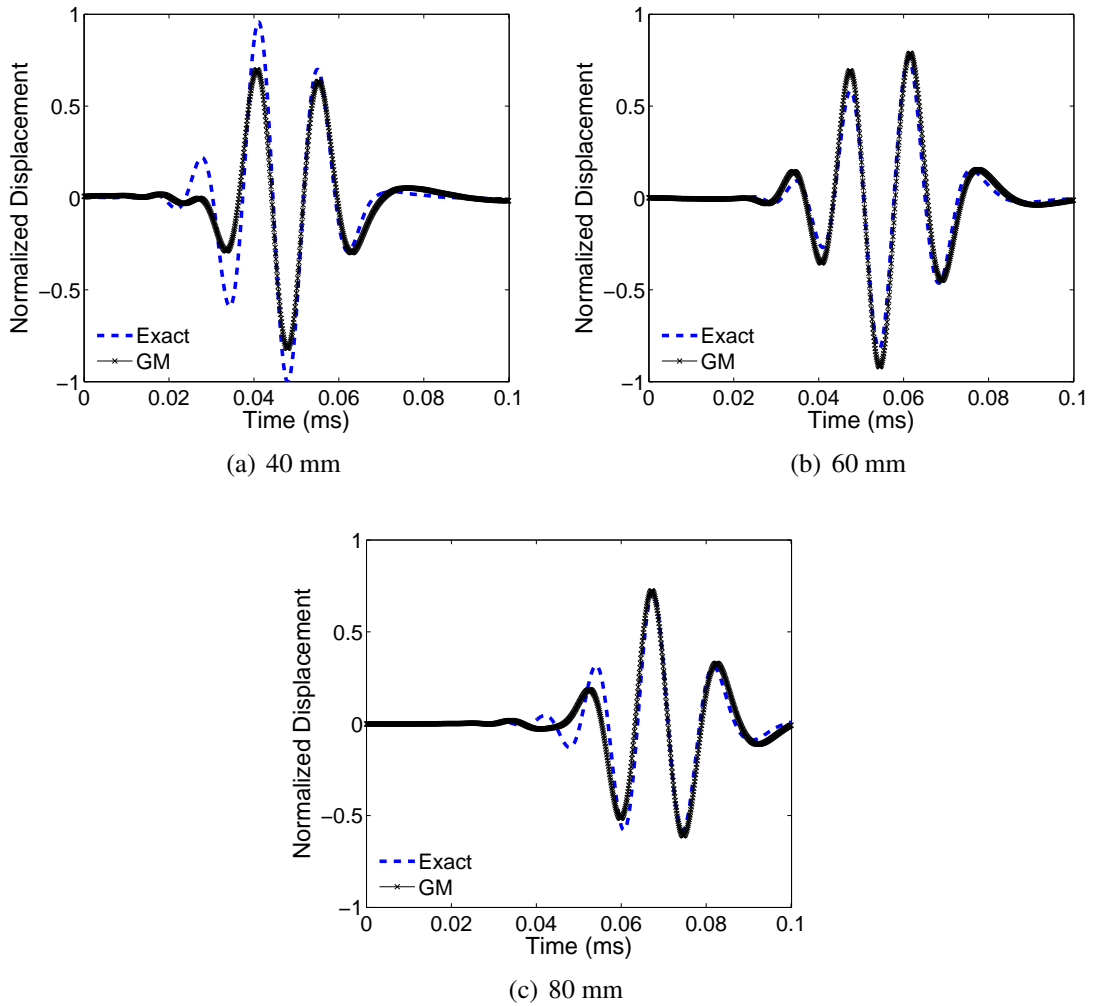


Figure E.5: Outward propagating wave solution for an aluminum laminate at 40, 60, and 80 mm, showing the effect of reducing the region of integration to  $\theta \pm 45^\circ$ .

qualitative match with the exact solution. However, these limits resulted in distorted waves at points closer and farther from the actuator, as shown in Fig. E.5.

It was hypothesized that the wavenumbers near  $\theta \pm 90^\circ$  were the source of the displacement artifact. Furthermore, it was considered that a more gradual weighting of the azimuthal wavenumbers closer to  $\theta$  may maintain the integrity of the outward solution while still excluding the majority of the contribution from those wavenumbers creating the artifact. Based on these possibilities, the idea of using the cosine function surfaced as an

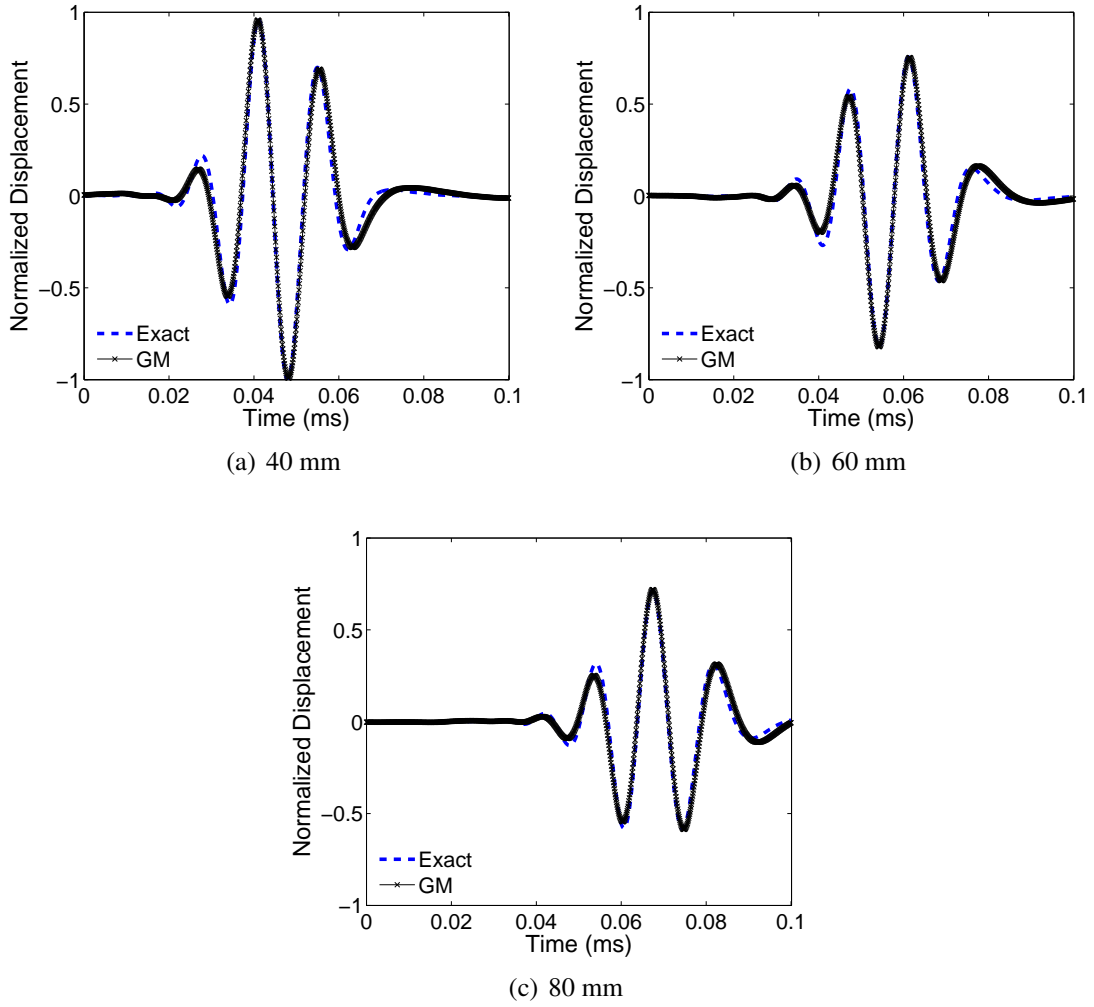


Figure E.6: Outward propagating wave solution for an aluminum laminate at 40, 60, and 80 mm, showing the the effect of adding the cosine term to the inversion equation.

option. Addition of the cosine term to the outward solution as in

$$u_i(r, \theta, X_3, \omega) = \sum_{\hat{K}} \frac{\tau_0}{2\pi} \int_{\theta-\frac{\pi}{2}}^{\theta+\frac{\pi}{2}} \frac{\Psi_i(\hat{K}, \Gamma, X_3, \omega)}{\Delta'(\hat{K}, \Gamma, \omega)} e^{-i\hat{K}r \cos(\theta-\Gamma)} \hat{K} \cos(\theta-\Gamma) d\Gamma \quad (\text{E.6})$$

successfully removed the artifact while leaving intact the outward wave solution, as shown in Fig. E.6. When the cosine term was added to the equation for the inward solution, it removed the artifact, as seen in Fig. E.7. However, an additional effect was also produced,

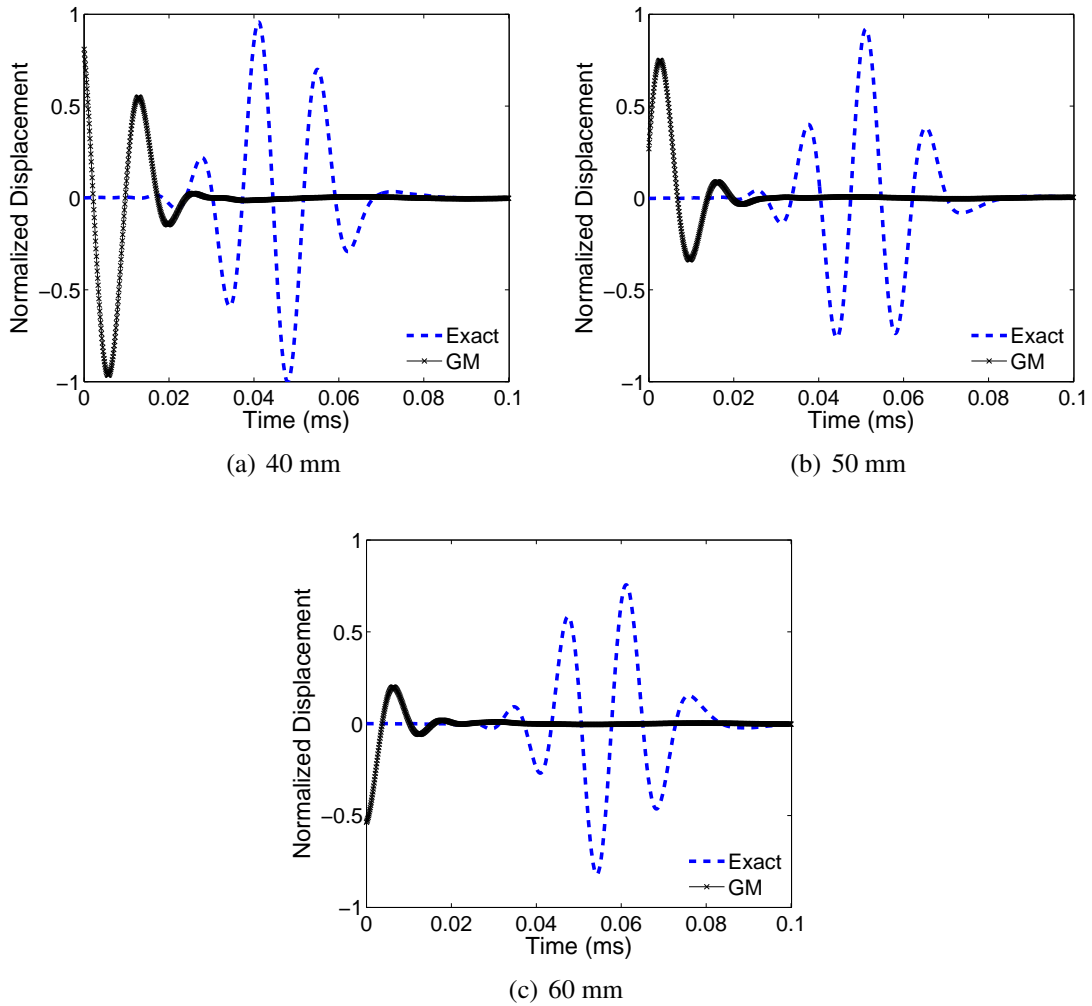


Figure E.7: Inward propagating wave solution for an aluminum laminate at 40, 50, and 60 mm, showing the the effect of adding the cosine term to the inversion equation.

where the sign of the inward wave was flipped. This effect was easily attributable to the fact that cosine is an even function.

For the more general solution shown at the beginning of this appendix, the artifact in the displacement time history never appeared. However, the inclusion of the cosine term created the reversal effect on the inward wave, which facilitated the creation of the correction signal. Even for this case, however, the cosine did more than just reverse the sign. If instead of using the cosine term, the sign of the integrand was reversed for values

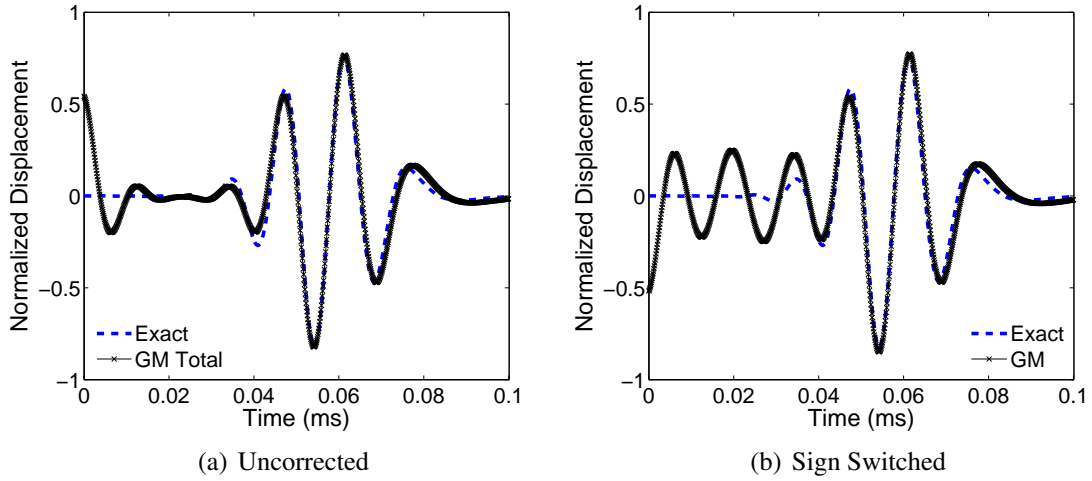


Figure E.8: Displacement time histories for an aluminum laminate at 60 mm, showing the effect of only switching the sign of the inward wave solution.

where the coefficient of  $\hat{K}$  was negative, the sign change was preserved and the inward portion of the wave was flipped. However, a new artifact was produced, which was double the value of the artifact seen in the Eq. E.4 solution. This result is shown in Fig. E.8. Thus even in the general case, the cosine term seems to have prevented the formation of the displacement artifact that would otherwise have appeared.

## E.2 Examination of Alternate Correction Options

Based on the results presented to this point, it is clear that the effect of the cosine term was two-fold. For the general case with integration limits 0 to  $2\pi$ , the cosine term reversed the sign of the inward wave and prevented the appearance of a spurious displacement artifact. Similarly, for the case where the limits of integration were reduced to half of the original region, the cosine term both reversed the sign of the inward wave and eliminated the presence of the displacement artifact. The sign of the cosine function explains the sign reversal, but it appears the elimination of the artifact was due to a filtering effect where the azimuthal wavenumbers closest to the angle of interest  $\theta$  were given predominance. For this reason,



other filtering options were considered to see how that choice affected the results. A new filtering function was introduced for the outward wave case

$$u_i(r, \theta, X_3, \omega) = \sum_{\hat{K}} \frac{\tau_0}{2\pi} \int_{\theta - \frac{\pi}{2}}^{\theta + \frac{\pi}{2}} \frac{\Psi_i(\hat{K}, \Gamma, X_3, \omega)}{\Delta'(\hat{K}, \Gamma, \omega)} e^{-i\hat{K}r \cos(\theta - \Gamma)} \hat{K}(F) d\Gamma \quad (\text{E.7})$$

where

$$F = 1 - \left| \frac{(\theta - \Gamma)}{\pi/2} \right|^b \quad (\text{E.8})$$

Figure E.9 shows the profiles of this filter function for various values of the filter exponent,  $b$ . As the value of the exponent increases, the equation approaches the unfiltered case in Eq. E.4. The time histories for a point 60 mm from the actuator are shown in Fig. E.10 for values of  $b$  less than 2 and in Fig. E.11 for values of  $b$  greater than or equal to 2. The results show that for very small values of  $b$ , the artifact was filtered out of the solution, but additional information needed to properly represent the outward wave was also filtered. The results for  $b = 1.5$  and  $b = 2$  showed the closest match to the exact solution, and these two cases have filter profiles closely resembling the cosine function. As the value of  $b$  increased further, the effect of the filter decreased, and the size of the displacement artifact increased toward the unfiltered case.

These results indicate that the cosine function produces an optimal weighting of the azimuthal wavenumbers near the angle of interest,  $\theta$ . More or less aggressive filtering approaches do not eliminate the presence of the the displacement artifact as effectively as the cosine approach presented in Chapter 2.

### E.3 Direction for Additional Study

It remains to be shown in detail how the cosine function interacts with the exponential term included in the inversion integral to eliminate the spurious displacement signal, and this may be of interest in the future. For the simplified case of a circular actuator on an

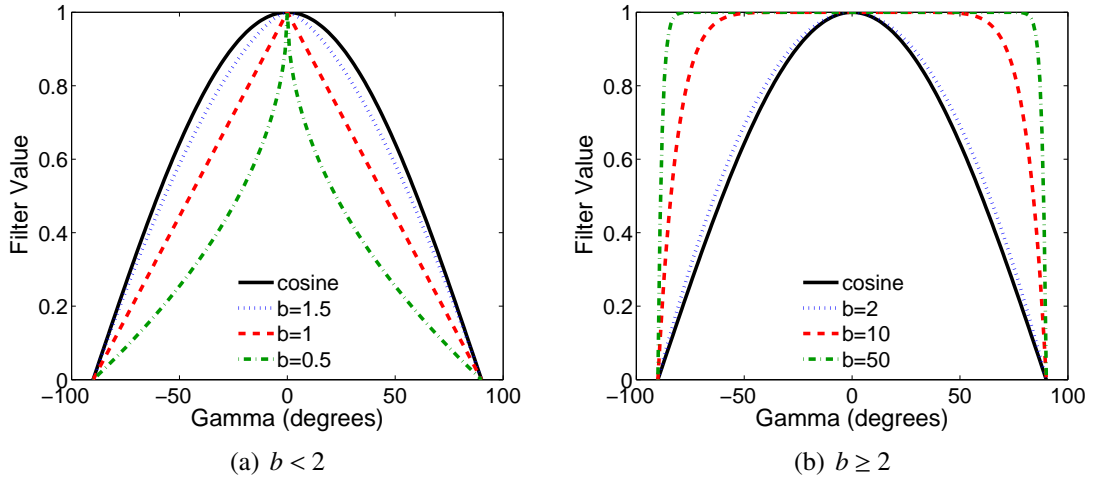


Figure E.9: Filter profiles for various filter exponent values,  $b$ . The profile of the cosine function is shown for comparison purposes in each figure.

isotropic plate, future consideration of this issue can focus on a reduced version of the equation. In this case, a single mode can be assumed, which eliminates the summation with respect to the admissible radial wavenumber  $\hat{K}$ . Furthermore, the expression

$$\frac{\Psi_i(\hat{K}, \Gamma, X_3, \omega)}{\Delta'(\hat{K}, \Gamma, \omega)} \hat{K} \quad (\text{E.9})$$

does not change with respect to the azimuthal wavenumber, and it can be moved out of the integral and treated as a constant value. After a change of variables, it can be shown that the critical aspect of calculating the displacement time history is the evaluation of the integral:

$$\int_0^{2\pi} e^{-i\alpha \cos \gamma} d\gamma \quad (\text{E.10})$$

where  $\alpha$  is a constant that depends on the angular frequency,  $\omega$ . Of course, for the isotropic case, this integral can be represented as a Bessel function as shown in Chapter 2. However, to be useful for more general cases as well, it must be remembered that this integral will be evaluated numerically, and the Bessel function substitution will not be permissible.

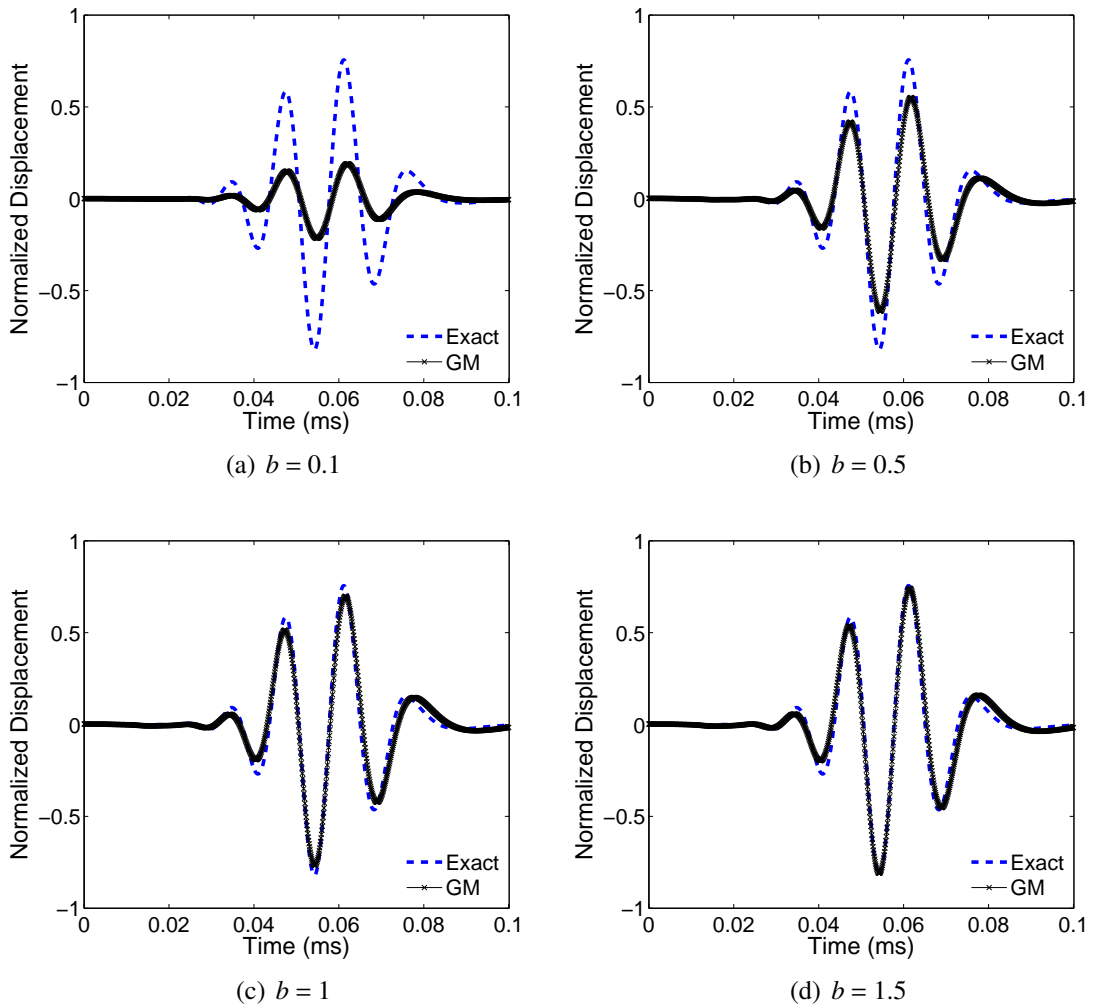


Figure E.10: Outward propagating wave solution for an aluminum laminate at 60 mm, showing the effect of various filter exponent values,  $b$ , less than 2.

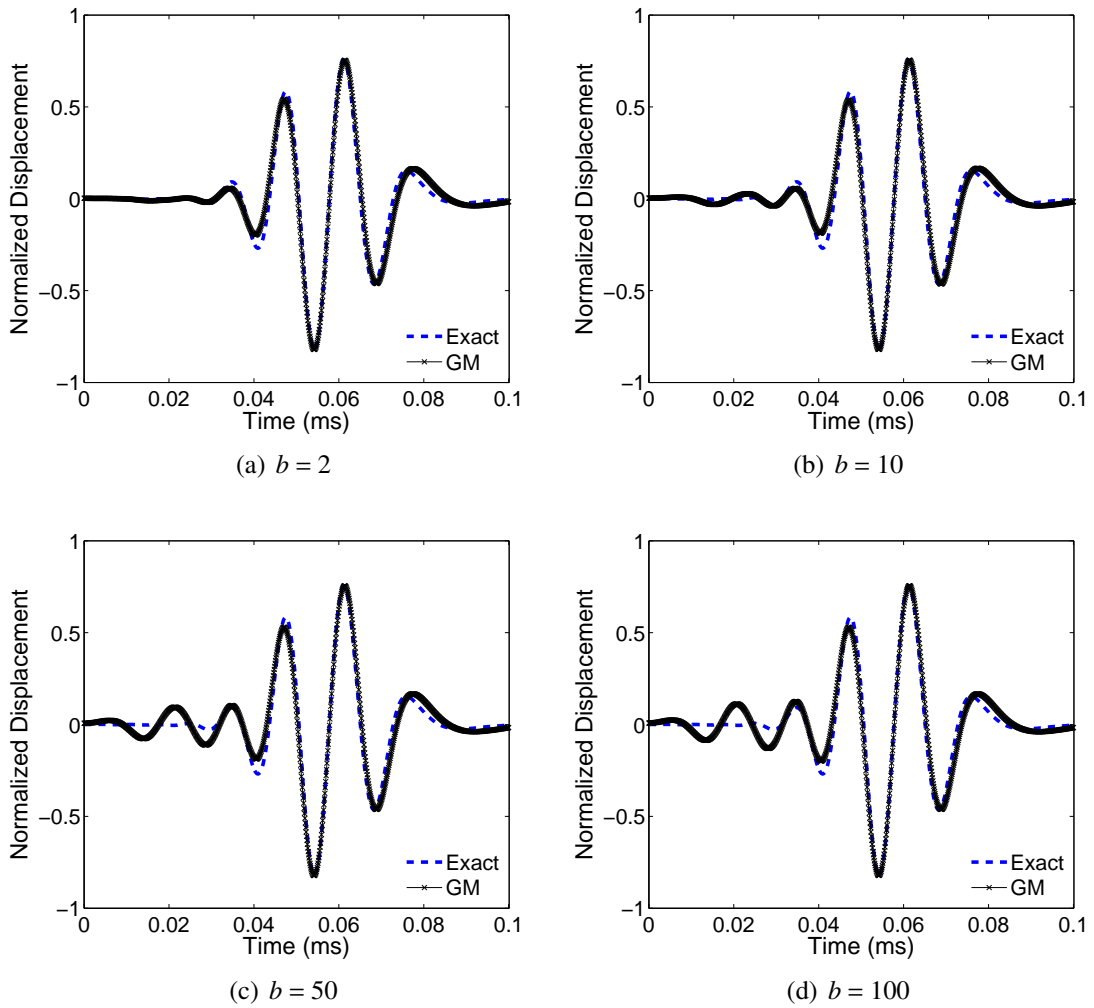


Figure E.11: Outward propagating wave solution for an aluminum laminate at 60 mm, showing the effect of various filter exponent values,  $b$ , greater than or equal to 2.

## BIBLIOGRAPHY

- [1] Negaard, G., *The History of the Aircraft Structural Integrity Program*, Aerospace Structures Information Analysis Center, Report 680.1B, Flight Dynamics Laboratory, 1980.
- [2] Wanhill, R. J. H., “Milestone Case Histories in Aircraft Structural Integrity,” *Comprehensive Structural Integrity*, Vol. 1, 2003, pp. 61–72. doi:[10.1016/B0-08-043749-4/01002-8](https://doi.org/10.1016/B0-08-043749-4/01002-8).
- [3] *Damage Tolerant Design Handbook*, Air Force Research Laboratory, 2011.
- [4] Giurgiutiu, V., “Damage Assessment of Structures—An Air Force Office of Scientific Research Structural Mechanics Perspective,” *Key Engineering Materials*, Vol. 347, 2007, pp. 69–74. doi:[10.4028/www.scientific.net/KEM.347.69](https://doi.org/10.4028/www.scientific.net/KEM.347.69).
- [5] Achenbach, J. D., “Structural Health Monitoring—What is the Prescription?” *Mechanics Research Communications*, Vol. 36, No. 2, 2009, pp. 137–142. doi:[10.1016/j.mechrescom.2008.08.011](https://doi.org/10.1016/j.mechrescom.2008.08.011).
- [6] Derriso, M. and Olson, S., “The Role of Structural Health Monitoring for Future Air Vehicles,” *Proceedings of the 47th AIAA/ASME/ASCE/AHS/ASC Structures, Structural Dynamics, and Materials Conference, Newport, Rhode Island*, 2006. doi:[10.2514/6.2006-1952](https://doi.org/10.2514/6.2006-1952).
- [7] Boller, C. and Buderath, M., “Fatigue in Aerostructures—Where Structural Health Monitoring Can Contribute to a Complex Subject,” *Philosophical Transactions of the Royal Society A: Mathematical, Physical and Engineering Sciences*, Vol. 365, No. 1851, 2007, pp. 561–587. doi:[10.1098/rsta.2006.1924](https://doi.org/10.1098/rsta.2006.1924).
- [8] Farrar, C. R. and Worden, K., “An Introduction to Structural Health Monitoring,” *Philosophical Transactions of the Royal Society A: Mathematical, Physical and Engineering Sciences*, Vol. 365, No. 1851, 2007, pp. 303–315. doi:[10.1098/rsta.2006.1928](https://doi.org/10.1098/rsta.2006.1928).
- [9] Raghavan, A. and Cesnik, C. E. S., “Review of Guided Wave Structural Health Monitoring,” *The Shock and Vibration Digest*, Vol. 39, No. 2, 2007, pp. 91–144. doi:[10.1177/0583102406075428](https://doi.org/10.1177/0583102406075428).

- [10] Giurgiutiu, V. and Soutis, C., “Enhanced Composites Integrity Through Structural Health Monitoring,” *Applied Composite Materials*, Vol. 19, 2012, pp. 813–829. doi:[10.1007/s10443-011-9247-2](https://doi.org/10.1007/s10443-011-9247-2).
- [11] Achenbach, J., *Wave Propagation in Elastic Solids*, Elsevier Science Publishers, Amsterdam, 1984.
- [12] Graff, K. F., *Wave Motion in Elastic Solids*, Dover Publications, New York, 1991.
- [13] Auld, B. A., *Acoustic Fields and Waves in Solids: Volumes I and II*, R. E. Kreiger Publishing, Malabar, Florida, 1990.
- [14] Rose, J. L., *Ultrasonic Waves in Solid Media*, Cambridge University Press, Cambridge, 2004.
- [15] Rayleigh, J. W. S., “On Wave Propagated Along the Plane Surface of an Elastic Solid,” *Proceedings of the London Mathematical Society*, Vol. 17, 1887, pp. 4–11.
- [16] Stoneley, R., “Elastic Waves at the Surface of Separation of Two Solids,” *Proceedings of the Royal Society of London. Series A, Containing Papers of a Mathematical and Physical Character*, Vol. 106, No. 738, 1924, pp. 416–428.
- [17] Love, A. E. H., *Some Problems of Geodynamics*, Cambridge University Press, Cambridge, 1926.
- [18] Lamb, H., “On Waves in an Elastic Plate,” *Proceedings of the Royal Society of London. Series A*, Vol. 93, No. 648, 1917, pp. 114–128.
- [19] Worlton, D., “Experimental Confirmation of Lamb Waves at Megacycle Frequencies,” *Journal of Applied Physics*, Vol. 32, No. 6, 1961, pp. 967–971. doi:[10.1063/1.1736196](https://doi.org/10.1063/1.1736196).
- [20] Jia, X., “Modal Analysis of Lamb Wave Generation in Elastic Plates by Liquid Wedge Transducers,” *The Journal of the Acoustical Society of America*, Vol. 101, 1997, pp. 834–842. doi:[10.1121/1.418041](https://doi.org/10.1121/1.418041).
- [21] Rose, J., Pelts, S., and Quarry, M., “A Comb Transducer Model for Guided Wave NDE,” *Ultrasonics*, Vol. 36, No. 1, 1998, pp. 163–169. doi:[10.1016/S0041-624X\(97\)00042-5](https://doi.org/10.1016/S0041-624X(97)00042-5).
- [22] Alers, G. and Burns, L., “EMAT Designs for Special Applications,” *Materials Evaluation*, Vol. 45, No. 10, 1987, pp. 1184–1194.
- [23] Wilcox, P., Lowe, M., and Cawley, P., “Omnidirectional Guided Wave Inspection of Large Metallic Plate Structures Using an EMAT Array,” *IEEE Transactions on Ultrasonics, Ferroelectrics and Frequency Control*, Vol. 52, No. 4, 2005, pp. 653–665. doi:[10.1109/TUFFC.2005.1428048](https://doi.org/10.1109/TUFFC.2005.1428048).

- [24] Gao, H., Ali, S., and Lopez, B., “Efficient Detection of Delamination in Multilayered Structures Using Ultrasonic Guided Wave EMATs,” *NDT & E International*, Vol. 43, No. 4, 2010, pp. 316–322. doi:[10.1016/j.ndteint.2010.03.004](https://doi.org/10.1016/j.ndteint.2010.03.004).
- [25] Betz, D. C., Thursby, G., Culshaw, B., and Staszewski, W. J., “Acousto-ultrasonic Sensing Using Fiber Bragg Gratings,” *Smart Materials and Structures*, Vol. 12, No. 1, 2003, pp. 122–128. doi:[10.1088/0964-1726/12/1/314](https://doi.org/10.1088/0964-1726/12/1/314).
- [26] Moyo, P., Brownjohn, J., Suresh, R., and Tjin, S., “Development of Fiber Bragg Grating Sensors for Monitoring Civil Infrastructure,” *Engineering Structures*, Vol. 27, No. 12, 2005, pp. 1828–1834. doi:[10.1016/j.engstruct.2005.04.023](https://doi.org/10.1016/j.engstruct.2005.04.023).
- [27] Light, G. M., Kwun, H., Kim, S., and Spinks, R. L., “Magnetostrictive Sensor for Active Health Monitoring in Structures,” *Smart NDE For Health Monitoring of Structural and Biological Systems*, International Society for Optics and Photonics, 2002, pp. 282–288. doi:[10.1117/12.469887](https://doi.org/10.1117/12.469887).
- [28] Kwun, H., Kim, S. Y., and Light, G. M., “The Magnetostrictive Sensor Technology for Long Range Guided Wave Testing and Monitoring of Structures,” *Materials Evaluation*, Vol. 61, No. 1, 2003, pp. 80–84.
- [29] Monkhouse, R., Wilcox, P., and Cawley, P., “Flexible Interdigital PVDF Transducers for the Generation of Lamb Waves in Structures,” *Ultrasonics*, Vol. 35, No. 7, 1997, pp. 489–498. doi:[10.1016/S0041-624X\(97\)00070-X](https://doi.org/10.1016/S0041-624X(97)00070-X).
- [30] Crawley, E. F. and De Luis, J., “Use of Piezoelectric Actuators as Elements of Intelligent Structures,” *AIAA journal*, Vol. 25, No. 10, 1987, pp. 1373–1385. doi:[10.2514/3.9792](https://doi.org/10.2514/3.9792).
- [31] Keilers, C. H., Chang, F.-K., et al., “Identifying Delamination in Composite Beams Using Built-in Piezoelectrics: Part I—Experiments and Analysis,” *Journal of Intelligent Material Systems and Structures*, Vol. 6, No. 5, 1995, pp. 649–663.
- [32] Giurgiutiu, V. and Zagari, A. N., “Characterization of Piezoelectric Wafer Active Sensors,” *Journal of Intelligent Material Systems and Structures*, Vol. 11, No. 12, 2000, pp. 959–976. doi:[10.1107/A1HU-23JD-M5AU-ENGW](https://doi.org/10.1107/A1HU-23JD-M5AU-ENGW).
- [33] Kessler, S. S., Spearing, S. M., and Soutis, C., “Damage Detection in Composite Materials Using Lamb Wave Methods,” *Smart Materials and Structures*, Vol. 11, No. 2, 2002, pp. 269–278. doi:[10.1088/0964-1726/11/2/310](https://doi.org/10.1088/0964-1726/11/2/310).
- [34] Valdés, S. H. D. and Soutis, C., “Real-time Nondestructive Evaluation of Fiber Composite Laminates Using Low-frequency Lamb Waves,” *The Journal of the Acoustical Society of America*, Vol. 111, 2002, pp. 2026–2033. doi:[10.1121/1.1466870](https://doi.org/10.1121/1.1466870).
- [35] Bent, A. A. and Hagood, N. W., “Piezoelectric Fiber Composites with Interdigitated Electrodes,” *Journal of Intelligent Material Systems and Structures*, Vol. 8, No. 11, 1997, pp. 903–919. doi:[10.1177/1045389X9700801101](https://doi.org/10.1177/1045389X9700801101).

- [36] High, J. W. and Wilkie, W. K., *Method of Fabricating NASA-standard Macro-fiber Composite Piezoelectric Actuators*, National Aeronautics and Space Administration TM-2003-212427, Langley Research Center, 2003.
- [37] Salas, K. I. and Cesnik, C. E. S., “Guided Wave Excitation by a CLoVER Transducer for Structural Health Monitoring: Theory and Experiments,” *Smart Materials and Structures*, Vol. 18, No. 7, 2009. doi:[10.1088/0964-1726/18/7/075005](https://doi.org/10.1088/0964-1726/18/7/075005).
- [38] Salas, K. and Cesnik, C., “CLOVER: An Alternative Concept for Damage Interrogation in Structural Health Monitoring Systems,” *Aeronautical Journal*, Vol. 113, No. 1144, 2009, pp. 339–356.
- [39] Senesi, M. and Ruzzene, M., “A Spiral Frequency Steerable Acoustic Transducer for SHM,” *Sensors and Smart Structures Technologies for Civil, Mechanical, and Aerospace Systems*, International Society for Optics and Photonics, 2011, pp. 798136–798136. doi:[10.1117/12.880332](https://doi.org/10.1117/12.880332).
- [40] Senesi, M. and Ruzzene, M., “A Frequency Selective Acoustic Transducer for Directional Lamb Wave Sensing,” *The Journal of the Acoustical Society of America*, Vol. 130, 2011, pp. 1899–1907. doi:[10.1121/1.3626165](https://doi.org/10.1121/1.3626165).
- [41] Viktorov, I. A., *Rayleigh and Lamb Waves: Physical Theory and Applications*, Plenum Press, New York, 1967.
- [42] Santosa, F. and Pao, Y.-H., “Transient Axially Asymmetric Response of an Elastic Plate,” *Wave Motion*, Vol. 11, No. 3, 1989, pp. 271–295. doi:[10.1016/0165-2125\(89\)90006-1](https://doi.org/10.1016/0165-2125(89)90006-1).
- [43] Lin, X. and Yuan, F., “Diagnostic Lamb Waves in an Integrated Piezoelectric Sensor/actuator Plate: Analytical and Experimental Studies,” *Smart Materials and Structures*, Vol. 10, No. 5, 2001, pp. 907–913. doi:[10.1088/0964-1726/10/5/307](https://doi.org/10.1088/0964-1726/10/5/307).
- [44] Rose, L. and Wang, C., “Mindlin Plate Theory for Damage Detection: Source Solutions,” *The Journal of the Acoustical Society of America*, Vol. 116, 2004, pp. 154–171. doi:[10.1121/1.1739482](https://doi.org/10.1121/1.1739482).
- [45] Giurgiutiu, V., “Tuned Lamb Wave Excitation and Detection with Piezoelectric Wafer Active Sensors for Structural Health Monitoring,” *Journal of Intelligent Material Systems and Structures*, Vol. 16, No. 4, 2005, pp. 291–306. doi:[10.1177/1045389X05050106](https://doi.org/10.1177/1045389X05050106).
- [46] Raghavan, A. and Cesnik, C. E. S., “Finite-dimensional Piezoelectric Transducer Modeling for Guided Wave Based Structural Health Monitoring,” *Smart Materials and Structures*, Vol. 14, 2005, pp. 1448–1461. doi:[10.1088/0964-1726/14/6/037](https://doi.org/10.1088/0964-1726/14/6/037).
- [47] Ditri, J. J. and Rose, J. L., “Excitation of Guided Waves in Generally Anisotropic Layers Using Finite Sources,” *Journal of Applied Mechanics*, Vol. 61, 1994, pp. 330–338. doi:[10.1115/1.2901449](https://doi.org/10.1115/1.2901449).



- [48] Datta, S. K., Shah, A. H., Bratton, R. L., and Chakraborty, T., “Wave Propagation in Laminated Composite Plates,” *Journal of the Acoustical Society of America*, Vol. 83, No. 6, 1988, pp. 2020–2026. doi:[10.1121/1.396382](https://doi.org/10.1121/1.396382).
- [49] Moulin, E., Assaad, J., and Delebarre, C., “Modeling of Lamb Waves Generated By Integrated Transducers in Composite Plates Using a Coupled Finite Element-Normal Modes Expansion Method,” *Journal of the Acoustical Society of America*, Vol. 107, No. 1, 2000, pp. 87–94. doi:[10.1121/1.428294](https://doi.org/10.1121/1.428294).
- [50] Velichko, A. and Wilcox, P. D., “Modeling the Excitation of Guided Waves in Generally Anisotropic Multilayered Media,” *Journal of the Acoustical Society of America*, Vol. 121, No. 1, 2007, pp. 60–69. doi:[10.1121/1.2390674](https://doi.org/10.1121/1.2390674).
- [51] Lowe, M. J. S., “Matrix Techniques for Modeling Ultrasonic Waves in Multilayered Media,” *IEEE Transactions on Ultrasonics, Ferroelectrics, and Frequency Control*, Vol. 42, No. 4, 1995, pp. 525–542. doi:[10.1109/58.393096](https://doi.org/10.1109/58.393096).
- [52] Thomson, W. T., “Transmission of Elastic Waves Through a Stratified Solid Medium,” *Journal of Applied Physics*, Vol. 21, 1950, pp. 89–93. doi:[10.1063/1.1699629](https://doi.org/10.1063/1.1699629).
- [53] Haskell, N., “The Dispersion of Surface Waves on Multilayered Media,” *Bulletin of the Seismological Society of America*, Vol. 43, No. 1, 1953, pp. 17–34.
- [54] Nayfeh, A. H., “The General Problem of Elastic Wave Propagation in Multilayered Anisotropic Media,” *The Journal of the Acoustical Society of America*, Vol. 89, 1991, pp. 1521–1531. doi:[10.1121/1.400988](https://doi.org/10.1121/1.400988).
- [55] Bottai, G. S., Chrysochoidis, N. A., Giurgiutiu, V., and Saravanos, D. A., “Analytical and Experimental Evaluation of Piezoelectric Wafer Active Sensors Performances for Lamb Waves Based Structural Health Monitoring in Composite Laminates,” *Health Monitoring of Structural and Biological Systems*, International Society for Optics and Photonics, 2007, pp. 65320N–65320N. doi:[10.1117/12.714970](https://doi.org/10.1117/12.714970).
- [56] Mienczakowski, M., Holmes, A., and Challis, R., “Modeling of Ultrasonic Wave Propagation in Composite Airframe Components,” *AIP Conference Proceedings*, Vol. 975, 2008, pp. 995–1001. doi:[10.1063/1.2902775](https://doi.org/10.1063/1.2902775).
- [57] Knopoff, L., “A Matrix Method for Elastic Wave Problems,” *Bulletin of the Seismological Society of America*, Vol. 54, No. 1, 1964, pp. 431–438.
- [58] Mal, A. K., “Wave Propagation in Layered Composite Laminates Under Periodic Surface Loads,” *Wave Motion*, Vol. 10, 1988, pp. 257–266. doi:[10.1016/0165-2125\(88\)90022-4](https://doi.org/10.1016/0165-2125(88)90022-4).
- [59] Lih, S. S. and Mal, A. K., “On the Accuracy of Approximate Plate Theories for Wave Field Calculations in Composite Laminates,” *Wave Motion*, Vol. 21, 1995, pp. 17–34. doi:[10.1016/0165-2125\(94\)00038-7](https://doi.org/10.1016/0165-2125(94)00038-7).

- [60] Mal, A. K. and Banerjee, S., “Guided Acoustic Emission Waves in a Thick Composite Plate,” *Health Monitoring and Smart NDE of Structural and Biological Systems*, Vol. 5394, International Society for Optics and Photonics, 2004, pp. 42–52. doi:[10.1117/12.543818](https://doi.org/10.1117/12.543818).
- [61] Banerjee, S., Prosser, W., and Mal, A., “Calculation of the Response of a Composite Plate to Localized Dynamic Surface Loads Using a New Wave Number Integral Method,” *Journal of Applied Mechanics*, Vol. 72, No. 1, 2005, pp. 18–24. doi:[10.1115/1.1828064](https://doi.org/10.1115/1.1828064).
- [62] Raghavan, A. and Cesnik, C. E. S., “Modeling of Guided-wave Excitation by Finite-dimensional Piezoelectric Transducers in Composite Plates,” *Proceedings of the 48th AIAA/ASME/ASCE/AHS/ASC Structures, Structural Dynamics, and Materials Conference, Honolulu, Hawaii*, 2007. doi:[10.2514/6.2007-1725](https://doi.org/10.2514/6.2007-1725).
- [63] Sundararaman, S. and Adams, D. E., “Modeling Guided Waves for Damage Identification in Isotropic and Orthotropic Plates Using a Local Interaction Simulation Approach,” *Journal of Vibration and Acoustics*, Vol. 130, No. 4, 2008. doi:[10.1115/1.2890389](https://doi.org/10.1115/1.2890389).
- [64] Lee, B. C. and Staszewski, W. J., “Modeling of Lamb Waves for Damage Detection in Metallic Structures: Part I. Wave Propagation,” *Smart Materials and Structures*, Vol. 12, No. 5, 2003, pp. 804–814. doi:[10.1088/0964-1726/12/5/018](https://doi.org/10.1088/0964-1726/12/5/018).
- [65] Strikwerda, J., *Finite Difference Schemes and Partial Differential Equations*, Society for Industrial and Applied Mathematics, Philadelphia, 2007.
- [66] Virieux, J., “P-SV Wave Propagation in Heterogeneous Media: Velocity-stress Finite-difference Method,” *Geophysics*, Vol. 51, No. 4, 1986, pp. 889–901.
- [67] Yamawaki, H. and Saito, T., “Numerical Calculation of Ultrasonic Propagation with Anisotropy,” *NDT & E International*, Vol. 33, No. 7, 2000, pp. 489–497. doi:[10.1016/S0963-8695\(00\)00020-7](https://doi.org/10.1016/S0963-8695(00)00020-7).
- [68] Ihlenburg, F., *Finite Element Analysis of Acoustic Scattering*, Vol. 132, Springer, New York, 1998.
- [69] J Talbot, R. and Przemieniecki, J., “Finite Element Analysis of Frequency Spectra for Elastic Waveguides,” *International Journal of Solids and Structures*, Vol. 11, No. 1, 1975, pp. 115–138. doi:[10.1016/0020-7683\(75\)90106-7](https://doi.org/10.1016/0020-7683(75)90106-7).
- [70] Alleyne, D. N., *Nondestructive Testing of Plates Using Ultrasonic Lamb Waves*, Ph.D. thesis, University of London, 1991.
- [71] Patera, A. T., “A Spectral Element Method for Fluid Dynamics: Laminar Flow in a Channel Expansion,” *Journal of Computational Physics*, Vol. 54, No. 3, 1984, pp. 468–488. doi:[10.1016/0021-9991\(84\)90128-1](https://doi.org/10.1016/0021-9991(84)90128-1).

- [72] Fornberg, B., *A Practical Guide to Pseudospectral Methods*, Vol. 1, Cambridge University Press, Cambridge, 1998.
- [73] Ostachowicz, W., Krawczuk, M., et al., “Spectral Finite Element and Genetic Algorithm for Crack Detection in Cantilever Rod,” *Key Engineering Materials*, Vol. 204, 2001, pp. 241–250. doi:[10.4028/www.scientific.net/KEM.204-205.241](https://doi.org/10.4028/www.scientific.net/KEM.204-205.241).
- [74] Zak, A., Krawczuk, M., and Ostachowicz, W., “Propagation of In-plane Elastic Waves in a Composite Panel,” *Finite Elements in Analysis and Design*, Vol. 43, No. 2, 2006, pp. 145–154. doi:[10.1016/j.finel.2006.08.003](https://doi.org/10.1016/j.finel.2006.08.003).
- [75] Zak, A., Radziński, M., Krawczuk, M., and Ostachowicz, W., “Damage Detection Strategies Based on Propagation of Guided Elastic Waves,” *Smart Materials and Structures*, Vol. 21, No. 3, 2012. doi:[10.1088/0964-1726/21/3/035024](https://doi.org/10.1088/0964-1726/21/3/035024).
- [76] Kim, Y., Ha, S., and Chang, F.-K., “Time-domain Spectral Element Method for Built-in Piezoelectric-actuator-induced Lamb Wave Propagation Analysis,” *AIAA journal*, Vol. 46, No. 3, 2008, pp. 591–600. doi:[10.2514/1.27046](https://doi.org/10.2514/1.27046).
- [77] Brebbia, C. A., Telles, J. C. F., and Wrobel, L. C., *Boundary Element Techniques: Theory and Applications in Engineering*, Vol. 5, Springer-Verlag, Berlin, 1984.
- [78] Cho, Y. and Rose, J. L., “A Boundary Element Solution for a Mode Conversion Study on the Edge Reflection of Lamb Waves,” *The Journal of the Acoustical Society of America*, Vol. 99, 1996, pp. 2097–2109. doi:[10.1121/1.415396](https://doi.org/10.1121/1.415396).
- [79] Zou, F., Benedetti, I., and Aliabadi, M., “A Boundary Element Model for Structural Health Monitoring Using Piezoelectric Transducers,” *Smart Materials and Structures*, Vol. 23, No. 1, 2014. doi:[10.1088/09641726/23/1/015022](https://doi.org/10.1088/09641726/23/1/015022).
- [80] Delsanto, P. P., Whitcombe, T., Chaskelis, H. H., and Mignogna, R. B., “Connection Machine Simulation of Ultrasonic Wave Propagation in Materials I: the One-dimensional Case,” *Wave Motion*, Vol. 16, 1992, pp. 65–80. doi:[10.1016/0165-2125\(92\)90047-6](https://doi.org/10.1016/0165-2125(92)90047-6).
- [81] Delsanto, P. P., Schechter, R. S., Chaskelis, H. H., Mignogna, R. B., and Kline, R., “Connection Machine Simulation of Ultrasonic Wave Propagation in Materials II: the Two-dimensional Case,” *Wave Motion*, Vol. 20, 1994, pp. 295–314. doi:[10.1016/0165-2125\(94\)90016-7](https://doi.org/10.1016/0165-2125(94)90016-7).
- [82] Delsanto, P. P., Schechter, R. S., and Mignogna, R. B., “Connection Machine Simulation of Ultrasonic Wave Propagation in Materials III: the Three-dimensional Case,” *Wave Motion*, Vol. 26, 1997, pp. 329–339. doi:[10.1016/S0165-2125\(97\)00013-9](https://doi.org/10.1016/S0165-2125(97)00013-9).
- [83] Lee, B. C. and Staszewski, W. J., “Modeling of Lamb Waves for Damage Detection in Metallic Structures: Part II. Wave Interactions with Damage,” *Smart Materials and Structures*, Vol. 12, No. 5, 2003, pp. 815–824. doi:[10.1088/0964-1726/12/5/019](https://doi.org/10.1088/0964-1726/12/5/019).

- [84] Lee, B. C. and Staszewski, W. J., “Lamb Wave Propagation Modeling for Damage Detection: I. Two-dimensional Analysis,” *Smart Materials and Structures*, Vol. 16, No. 5, 2007, pp. 249–259. doi:[10.1088/0964-1726/16/2/003](https://doi.org/10.1088/0964-1726/16/2/003).
- [85] Lee, B. C. and Staszewski, W. J., “Lamb Wave Propagation Modeling for Damage Detection: II. Damage Monitoring Strategy,” *Smart Materials and Structures*, Vol. 16, No. 5, 2007, pp. 260–274. doi:[10.1088/0964-1726/16/2/004](https://doi.org/10.1088/0964-1726/16/2/004).
- [86] Sinor, M., “Numerical Modeling and Visualization of Elastic Waves Propagation in Arbitrary Complex Media,” *8th Workshop on Multimedia in Physics Teaching and Learning of the European Physical Society, Graz*, 2004.
- [87] Sundararaman, S. and Adams, D. E., “Accuracy and Convergence Using a Local Interaction Simulation Approach in One, Two, and Three Dimensions,” *Journal of Applied Mechanics*, Vol. 76, No. 3, 2009. doi:[10.1115/1.2871105](https://doi.org/10.1115/1.2871105).
- [88] Nadella, K. S. and Cesnik, C. E. S., “Numerical Simulation of Wave Propagation in Composite Plates,” *Health Monitoring of Structural and Biological Systems*, Vol. 8348, International Society for Optics and Photonics, 2012. doi:[10.1117/12.915239](https://doi.org/10.1117/12.915239).
- [89] Nadella, K. S. and Cesnik, C. E. S., “Simulation of Guided Wave Propagation in Isotropic and Composite Structures using LISA,” *Proceedings of the 53rd AIAA/ASME/ASCE/AHS/ASC Structures, Structural Dynamics, and Materials Conference, Honolulu, Hawaii*, 2012. doi:[10.2514/6.2012-1387](https://doi.org/10.2514/6.2012-1387).
- [90] Nadella, K. S. and Cesnik, C. E., “Local Interaction Simulation Approach for Modeling Wave Propagation in Composite Structures,” *CEAS Aeronautical Journal*, 2013, pp. 1–14. doi:[10.1007/s13272-012-0061-9](https://doi.org/10.1007/s13272-012-0061-9).
- [91] Nadella, K. S. and Cesnik, C. E. S., “Piezoelectric Coupled LISA for Guided Wave Generation and Propagation,” *Health Monitoring of Structural and Biological Systems*, Vol. 8695, International Society for Optics and Photonics, 2013. doi:[10.1117/12.2008959](https://doi.org/10.1117/12.2008959).
- [92] Alleyne, D. N. and Cawley, P., “The Interaction of Lamb Waves with Defects,” *IEEE Transactions on Ultrasonics, Ferroelectrics and Frequency Control*, Vol. 39, No. 3, 1992, pp. 381–397. doi:[10.1109/58.143172](https://doi.org/10.1109/58.143172).
- [93] Ghosh, T., Kundu, T., and Karpur, P., “Efficient Use of Lamb Modes for Detecting Defects in Large Plates,” *Ultrasonics*, Vol. 36, No. 7, 1998, pp. 791–801. doi:[10.1016/S0041-624X\(98\)00012-2](https://doi.org/10.1016/S0041-624X(98)00012-2).
- [94] McKeon, J. and Hinders, M., “Lamb Wave Scattering From a Through Hole,” *Journal of Sound and Vibration*, Vol. 224, No. 5, 1999, pp. 843–862. doi:[10.1006/jsvi.1999.2164](https://doi.org/10.1006/jsvi.1999.2164).
- [95] Fromme, P. and Sayir, M. B., “Measurement of the Scattering of a Lamb Wave by a Through Hole in a Plate,” *The Journal of the Acoustical Society of America*, Vol. 111, No. 3, 2002, pp. 1165–1170. doi:[10.1121/1.1448338](https://doi.org/10.1121/1.1448338).

- [96] Grahn, T., “Lamb Wave Scattering From a Circular Partly Through-thickness Hole in a Plate,” *Wave Motion*, Vol. 37, No. 1, 2003, pp. 63–80. doi:[10.1016/S0165-2125\(02\)00051-3](https://doi.org/10.1016/S0165-2125(02)00051-3).
- [97] Giurgiutiu, V., “Lamb Wave Generation With Piezoelectric Wafer Active Sensors for Structural Health Monitoring,” *Smart Structures and Materials*, International Society for Optics and Photonics, 2003, pp. 111–122. doi:[10.1117/12.483492](https://doi.org/10.1117/12.483492).
- [98] Yu, L. and Giurgiutiu, V., “In-situ 2-D Piezoelectric Wafer Active Sensor Arrays for Guided Wave Damage Detection,” *Ultrasonics*, Vol. 48, No. 2, 2008, pp. 117–134. doi:[10.1016/j.ultras.2007.10.008](https://doi.org/10.1016/j.ultras.2007.10.008).
- [99] Basri, R. and Chiu, W., “Numerical Analysis on the Interaction of Guided Lamb Waves with a Local Elastic Stiffness Reduction in Quasi-isotropic Composite Plate Structures,” *Composite Structures*, Vol. 66, No. 1, 2004, pp. 87–99. doi:[10.1016/j.compstruct.2004.04.025](https://doi.org/10.1016/j.compstruct.2004.04.025).
- [100] Giurgiutiu, V. and Santoni-Bottai, G., “Structural Health Monitoring of Composite Structures with Piezoelectric-Wafer Active Sensors,” *AIAA journal*, Vol. 49, No. 3, 2011, pp. 565–581. doi:[10.2514/1.J050641](https://doi.org/10.2514/1.J050641).
- [101] Ng, C. T. and Veidt, M., “A Lamb-wave-based Technique for Damage Detection in Composite Laminates,” *Smart Materials and Structures*, Vol. 18, 2009. doi:[10.1088/0964-1726/18/7/074006](https://doi.org/10.1088/0964-1726/18/7/074006).
- [102] Veidt, M. and Ng, C.-T., “Influence of Stacking Sequence on Scattering Characteristics of the Fundamental Anti-symmetric Lamb Wave at Through Holes in Composite Laminates,” *The Journal of the Acoustical Society of America*, Vol. 129, No. 3, 2011, pp. 1280–1287. doi:[10.1121/1.3533742](https://doi.org/10.1121/1.3533742).
- [103] Guo, N. and Cawley, P., “The Interaction of Lamb Waves with Delaminations in Composite Laminates,” *The Journal of the Acoustical Society of America*, Vol. 94, 1993, pp. 2240–2246. doi:[10.1121/1.407495](https://doi.org/10.1121/1.407495).
- [104] Li, F., Peng, H., Sun, X., Wang, J., and Meng, G., “Wave Propagation Analysis in Composite Laminates Containing a Delamination Using a Three-Dimensional Spectral Element Method,” *Mathematical Problems in Engineering*, Vol. 2012, 2012. doi:[10.1155/2012/659849](https://doi.org/10.1155/2012/659849).
- [105] Hu, N., Shimomukai, T., Yan, C., and Fukunaga, H., “Identification of Delamination Position in Cross-ply Laminated Composite Beams Using  $S_0$  Lamb Mode,” *Composites Science and Technology*, Vol. 68, No. 6, 2008, pp. 1548–1554. doi:[10.1016/j.compscitech.2007.10.015](https://doi.org/10.1016/j.compscitech.2007.10.015).
- [106] Ip, K.-H. and Mai, Y.-W., “Delamination Detection in Smart Composite Beams Using Lamb Waves,” *Smart Materials and Structures*, Vol. 13, No. 3, 2004, pp. 544–551. doi:[10.1088/0964-1726/13/3/013](https://doi.org/10.1088/0964-1726/13/3/013).

- [107] Ng, C. T. and Veidt, M., “Scattering of the Fundamental Anti-symmetric Lamb Wave at Delaminations in Composite Laminates,” *Journal of the Acoustical Society of America*, Vol. 129, No. 3, 2011, pp. 1288–1296. doi:[10.1121/1.3533741](https://doi.org/10.1121/1.3533741).
- [108] Toyama, N., Noda, J., and Okabe, T., “Quantitative Damage Detection in Cross-ply Laminates Using Lamb Wave Method,” *Composites Science and Technology*, Vol. 63, No. 10, 2003, pp. 1473–1479. doi:[10.1016/S0266-3538\(03\)00163-5](https://doi.org/10.1016/S0266-3538(03)00163-5).
- [109] Duflo, H., Morvan, B., and Izbicki, J.-L., “Interaction of Lamb Waves on Bonded Composite Plates with Defects,” *Composite Structures*, Vol. 79, No. 2, 2007, pp. 229–233. doi:[10.1016/j.compstruct.2006.01.003](https://doi.org/10.1016/j.compstruct.2006.01.003).
- [110] Ramadas, C., Balasubramaniam, K., Joshi, M., and Krishnamurthy, C., “Interaction of the Primary Anti-symmetric Lamb Mode ( $A_0$ ) with Symmetric Delaminations: Numerical and Experimental Studies,” *Smart Materials and Structures*, Vol. 18, No. 8, 2009. doi:[10.1088/0964-1726/18/8/085011](https://doi.org/10.1088/0964-1726/18/8/085011).
- [111] Ramadas, C., Balasubramaniam, K., Joshi, M., and Krishnamurthy, C., “Interaction of Guided Lamb Waves with an Asymmetrically Located Delamination in a Laminated Composite Plate,” *Smart Materials and Structures*, Vol. 19, No. 6, 2010. doi:[10.1088/0964-1726/19/6/065009](https://doi.org/10.1088/0964-1726/19/6/065009).
- [112] Kaczmarek, H., “Lamb Wave Interaction with Impact-induced Damage in Aircraft Composite: Use of the  $A_0$  Mode Excited by Air-coupled Transducer,” *Journal of Composite Materials*, Vol. 37, No. 3, 2003, pp. 217–232. doi:[10.1177/0021998303037003423](https://doi.org/10.1177/0021998303037003423).
- [113] Schubert, L., Barth, M., Klesse, T., Köhler, B., and Frankenstein, B., “Guided Elastic Waves and Their Impact Interaction in CFRP Structures Characterized by 3-D Laser Scanning Vibrometry,” *Health Monitoring of Structural and Biological Systems*, International Society for Optics and Photonics, 2008, pp. 69350G–69350G. doi:[10.1117/12.777510](https://doi.org/10.1117/12.777510).
- [114] Sekhar, B. V. S., Balasubramaniam, K., and Krishnamurthy, C. V., “Structural Health Monitoring of Fiber-reinforced Composite Plates for Low-velocity Impact Damage Using Ultrasonic Lamb Wave Tomography,” *Structural Health Monitoring*, Vol. 5, No. 3, 2006, pp. 243–253. doi:[10.1177/1475921706067739](https://doi.org/10.1177/1475921706067739).
- [115] Reynolds, W. D., Coelho, C., Kim, S. B., Chattopadhyay, A., and Arnold, S. M., “Active Damage Localization in Anisotropic Materials Using Guided Waves,” *Proceedings of 50th AIAA/ASME/ASCE/AHS/ASC Structures, Structural Dynamics, and Materials Conference, Palm Springs, CA*, 2009. doi:[10.2514/6.2009-2327](https://doi.org/10.2514/6.2009-2327).
- [116] Sohn, H., Swenson, E. D., Olson, S. E., DeSimio, M. P., and Dutta, D., “Delamination Detection in Composite Structures Using Laser Vibrometer Measurement of Lamb Waves,” *Health Monitoring of Structural and Biological Systems*, International Society for Optics and Photonics, 2010, pp. 76500P–76500P. doi:[10.1117/12.847316](https://doi.org/10.1117/12.847316).

- [117] Diamanti, K., Hodgkinson, J. M., and Soutis, C., “Detection of Low-velocity Impact Damage in Composite Plates Using Lamb Waves,” *Structural Health Monitoring*, Vol. 3, No. 1, 2004, pp. 33–41. doi:[10.1177/1475921704041869](https://doi.org/10.1177/1475921704041869).
- [118] Rogge, M. D. and Leckey, C. A. C., “Characterization of Impact Damage in Composite Laminates using Guided Wavefield Imaging and Local Wavenumber Domain Analysis,” *Ultrasonics*, Vol. 53, No. 7, 2013. doi:[10.1016/j.ultras.2012.12.015](https://doi.org/10.1016/j.ultras.2012.12.015).
- [119] Pavelko, I., Pavelko, V., Smolyaninovs, M., Pfeifer, H., and Wevers, M., “Simulation of Impact Damage in a Composite Plate and its Detection,” *Proceedings of the 2012 COMSOL Conference, Milan, Italy*, 2012.
- [120] Singh, D., El Guerjouma, R., and Bentahar, M., “Interaction of Fundamental Lamb Modes with a Point Impact Damaged Zone in Composite Plates,” *Acoustics 2012 Nantes*, 2012.
- [121] Balasubramaniam, K., Ramadas, C., Padiyar, J., and Krishnamurthy, C., “Interaction of Guided Lamb Waves with Delaminations and Discontinuities in Composite Plate-like Structures,” *AIP Conference Proceedings*, Vol. 1335, 2011, pp. 1483–1490. doi:[10.1063/1.3592106](https://doi.org/10.1063/1.3592106).
- [122] Lamboul, B., Passilly, B., Roche, J.-M., and Osmont, D., “Impact Damage Detection in Sandwich Composite Structures Using Lamb Waves and Laser Vibrometry,” *AIP Conference Proceedings*, Vol. 1511, 2013, pp. 1003–1010. doi:[10.1063/1.4789153](https://doi.org/10.1063/1.4789153).
- [123] Liu, Y. and Chattopadhyay, A., “Low-velocity Impact Damage Monitoring of a Sandwich Composite Wing,” *Journal of Intelligent Material Systems and Structures*, 2012. doi:[10.1177/1045389X12453964](https://doi.org/10.1177/1045389X12453964).
- [124] Ajith, V. and Gopalakrishnan, S., “Guided-wave-based Structural Health Monitoring of Built-up Composite Structures Using Spectral Finite Element Method,” *Health Monitoring of Structural and Biological Systems*, International Society for Optics and Photonics, 2012, pp. 83480O–83480O. doi:[10.1117/12.914775](https://doi.org/10.1117/12.914775).
- [125] Staszewski, W. and Worden, K., “Signal Processing for Damage Detection,” *Health Monitoring of Aerospace Structures*, 2004, pp. 163–206.
- [126] Niethammer, M., Jacobs, L. J., Qu, J., and Jarzynski, J., “Time-frequency Representations of Lamb Waves,” *The Journal of the Acoustical Society of America*, Vol. 109, No. 5, 2001, pp. 1841–1847. doi:[10.1121/1.1357813](https://doi.org/10.1121/1.1357813).
- [127] Kim, Y. Y. and Kim, E.-H., “Effectiveness of the Continuous Wavelet Transform in the Analysis of Some Dispersive Elastic Waves,” *The Journal of the Acoustical Society of America*, Vol. 110, No. 1, 2001, pp. 86–94. doi:[10.1121/1.1378348](https://doi.org/10.1121/1.1378348).
- [128] Okabe, Y., Fujibayashi, K., Shimazaki, M., Soejima, H., and Ogisu, T., “Delamination Detection in Composite Laminates Using Dispersion Change Based on Mode Conversion of Lamb Waves,” *Smart Materials and Structures*, Vol. 19, No. 11, 2010. doi:[10.1088/0964-1726/19/11/115013](https://doi.org/10.1088/0964-1726/19/11/115013).

- [129] Sohn, H., Park, G., Wait, J. R., Limback, N. P., and Farrar, C. R., “Wavelet-based Active Sensing for Delamination Detection in Composite Structures,” *Smart Materials and Structures*, Vol. 13, No. 1, 2004, pp. 153–160. doi:[10.1088/0964-1726/13/1/017](https://doi.org/10.1088/0964-1726/13/1/017).
- [130] Mallat, S. G. and Zhang, Z., “Matching Pursuits with Time-frequency Dictionaries,” *Signal Processing, IEEE Transactions on*, Vol. 41, No. 12, 1993, pp. 3397–3415. doi:[10.1109/78.258082](https://doi.org/10.1109/78.258082).
- [131] Zhang, G., Zhang, S., and Wang, Y., “Application of Adaptive Time-frequency Decomposition in Ultrasonic NDE of Highly-scattering Materials,” *Ultrasonics*, Vol. 38, No. 10, 2000, pp. 961–964. doi:[10.1016/S0041-624X\(00\)00036-6](https://doi.org/10.1016/S0041-624X(00)00036-6).
- [132] Hong, J.-C., Sun, K. H., and Kim, Y. Y., “The Matching Pursuit Approach Based on the Modulated Gaussian Pulse for Efficient Guided-wave Damage Inspection,” *Smart Materials and Structures*, Vol. 14, No. 4, 2005, pp. 548–560. doi:[10.1088/0964-1726/14/4/013](https://doi.org/10.1088/0964-1726/14/4/013).
- [133] Das, S., Kyriakides, I., Chattopadhyay, A., and Papandreou-Suppappola, A., “Monte Carlo Matching Pursuit Decomposition Method for Damage Quantification in Composite Structures,” *Journal of Intelligent Material Systems and Structures*, Vol. 20, No. 6, 2009, pp. 647–658. doi:[10.1177/1045389X08097386](https://doi.org/10.1177/1045389X08097386).
- [134] Vizzini II, A. J. and Chattopadhyay, A., “Lamb-wave-based Feature Extraction of Damage in a Stiffened Composite Panel Under Varying Temperature,” *Health Monitoring of Structural and Biological Systems*, International Society for Optics and Photonics, 2012, pp. 83481P–83481P. doi:[10.1117/12.915413](https://doi.org/10.1117/12.915413).
- [135] Gribonval, R., “Fast Matching Pursuit with a Multiscale Dictionary of Gaussian Chirps,” *Signal Processing, IEEE Transactions on*, Vol. 49, No. 5, 2001, pp. 994–1001. doi:[10.1109/78.917803](https://doi.org/10.1109/78.917803).
- [136] Raghavan, A. and Cesnik, C. E., “Guided-wave Signal Processing Using Chirplet Matching Pursuits and Mode Correlation for Structural Health Monitoring,” *Smart Materials and Structures*, Vol. 16, No. 2, 2007, pp. 355–366. doi:[10.1088/0964-1726/16/2/014](https://doi.org/10.1088/0964-1726/16/2/014).
- [137] Nadella, K. S., Salas, K. I., and Cesnik, C. E. S., “Characterization of Guided-wave Propagation in Composite Plates,” *Health Monitoring of Structural and Biological Systems*, Vol. 7650, International Society for Optics and Photonics, 2010. doi:[10.1117/12.847887](https://doi.org/10.1117/12.847887).
- [138] Brown, J. W. and Churchill, R. V., *Complex Variables and Applications*, Vol. 7, McGraw-Hill, New York, 1996.
- [139] Raghavan, A. and Cesnik, C. E. S., “Modeling of Piezoelectric-based Lamb-wave Generation and Sensing for Structural Health Monitoring,” *Sensors and Smart Structures Technologies for Civil, Mechanical, and Aerospace Systems*, Vol. 5391, International Society for Optics and Photonics, 2004. doi:[10.1117/12.540269](https://doi.org/10.1117/12.540269).



- [140] Agrawal, S., Singh, K. K., and Sarkar, P. K., “Impact Damage on Fibre-reinforced Polymer Matrix Composite - A Review,” *Journal of Composite Materials*, 2013. doi:10.1177/0021998312472217.
- [141] Rhodes, M. D., Williams, J. G., and Starnes, J. H., “Low-velocity Impact Damage in Graphite-fiber Reinforced Epoxy Laminates,” *Polymer Composites*, Vol. 2, No. 1, 1981, pp. 36–44. doi:10.1002/pc.750020108.
- [142] Shyr, T. and Pan, Y., “Impact Resistance and Damage Characteristics of Composite Laminates,” *Composite Structures*, Vol. 62, No. 2, 2003, pp. 193–203. doi:10.1016/S0263-8223(03)00114-4.
- [143] Bacry, E., “LastWave 3.1 Software,” <http://www.cmap.polytechnique.fr/~bacry/LastWave>, accessed 5 April 2014.